

FABRICATION OF SILICON CARBIDE-ON-SILICON BASED DEVICES FOR
EFFECTIVE NEAR-FIELD THERMAL RADIATION TRANSFER

A THESIS SUBMITTED TO
THE GRADUATE SCHOOL OF NATURAL AND APPLIED SCIENCES
OF
MIDDLE EAST TECHNICAL UNIVERSITY

BY

ELİF BEGÜM ELÇİOĞLU

IN PARTIAL FULFILLMENT OF THE REQUIREMENTS
FOR
THE DEGREE OF DOCTOR OF PHILOSOPHY
IN
MECHANICAL ENGINEERING

NOVEMBER 2018

Approval of the thesis:

**FABRICATION OF SILICON CARBIDE-ON-SILCON BASED DEVICES
FOR EFFECTIVE NEAR-FIELD THERMAL RADIATION TRANSFER**

submitted by **ELİF BEGÜM ELÇİOĞLU** in partial fulfillment of the requirements
for the degree of **Doctor of Philosophy in Mechanical Engineering Department,**
Middle East Technical University by,

Prof. Dr. Halil Kalıpçılar
Dean, Graduate School of **Natural and Applied Sciences** _____

Prof. Dr. Mehmet Ali Sahir Arıkan
Head of Department, **Mechanical Engineering** _____

Assoc. Prof. Dr. Hanife Tuba Okutucu Özyurt
Supervisor, **Mechanical Eng. Dept., METU** _____

Prof. Dr. M. Pınar Mengüç
Co-Supervisor, **Mechanical Eng. Dept., Özyeğin Uni.** _____

Examining Committee Members:

Asst. Prof. Dr. Özgür Bayer
Mechanical Eng. Dept., METU _____

Assoc. Prof. Dr. Hanife Tuba Okutucu Özyurt
Mechanical Eng. Dept., METU _____

Asst. Prof. Dr. Kıvanç Azgın
Mechanical Eng. Dept., METU _____

Prof. Dr. Hilmi Volkan Demir
Electrical and Electronics Eng. Dept., Bilkent Uni. _____

Assoc. Prof. Dr. Mustafa Kulakcı
Institute of Earth and Space Sciences, Eskişehir Technical
Uni. _____

Date: _____

I hereby declare that all information in this document has been obtained and presented in accordance with academic rules and ethical conduct. I also declare that, as required by these rules and conduct, I have fully cited and referenced all material and results that are not original to this work.

Name, Last name : Elif Begüm Elçiođlu

Signature :

ABSTRACT

FABRICATION OF SILICON CARBIDE-ON-SILICON BASED DEVICES FOR EFFECTIVE NEAR-FIELD THERMAL RADIATION TRANSFER

Elçioğlu, Elif Begüm
Ph.D., Department of Mechanical Engineering
Supervisor: Doç. Dr. Hanife Tuba Okutucu Özyurt
Co-Supervisor: Prof. Dr. M. Pınar Mengüç

November 2018, 183 pages

Near-field radiative transfer (NFRT) has attracted attention due to the potential of obtaining improved amount of heat transfer between media separated by distances comparable to or smaller than the dominant wavelength of emission. Such potential has been demonstrated in vacuum environments to form the basis of mainly near-field thermophotovoltaic systems and further, conversion into electricity with high system efficiency. In this thesis, an analytical analysis is performed to gain insight on near-field radiative transfer of p- and n-type Si, GaAs, InSb, InP wafers, along with SiC. Results show that the wafer type, doping level, and crystal structure are effective parameters on such systems. The spectral NFRT flux between SiC and n-type InSb pair exceeded the blackbody limit by more than 3 orders of magnitude. Along with the analytical studies, another objective of this thesis is to conceptualize and construct a device consisting of SiC-on-Si media, bonded through patterned SiO₂ walls, encapsulating vacuum towards a nanoscale gap. SiC, supporting surface phonon polaritons which is studied in detail in relation to its crystallization behavior through thermal annealing. Here it is aimed to investigate its phononic behavior both in the amorphous and crystalline states. To the best of the author's knowledge, a materials crystal state dependence of near-field radiative transfer is discovered for the first time, in this dissertation. Achievements and challenges faced during the fabrication of a

NFRT device are presented in detail. The proposed device is designed and fabricated to operate under ambient conditions, and explore a wider application framework.

Keywords: Near-Field Radiative Transfer, Silicon Carbide, Sputtering, Thermal Annealing, Fusion Bonding.

ÖZ

ETKİN YAKIN ALAN IŞINIM TRANSFERİ İÇİN SİLİSYUM ÜZERİNE SİLİSYUM KARBÜR BAZLI CİHAZLARIN ÜRETİMİ

Elçioğlu, Elif Begüm
Doktora, Makina Mühendisliği Bölümü
Tez Yöneticisi: Doç. Dr. Hanife Tuba Okutucu Özyurt
Ortak Tez Yöneticisi: Prof. Dr. M. Pınar Mengüç

Kasım 2018, 183 sayfa

Isıl ışınım dalga boyu ile kıyaslanabilir ya da daha küçük mesafeler ile birbirinden ayrılmış ortamlar arasında gerçekleşecek ısı transferinde elde edilen potansiyel artışlar, yakın alan ışınımı konusunu ön plana çıkarmıştır. Bu potansiyel, çoğunlukla kontrollü vakum ortamlarında gözlenmiş, ilgili çalışmalar ısı transferindeki bu artışı elektrik enerjisine dönüştürme amacını taşıyan yakın alan ışınımı bazlı yüksek verimli termofotovoltaik sistemlerin temelini oluşturmuştur. Konunun fiziksel altyapısının ayrıntılandırılması amaçlı yapılan analitik çalışmada p-türü ve n-türü Si, GaAs, InSb, InP altaşlar ile SiC malzemelerinin yakın alan ışınımı davranışı incelenmiştir. Altaş türü, altaş katkılama oranı ve kristal yapının sistemlerin yakın alan ışınımı davranışı üzerinde etkili olduğu görülmüştür. Özellikle SiC ve n-türü InSb malzemeler arasındaki yakın alan ışınımı spektral ısı akısının, siyah cisim limitine kıyasla üç mertebeden daha fazla artış sağladığı görülmüştür. Yapılan analizlere ek olarak, yakın alan ışınımını gözlemlemede kullanılabilecek, Si üzerine kaplanmış SiC ince film temelli ve SiO₂ birleşim alanına sahip ortamlar arasında nano ölçekte bir vakum boşluğu içeren kapalı bir cihaz üretilmesi amaçlanmıştır. Yüzey fonon polaritonlarını destekleyen bir malzeme olan SiC'ün ısı işleme tabi tutularak kristalleşme davranışı incelenmiş ve fononik davranışının amorf ve kristal yapıda araştırılması amaçlanmıştır.

Yazarın bilgisi dahilinde, bir malzemenin yakın alan ışınımı davranışının içyapı ile bağlantısı bu çalışma ile literatürde ilk kez yer alacaktır. Cihaz fabrikasyonunda elde edilen başarılı sonuçlar ile birlikte karşılaşılan güçlüklerle de detaylıca değinilmiştir. Bahsi geçen cihaz ortam koşullarında çalışabilecek şekilde tasarlanıp üretilmiştir ve bu şekilde daha çok sayıda yakın alan ışınımı uygulamasının yapılabilirliğinin keşfedilmesi amaçlanmıştır.

Anahtar Kelimeler: Yakın Alan Işınımı, Silisyum Karbür, Magnetron Saçtırma, Isıl İşlem, Füzyon Birleştirme.

To My Mother

ACKNOWLEDGMENTS

The course of this work has been a unique period of my life. Many people offered their valuable support and contribution, all of which I am grateful for.

First, I am sincerely grateful for the guidance provided by my advisor Assoc. Prof. Dr. Hanife Tuba Okutucu Özyurt and letting me study this topic. Prof. Okutucu has been not only a source of scientific support and encouragement whenever I needed, but also an inspiration for being such a determined and hardworking academician. I appreciate the guidance and support provided by my co-advisor Prof. Dr. M. Pınar Mengüç, whom I had many hours of brainstorming not only face to face but also online and on the phone, regarding my studies. The feedbacks and enlightening suggestions made by my Thesis Committee Members, Prof. Dr. Hilmi Volkan Demir and Asst. Prof. Dr. Kıvanç Azgın are gratefully acknowledged.

I am grateful to members of Nanoboyut Laboratory of Physics Dept., Eskişehir Technical University, especially to Assoc. Prof. Dr. Mustafa Kulakcı for letting me gain my know-how about MEMS processes by letting me directly perform thin film deposition, thermal annealing, etching, and photolithography processes. I thank Asst. Prof. Dr. İsmail Özgür Özer for letting me use the annealing furnace at the Dept. of Materials Science and Engineering of Eskişehir Technical University.

The later stages of sample fabrication (thin film deposition, etching, photolithography, wafer level bonding, and dicing) are performed at METU-MEMS Research and Applications Center. I thank the Director of METU-MEMS Center, Prof. Dr. Tayfun Akın for letting me use the facilities. I am grateful to Orhan Akar, Scientific Project Specialist at the METU-MEMS Center, for letting me take the clean room training focused on essentials and keeping the clean room and thereby the samples clean, as well as his continuous help and critical thinking during the processes. I thank Levent Abat for performing chemical processes; Selçuk Keskin, Adem Saraç, and Oğuzhan Temel for their support during the fabrication processes.

Within a certain part of the research for this dissertation and TÜBİTAK research project (under grant no: 214M308), a collaboration has been made with Assoc. Prof. Dr. Keunhan (Kay) Park and Mohammad Ghashami, at the University of Utah. I am grateful to their efforts and suggestions in our ongoing joint work.

Special thanks go to my teammate and very good friend Dr. Azadeh Didari, whom I had countless hours discussing near-field radiative transfer, and sharing curiosity. I thank Melih Korkmaz from Nanoboyut Laboratory for his continuous help and support during the hours I spent in the cleanroom. I thank my teammate Reha Denker for his contributions to our joint work. I am grateful to Aziz Koyuncuoğlu who was ready to share his knowledge and experience when I needed a second opinion about the processes. I thank my teammate Ahmet Güngör for his contributions in modeling SiO₂ wall patterns. I am thankful to my dear friend Serel Akyol, who has been a source of support whenever I needed.

I am grateful to Prof. Dr. Nevzat Kırış, the Director of Sivrihisar Vocational School at Eskişehir Osmangazi University, for letting me take the courses and perform the studies required to complete my Ph.D. work, as well as for his continuous support from the start date of my work as an instructor at Mechanics Program of Sivrihisar Vocational School, Eskişehir Osmangazi University.

I could not be able to ever fully express my gratitude to my dear mother, my best friend, and my source of inspiration, Prof. Dr. Ömür Şaylıgil. She has shown being a great mother, a successful academician and mentor at the same time as effortless. Without having her by my side, I could never pursue my dreams this confidently and comfortably. Thank you for giving me this great life.

The financial support provided by TÜBİTAK under the grant no 214M308 is acknowledged.

TABLE OF CONTENTS

ABSTRACT.....	v
ÖZ	vii
ACKNOWLEDGMENTS	x
TABLE OF CONTENTS.....	xii
LIST OF TABLES	xv
LIST OF FIGURES	xvi
NOMENCLATURE	xx
CHAPTERS	
INTRODUCTION	1
1.1. Worldwide Energy Consumption and Demand	1
1.2. Promising Energy Conversion Techniques.....	2
1.3. Shrinkage of Length-Scale of Contemporary Energy Devices.....	3
1.4. Why Near-Field Radiative Transfer Holds Potential in TPV's?	4
1.5. Aim of the Dissertation.....	6
CHAPTER 2	7
LITERATURE REVIEW	7
2.1. Part I: Overview of Near-Field Radiative Transfer Literature.....	7
2.1.1. Near-Field Radiative Transfer	7
2.1.2. Effects of Emitter and Receiver Thickness with Vacuum Gap	12
2.1.3. Previous Work on Near-Field Thermophotovoltaics.....	14
2.2. Part II: Overview of SiC Fabrication Literature	17
CHAPTER 3	29
AN ANALYTICAL ASSESSMENT TO NEAR-FIELD RADIATIVE TRANSFER	29

3.1. Evanescent and Propagating Waves.....	29
3.2. Materials to be integrated in a Near-Field Radiative Transfer Device	30
3.3. Analytical Work on the Spectral Radiative Flux between Parallel Bulks	32
3.4. Material Dependence of the Spectral Heat Flux Between Parallel Media.....	33
3.4.1. Si Wafer Type Dependence of Near-Field Radiative Flux	34
3.4.2. Near-Field Radiative Flux Between III-V Group Semiconductors.....	38
3.4.3. Near-Field Radiative Flux Between SiC Media with Different Crystal Structure	41
3.5. Discussions on the Thin Film Thickness, Substrate Material, Nanostructure Material and Size on Near-Field Radiative Transfer Performance	44
3.6. Results	45
3.7. Summary	46
CHAPTER 4	49
NEAR-FIELD RADIATIVE TRANSFER HARVESTING DEVICE FABRICATION	49
4.1. Introduction	49
4.2. Fabrication Processes - Part I.....	53
4.2.1. SiC Film Deposition via RF Magnetron Sputtering.....	54
4.2.2. Wet Etching of SiC – Trial Study Results	65
4.2.3. Photolithography and Lift-off – Trial Study Results	67
4.2.4. Thermal Annealing of SiC: Part I	70
4.2.5. Thermal Annealing of SiC: Part II.....	84
4.2.6. Thermal Annealing of SiC: Part III.....	100
4.3. Fabrication Processes- Part II.....	107
4.3.1. Fabrication Scenarios and Process Steps	107
4.3.2. SiO ₂ Wall Geometry and Photolithography Mask Design.....	111
4.3.3. SiC Thin Film Deposition by RF Magnetron Sputtering	114
4.3.4. SiO ₂ Thin Film Deposition by PECVD	116
4.3.5. Photolithography	116
4.3.6. Wet Etching of SiO ₂ and Removal of the PR	117
4.3.7. Surface Characterization Using Atomic Force Microscopy	118
4.3.8. Wafer Bonding at METU-MEMS Center: Part I.....	120

4.3.9. Sample Preparation for Wafer Bonding at EVG.....	126
4.3.10. Wafer Bonding Efforts at EVG.....	130
4.3.11. Wafer Bonding at METU-MEMS Center: Part II.....	138
4.3.12. Wafer Bonding at METU-MEMS Center: Part III	140
CHAPTER 5	145
NEAR-FIELD RADIATIVE TRANSFER MEASUREMENTS	145
2.5. Near-Field Radiative Transfer Tests: Part I (Vacuum).....	145
2.6. Near-Field Radiative Transfer Tests: Part II (Ambient Environment)	148
2.7. Summary of the Near-Field Radiative Transfer Tests	150
CHAPTER 6	151
CONCLUSIONS AND FUTURE WORK	151
6.1. Conclusions.....	151
6.2. Future Work.....	154
REFERENCES	155
APPENDICES	171
A. Permission for the Reuse of Figure 5	171
B. Permission for the Reuse of Figure 42	172
C. Preliminary Near-Field Radiative Transfer Test Results from Utah Nano- Energy Laboratory	177
CURRICULUM VITAE.....	179

LIST OF TABLES

TABLES

Table 1. Band positions and their origins for IR spectra.....	22
Table 2. Crystal type, orientation and diffraction angle information.....	25
Table 3. Drude Model parameters of Si wafers, by [111].....	34
Table 4. Drude Model parameters of Si wafers and silicide films, by [112].	35
Table 5. Drude-Lorentz Model parameters of GaAs, InP, and InAs wafers, by [115].	38
Table 6. Drude-Lorentz Model parameters of SiC, by [95] and [119].	43
Table 7. Reference sample characteristics (purchased from Griffith University).	53
Table 8. RF power and corresponding voltages for low RF power calibration deposition.	60
Table 9. TM outputs recorded during the process.....	60
Table 10. Surface colors for certain SiC thin film thicknesses. Adapted from [69].	63
Table 11. Photolithography and lift-off parameters.....	68
Table 12. Allowed temperature and process duration limits of the RTP device.....	71
Table 13. RTA process parameters (Part I).....	72
Table 14. RTA process variables (Part II).	84
Table 15. Si-C vibration peak locations of the fast-annealed samples, under vacuum.	90
Table 16. Si-C vibration peak locations of the fast-annealed samples, under N ₂	99
Table 17. Conventional furnace annealing process parameters (Part III).....	101
Table 18. PECVD parameters for SiO ₂ thin film deposition.	116
Table 19. AFM imaging and measurement parameters.	118

LIST OF FIGURES

FIGURES

Figure 1. A basic TPV system and main energy inputs [5].	3
Figure 2. Plane parallel-plates configuration, as a simplification for a TPV system...	5
Figure 3. Map showing the theoretical and applied efforts of our research group. ...	28
Figure 4. Evanescent wave as a result of total internal reflection.	30
Figure 5. Variation of heat transfer coefficient with the gap between SiC and SiO ₂ emitter and receiver [109]. Reprinted with permission from (S. Shen, A. Narayanaswamy, G. Chen “Surface Phonon Polaritons Mediated Energy Transfer between Nanoscale Gaps” Nano Lett. 2009, 9, 8, 2909-2913.). Copyright (2018) American Chemical Society.	31
Figure 6. Spectral NFRT flux for n- and p-type Si wafers at 293 K [104].	35
Figure 7. Spectral NFRT flux for n- and p-type Si wafers at 80 K.	36
Figure 8. Spectral NFRT flux for metal silicides at 293 K [101].	37
Figure 9. Spectral NFRT flux between n- and p-type GaAs wafer pairs at 1000 K [105].	39
Figure 10. Spectral NFRT flux between n-/p-type, undoped InSb wafer pairs at 750 K [105].	40
Figure 11. Spectral NFRT flux between n-type GaAs, InSb, InP wafer pairs at 750 K [105].	40
Figure 12. Dielectric properties of SiC, dependent on internal structure.	42
Figure 13. Spectral NFRT flux between structurally different SiC pairs, at 1000 K.	43
Figure 14. Geometry of the problem, adapted from [42].	45
Figure 15. NFRT device general fabrication scheme [97].	50
Figure 16. Process steps and the facilities used in NFRT device fabrication.	51
Figure 17. Photographs of RF magnetron sputtering chamber, A: target location, B: substrate holder, C: thickness monitors, D: view ports.	54
Figure 18. Wafer pieces and shadow masks. Left: (A) shadow masks, (B) wafer pieces before deposition, right: after deposition.	55
Figure 19. SiC film thickness data collection points (top), example data output (bottom).	56
Figure 20. Targets situation and melted In pieces.	57
Figure 21. SiC-on-Si surface appearance dependent on SiC film thickness.	61
Figure 22. Photographs of deposited SiC thin films on full-size Si wafers.	62
Figure 23. Voltage - RF power characteristics of the developed sputtering recipe (along with the dates of the processes).	64
Figure 24. TM output during depositions (along with the dates of the processes).	65

Figure 25. Samples, after etching a 1 cm × 1 cm coated wafer piece.....	67
Figure 26. Photolithography and lift-off trial scheme.....	68
Figure 27. Sample surfaces after step 4.	69
Figure 28. Surfaces of the SiC coated samples after lift-off process.	69
Figure 29. FTIR transmission spectra of the samples annealed in forming gas.	73
Figure 30. FTIR transmission spectra of the samples annealed under vacuum.	73
Figure 31. FTIR absorbance values of samples annealed at 900°C (forming gas and vacuum).....	74
Figure 32. FTIR absorbance values of samples annealed at 1000°C (forming gas and vacuum).....	75
Figure 33. FTIR absorbance values of samples annealed at 1100°C (forming gas and vacuum).....	75
Figure 34. FTIR absorbance values of samples annealed at 1200°C (forming gas and vacuum).....	76
Figure 35. Si-C stretching band shape and curve fits for forming gas annealed samples.	77
Figure 36. Si-C stretching band shape and curve fits for vacuum annealed samples.....	77
Figure 37. Surface colors of the samples before and after annealing.	78
Figure 38. Surface changes after forming gas annealing.	79
Figure 39. Surface changes after vacuum annealing.....	80
Figure 40. XRD spectra of the samples annealed under forming gas.....	81
Figure 41. XRD spectra of samples annealed under vacuum.	83
Figure 42. Transmission spectra of SiC samples, by Spitzer et al. [131] "Reprinted (figure) with permission from [W. G. Spitzer, D. A. Kleinman, C. J. Frosch, Physical Review, 113, 1, 133-136, 1959.] Copyright (2018) by the American Physical Society. https://doi.org/10.1103/PhysRev.113.133 "	85
Figure 43. FTIR absorbance of untreated and vacuum annealed 100 nm SiC samples.	86
Figure 44. FTIR absorbance of untreated and vacuum-annealed 200 nm SiC samples.	87
Figure 45. Raw transmission data for vacuum-annealed samples and Si.	88
Figure 46. Transmission of vacuum-annealed 100 nm SiC samples, and data of Spitzer et al. [131].	89
Figure 47. Transmission of vacuum-annealed 200 nm SiC samples, and data of Spitzer et al [131].	89
Figure 48. XRD spectra of the 100 nm SiC samples annealed under vacuum.	91
Figure 49. XRD spectra of the 200 nm SiC samples annealed under vacuum.	92
Figure 50. Surface conditions of the samples after RTA under vacuum.	93
Figure 51. Hardness of the SiC-on-Si samples, in comparison with literature.....	95
Figure 52. Elastic moduli of the SiC-on-Si samples, in comparison with literature..	96
Figure 53. FTIR absorbance of untreated and N ₂ -annealed 100 nm SiC samples.....	97
Figure 54. FTIR absorbance of untreated and N ₂ -annealed 200 nm SiC.....	97

Figure 55. Transmission of N ₂ -annealed 100 nm SiC samples, and data of Spitzer et al [131].	98
Figure 56. Transmission of N ₂ -annealed 200 nm SiC samples, and data of Spitzer et al [131].	98
Figure 57. XRD spectra of the samples annealed under N ₂ (Part II).	100
Figure 58. FTIR absorbance of the samples (100 nm, 200 nm) annealed in Ar.	102
Figure 59. XRD spectra of the SiC samples annealed under Ar, at 1300°C.	103
Figure 60. Photographs of the samples after annealing at 1300°C, in Ar.	104
Figure 61. Transmission of Ar-annealed samples at 1300°C, and data of Spitzer et al [131].	105
Figure 62. Photographs of the samples after annealing at 1200°C, in Ar.	105
Figure 63. Transmission of Ar-annealed samples at 1200°C, and data by of Spitzer et al [131].	106
Figure 64. Raw transmission data for Ar-annealed samples and Si.	106
Figure 65. Process stages of Scenario A. The dimensions are not drawn to scale.	109
Figure 66. Process stages of Scenario B. The dimensions are not drawn to scale.	110
Figure 67. SiO ₂ wall structures integrated in NFRT device. Units are in millimeters.	112
Figure 68. Photolithography mask design with optimized configurations. The dimensions are in millimeters.	113
Figure 69. Photolithography mask design for the outer surface of the device.	114
Figure 70. Sample surface after step 6 of photolithography.	117
Figure 71. AFM characterizations: Scenario A.	119
Figure 72. AFM characterizations: Scenario B.	119
Figure 73. c-SAM image of the bonded pair at 500 μm resolution.	125
Figure 74. c-SAM image of the bonded pair at 10 μm resolution.	125
Figure 75. Fabrication scheme designed for the double-sided patterning of EF 3677.	128
Figure 76. Inner patterns of the samples EF 3677 and EF 3679.	129
Figure 77. Alignment markers on EF 3677 and EF 3679.	130
Figure 78. AFM characterization locations on EF 3677.	131
Figure 79. AFM image and roughness characterization from near the center of EF 3677.	132
Figure 80. AFM image and roughness characterization away from the center of EF 3677.	133
Figure 81. Optical microscope images from the surfaces of EF 3677 and EF 3679.	134
Figure 82. AFM characterization from near the center of EF 3677, after chemical cleaning.	135
Figure 83. AFM characterization away from the center of EF 3677, after chemical cleaning.	136
Figure 84. IR inspection on the bonded EF 3677-EF 3679 pair.	137

Figure 85. c-SAM image of the test pair, after plasma activation, at METU-MEMS.	138
Figure 86. c-SAM image of the actual pair, after plasma activation, at METU-MEMS.	139
Figure 87. High resolution c-SAM image of the bonded (thermal-oxide) pair.	140
Figure 88. Samples preparation for measurements (left), electrical connection pads (right).....	146
Figure 89. The vacuum chamber hosting NFRT measurements (left), sample mounting on the nano-positioner (right).....	146
Figure 90. NFRT experiment results with 231 nm SiC-on-Si samples.	147
Figure 91. Experiment results with 100 nm SiO ₂ on 50 nm SiC-on-Si samples (with air-gap).	148
Figure 92. Experiment results with 100 nm SiO ₂ on 50 nm SiC-on-Si samples (with vacuum gap).	149
Figure 93. NFRT experiment results with 50 nm SiC-on-Si samples.	177
Figure 94. NFRT experiment results with 200 nm SiC-on-Si samples.	178

NOMENCLATURE

Symbols

A	Amplitude
C	Speed of light in vacuum, 2.998×10^8 [m/s]
d	Gap [nm]
h	Planck constant, 6.626×10^{-34} [J s]
H	Full width half maximum
I	Current [A]
k_B	Boltzmann constant, 1.381×10^{-23} [J/ K]
L	Grain size
n	Refractive index
P	PV system power output [W]
q''	Heat flux [W/m^2]
t	Thickness [nm]
T	Absolute temperature [K]
V	Voltage [V]

Greek symbols

ε	Dielectric function
Γ	Damping rate
λ	Wavelength of thermal radiation [m]
Θ	Mean energy of a Planck oscillator [J]
θ	Bragg diffraction angle [$^\circ$]
ω	Angular frequency [rad/s]
V	Voltage [V]

Subscripts

a	Annealing
∞	High frequency
L	Lattice vibration
LO	Longitudinal optical
oc	Open circuit
p	Plasma
sc	Short circuit
TO	Transverse optical

CHAPTER 1

INTRODUCTION

1.1. Worldwide Energy Consumption and Demand

Homo-sapiens are known as the species that have been able to build tools, think rationally, and consume energy. Energy is the key requirement for the continuation of life even at the basic level, and hence described by the capacity for doing work. In the ever-increasing need for efficient energy use, new perspectives are under extensive research to find out more about both eco-friendly and efficient energy conversion techniques, and their scaling up to larger communities.

Fossil fuels that have been under extensive use globally are to be available for a finite time dependent on the reserves left. International Energy Agency reported from 1971-2016 statistics [1] that coal (38.4%) and natural gas (23.2%) were the primary sources in electricity generation, while the non-hydro renewable sources (e.g., geothermal, solar, wind, biofuels, etc.) and waste had a 8% share in total electric energy generation worldwide. In contrary to the fossil fuels, renewable sources such as solar, wind, wave, and so forth are available based on their utility potential at the geographical region concerned. Dependence on fossil fuels and increased energy demand worldwide are expected to cause increase of CO₂ emissions. It is therefore required to develop efficient systems utilizing renewable sources rather than fossil fuel based power generation systems [2].

Photovoltaic (PV) energy conversion is one prominent technology utilizing solar radiation. Carbajales-Dale et al. [3] reported for every unit of electric energy invested that the electricity return of solar PV is much less than that of wind power as an alternative energy source, and the PV industry itself consumes around 90% of its electric energy output. In this respect, it is required to upgrade the efficiency of PV systems.

Thermophotovoltaic (TPV) energy conversion systems operate according to the PV principle, by utilizing a thermal source other than the sun. Application of the near-field radiative transfer (NFRT) principles to improve the efficiency of TPV devices or devices resembling TPV systems is under research. In this dissertation, how NFRT principles have been applied to such systems are also outlined.

1.2. Promising Energy Conversion Techniques

With the emerging trend of seeking for highly efficient power generation methods that comply with environmental consciousness, it is seen that some of the criteria are conflicting with one another in the system design stage. These parameters should be optimized. As pointed out by [2], while minimization of emissions is desired, this criteria might be conflicting with minimization of operation cost and investment and minimization of fuel cost, while it supports minimizing the wastes. Designing an efficient and eco-friendly system is a multivariate task.

TPV energy conversion describes the process of directly converting heat into electricity. In contrary to central power generation in large power plants in industrialized regions for which the waste heat may be up to 50% of the input, a more distributed generation of heat and electricity would be desired if such systems are accompanied by renewable generators (e.g., solar PV's) and electrical storage systems [4]. When compared to (solar) PV's, for which the intensity of thermal radiation decreases due to the large distance between the surface of the sun and the earth, and could change considerably due to location, cycle, and atmospheric absorption dependent intensity, spectrum and angle; in TPV's a large number of heat sources including waste heat could be potentially used [4]. A generic TPV system consists of an infrared (IR) emitter, a PV cell, and an optional filter for spectral control. A schematic showing the components and main energy inputs of a TPV system are shown in Figure 1 [5].

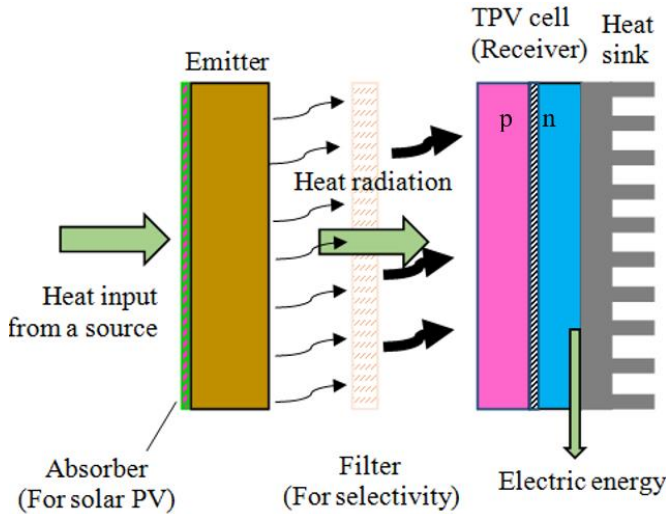


Figure 1. A basic TPV system and main energy inputs [5].

1.3. Shrinkage of Length-Scale of Contemporary Energy Devices

In “There’s Plenty of Room at the Bottom” [6], Richard P. Feynman touches on to possibilities of controlling and manipulating things in the small scale, by addressing issues that attracted significant attention later by the scientific community. Most of his predictions such as development of data storage systems and use of nanorobots in biomedical applications have been proven to be realized by the tools of modern technology and have been in use for a considerable time. In “The Theory of Heat Radiation” [7], Max Planck expressed that the ordinary laws of emission and absorption of light are applicable to systems of dimensions larger than the wavelengths of the rays. When the distance between objects is compared to the wavelength (λ) of radiation, two regimes governed by different physical laws are identified. If the objects are located at a distance greater than this limit, thermal radiation takes place in the far-field regime; while for a sub- λ separation between objects, radiative heat transfer effects due to the near-field interactions should be considered [8]. In order to determine the near-field radiative transfer contributions, the wave nature of the radiation should thus be considered, whereas ray tracing or geometric optics approach may be sufficient, depending on the problem, in studying far-field radiative transfer

[8]. The near-field effects that have a critical impact on the radiative transfer are radiation tunneling and plasmonic/phononic interactions [8].

Building such systems in small length scale to utilize such phenomena require advances in microfabrication. Gordon E. Moore reported [9] that implementation of a larger number of devices on a single semiconductor substrate had the advantage of reducing costs. He predicted that the number of components in an integrated function would double in every two years. Together with the advances in nanotechnology (enabling fabrication, characterization, and implementation of smaller components to obtain more efficient devices) and improvements in modeling and simulations, sophisticated small length-scale systems have been realized, and energy harvesting at small length-scales has come to the fore. One example would be the use of waste heat at moderate temperatures (around 500 K) and potential of harvesting lukewarm photons as discussed by Ben-Abdallah [10] in a near-field TPV scheme potentially reaching the Carnot limit.

1.4. Why Near-Field Radiative Transfer Holds Potential in TPV's?

Net radiative heat transfer calculations in a basic TPV system can be performed by the assumption of two isothermal blackbody surfaces (one being held at a higher temperature than the other) with a nonparticipating medium in between [4]. This basic picture is similar to one of the fundamental scenarios that have been comprehensively investigated in the literature (as it will be elaborated in Chapter 2), termed as parallel plates configuration, and illustrated in Figure 2.

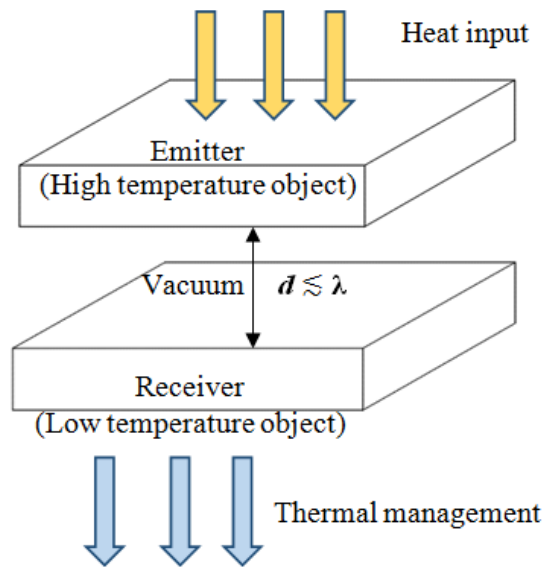


Figure 2. Plane parallel-plates configuration, as a simplification for a TPV system.

Application of energy transfer modalities to TPV systems were discussed by [11]. The researchers identified possible mechanisms based on their impacts on system efficiency. When the photon energy is lower than the PV cell bandgap, they do not serve in creating electron-hole pairs, and they only heat up the cell. Photon energies much higher than the TPV cell bandgap causes Joule heating from the unused part of the heat input. It is therefore important to use a proper heat source with minimum amount of inaccessible portions [11]. In relation to spectral selectivity concept, the advantage of obtaining potentially quasi-monochromatic near-field radiative heat fluxes were regarded an important advantage [11]. Through theoretical calculations, researchers showed that both the electrical output power and TPV system efficiency could be positively affected if there are near-field effects.

Inclusion of far- and near-field radiative transfer principles in TPV and TPV-like systems are outlined in Chapter 2 with potential improvements and challenges reported.

1.5. Aim of the Dissertation

The main aim of this dissertation is to fabricate a device that could be utilized in demonstrating near-field radiative transfer. The device has been fabricated such that NFRT measurements can be performed under ambient laboratory conditions to explore applications under realistic conditions, unlike the fundamental tests conducted in vacuum chambers. The device has nano- and microscale resolution in components' dimensions, by depositing nanometer thick SiC and SiO₂ thin films on Si substrates. The ultimate aim in investigating NFRT is development of an understanding on harvesting of the increased IR radiation in the near-field, into electricity. On the other hand, conversion of heat into electricity through the built device is not within the scope of this dissertation. Chapter 2 outlines the experimental efforts on NFRT, along with the summaries of the related parts of theoretical and TPV-system scale efforts from the literature.

Through the fabrication processes, it is also aimed at providing discussions from the materials point of view. It has been shown through the theoretical analyses provided in Chapter 3 that fabrication and material related parameters are also variables of near-field radiative transfer and should be considered in building nano-energy harvesting devices. To the best of the author's knowledge, this study is the first in reporting crystal structure's potential effects on NFRT behavior of SiC structures.

Details on the material selection procedures and the methodology of device fabrication are provided in detail in Chapter 4. As materials-related characteristics such as material type, wafer type (p-type, n-type, or undoped), doping level, crystal structure have been shown to be affecting the performances of systems (in Chapter 3), crystallization of SiC was also aimed by means of thermal annealing. In Chapter 5, outcomes of a joint work concerned with the measurements of the samples fabricated in this work, under vacuum, are presented. Results clearly show proximity effects. Conclusions and future work suggestions are provided in Chapter 6.

CHAPTER 2

LITERATURE REVIEW

2.1. Part I: Overview of Near-Field Radiative Transfer Literature

To date, near-field radiative transfer has been studied both experimentally and theoretically, and orders of magnitude greater energy transfer had been shown to take place in NFRT systems, when compared to the blackbody limit. A systematic literature review is given in this Section based on the configurations and parameters studied.

2.1.1. Near-Field Radiative Transfer

NFRT phenomenon has been investigated for systems of plane-parallel media, as well as tip-plate, and sphere-plate configurations. Apart from a few reports (outlined herein), NFRT between media with a finite temperature gradient were investigated only in controlled vacuum environments.

In plane-parallel configuration, the work by Hargreaves [12] was the first concerned with the proximity effect on NFRT between two optically flat and ≈ 100 nm thick Cr coated plates in a vacuum environment ($<10^{-5}$ Torr). Domoto et al. [13] measured the radiative flux between two Cu disks (of 8.5 cm diameter) held at liquid He temperatures, in a vacuum chamber (10^{-12} Torr). They considered gap values between emitter and receiver of 0.201 cm – 0.001 cm. Both the results of [12] and [13] indicated a strong separation dependence of radiative flux between objects. Ito et al. [14] measured the NFRT between two diced fused-quartz wafers in vacuum (5×10^{-3} Pa). The gap between substrates (receiver held at 293 K, with emitter-receiver temperature differences of 5 K - 20 K) was formed by means of pillars of 0.5 μm , 1 μm , and 2 μm height. Pillars were fabricated through conventional micromachining approaches. Results showed that the heat flux and heat transfer coefficient increased with decreasing separation. Hu et al. [15] employed polystyrene particles (with diameter of 1 μm) as spacers between glass optical flats (diameter: 1.27 cm, thickness: 0.635 cm)

and measured the radiative flux in a vacuum chamber (at 8.5×10^{-3} Pa). Results showed that the radiative flux increased with increasing hot surface temperature. Ottens et al. [16] studied the near-field heat flux between two macroscopic sapphire plates ($50 \times 50 \times 5$ mm³) with temperature differences of 2.5 K-30 K, in a vacuum environment (2.5×10^{-7} Torr). Results showed the near-field heat fluxes' inverse proportionality with distance and direct proportionality with temperature difference.

Kralik et al. [17] measured the NFRT between two W layers (150 nm thick) coated on Al₂O₃ substrates by keeping the receiver and emitter respectively at 5 K and 10 K - 40 K, in a vacuum environment ($< 10^{-8}$ Pa). They formed gaps of around 1 μ m - 300 μ m between emitter and receiver. Their results revealed for all the cases that the heat flux was larger than that between blackbodies. St-Gelais et al. [18] reported on NFRT by an on-chip platform consisted of two parallel suspended nano-beams, in a vacuum environment (1.5×10^{-4} Torr). They modulated the distance between the nano-beams electrostatically, and studied the NFRT between SiO₂ coated (100 nm thick) Si₃N₄ parts (via successive deposition of SiO₂, Si₃N₄, and SiO₂ on a Si wafer) by forming a temperature gradient of 130 K. Their results revealed that the NFRT was larger than the blackbody limit for gaps up to 600 nm. Ijiro and Yamada [19] measured the NFRT between two macroscopic SiO₂ substrates (of diameter 25 mm and thickness 5 mm) near 300 K, located around 1 μ m - 50 μ m away from each other with 4.1 K - 19.5 K temperature difference, in vacuum (4.5×10^{-4} Pa). They considered both plane plates and plates with Au coated micro-cavities (of size 5 μ m \times 5 μ m). Results showed that the presence of Au affected NFRT, and the radiative flux was significantly improved for the cavity-cavity case in comparison to a pair of plane plates case, for separations smaller than 3 μ m. The radiative flux decreased with increasing gap and decreasing temperature difference, outperforming the blackbody limit for the temperature gradients considered for gap values ≤ 3 μ m. Lim et al. [20] investigated the NFRT between P doped Si coated (around 600 nm) fused silica wafers, down to gaps of 400 nm, under vacuum ($< 10^{-3}$ Pa). Their results showed that the radiative heat transfer coefficient decreased with increasing gap value between media, and outperformed the blackbody limit for gaps up to ≈ 900 nm.

Watjen et al. [21] considered two doped Si plates (of 1 cm×1 cm size, and around 500 μm thickness), and measured the radiative flux for separations of 200 nm - 780 nm, near room temperature, with temperature differences of 2 K - 30 K. To ensure the gap between the emitter and receiver, SiO₂ posts (with 200 nm - 800 nm height) were fabricated. Their measurements showed that the radiative transfer coefficient decreased significantly with increasing gap spacing between objects. Bernardi et al. [22] measured the NFRT between two structured Si wafers with SiO₂ stoppers (of height 150 nm) and SU-8 posts (of height 3.5 μm) by adjusting the gap in between the emitter and receiver by applying a force on the top object, in vacuum ($\approx 10^{-4}$ Pa). They formed temperature differences up to 120 K. Their results showed that the heat rate increased with increasing temperature difference and decreasing separation. The radiative fluxes were greater than the blackbody limit for all temperature differences in 150 nm – 1350 nm vacuum gap range, while it was lower than the blackbody limit for 3.5 μm vacuum gap between emitter and receiver. Ghashami et al. [23] reported on NFRT measurements between quartz plates (with an overlapping surface area of 5 × 5 mm²) with thermal gradients up to 156 K, down to gaps of 200 nm, under vacuum (8×10^{-7} Torr). They coated corners of their samples (of size 5 × 15 mm²) with Ag (to around 10 nm thickness), which served as contact sensors.

The mentioned efforts were conducted at vacuum environments for convenient measurement of thermal radiation across the hot and cold objects, but set-up related and gap stabilization challenges were present. Domoto et al. [13] pointed out that maintaining a parallel alignment of emitter and receiver, and a uniform gap between them were main difficulties during the experiments. Ito et al. [14] reported that the gap value was sometimes smaller than the pillar height used to provide the gap due to the deformation caused by the pressure applied. Hu et al. [15] reported experimental results for a gap of 1 μm, while their results agree well with theoretical results for a gap of 1.6 μm. This slightly larger gap was attributed to possible non-uniformities in the polystyrene particles (used to provide the gap) diameter. Ghashami et al. [23] reported that maintaining the receiver temperature was challenging at high temperature gradients and better cooling capacities should be sought when working with emitters at higher temperatures.

They reported that the NFRT rate varied as $\pm 5\%$ when the bottom stage was tilted by $\pm 0.002^\circ$, indicating the effects of parallelism. Rousseau et al. [24] stressed that they preferred to investigate a sphere-plate system to avoid parallelism related challenges faced during investigations of plane-parallel systems.

In the light of the mentioned challenges for the parallel emitter and receiver configuration, it can be seen that formation of a nanoscale gap between perfectly smooth objects in exact parallelism is challenging in systems built for NFRT investigations. Such a system can be considered as an ideal system, while real life applications include objects with non-ideal surfaces with a certain extent of micro-roughness, thickness variation, etc., and harvesting energy in a TPV-related system requires an ambient operation. For this purpose, Artvin [25] fabricated a vacuum-enclosing test sample for NFRT measurements, which was consisted of SiO₂ coated Si wafers bonded together with a vacuum gap of 200 nm in between.

Webb et al., in [26] and [27], measured the radiative heat transfer through the device fabricated by Artvin [25] under ambient conditions. So far, to the best of the author's literature review, all platforms were built to measure the flux between objects in vacuum chambers, rather than ambient conditions, apart from the efforts by [25], [26], and [27]. Some of the main difficulties of constructing a device that encloses a vacuum gap inside, and developing an experiment setup operating under ambient conditions are maintaining a satisfactory vacuum lifetime [27], the necessity of accounting for conductive [27] and convective transfers, and forming a uniform gap between smooth- and parallel-enough surfaces of objects considered.

Apart from the plane-parallel configuration; sphere-plate and tip-plate configurations were also experimentally realized. Kittel et al. [28] reported on NFRT measurements between a SThM (Scanning Thermal Microscope) tip with an evaporated Au film on (emitter), and a flat substrate (receiver, Au or GaN). The receiver was held at 100 K and temperature difference was around 200 K. The authors also reached to the extreme near-field during measurements.

Narayanaswamy et al. [29] attached a SiO₂ sphere onto the tip of a SiN/Au bi-material cantilever of an AFM (Atomic Force Microscope) and measured the NFRT between the SiO₂ sphere and a SiO₂ microscope slide, in vacuum (6.7×10^{-3} Pa). Their results showed that the near-field effects were pronounced for gaps of around 10 μm or less, and the conductance decreased as the gap value increased. Rousseau et al. [24] attached a microsphere onto a bi-morph SiN AFM cantilever with an Au (60 nm) and Cr (15 nm) layer deposited, at gap values of 30 nm - 2.5 μm , and thermal gradients of 10 K - 20 K, in vacuum (10^{-6} mbar). They measured the thermal conductance as a function of sphere-plate distance and sphere diameter, and reported that it decreased with increasing separation and decreasing sphere diameter.

Shen et al. [30] measured the NFRT between a SiO₂ microsphere (of 50 μm diameter, coated with Au film of 100 nm thickness) attached to the tip of a bi-material (SiN_x/Au) AFM cantilever and a substrate (coated with Au film of 1 μm thickness). They reported that the heat transfer coefficient for the case of a SiO₂-SiO₂ pair was larger than that for an Au-Au pair, and the near-field radiative transfer was much larger than the blackbody limit for a separation of around 30 nm. Shi et al. [31] reported on near-field thermal extraction between a SiO₂ microsphere attached to a bi-material (SiN_x/Au) cantilever's tip and a hyperbolic metamaterial (metal (Ni) nanowire array based, with anodic Al-oxide nano-porous template) substrate. Results showed that the near-field conductance increased with the integration of nanowires when compared to the absence of nanowires and decreased with increasing sphere-plate separation. Cui et al. [32] reported on radiative transfer measurements across a few- \AA 's to 5 nm separations between an Au coated SThM probe with a spherical Au tip (of diameter around 300 nm), and an Au coated substrate. Substrate was held at 343 K while the probe was held at 303 K. They reported thermal conductance values for different cleaning procedures applied to the probe and results showed that the conduction values are different for different cleaning procedures.

2.1.2. Effects of Emitter and Receiver Thickness with Vacuum Gap

Use of macroscopic or bulk-like components is not mandatory in an energy harvesting system, as thin films with good thickness uniformity can also be integrated. Presence of thin films and coatings may result in differences in system behavior when compared to a system of bulks, since the dominant surface polaritons' penetration depth can be approximated to be equal to the gap in between emitter and receiver [33] in the near-field. In other words, such structures of size comparable to or smaller than the dominant wavelength cause alterations in near-field behavior in comparison to their absence. A thin film with a thickness of 5-10 times of the penetration depth is considered opaque [34]. Studying the NFRT between two parallel plates, Basu and Zhang [34] stated that evanescent waves had a penetration depth of around a few tenths of a wavelength.

Francoeur et al. [35] defined different regimes for the NFRT between two SiC layers, and defined a non-dimensional parameter D , as $D = t/d$. In this relation t and d stand respectively for thickness of the media and vacuum gap. When $t \gg d$ ($D \gg 1$) for both the emitter and receiver, these objects behaved as bulks since they were relatively thicker than the gap. In this case surface polaritons coupled only between layers (i.e., did not couple within the layers). When $t \ll d$ ($D \ll 1$) for both media, all interfaces in the system contributed to the heat transfer, and split of the resonance peak into multiple peaks were observed. In this case, surface polaritons coupled within the layers, as well. Ben-Abdallah et al. [36] studied the NFRT between two parallel, doped semiconductor slabs. Results showed that for $d= 1 \text{ nm} - 100 \text{ nm}$; the NFRT coefficient was different for semi-infinite, 1 nm thick, and 10 nm thick films. Francoeur et al. [37] studied two SiC layers separated by a sub- λ gap. Results showed that presence of a receiver (medium 3) changed the Local Density of States (LDOS) significantly, and LDOS was strongly dependent on the receiver thickness. For the case of a receiver thickness of 10 nm, and emitter (medium 1) thickness of 10 nm and 100 nm, the LDOS for gaps between 10 nm -500 nm differed critically. Multiple peaks were observed for $t_1= 10 \text{ nm}$ and $t_3= 10 \text{ nm}$ with $d= 100 \text{ nm}$ and $d= 500 \text{ nm}$ due to thin films and effects of inter-film couplings.

Basu and Francoeur [38] studied the penetration depth of surface polaritons for the case of NFRT between metamaterials modeled as planar half-spaces. For a gap of 100 nm, the penetration depths were reported as 70 nm and 120 nm respectively for electric and magnetic resonance. In another study of Basu and Francoeur [39], maximum radiative transfer between two thin films were studied, and optimum values of materials permittivity were determined. It was stressed that when $D \gg 5$, the behavior obtained was similar to $D \rightarrow \infty$, i.e., bulk behavior; while for $D \ll 1$ surface phonon polariton (SPhP) coupling within the layers was also observed. As a result, the NFRT peak split into symmetric and antisymmetric modes.

For systems of thin film coated substrates, the near-field behaviors could be modulated based on the film (coating) thickness (t_{film}) and gap (d), from the definition of the penetration depth. Fu and Tan [40] considered a system of a dielectric emitter with a coating (SiC or SiO₂) on a metallic or dielectric substrate, and a bulk dielectric or metal receiver. For the case of Al emitter coated with a SiC film and Al receiver, results showed that for $d = 1 \text{ nm} - 1 \text{ }\mu\text{m}$, the total radiative flux was nearly the same for $t_{SiC} = 0 \text{ nm}$ and $t_{SiC} = 10 \text{ nm}$, while it reduced significantly when $t_{SiC} = 100 \text{ }\mu\text{m}$. On the other hand, as the vacuum gap value increased to 10 μm and more, $t_{SiC} = 100 \text{ }\mu\text{m}$ case provided higher total radiative flux in comparison to that for $t_{SiC} = 0 \text{ nm}$ and $t_{SiC} = 10 \text{ nm}$. Reduced radiative flux for $t_{SiC} = 100 \text{ }\mu\text{m}$ was attributed to the fact that such a coating thickness resulted in a far-field regime in between Al emitter and receiver, and the near-field effects were only due to SiC film. Basu et al. [41] studied the near-field radiative transfer between SiC coated metamaterials. Their results showed that the impact by the presence of SiC film augmented as t_{SiC} decreased. When $t_{SiC} < d$, the SiC film was nearly transparent to thermal radiation emitted from the metamaterial, enabling absorption of the thermal emission by the metamaterial and additional channels for heat transfer by the presence of the SiC film. For $t_{SiC} \geq d$ the thermal emission was mostly absorbed inside the SiC film, and the overall heat transfer was reduced when compared to that between two bulk metamaterials.

Didari et al. [42] considered a system of double-layered metamaterials with h-BN or GaN substrate (outer layer, 250 nm thick) coated with SiC thin film (inner layer, 0-100 nm thick). The results showed that for $d = 100$ nm, $t_{SiC} = 20$ nm on GaN substrate resulted in an LDOS maximum with a peak value around 20 times greater than that for $t_{SiC} = 0$ nm. Also, the highest LDOS magnitude among the studied cases ($t_{SiC} = 0$ nm, 20 nm, 40 nm, 60 nm, 80 nm, 100 nm; $d = 100$ nm) was obtained for $t_{SiC} = 20$ nm, which is in agreement with the result obtained by Basu et al. [41]. Another system of coated media was studied by Czaplá and Narayanaswamy [43]. They studied the effect of the SiO₂ coating thickness (t_{SiO_2}) on the NFRT between two Ag spheres (of 5 μ m diameter). Results showed based on the gap value that spheres could be modeled as homogeneous SiO₂ (in the extreme near-field) or homogeneous Ag (in the far-field). In the near field, it has been shown, for example for $d \geq 20$ nm and $t_{SiO_2} = 50$ nm that SiO₂ coating had an important role such that the conductance between media was 70% of that for two homogeneous SiO₂ spheres.

2.1.3. Previous Work on Near-Field Thermophotovoltaics

TPV energy conversion has been considered a promising scheme with main components of emitter and TPV cell (see Figure 1), and considered to be potentially mimicked by a system of parallel emitter and receiver placed in close proximity (see Figure 2). In this way, orders of magnitude improved amount of radiative transfer can be obtained to increase TPV system efficiency.

From the PV's point of view, energy of the incident photons should be matching the PV cells energy bandgap to create electron-hole pairs, which would as well be possible by the use of a quasi-monochromatic source. Photons with energy smaller than the PV cell bandgap would not be of use to create electron-hole pairs, and cause PV cell heating, thereby decreasing the efficiency. Photons with energy higher than the PV cell bandgap enable creating electron-hole pairs, but the difference of photon energy and PV cell bandgap would be lost. It is therefore important to select operation parameters with an emission source matching PV cell characteristics. Near-field TPV (NFTPV) is considered advantageous due to the possibility of obtaining quasi-monochromatic behavior, manifesting potentially minimum unused thermal emission.

Laroche et al. [11] studied a near-field TPV (nano-TPV) system by considering a W source with a flat surface, at 2000 K, placed at the near-field of a TPV cell (GaSb) at 300 K; and modeled the power output and efficiency. Results showed that for $d = 10$ nm and 30 nm, the radiative heat exchange was dominantly by the evanescent waves while for $d = 10$ μm , the radiative heat exchange was through propagating waves. Total radiative transfer and photo-generation current were higher in the case of near-field than those for far-field. Hanamura and Mori [44] experimentally studied a system with a GaSb TPV cell and a W emitter at 1000 K, placed in a vacuum chamber. Results showed that the maximum output power increased with decreasing gap (between 14.6 μm – 1048 μm).

Molesky and Jacob [45] reported that the potential enhancements expected by placing the emitter and receiver (TPV cell) in each other's near-field also bring about some concerns. To extract electrical power, integration of a PV cell as the absorber in a system with a metal emitter reduced the radiative transfer when compared to that between a metal-metal pair. It was also noted that placing the PV cell in close proximity to the emitter resulted in increase of PV cell temperature and thereby reducing its efficiency. Park et al. [46] numerically investigated a TPV system with a W emitter and a $\text{In}_{0.18}\text{Ga}_{0.82}\text{Sb}$ TPV cell held respectively at 2000 K and 300 K. Results showed that the radiative flux enhanced for more than an order of magnitude when the gap value was decreased from 10 μm to 5 nm - 10 nm. On the other hand, the quantum efficiency decreased with the gap value, due to small penetration depths at short gaps, resulting in recombination of carriers near the surfaces. Elzouka and Ndao [47] numerically studied a TPV system with a 2D Ta photonic crystal absorber, W emitter, and an $\text{In}_{0.18}\text{Ga}_{0.82}\text{Sb}$ PV cell, placed in a vacuum environment. The emitter and the PV cell were brought close to each other to observe near-field effects. Results showed that the thermal efficiency of both cylindrical and planar arrangements increased as the separation decreased. It was also noted that higher emitter temperatures and smaller separations resulted in higher power densities, but also better cooling was also a requirement.

Importance of the PV cell temperature was also reported by Francoeur et al. [48] who numerically studied a system consisted of a W emitter and $\text{In}_{0.18}\text{Ga}_{0.82}\text{Sb}$ PV cell. They stressed that the conversion efficiency and electrical output power was strongly affected by the PV cell temperature, such that for $d=20$ nm they obtained conversion efficiencies of 3.2% and 24.8% for 500 K and 300 K PV cell temperatures. Lenert et al. [49] studied a system of multi walled carbon nanotube (MWCNT) absorber (with 10 nm - 15 nm outer diameter, and 80 μm - 100 μm height) and a 1D Si/SiO₂ photonic crystal emitter (composed of 5 alternating layers of Si and SiO₂) integrated together on the same substrate, and an InGaAsSb PV cell, all of which were placed inside a vacuum environment (< 0.5 Pa). They reported that the optimum emitter-to-absorber area ratio was 7, and the output power increased with increasing absorber-emitter temperature. Chen et al. [50] numerically investigated a NFTPV system with an emitter (W or TiN) and a PV cell (GaSb or Ge, held at 300 K). They reported that, for a relatively low emitter temperature (800 K), which would be attractive for waste heat recovery applications, use of a nonpolar material (e.g., Ge) would be beneficial instead of a III-V group semiconductor (e.g., GaSb), such that as the separation decreases the power density and system efficiency improves. Lim et al. [51] numerically studied a system consisted of a Si emitter and InSb TPV cell coated with graphene layers separated by SiO₂ layers. In the system, the emitter was considered to be at a rather low temperature (500 K) and the system was considered to be placed in vacuum. Results showed that the spectral heat flux varied as the number of graphene layers for a specific gap ($d = 10$ nm - 200 nm). For $t_{\text{SiO}_2} = 5$ nm, the power output for the studied number of graphene layers (i.e., 0 - 6) reduced as the gap value increased. For $d = 10$ nm - 50 nm, although the number of layers' dependence was not monotonic, presence of a graphene layer resulted in a greater power output in comparison to the absence of graphene. It was also shown that the interfacial SiO₂ layer thickness, in relation to the number of graphene layers, had an impact on the power output. Liao et al. [52] studied a system with a W emitter at 1000 K and a PV cell (InSb, InAs, or InGaAsSb), and reported optimum values of separation distance (d) and respective TPV cell characteristics yielding maximum efficiency and power output density.

The optimum separation distances were reported as 162 nm, 12.7 nm, and 3 nm for InSb, InAs, and InGaAsSb PV cells, in the systems considered.

Current (I) and voltage (V) values at a specified insolation (solar radiation) level are critical in determining solar cell (or panel) efficiency. In a characteristic $I - V$ curve of a single solar cell, several V and I values and corresponding power outputs ($P = V \times I$) are noted. I_{max} (i.e., short-circuit current, I_{sc}) and V_{max} (open-circuit current, V_{oc}) are the maximum available current and voltage, while the power outputs for open-circuit and short-circuit cases are essentially zero. Among the minimum and maximum values of I and V , I_{mp} and V_{mp} are the current and voltage values at a maximum power point ($MPP = V_{mp} \times I_{mp}$) of a solar cell. Yang et al. [53] theoretically studied a system consisted of a selective emitter at 2000 K composed of alternating W and Al_2O_3 layers and an $In_{0.18}Ga_{0.82}Sb$ PV cell at 300 K. It was reported that the spectral radiative flux was enhanced for the case of multilayered emitter when compared to that for a plane W emitter. Also, integrating an Au back-reflector and an indium tin oxide (ITO) layer as a front contact, the conversion efficiency was greater than 20% for $d = 100$ nm. Fiorino et al. [54] recorded the $I - V$ characteristics of the system at specific gap values ($d = 60 \pm 6$ nm – 12 μ m) between a Si emitter with circular mesa (of height 15 μ m and diameter 80 μ m) and a PV cell (a photodiode) with 0.345 eV bandgap. The system was placed in vacuum ($\sim 10^{-7}$ Torr). Their results showed at 655 K emitter temperature that the maximum power output increased for about 40 times at 60 nm thick gap (i.e., in the near-field regime), when compared to that at the far-field regime.

2.2. Part II: Overview of SiC Fabrication Literature

The compound of silicon (Si) and carbon (C), silicon carbide (SiC) is a wide bandgap material and is advantageous in power semiconductor devices; when compared to the commonly used Si [55], especially in high-temperature, high-frequency, and corrosive applications. Integration of SiC thin films in small scale devices had been achieved by the use of techniques such as metalorganic chemical vapor deposition (MOCVD), electron cyclotron resonance plasma (ECR), and epitaxial growth to obtain monocrystalline SiC; low pressure CVD (LPCVD) and plasma enhanced CVD (PECVD) to obtain poly-crystalline SiC; and laser ablation deposition and sputtering

to obtain amorphous SiC (a-SiC) thin films [56]. a-SiC gained attention due to the possibility of manipulating its properties by adjusting deposition method and conditions, and post-deposition procedures. Among the deposition methods, sputtering has an important place due to its relative simplicity, its common use in many industrial fields, and reasonable deposition rates [57].

The Si-C chemical bond, which is very strong (4.6 eV), makes SiC a hard, inert, and a wide bandgap material [58], and enables its use in many applications including those in harsh environments. SiC holds potential in many areas due to its outstanding properties such as hardness, mechanical strength, red hardness, and poly-morphism, to name a few. One prominent application area of SiC is protection of materials from corrosion. Suitability of SiC as a protective coating for electronics packaging was studied by [59]. USB flash drives were coated by SiC films of 150 nm - 500 nm thickness via RF magnetron sputtering. Test for protection against salt water corrosion and KOH etchant revealed that presence of SiC coatings were beneficial. Also, SiC coated devices resistance against KOH at room temperature were excellent. On the other hand, this strong durability stands as a challenge for monocrystalline SiC, as performing most MEMS processes onto monocrystalline SiC is not possible [60].

In the literature, reports of SiC thin film deposition by PECVD (e.g., [61], [62], [63], [64], [65], [66], and [67]), polymer source chemical vapor deposition [68], LPCVD [69], sublimation method [70], DC magnetron sputtering (e.g., [71]), and RF magnetron sputtering are available. Since RF magnetron sputtering has been used in this dissertation for SiC deposition, details of the studies reporting other methods are not provided herein.

Singh et al. [60] deposited SiC thin films by means of RF magnetron sputtering and reported on films characterization. SiC films were deposited on Si (100) wafers with a 3-inch diameter and 6 mm thick sputtering target, under Ar atmosphere, and 50 mm target-substrate distance. Researchers did not apply any intentional substrate heating. Depositions were performed at 100 W, 200 W, and 300 W. The deposition rate increased with increasing RF power, at a given deposition pressure. At a certain sputtering RF power, the residual stress of the films increased with increasing

deposition pressure. Basa and Smith [72] deposited hydrogenated amorphous SiC thin films ($a\text{-Si}_{1-x}\text{C}_x\text{H}$, $x \approx 0.29$) by RF glow discharge, on Si wafers, at a substrate temperature of 250°C , 0.072 Torr chamber pressure, and 1.2 W/cm^2 discharge power. Carbone et al. [73] sputtered SiC thin films at power densities of $0.6 \text{ W/cm}^2 - 1.6 \text{ W/cm}^2$, 0.012 Torr process pressure, and 200°C substrate temperature. Inoue et al. [74] deposited SiC films to $100 \text{ nm} - 1.2 \mu\text{m}$ thickness onto Si (100) wafers using a SiC disk of 75 mm diameter as a sputter target, 6.1 W/cm^2 RF power density, under Ar atmosphere, at 4.9 mTorr, and a target to substrate distance of 50 mm. They performed the deposition at substrate temperatures wither equal to room temperature or 250°C . Costa et al. [57] deposited SiC films on Si (100) substrates by RF magnetron sputtering at 50 W - 400 W, 0 V - 100 V polarization, and $150^\circ\text{C} - 500^\circ\text{C}$ substrate temperature range. The target to substrate distance was 70 mm. They obtained high deposition rates up to 30 nm/min, and reported that through annealing stress free SiC films were obtained without any decrease in hardness. Song et al. [75] performed co-sputtering by the use of a combined C and Si target to deposit $\text{Si}_{1-x}\text{C}_x$ films at 150 W, 9 mTorr, under Ar environment, for 45 minutes, and a film thickness of 250 nm - 400 nm was obtained. Shelberg [59] deposited SiC thin films by RF magnetron sputtering at 3 mTorr, 130 mm target to substrate distance, 200 W - 400 W RF power, $\approx 27^\circ\text{C}$ substrate temperature, and substrate rotation; resulting in a deposition rate of 0.9 \AA/sec . Results showed that the films were C rich and contained O_2 at their surface. Xue et al. [76] deposited amorphous ($a\text{-Si}_{0.4}\text{C}_{0.6}$) samples by RF magnetron sputtering, at 200 W RF power, -170 V substrate bias, under Ar atmosphere, at 3.75 mTorr chamber pressure. El khalfi et al. [77] deposited $\text{Si}_x\text{C}_{1-x}$ films on Si by RF magnetron co-sputtering, at 7.5 mTorr and 250 W RF power. Some of the previous works are also concerned with crystal structure of deposited SiC thin films. These efforts are also summarized below.

Deposition of SiC thin films in crystalline state requires high temperatures, and those deposited at low temperatures ($<500^\circ\text{C}$) were generally at amorphous state [57]. This was concluded by most of the studies in the literature suggesting that a post-annealing at high temperatures was necessary for RF magnetron sputtered SiC films' transition into crystalline state. The process reported by Ulrich et al. [78] is unique by performing sputtering process at high substrate temperature and low deposition rate to obtain

crystalline SiC, without utilizing thermal annealing. They stated that the phase transition temperature was 363°C for their deposition rate, i.e., 4 nm/ min at 80 W RF power, from amorphous to crystalline state. They obtained cubic SiC (111) at substrate temperatures $\geq 420^\circ\text{C}$. Regarding thermal annealing of thin film SiC, Costa et al. [57] reported that, annealing temperatures greater than 900°C were needed for transition of SiC from amorphous state into crystalline state. Also, referring to the study of Ulrich et al. [78], they emphasized the advantage of low deposition rates for crystallization. It can be inferred that, SiC thin films in crystalline state can be obtained at high substrate temperatures, low RF powers, and thus low deposition rates; and/or performing annealing process after deposition.

Singh et al. [60] performed annealing of the SiC-on-Si samples at 400°C, 600°C, and 800°C under N₂ environment for 1 hour. They observed the presence of 3C-SiC (111) phase in two samples; one deposited at ≈ 9.9 mTorr and 300 W, and more dominantly for the other deposited at the same parameters and post-annealed at 400°C. The sample processed at 19.5 mTorr at 300 W was amorphous. Basa and Smith [72] reported that through thermal annealing at temperatures from 800°C the amorphous structure of a-Si_{1-x}C_x:H films started changing into microcrystalline and at 1200°C into crystalline. Carbone et al. [73] annealed the samples under vacuum (0.075 mTorr) for 1 hour between 400°C-700°C. They reported formation of submicron-crystallites and micro-crystallites within the amorphous matrix respectively through annealing at 400°C and 700°C. Inoue et al. [74] annealed their samples at 800°C - 1100°C for 6 minutes - 20 hours at 0.0037 mTorr. They reported early stages of crystallization of the samples annealed for 6 minutes at 1100°C within the amorphous matrix, and transition into cubic SiC in the case of annealing at 1100°C for longer than 1 hour. Their samples which were not annealed were amorphous. Costa et al. [57] annealed some of the samples under vacuum (7.5×10^{-8} Torr) at temperatures up to 1100°C for 30 minutes. Song et al. [75] performed annealing of the Si_{1-x}C_x films under N₂ environment, within 800°C - 1100°C by the use of a conventional furnace. They reported that for intermediate and high, near-stoichiometric C/Si ratio, SiC nano-crystals were formed by annealing at 1100°C. Xue et al. [76] performed annealing of their Si_{0.4}C_{0.6} films at 800°C and 1100°C, under vacuum (0.0075 mTorr) for 30 minutes. Results showed that

crystallization started at 800°C annealing and became more pronounced for the samples annealed at 1100°C. El Khalfi et al. [77] performed rapid thermal annealing of their $\text{Si}_x\text{C}_{1-x}$ films under Ar atmosphere, for 15 minutes, at 700°C - 1000°C. They reported that onset of crystallization was at 1000°C annealing, and crystallization did not occur at annealing temperatures below 850°C.

As reported by many researches in the literature, inducing crystallization of a deposited amorphous SiC film requires high processing temperature. In the majority of the studies on SiC crystallization, SiC thin films were deposited on Si substrates. In cases similar to this dissertation, processing temperatures should not approach or be greater than $\approx 1400^\circ\text{C}$, around which Si melts.

Following crystallization attempts, a common approach has been investigating the internal structures by means of spectroscopic methods and imaging. For investigation of internal structures of this work and comparison with the literature, reference Fourier Transform Infrared Spectroscopy (FTIR) and X-Ray Diffraction (XRD) data collected from the literature are presented in Table 1 and Table 2. Briefly, Table 1 provides details of FTIR spectra from the literature, corresponding to the commonly observed chemical bonds for SiC and Si systems, e.g., Si-H, Si-O, C-H_n, and so forth, in addition to the fundamental Si-C stretching vibration. Peaks in the FTIR spectra are correlated to specific chemical bonds, with peaks height and width may refer to the density of the respective bond. In Table 1, symmetrical and asymmetrical are abbreviated as “sym.” and “asym.”, respectively. Table 2 provides diffraction angle data reported for Si and SiC to compare the obtained spectra with the ones reported in the literature to conclude on crystal structures. Such comparisons of the findings with the literature are presented in detail, in Chapter 4.

Table 1. Band positions and their origins for IR spectra.

Chemical bond	Band position	Reference
Si-O rocking	440-470 cm ⁻¹	[77]
Si-H wagging	640 cm ⁻¹ ; 640 cm ⁻¹	[79]; [61]
Si-H rocking/wagging	640 cm ⁻¹	[63]
SiH _n wagging	640-650 cm ⁻¹	[64]
Si-H rocking/wagging	650 cm ⁻¹ ; 660 cm ⁻¹	[72]; [65]
Si-H _n wagging	670 cm ⁻¹	[79]
SiH wagging	670 cm ⁻¹	[80]
Si-C stretching vibration	700-700 cm ⁻¹ ; 780 cm ⁻¹ ; 770 cm ⁻¹ ; 778 cm ⁻¹ ; 780 and 800 cm ⁻¹ ; 770 and 800 cm ⁻¹ ; 780 cm ⁻¹ ; 700-800 cm ⁻¹ ; 780 cm ⁻¹ , 750 cm ⁻¹ ; 800 cm ⁻¹ ; 780 cm ⁻¹ ; 780 and 800 cm ⁻¹ ; 737 and 800 cm ⁻¹ ; 760-780 cm ⁻¹ ; 760-780 cm ⁻¹ ; 770-780 cm ⁻¹ ; 700-800 cm ⁻¹ ; 775 and 809 cm ⁻¹ ; 740-770 cm ⁻¹ ; 770-840 cm ⁻¹	[81]; [82]; [79]; [68]; [80]; [83]; [84]; [67]; [72]; [62]; [74]; [71]; [65]; [75]; [63]; [64]; [61]; [85]; [81]; [76]; [86]; [77]
Si-CH ₃ rocking and/or wagging	770 cm ⁻¹ ; 780 cm ⁻¹	[79]; [80]
(Si-H ₂) _n bending	850-900 cm ⁻¹	[79]
CH _n wagging	980-1000 cm ⁻¹	[64]
C-H _n wagging and/or rocking	1000 cm ⁻¹ ; 1000 cm ⁻¹	[79]; [61]
Wagging and/or rocking mode of C-H ₂ in Si-CH ₂	1000 cm ⁻¹	[82]
CH _n rocking or wagging	950-1100 cm ⁻¹	[80]
C-H wagging in SiCH ₃	1000 cm ⁻¹	[65]
Either Si-CH _n bonds rocking/wagging mode or Si-O-Si bridging absorption	1000 cm ⁻¹	[84]
Oxygen related vibration modes	960 cm ⁻¹	[86]
Si-O(s)	1000 cm ⁻¹	[72]
Si-O-Si sym. (TO)	1040-1070 cm ⁻¹	[77]
Si-O-Si stretching (TO)	1060 cm ⁻¹	[64]

Table 1. Band positions and their origins for IR spectra (cont'd).

Chemical bond	Band position	Reference
Si-O stretching	1070 cm ⁻¹	[75]
Due to oxidation of Si	1070 cm ⁻¹	[61]
SiO _x	1080 cm ⁻¹	[64]
Presence of oxide at the deposited film surface and film-Si wafer interface	1100 cm ⁻¹	[85]
Optical transverse elongation (TO) of Si-O bonds	1100 cm ⁻¹	[71]
SiO ₂	1100 cm ⁻¹ ; 1100 cm ⁻¹	[64]; [77]
Si-O-Si asym. stretch	1105 cm ⁻¹ ; 1106-1110 cm ⁻¹	[64]; [77]
Si-O-Si stretch (LO)	1170 cm ⁻¹	[64]
Si-O-Si sym. stretch (LO)	1170-1190 cm ⁻¹	[77]
CH _n bending or scissoring modes	1200-1500 cm ⁻¹	[80]
Si-CH _n vibration absorption modes	1250-1470 cm ⁻¹	[86]
Bending and scissoring modes of CH ₂ , CH ₃ , Si(CH ₃) and C(CH ₃)	1200-1500 cm ⁻¹	[72]
Si-CH ₃ bending (sym.)	1245 cm ⁻¹ ; 1250 cm ⁻¹ ; 1250 & 1340 & 1400 cm ⁻¹	[79]; [80]; [65]
Typical Si-CH ₃ peaks	1240 & 1300 & 1400 cm ⁻¹	[85]
Si-CH ₃ asym. bending or CH ₂ wagging	1350 cm ⁻¹	[80]; [79]
CH ₂ scissoring or bending	1400 cm ⁻¹	[80]; [79]
C=O stretch	1740 cm ⁻¹	[64]
Si-H(s)	2000-2300 cm ⁻¹	[72]
Si-H related absorption bands	2000-2140 cm ⁻¹	[86]
Si-H	2090 cm ⁻¹	[82]

Table 1. Band positions and their origins for IR spectra (cont'd).

Chemical bond	Band position	Reference
Si-H ₂	2150 cm ⁻¹	[82]
Si-H stretching	2000 cm ⁻¹ ; 2000-2100 cm ⁻¹ ; 2100 cm ⁻¹ ; 2100 cm ⁻¹ ; 2100 cm ⁻¹	[79]; [80]; [68]; [84]; [65]
Si-H _{1,2} stretch	2080-2087 cm ⁻¹	[64]
SiH/SiH ₂ stretching mode	2000-2100 cm ⁻¹	[63]
Si-H ₂ stretching	2090 cm ⁻¹	[79]
Si-H _n stretching	2000-2200 cm ⁻¹	[61]
Stretching of single Si-H bonds with 1-3 C atoms attached to one Si atom	2100 cm ⁻¹	[80]
CSi-H stretching	2060-2100 cm ⁻¹	[79]
CSi-H ₂ stretching	2150 cm ⁻¹	[79]
C-H(s)	2800-3000 cm ⁻¹ ; 2800-3000 cm ⁻¹	[72]; [84]
Stretching vibration of CH _n groups	2800-3000 cm ⁻¹ ; 2800-2900 cm ⁻¹ ; 2750-3000 cm ⁻¹	[63]; [64]; [61]
Several C-H _n absorption peaks	2850-2960 cm ⁻¹	[86]
C-H vibrations	2800-3100 cm ⁻¹ ; 2800 cm ⁻¹	[80]; [79]
C-H ₂ stretching (sym.)	2850 cm ⁻¹	[79]
sp ³ CH ₂ sym. vibrations	2860 cm ⁻¹	[80]
sp ³ CH ₃ sym. and/or CH ₂ stretching vibrations	2880 cm ⁻¹	[80]
C-H ₃ stretching (sym.)	2880 cm ⁻¹	[79]
sp ³ C-H _{2,3} stretching	2900 cm ⁻¹	[82]
C-H stretching	2900 cm ⁻¹	[65]
C-H ₂ stretching (asym.)	2910 cm ⁻¹	[79]
Asym. stretching of sp ³ CH ₂ groups	2920 cm ⁻¹ ; 2920 cm ⁻¹	[80]; [82]
C-H ₃ stretching (asym.)	2950 cm ⁻¹	[79]
sp ² CH ₂ olefinic	2956 cm ⁻¹	[82]
Asym. stretching of CH ₃ groups in the sp ³ configuration	2960 cm ⁻¹	[80]
C-H, C-H ₂ stretching (sp ²)	2970 cm ⁻¹	[79]

Table 2. Crystal type, orientation and diffraction angle information.

Crystal type and orientation	2θ (°)	Reference
<i>β</i> -SiC (111); 3C-SiC (111)	35.6°; 35.6°; 36.36 ^{0*} and 35.9°; 35.774°; 35.8°; 35.6863 ^{0*} ; 35.6°; 35.67°	[68]; [65]; [75]; [78]; [76]; [87]; [88]; [86]
3C-SiC (111)	41.6°	[61]
c-SiC (111) [†]	35.6°	[63]
SiC (111) [†]	35.6°	[64]
SiC (111), poly-type not identified.	35.6° & 35.7°	[89]
3C-SiC (002)	41.5653 ^{0*} , 41.5682 ^{0*}	[87]
3C-SiC (200)	41.6°; 41.43°	[65]; [86]
<i>β</i> -SiC (220); 3C-SiC (220)	60°; 60°; 60.03°	[68]; [75]; [86]
c-SiC (220), 3C-SiC	60°	[63]; [90]
c-SiC	33.4°	[91]
3C-SiC (220)	61°	[92]
<i>β</i> -SiC (311)	71.81 ^{0*} ; 71.82°	[75]; [86]
3C-SiC (222)	75.56°	[86]
<i>α</i> -SiC (100)	33.537°	[78]
<i>α</i> -SiC (101)	38.108°	[78]
2H-SiC (002)	41.5°	[61]
4H-SiC(004)	41.7°	[61]
4H-SiC (101)	34.88°	[86]
4H-SiC (102)	38.27° & 38°	[86]
4H-SiC (103)	43.43°	[86]
6H-SiC (101)	34.22° & 34.1°	[86]
6H-SiC (103)	38.27° & 38°	[86]
6H-SiC (105)	45.46° & 45.2°	[86]
Hexagonal phase or a high density of stacking faults & twins	≈ 34°	[83]
Amorphous nature of SiC	A broad hump at 37°	[91]
Graphite	55°	[68]
Graphite (100)	43.8°	[93]

Table 2. Crystal type, orientation and diffraction angle information (cont'd).

Crystal type and orientation	2θ (°)	Reference
Si (002)	33.0686 ^{0*} , 33.0698 ^{0*} , 33.0731 ^{0*}	[87]
Si (004)	68.6842 ^{0*} , 69.7732 ^{0*}	[87]
Si (111)	28.4° and 28.3°; 28.3°; 28.445°; 28.5°; 28.3°	[75]; [63]; [64]; [89]; [88]
Si (220)	47.27 ^{0*} ; 47.2°; 47.307°; 47.3°; 47.2°	[75]; [63]; [64]; [89]; [88]
Si (311)	56.36 ^{0*} ; 56°; 56.127°; 56.1°; 56°	[75]; [63]; [64]; [89]; [88]
Si (331)	76.36 ^{0*} ; 76.834°; 76.4°	[75]; [64]; [89]
Si (400)	69°	[63]
Si (422)	88.039°; 88.1°	[64]; [89]

* Digitized from the XRD spectroscopy data from the given reference.

† Data possibly belong to cubic (3C)-SiC.

2.3. Critical Assessment of the Literature

In this Chapter, a critical literature survey is reported mainly on (i) experimental efforts on NFRT followed by NFTPV investigations, and (ii) deposition of SiC thin films and thermal annealing for crystallization.

All studies so far support that deposited SiC thin films mechanical characteristics can be directly tuned by performing thermal annealing, to yield different internal structures. Also, electronic structures of SiC are poly-type dependent, and it has been shown that the energy bandgap of 3C-SiC and 2H-SiC are 2.40 eV and 4.04 eV, respectively [94]. Poly-type dependence of SiC and selecting a proper IR emitter to be used with a specific SiC poly-type are important for NFTPV's. In this dissertation, crystallization behavior of SiC is studied by thermal annealing, after deposition of SiC thin films by RF magnetron sputtering. It is considered important to reproducibly fabricate a certain SiC internal structure to be implemented in NFRT systems, starting from amorphous state.

Review of the literature reveals in contrary to the elaborative investigations conducted in vacuum that devices operating under ambient laboratory conditions are necessary to explore harvesting of NFRT. Critical review of the literature provided the opinion of building closed systems, consisting of emitter and receiver media in parallel configuration, enclosing a vacuum cavity for NFRT to take place, and operating under realistic conditions.

2.4. Contribution of this Thesis

Developing an understanding on an emerging energy conversion scheme requires full system treatment. In order to emphasize on the contribution of this dissertation, a map showing both the theoretical and applied efforts of our research group on near-field radiative transfer are presented in Figure 3. In Figure 3, ME stands for Mechanical Engineering.

Along with the numerical ([95]) and experimental setup development ([5], [96], [97], and [98]) efforts mentioned in Figure 3 (with full-system related efforts in [42], [99], [100], [101] and [102]), this dissertation is particularly concerned with fabrication of a NFRT device ([103]) that could shed a light on harvesting energy between two SiC-on-Si systems. To develop a fundamental understanding of the device components effects on near-field radiative transfer, an analytical investigation was also performed. It has been shown ([104], [105]) that the wafer type, wafer dopant density, and SiC internal structure are effective parameters on spectral near-field radiative flux. Also presence of structures (thin films, particles, etc.) with sub- λ size [42] was determined to be a NFRT system variable. These effects were considered in device fabrication, aiming at obtaining system features to lead a heat transfer performance as high as possible.

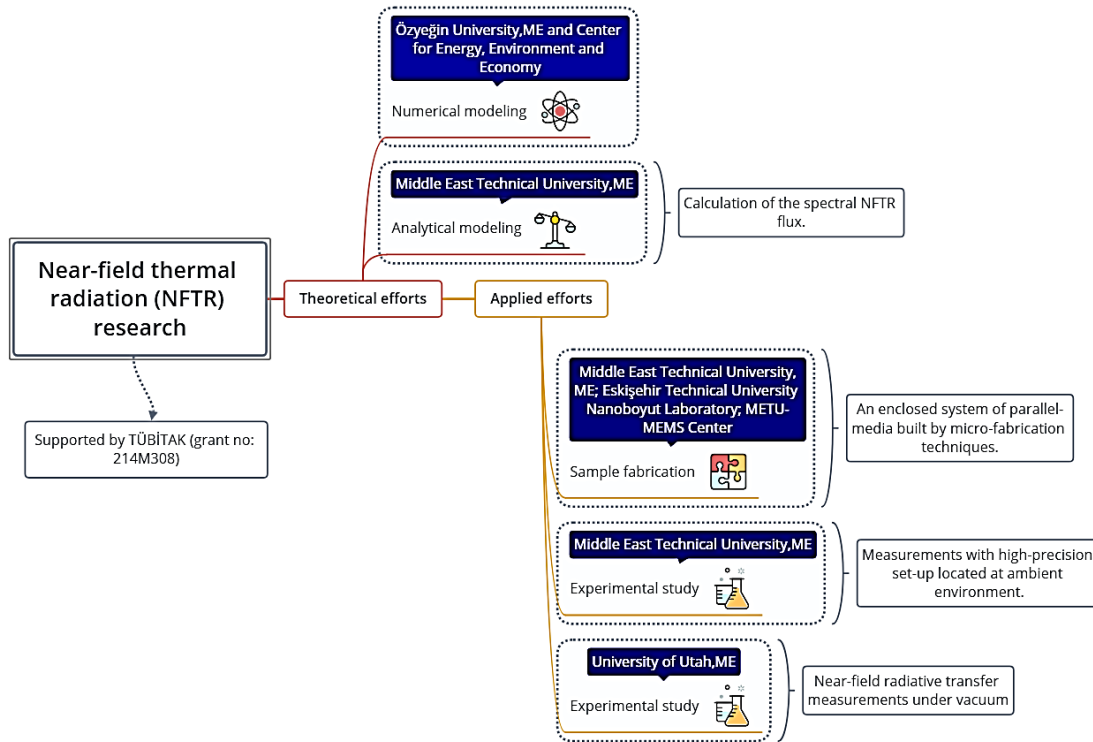


Figure 3. Map showing the theoretical and applied efforts of our research group.

The device fabrication consisted of SiC deposition via RF magnetron sputtering and crystallization by post-annealing. In the closed device; SiC, SiO₂, and Si parts are present. The SiO₂ walls (formed by patterning SiO₂ films) deposited on SiC were in the form of pillars, square shaped walls, and hexagonal honeycomb walls, selected from a large number of designs. The selection criteria were minimum conductive heat transfer area over radiative transfer area, and minimum deflection. Wafer level bonding via fusion bonding, with chemical and plasma activation was achieved. This work, in terms of both the SiC fabrication and crystallization, as well as detailed discussions of film deposition, photolithography, etching, wafer-level bonding, and dicing, provides a full-MEMS based treatment in building nano-TPV system, to be operated under ambient conditions.

CHAPTER 3

AN ANALYTICAL ASSESSMENT TO NEAR-FIELD RADIATIVE TRANSFER

In this Chapter, fundamentals and driving forces of NFRT are briefly described. A discussion is made on the dependence of material-related parameters of the NFRT flux of systems. For this purpose, the spectral near-field radiative flux formulation reported by Basu [106] was used, in this dissertation. Findings of the analytical work are used to draw conclusions for the development of NFRT systems at the device level, from material selection and microfabrication points of view.

3.1. Evanescent and Propagating Waves

When the wave nature of the radiation is considered, two types of waves are identified: evanescent waves and propagating waves. Evanescent waves are decaying waves with an exponential behavior such that their intensity diminishes in a short distance. Their decay length is proportional to the wavelength of emission [33], and their mechanism is thus dominant for the case of sub- λ distances between media, i.e., where NFRT takes place. An evanescent wave is created as a result of the total internal reflection phenomenon (as depicted in Figure 4). Energy transfer can take place if another object (medium 3) is brought into close proximity of the material (medium 1) [107]. In the figure, n_1 , n_2 , and n_3 stand for the refractive indices of respective media.

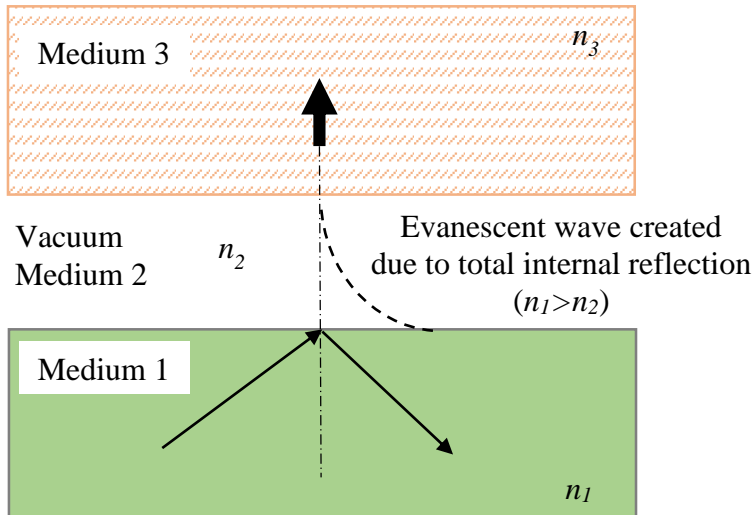


Figure 4. Evanescent wave as a result of total internal reflection.

As a result of heat exchanging material related excitations, surface polaritons, another type of evanescent waves, are created [33]. For the case of metals and semiconductors, the dominant heat carriers are free electrons and their oscillations form surface plasmon polaritons (SPP's), while the energy is carried by lattice vibrations (phonons) for the case of dielectrics, resulting in formation of surface phonon polaritons (SPhP's).

3.2. Materials to be integrated in a Near-Field Radiative Transfer Device

As microfabrication techniques allow researchers to perform processes with good control in thin film thickness, composition and mechanical properties, it has been possible to experimentally explore some of the theoretically demonstrated mechanisms. For example, in Chapter 2, previous research on the effect of film thickness (t) to vacuum gap (d) ratio (i.e., t/d) on NFRT performance was outlined. When paired under vacuum, it would be possible to demonstrate this phenomenon experimentally once highly uniform (in thickness) thin films with low roughness are deposited onto the selected substrate.

Either in thin film or bulk form, materials NFRT responses are dependent on the material type. Specifically, for IR applications, materials supporting surface phonon

polaritons (SPhP's) exhibit interesting features, since SPhP's can be excited via IR radiation [108]. Some of the materials supporting SPhP's are SiC, GaN, and c-BN, h-BN, to name a few. Figure 5 shows a comparison made by [109] between SiC and SiO₂, in terms of the heat transfer coefficient, by also accounting for conduction by air and spacers.

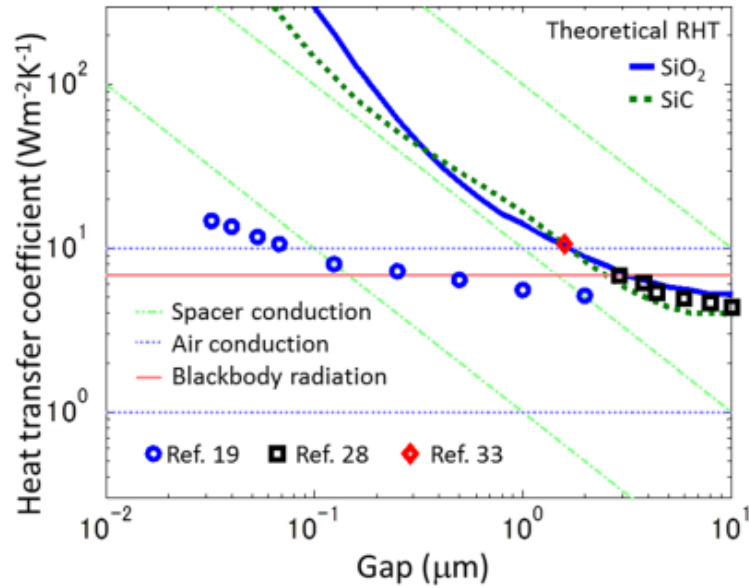


Figure 5. Variation of heat transfer coefficient with the gap between SiC and SiO₂ emitter and receiver [109]. Reprinted with permission from (S. Shen, A. Narayanaswamy, G. Chen “Surface Phonon Polaritons Mediated Energy Transfer between Nanoscale Gaps,” Nano Lett. 2009, 9, 8, 2909-2913.). Copyright (2018) American Chemical Society.

Figure 5 by [109] represents the heat transfer coefficient depending on the gap between SiO₂ and SiC media. For both materials, the heat transfer coefficient exceeds that for a pair of blackbodies at gap values smaller than 3 μm - 4 μm, while the use of either of materials is a selection confronted when building a NFRT system and performing fabrication processes in building NFRT devices.

3.3. Analytical Work on the Spectral Radiative Flux between Parallel Bulks

To determine the NFRT characteristics of parallel-media, the spectral heat flux from the emitter (medium 1) to the receiver (medium 2), i.e., $q''_{\omega,1-2}$, is calculated by solving Eq. (1). Details of Eq. (1) and its derivation were presented in [106], [34], and [110].

$$q''_{\omega,1-2} \approx \frac{4\Theta(\omega, T_1)}{\pi^2 d^2} \int_{\xi_0}^{\infty} \frac{\varepsilon''^2 e^{-2\xi} \xi d\xi}{|(\varepsilon + 1)^2 - (\varepsilon - 1)^2 e^{-2\xi}|^2} \quad (1)$$

In Eq. (1); ω , Θ , T_1 , d , and ε stand respectively for the angular frequency, mean energy of a Planck oscillator at ω in thermal equilibrium, absolute temperature of the emitter, vacuum gap separating emitter and receiver, and the dielectric function (relative permittivity) of the media. It is assumed that the both media are made up of the same type of material such that $\varepsilon_1 = \varepsilon_2$, and thereby denoted as ε . Here, $\varepsilon = \varepsilon' + i\varepsilon''$. In Eq. (1), $\xi = \beta d$ and $\xi_0 = d\omega/c$.

The mean energy of a Planck oscillator at an angular frequency of ω , and temperature of T is defined as in Eq. (2):

$$\Theta(\omega, T) = \frac{\hbar\omega}{e^{\hbar\omega/k_B T} - 1} \quad (2)$$

In Eq. (2), \hbar and k_B stand respectively for $h/2\pi$ where h is Planck constant, and Boltzmann constant.

When Eq. (1) is examined, it is seen that the spectral heat flux is defined dependent on the materials dielectric function, temperature, and the vacuum gap in between the emitter and receiver. In Eq. (1), emitter and receiver thicknesses (sizes) are not variables, and the media are considered to be semi-infinite, nonmagnetic, isotropic, and homogeneous [106]. Also, the emitter and the receiver are assumed to be made up of the same material. In this context, using Eq. (1), the temperature of the emitter (i.e., T_1) is defined only, to simplify the problem by neglecting the emission from the receiver, i.e., the receiver is assumed to be held at 0 K, non-emitting. One may as well set a nonzero temperature for the receiver and consider the emission from the receiver by replacing $\Theta(\omega, T_1)$ in Eq. (1) by $\Theta(\omega, T_1) - \Theta(\omega, T_2)$. Dielectric function is a material dependent characteristic, and depends on the atomic structure. For a non-conducting material (i.e., electric insulator, dielectric), the electrons are bounded and

when an electric field is applied, it interacts with these bounded electrons and lattices. Since the electrons are bounded, they oscillate between certain energy states, which classically approximated by a damped oscillator. In this case, the Lorentz Model can be used for modeling the dielectric function of non-conducting (dielectric) materials. For conductors (metals) and semiconductors, the electric field interacts with free electrons. For metals, Drude Model, based on the kinetic theory of an electron gas, is used instead. In this context, Drude-Lorentz model is used as described by [95], and dielectric functions reported in the literature by fitting experimental data are used in Eq. (1).

Material type and structure dependence of near-field response of systems should be studied in detail, since realizing a NFRT device requires detailed material selection and adjustment of fabrication process parameters. For example, as in this dissertation, if fabrication of a device involves thin film deposition process; wafer material, wafer type, dopant density, thin film material, and thin film structure are among the critically important factors.

The following Section presents the spectral radiative fluxes for Si wafer pairs of n- and p- type, with different dopant densities; III-V group compound semiconductor wafers (e.g., GaAs, InSb, and InP), and SiC with different crystal structures.

3.4. Material Dependence of the Spectral Heat Flux Between Parallel Media

Analyses and results throughout this Section are gathered under the assumptions of non-emitting receiver (at 0 K), semi-infinite emitter and receiver with invariant geometrical characteristics, and a gap value of $d = 100$ nm, unless otherwise stated. The other assumptions previously reported by Basu [106] were mentioned earlier in this text, and hence not repeated here. Spectral NFRT flux profiles are provided based on the emitter and receiver material types in the following sub-Sections.

3.4.1. Si Wafer Type Dependence of Near-Field Radiative Flux

In this Section, spectral NFRT fluxes of different types (n- and p-type) of Si wafers, and with varying dopant densities are aimed to be shown. First, the dielectric function and parameter values reported by [111] for n- and p-type Si wafers with different dopant densities were used in solving Eq. (1). The authors of [111] used Drude Model (in Eq. 3), and reported the parameter values given below in Table 3. In Eq. (3); ε_∞ , ω_p , and Γ stand respectively for the contribution of the dielectric, plasma frequency, and damping rate [111].

$$\varepsilon = \varepsilon_\infty - \frac{\omega_p^2}{\omega(\omega + i\Gamma)} \quad (3)$$

Table 3. Drude Model parameters of Si wafers, by [111].

Si wafer type	T	$\omega_p/2\pi$ (THz)	$\Gamma/2\pi$ (THz)	N (cm ⁻³)
p	293 K	0.480	1.190	1.1×10^{15}
p	293 K	1.750	1.510	1.4×10^{16}
n	293 K	0.360	0.590	4.2×10^{14}
n	293 K	1.010	0.640	3.3×10^{15}
p	80 K	0.370	0.127	6.3×10^{14}
p	80 K	0.920	0.198	3.9×10^{15}
p	80 K	1.800	0.530	1.5×10^{16}
n	80 K	0.330	0.088	3.5×10^{14}
n	80 K	0.780	0.107	2.0×10^{15}
n	80 K	2.000	0.400	1.3×10^{16}

The value of ε_∞ is reported as 11.7 by [112]. Another study, on IR permittivity of Si was conducted by [112], along with those for silicides (NiSi_{1.38}, Pd_{2.13}Si, PtSi_{1.13}, and TiSi_{2.03} films grown on Si wafers). In [112], the real (ε') and imaginary (ε'') parts of the dielectric function for Si wafers and silicide films were modeled through Drude Theory, as in Eq. (4).

$$\varepsilon' = \varepsilon_\infty \left[1 - \frac{\omega_p^2}{\omega_\tau^2(1+\omega^2/\omega_\tau^2)} \right] ; \quad \varepsilon'' = \frac{\varepsilon_\infty \omega_p^2}{\omega_\tau \omega (1+\omega^2/\omega_\tau^2)} \quad (4)$$

Parameters of Eq. (4) as reported by [112] for Si wafers as well as silicide films are provided below in Table 4. For silicides, ϵ_∞ is reported as 1.

Table 4. Drude Model parameters of Si wafers and silicide films, by [112].

Parameter	NiSi _{1.38}	Pd _{2.13} Si	PtSi _{1.13}	TiSi _{2.03}	n-type Si	p-type Si
ω_p (eV)	3.840	3.630	3.690	3.200	0.036	0.140
ω_τ (eV)	0.075	0.049	0.080	0.030	0.037	0.070
Film thickness* (nm)	230	160	200	180	-	-

* Measured by profilometer [112].

Figure 6 shows a comparison of the spectral NFRT fluxes for relatively heavily-doped and lightly-doped p- and n- type Si wafers, at 293 K.

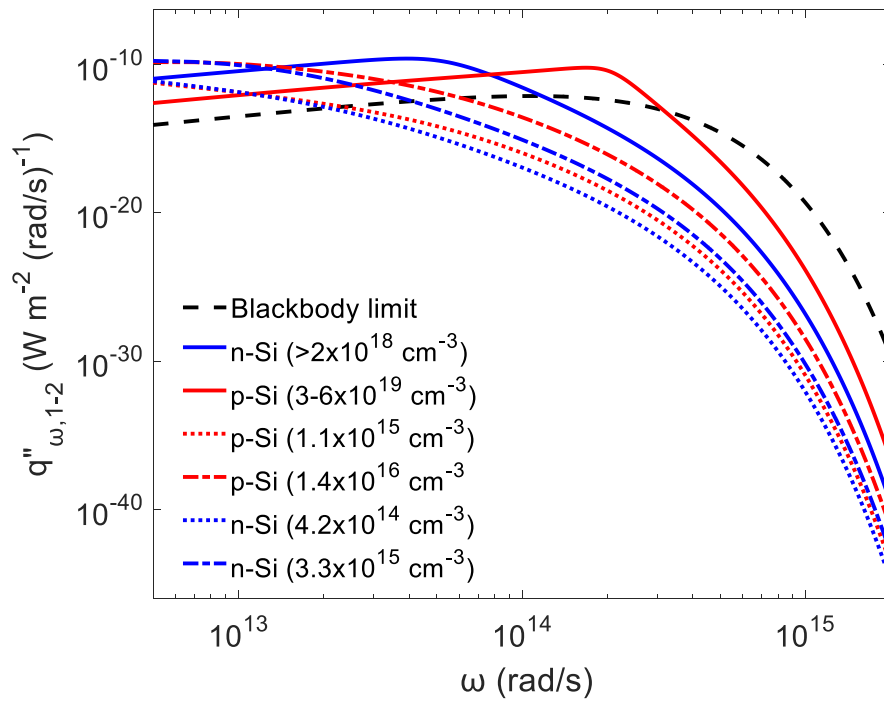


Figure 6. Spectral NFRT flux for n- and p-type Si wafers at 293 K [104].

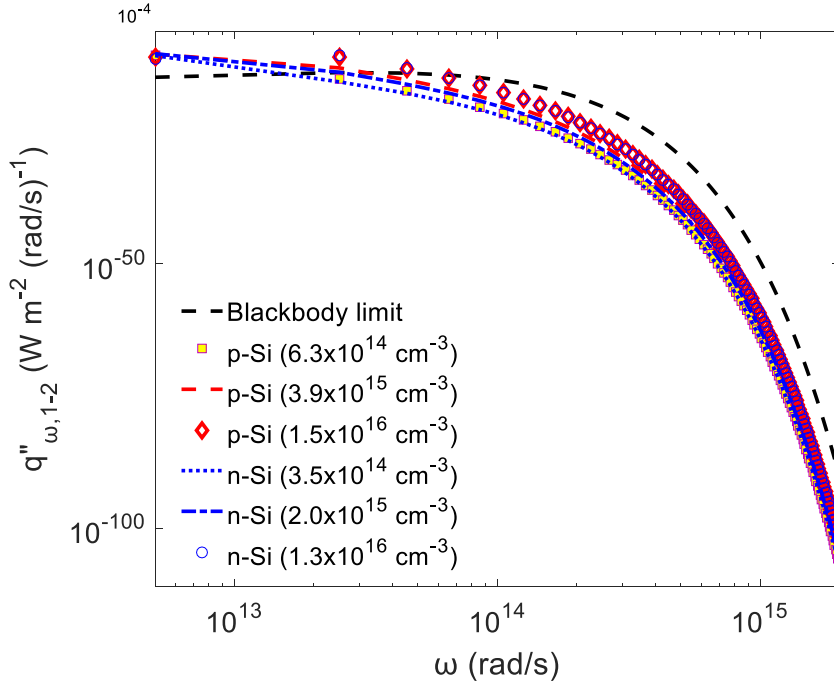


Figure 7. Spectral NFRT flux for n- and p-type Si wafers at 80 K.

Results presented in Figure 6 and Figure 7 shows that the spectral radiative flux in the near-field between Si wafer pairs depend strongly on the wafer type (and thus, dopant type), and dopant density. For these cases, the emitter temperatures were considered separately as 293 K and 80 K for the materials whose optical parameters were given at these temperatures. The amount of the spectral heat flux is positively correlated with the dopant density, as shown in Figure 6 and Figure 7. In other words, increasing dopant density of Si wafers in a pair yielded a higher flux magnitude for the cases studied. When the spectral NFRT fluxes for these Si wafer pairs are compared against the blackbody limit, it is clear that these pairs outperform blackbody limit at the lower edge of the studied frequency range, for more than 4 orders of magnitude at 80 K; and more than 5 orders of magnitude (wafers with relatively heavy doping) and 3 orders of magnitude (wafers with relatively light doping) at 293 K. Having observed the wafer type and dopant density dependence of the NFRT flux, it is concluded that these factors should be considered when constructing NFRT harvesting systems.

The spectral NFRT flux is plotted for the silicides in Figure 8. Silicides are composed of metals and Si, and their Si content makes them compatible with Si, in most MEMS processes. Applications of silicide films include gate electrodes, Schottky barrier contacts, and so forth [113].

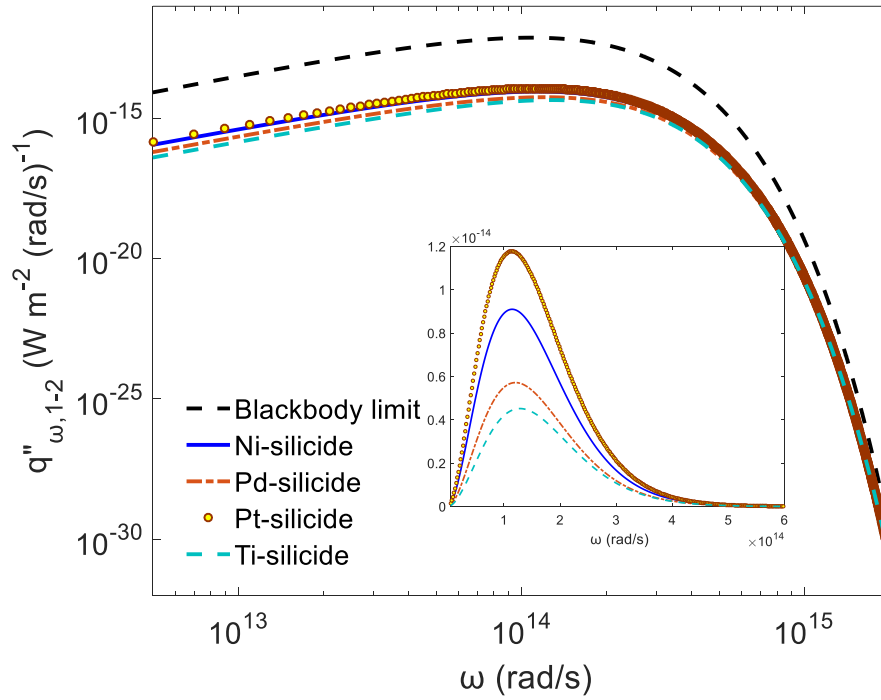


Figure 8. Spectral NFRT flux for metal silicides at 293 K [101].

From the inset of Figure 8, it can be observed that although the flux magnitudes are different, the peak locations of each of the flux profiles are very close. This similarity can be due to presence of Si as a component in silicides chemical composition, as well as the use of the same type of Si wafer [104]. In thin film on substrate systems, there is a strong dependence NFRT on the type of substrate. Also, when compared with the blackbody limit, it is seen that the performances of these silicides are not better. This is because of the fact that Ni, Pd, Pt, and Ti are transition metals, whose surface plasmon resonance lies in the UV region. Also, the plasmon resonance is damped and broadened due to the inter-band transitions [114].

3.4.2. Near-Field Radiative Flux Between III-V Group Semiconductors

Chochol et al. [115] studied III-V group semiconductors' plasmonic behavior in far-IR and THz range by measuring optical properties of monocrystalline GaAs, InP, and InSb wafers. Optical properties were modeled through the Drude-Lorentz Model, as described in Eq. (5):

$$\varepsilon_r = \varepsilon_\infty - \frac{\omega_p^2}{\omega^2 + i\gamma_p\omega} + \frac{A_L\omega_L^2}{\omega_L^2 - \omega^2 - i\gamma_L\omega} \quad (5)$$

In Eq. (5), γ_p is the damping constant, ω_L is lattice vibration frequency, and A_L is the lattice vibration amplitude at ω_L . The parameters of Eq. (5) as provided by [115] are given in Table 5, below.

Table 5. Drude-Lorentz Model parameters of GaAs, InP, and InAs wafers, by [115].

	GaAs n-type	GaAs p-type	InP n-type	InSb n-type	InSb p-type	InSb undoped
ω_p (10^{14} rad/s)	3.33±0.01	4.44±0.02	4.70±0.01	2.82±0.01	0.63±0.01	0.57±0.01
τ_p (10^{-1} ps)	0.71±0.01	0.09±0.01	0.71±0.01	2.65±0.04	0.75±0.01	5.16±0.06
ω_L (10^{13} rad/s)	5.06±0.01	5.06±0.01	5.73±0.01	3.38±0.01	3.38±0.01	3.38±0.01
τ_L (ps)	2.79±0.27	1.95±0.29	3.01±0.24	1.81±0.13	1.90±0.04	1.99±0.04
A_L	2.13	2.15	2.89	2.02	2	2.02
ε_∞	11.58	11.34	10.01	15.68	15.74	15.86

* $\tau_p = 1/\gamma_p$.

Here, the emitter temperature is set by considering an applicable temperature limit that is lower than the melting point of these materials, which are 1513 K, 797 K, and 1335 K respectively for GaAs, InSb, and InP [116]. Spectral NFRT fluxes for GaAs wafer pairs are plotted in Figure 9.

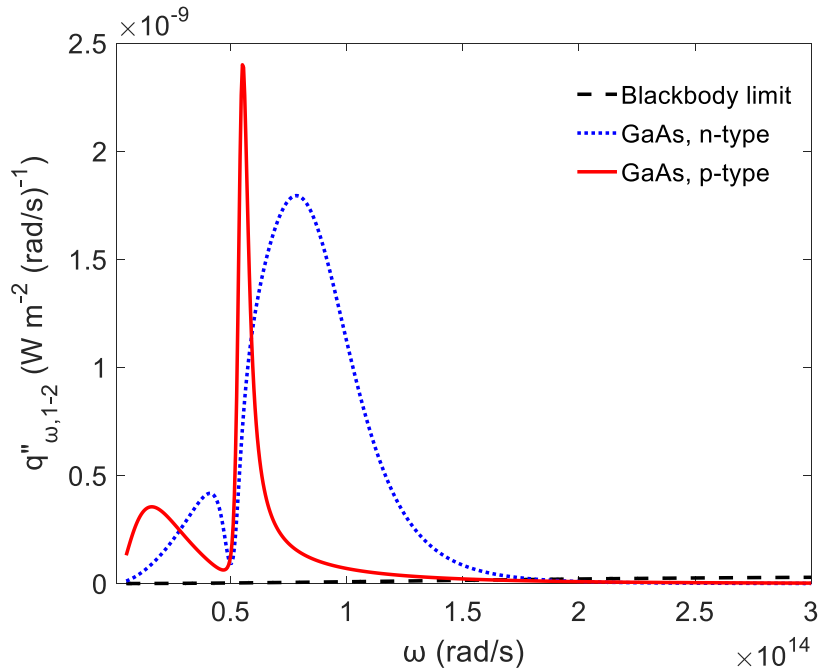


Figure 9. Spectral NFRT flux between n- and p-type GaAs wafer pairs at 1000 K [105].

Similar to the observations made for Si wafers, Figure 9 also shows that the spectral NFRT depends on the wafer type in the case of GaAs wafer pairs. In terms of the magnitude, p-type outperforms n-type in a narrow spectral band, while the heat flux peak for n-type GaAs is broader. Depending on the requirement of application, either could be considered feasible.

Figure 10 shows the spectral NFRT fluxes both for n-type, p-type, and undoped InSb wafers. Through examination of Figure 10, it would be possible to assess, for this material, whether doping process makes it advantageous in terms of NFRT when compared to the undoped version. As shown in Figure 10, InSb pair of n-type doping exhibited nearly an order of magnitude greater spectral heat flux in comparison to the p-type InSb pair. In certain spectral regions, undoped InSb has similar behavior to p-type, along with a nonzero behavior at smaller angular frequencies.

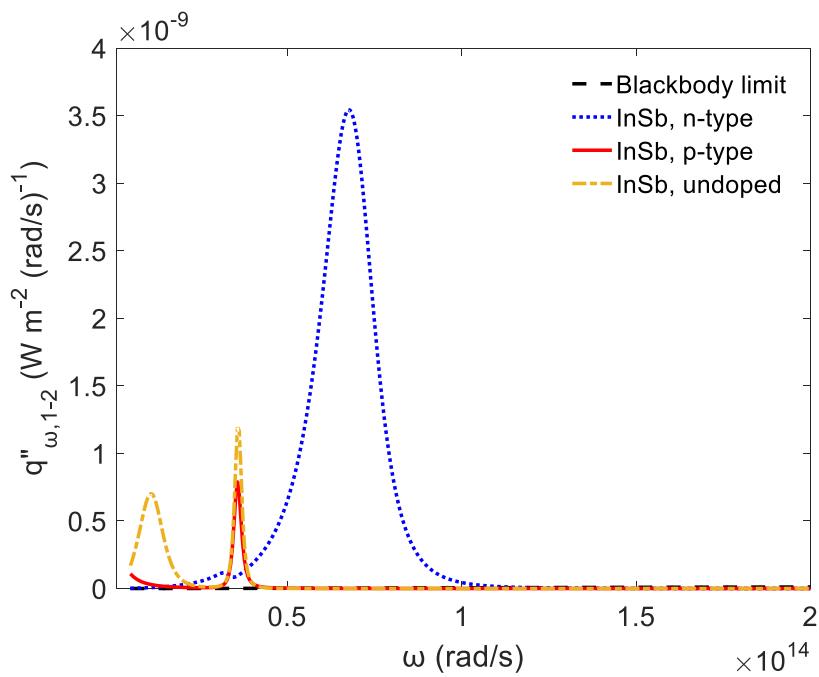


Figure 10. Spectral NFRT flux between n-/p-type, undoped InSb wafer pairs at 750 K [105].

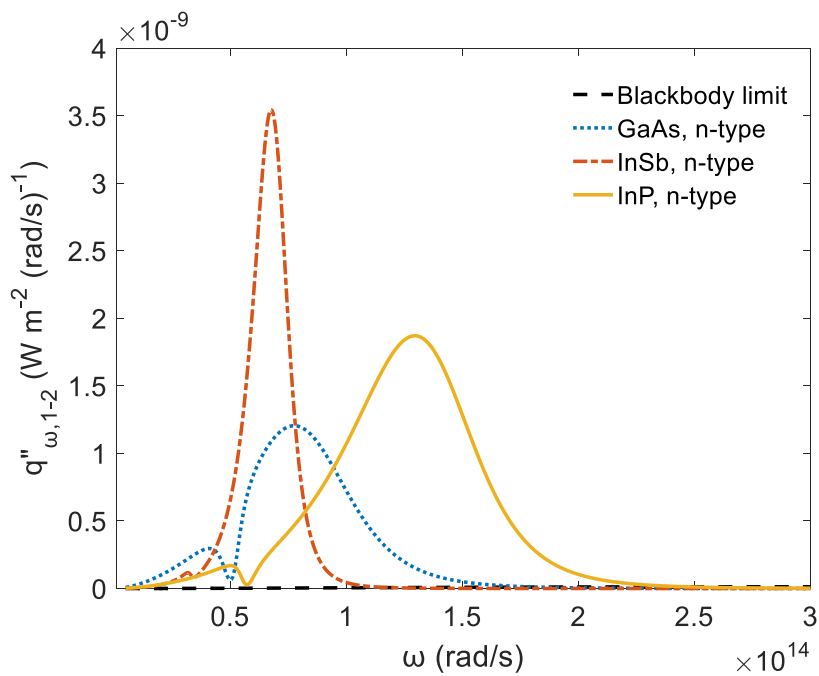


Figure 11. Spectral NFRT flux between n-type GaAs, InSb, InP wafer pairs at 750 K [105].

Since the type of doping is a variable, comparison of n-types of different pairs can be done. Figure 11 shows that in comparison to the n-type GaAs and InP, the peak shape of InSb is different, with a narrower width and greater magnitude. The flux peaks of GaAs and InP are broader in width, with additional increase and then decrease in magnitude at shorter angular frequencies.

3.4.3. Near-Field Radiative Flux Between SiC Media with Different Crystal Structure

As it was stated in Chapter 2, crystallization of SiC is a challenging task. Although research on deposition and crystallization has a relatively long history, no consensus has been established how to form a mono- or poly-crystalline SiC from an amorphous as-deposited film.

Based on the fabrication method, SiC can be formed in a large number of structures. SiC has poly-typism, i.e., one dimensional version of poly-morphism, which is defined for a material to occur in more than one crystal structure [117]. Some prominent poly-types of SiC are 3C-SiC (cubic), 2H-SiC, 4H-SiC, and 6H-SiC, to name a few; while more than 200 poly-types are identified for SiC [117]. In this dissertation, the reference materials obtained from Griffith University have 3C-SiC hetero-epitaxial layers grown on Si wafers.

Lei et al. [118] presented the index of refraction (n) and extinction coefficient (k) of SiC with different internal structures. Figure 12, involves the data presented by [118] for cSiC (crystalline SiC in cubic phase), a-SiC (amorphous SiC), and sputtered SiC; along with the Drude-Lorentz Model parameters of SiC (marked with *) presented by [95], shows variation of these properties with angular frequency. It is clear that, crystalline SiC exhibits different properties than sputtered and amorphous SiC. Since the index of refraction (n) and extinction coefficient (k) are correlated to the complex dielectric function by $\varepsilon(\omega) = (n \mp ik)$, it is expected that these SiC media will exhibit different near-field behaviors.

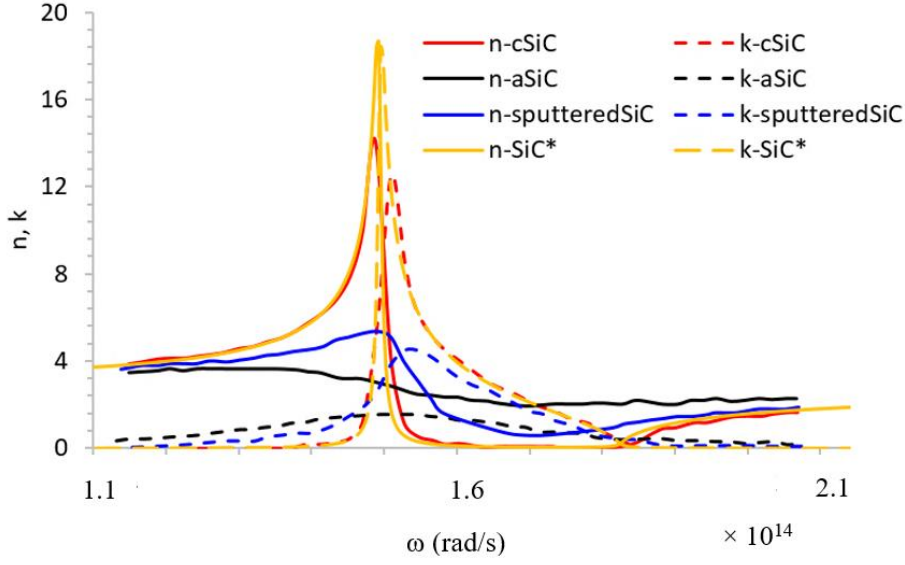


Figure 12. Dielectric properties of SiC, dependent on internal structure.

Tiwald et al. [119] presented IR spectral ellipsometry measurements on various SiC materials (4H-SiC, 6H-SiC, homo-epitaxial 4H-SiC layers, and H₂ implanted 6H-SiC) to report on their dielectric response. The values provided below in Table 6 gathered from [119] are employed within the Drude-Lorentz Model [95], as in Eq. (6).

$$\varepsilon_r(\omega) = \varepsilon_\infty \frac{\omega^2 - \omega_{LO}^2 + i\Gamma\omega}{\omega^2 - \omega_{TO}^2 + i\Gamma\omega} \quad (6)$$

In Eq. (6), ω_{LO} and ω_{TO} stand respectively for the longitudinal optical phonon frequency and transverse optical phonon frequency. Γ is the damping constant. Solving Eq. (1) together with Eq. (6) and the data in Table 6, the spectral radiative flux in the near-field for a number of SiC poly-types are plotted and presented in Figure 13.

Table 6. Drude-Lorentz Model parameters of SiC, by [95] and [119].

Sample	ϵ_∞	ω_{T0}	ω_{L0}	Γ
SiC [95]	6.7	1.494×10^{14} rad/s	1.825×10^{14} rad/s	8.966×10^{11} rad/s
4H-SiC [119]	6.6	797 cm^{-1}	971 cm^{-1}	2.8 cm^{-1}
6H-SiC [119]	6.3	797 cm^{-1}	972 cm^{-1}	4.7 cm^{-1}
Homoepitaxial 4H-SiC [119]	6.6	797 cm^{-1}	970 cm^{-1}	1.4 cm^{-1}
H ₂ implanted 6H-SiC [119]	6.6	797 cm^{-1}	973 cm^{-1}	12 cm^{-1}

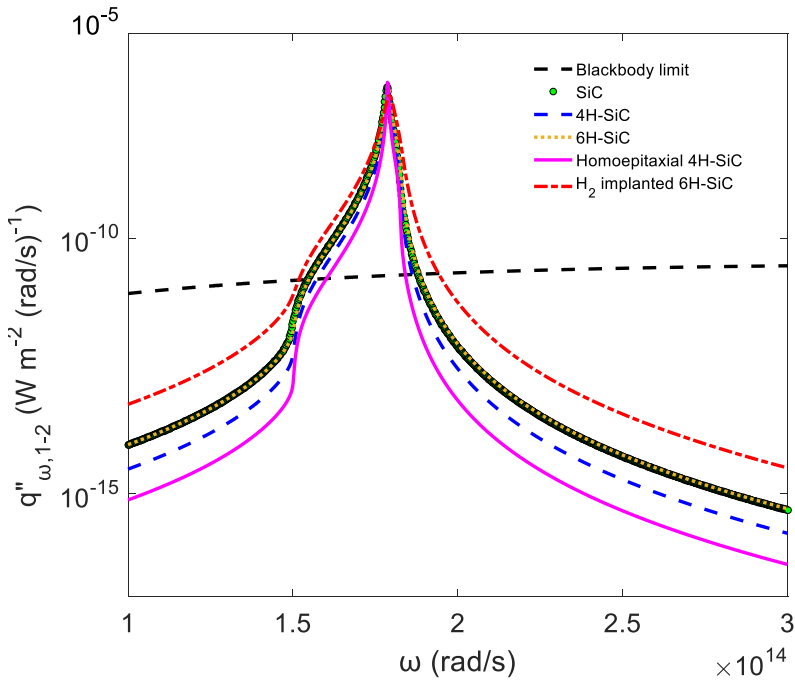


Figure 13. Spectral NFRT flux between structurally different SiC pairs, at 1000 K.

Results shown in Figure 13 reveal that, although the maxima locations of the studied SiC pairs radiative flux peak nearly coincide, the peak width and thus the total NFRT flux are expected to be different. While the homo epitaxial 4H-SiC pair's peak width is the narrowest, it is the widest for H₂ implanted 4H-SiC. One may therefore expect different net flux magnitudes for the pairs of SiC when fabricated via different methods and treated at different conditions. To the best of the author's knowledge, this

is the first report of the investigation of NFRT between SiC pairs of different structures.

3.5. Discussions on the Thin Film Thickness, Substrate Material, Nanostructure Material and Size on Near-Field Radiative Transfer Performance

Along with the results presented in Section 3.4, a numerical study was conducted by our research team, to explore the sole effects of thin film size, substrate material, nanostructure material, and nanostructure size on NFRT heat flux and/or LDOS [42]. This study was outlined in Chapter 2, but effects of the presence of thin films and nanostructures as well as the effect of type of materials are discussed herein in more depth. It should be noted that the results presented in this Section are not within the scope of this dissertation, rather, they are obtained to shed a light to sole effects of the presence of thin films and nanoparticles on near-field radiative transfer responses of systems, by *NF-RT-FDTD* algorithm reported by Didari and Mengüç [95], previously. Having observed the effects of thin film thickness (t) with vacuum gap value (d) on the NFRT transfer, it was decided to observe the mentioned parameters effects individually, since it has been shown that systems' LDOS or heat flux could be optimized by tuning these size-related parameters properly. The penetration depth of the dominant SPhP's being nearly equal to the gap between media [33] make inter-film and inter-cavity couplings possible, thereby providing potential increases in overall system performance. Results of this work were outlined in Chapter 2, while material related discussions are provided herein.

The system considered in [42] is shown in Figure 14, below. It is a double-layer metamaterial system, with a thicker outer layer (referred to as the substrate due to being considerably thicker than the thin film and the vacuum gap) of GaN, h-BN or SiC, an inner SiC layer, and rectangular nanostructures of GaN, h-BN- or SiC. The shape of nanoparticles sitting on the SiC thin films is a variable, both in fabrication of such systems and numerical work. It has been shown previously [99] that rectangular nanostructures outperformed elliptic, rectangular, and absence of nanoparticles cases. In this regard, only rectangular gratings were considered in [42].

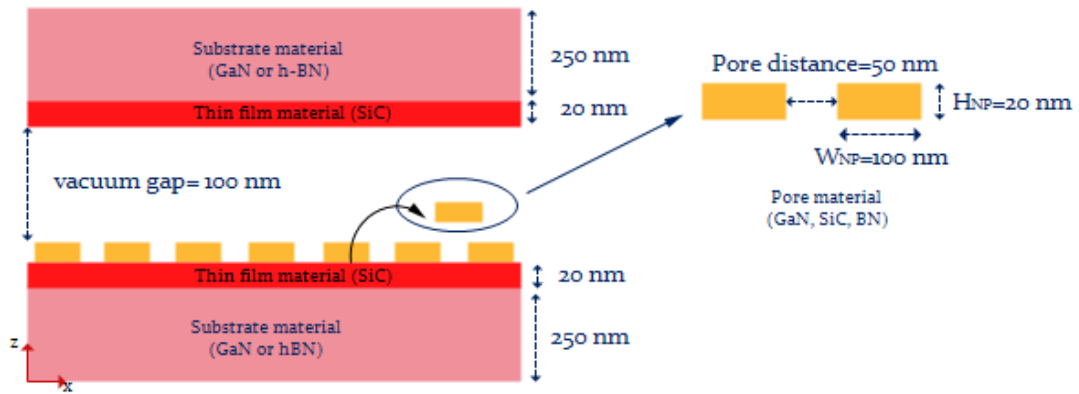


Figure 14. Geometry of the problem, adapted from [42].

Results showed that among GaN, h-BN and SiC, the highest NFRT flux was obtained with GaN substrates. For a SiC thin film located on a 250 nm thick GaN substrate, LDOS were calculated for 0 nm - 100 nm SiC film thickness. Results showed that, in agreement with, for example [40], 20 nm SiC film outperformed thicker (i.e., up to 100 nm) SiC films. The LDOS peak with highest magnitude was around 20 times greater with a 20 nm SiC film present on GaN surfaces when compared to the absence of SiC films. Integrating rectangular GaN nanoparticles (of height 20 nm and width 100 nm) into this scenario resulted in around 12 times enhancement in the LDOS peak magnitude, in comparison to the absence of nanoparticles. It was also shown that by varying the nanostructure size, additional peaks in the NFRT flux spectrum could be obtained.

3.6. Results

The aim of the analytical investigation provided in this Chapter is not presenting a new methodology to solve for the NFRT between parallel media. Indeed, that has been a well-established sub-area of NFRT, both analytically and numerically.

Here, the aim is to use a previously derived spectral NFRT flux equation considering parallel media of the same material. This approach enabled excluding effects of parameters other than vacuum gap value, emitter temperature, and emitter-receiver material and related characteristics.

This has been advantageous in exploring solely the material type and structure effect on NFRT performance of systems.

Results showed that the spectral heat flux for p-type Si wafer pair exceeds that for n-type Si wafer pair [5]. The dopant density for both the p- and n-type wafers is very important, since there is more than an order of magnitude difference in spectral heat flux between p-type Si wafers with $6.3 \times 10^{14} \text{ cm}^{-3}$ and $1.5 \times 10^{16} \text{ cm}^{-3}$ dopant density, and between n-type Si wafers with $3.5 \times 10^{14} \text{ cm}^{-3}$ and $1.3 \times 10^{16} \text{ cm}^{-3}$ dopant density. Both the angular frequency values corresponding to maximum heat flux and heat flux peak magnitudes are different for p- and n-type Si wafers.

Silicide films are interesting to be studied in this context. There is an analogy between Si wafer-silicide film systems and Si wafer-SiC thin film systems, since both silicides and SiC films include Si in their chemical structure. Silicide films NFRT behavior were spectrally similar, with different flux magnitudes for Ni, Pd, Pt, and Ti.

GaAs, InP, and InSb are common wafer materials. The spectral radiative flux peak (maximum) for p-type GaAs is narrower than that of n-type GaAs, requiring better spectral control of emission in case of its use in NFRT systems. n-type InSb exhibited around 10 times greater peak magnitude in its spectral heat flux when compared to that for p-type InSb.

Examination of different SiC structures has shown that the total NFRT flux difference, between for example H₂ implanted 4H-SiC and homo-epitaxial 4H-SiC would be noticeable, since the spectral NFRT flux peak shape for the former is broader than that for the latter. This outcome, presented for the first time in the literature to the best of the author's literature review, is important in selecting the proper SiC component and its accompanying emitting source, in NFRT systems.

3.7. Summary

Researchers aiming at forming a NFRT investigation/energy harvesting systems are confronted with critical material selections. Throughout the analytical results presented herein, the aim is to shed a light to the fact that wafer material, wafer type, wafer doping level, and emitter-receiver internal structure are all variables of systems' NFRT performance.

In this regard, when MEMS approaches are utilized in a NFRT device fabrication scheme, decision between n-type and p-type wafers (especially Si) should be carefully made. Also, the study material of this work, SiC, an interesting material naturally occurring in a large number of crystal structures, have intrinsic properties depending on the crystal type and structure. In this regard, either in thin film or wafer state, SiC internal structure should be tuned or selected based on the needs of the application. It has been seen from the market search that 3C-SiC and 4H-SiC wafers are more accessible.

CHAPTER 4

NEAR-FIELD RADIATIVE TRANSFER HARVESTING DEVICE FABRICATION

The SiC-on-Si NFRT device was fabricated using standard microfabrication techniques. The fabrication scheme consisted of material preparation and cleaning, thin film deposition, photolithography, etching, wafer-level bonding, and dicing processes. In this Chapter, fabrication processes and their optimization are presented.

Fabrication of the test samples are conducted at Nanoboyut Laboratory of Physics Department, Eskişehir Technical University (Part I); and Micro-Electro-Mechanical Systems Research and Application Center of Middle East Technical University, i.e., METU-MEMS Center (Part II).

4.1. Introduction

As a result of the tremendous progress made in microfabrication technology of integrated circuits, today Micro Electro Mechanical Systems (MEMS) have a very important place in electronics industry. MEMS device sizes mostly vary within $1\ \mu\text{m}$ – $1\ \text{cm}$, bring about the advantages of functional richness, low thermal mass (i.e., fast heat transfer), and low cost [120] to name a few, in comparison to larger devices.

The commonly used microfabrication processes were classified under 5 headings: *(i)* additive processes, *(ii)* subtractive processes, *(iii)* patterning, *(iv)* material modification, and *(v)* mechanical steps [120]. Fabrication of the NFRT device aimed to be constructed within the scope of this dissertation includes sub-classes of all of the mentioned processes, *(i)-(v)*.

Mainly, according to the classification made by [120], sputtering and chemical vapor deposition (CVD) are considered as additive processes, wet etching is considered as a subtractive process, photolithography is considered as a patterning process, thermal annealing is considered as a material modification process, and wafer bonding and wafer dicing are considered as mechanical steps. Using the processes classified as above, the NFRT device fabrication in general terms can be said to be consisted of the stages depicted in Figure 15 [97]. In Figure 15, the cross-sectional view of an individual die is illustrated to present the device features clearly.

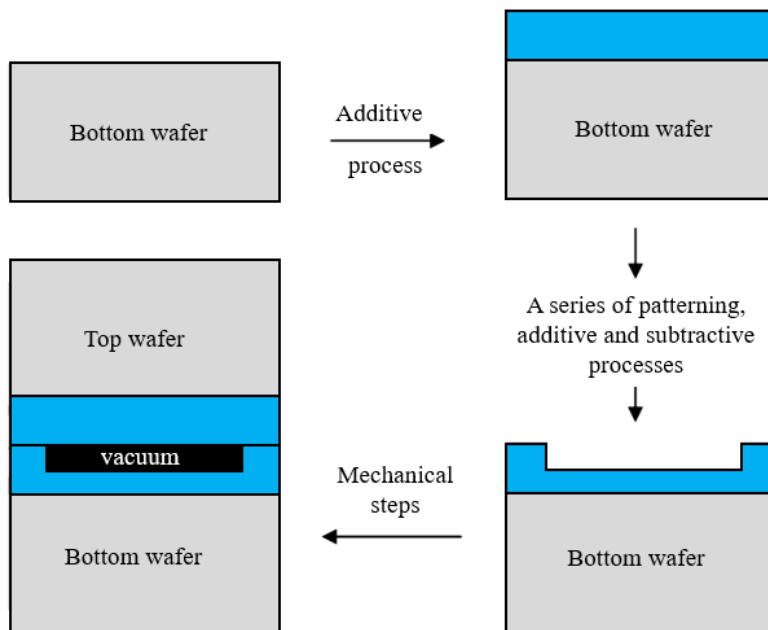


Figure 15. NFRT device general fabrication scheme [97].

The processes presented in Figure 15 in general terms are provided in detail based on the utilized materials and process details in the following Sections. Previously, a full-treatment on the fabrication of a NFRT harvesting device was performed by [25]. The device fabricated by [25] was a SiO₂-on-Si device with a vacuum cavity, to demonstrate the NFRT between two parallel SiO₂-on-Si media. Summaries of the other works involving microfabrication of test samples were provided in the literature review, in Chapter 2.

In this dissertation, processes are specified based on the materials used and accessible fabrication capabilities.

Briefly, the aim is fabricating a device enabling the demonstration and measurement of NFRT between two SiC thin films deposited on Si wafers, i.e., referred to as SiC-on-Si, herein. For this purpose, thin film deposition (by RF magnetron sputtering and PECVD), photolithography, wet etching, wafer-level bonding, and wafer dicing processes are performed. For this purpose, facilities of Nanoboyut Laboratory at the Physics Department of Eskişehir Technical University; Middle East Technical University, Micro Electro Mechanical Systems (METU-MEMS) Research and Application Center; and EV Group (EVG, at Austria) are used for device fabrication. A chart showing the fabrication stages and the respective places that the processes are performed is provided in Figure 16.

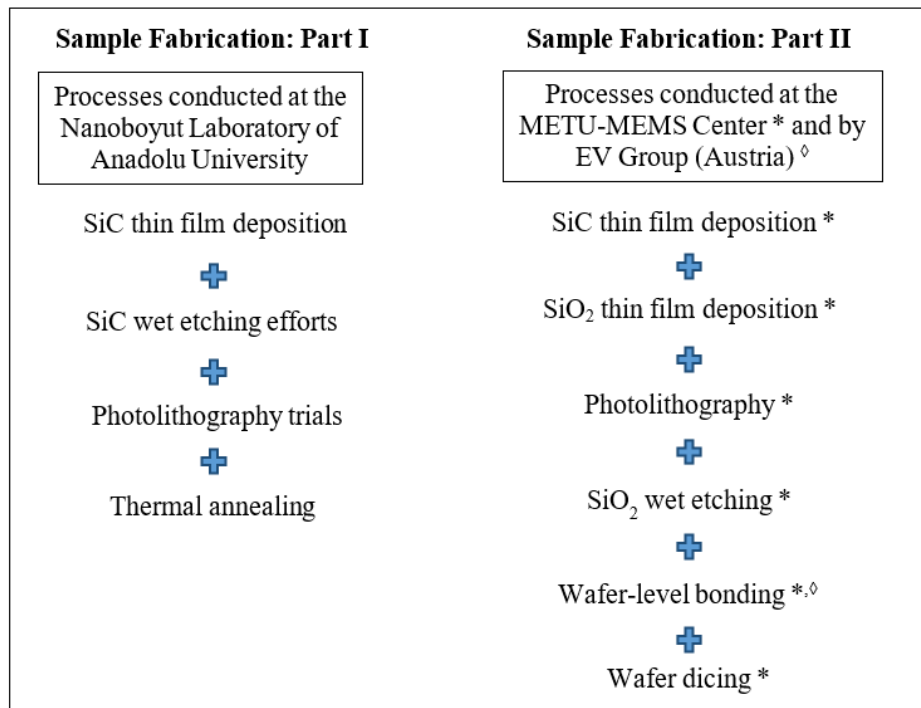


Figure 16. Process steps and the facilities used in NFRT device fabrication.

In addition to the process steps and Centers mentioned in Figure 16, reference samples were gathered from the Queensland Micro- and Nanotechnology Centre of Griffith University, Australia. These reference samples were provided as SiC coated, and the stages in Part II of Figure 16 were applied on them, only by skipping SiC thin film deposition. These samples were fabricated by low pressure chemical vapor deposition (LPCVD) technique [69], and the resulting SiC phase was cubic (i.e., 3C-SiC). Further details on NFRT device fabrication are given in the following Sections, individually for Part I and Part II of sample fabrication.

Apart from the process trials performed at METU-MEMS Center, Si (100) wafers used were B-doped (p-type), and of 4-inch diameter, 0.5 mm thickness, and 10-20 ohm-cm resistivity. During SiC thin film deposition processes conducted at Nanoboyut Laboratory (Part I), the SiC sputtering target used was a bonded assembly. The SiC disc (of 99.5% purity) was bonded to a Cu backing plate with In as the binder material. The target dimensions are 2-inch diameter and a total of 0.25-inch thickness for Cu backing plate and SiC disk. The mentioned Si wafers and bonded SiC target were purchased from Fotonika Yarı İletken Teknolojileri, at Ankara, Turkey. For Part II of the sample fabrication, the SiC sputtering target (of 99.9% purity) used was in monolithic (not bonded) state with 4-inch diameter and 0.125-inch thickness. This target was purchased from the Sindhhauser Materials, Germany.

The characteristics of the samples obtained from the Queensland Micro- and Nanotechnology Centre of Griffith University are provided in Table 7, below. The rms (root mean square) roughness values were determined by AFM measurements, by the Center.

Table 7. Reference sample characteristics (purchased from Griffith University).

Sample ID	Measured SiC thickness (requested SiC thickness)	Si wafer specifications	rms roughness
EF 3677	194.7 nm +/- 0.51% (200 nm)	Double side polished (DSP), <100>, diameter: 150 mm, thickness: 380 +/-10 μ m, p-type	Not reported*
EF 3679	198.43 nm (200 nm)	DSP, <100>, diameter: 150 mm, thickness: 380 +/-10 μ m, p-type	1.03 nm
EF 3680	200.78 nm (200 nm)	DSP, <100>, dia.: 150 mm, thickness: 380 +/-10 μ m, p-type	
EF 3416	148.50 nm (150 nm)	DSP, <100>, dia.: 150 mm, thickness: 400 μ m, n-type	cca. 1 nm
EF 3417	146.70 nm (150 nm)	DSP, <100>, dia.: 150 mm, thickness: 400 μ m, n-type	
EF 3763	51.30 nm (50 nm)	DSP, <100>, dia.: 150 mm, thickness: 400 μ m, n-type	cca. 1 nm
EF 3764	52.90 nm (50 nm)	DSP, <100>, dia.: 150 mm, thickness: 400 μ m, n-type	

* Since fabricated through the same methodology, it is expected that EF 3677 has a similar rms roughness value as EF 3679 and EF 3680.

4.2. Fabrication Processes - Part I

In this Section, processes performed at the Nanoboyut Laboratory of Physics Department at Eskişehir Technical University are presented. Studies outlined in this Section (as Part I) are exploratory in nature, since feasibility of the planned processes (thin film deposition, etching, photolithography, thermal annealing, etc.) was investigated. This Part thus presents both the achieved processes as well as practical challenges in studying SiC, in thin film state, on Si wafers.

In the first process, deposition of SiC thin films via RF magnetron sputtering was aimed to be optimized. In this respect, before and after optimization, calibration work, and resulting SiC samples were presented. As a result, a repeatable and reliable sputtering recipe was formed. The other aim was crystallization of the SiC films deposited on Si wafers. For this purpose, thermal annealing was performed. Characterizations were performed via FTIR Spectroscopy, XRD, optical and Scanning

Electron Microscopy (SEM) imaging, to indicate structural changes induced by thermal annealing.

4.2.1. SiC Film Deposition via RF Magnetron Sputtering

SiC thin films were deposited onto Si wafers via RF magnetron sputtering technique (device: Vaksis Midas PVD-MT/1M3T- PVD/1eB). Inside of the chamber with target location and substrate holder are marked as shown in Figure 17. During depositions, the process gas was Ar, due to its inert nature and large molecular structure (latter is advantageous in providing a sufficient level of momentum in material transfer).

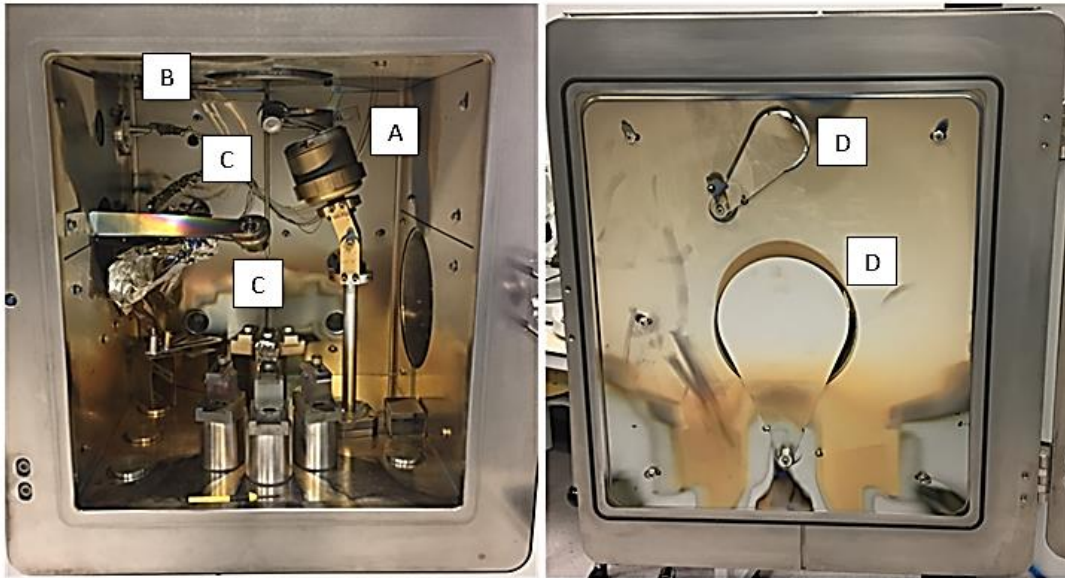


Figure 17. Photographs of RF magnetron sputtering chamber, A: target location, B: substrate holder, C: thickness monitors, D: view ports.

Initial efforts on determining the deposition rate (i.e., coating thickness obtained through a certain deposition duration) started by setting applicable process parameters and through the values reported in the literature. Through these first trials, depositions were conducted placing shadow masks on wafer pieces.

Wafer pieces were cut from a full wafer using scribe, and then cleaned by immersion in dilute HF acid (i.e., 200 ml of H₂O + 20 ml of HF (48%)). The pieces were placed in this solution for 20-30 seconds to remove the native oxide, rinsed with deionized water (DIW), and dried by N₂ flux. Cleaned wafer pieces were then placed on the sample holder. Shadow masks were placed onto the wafer pieces. In this way, both coated and uncoated regions were obtained on the same surface. This assisted in determination of coating thickness after a processes. A photograph showing the placement of wafer pieces and shadow masks on the sample holder before mounting into sputtering chamber is presented in left of Figure 18.

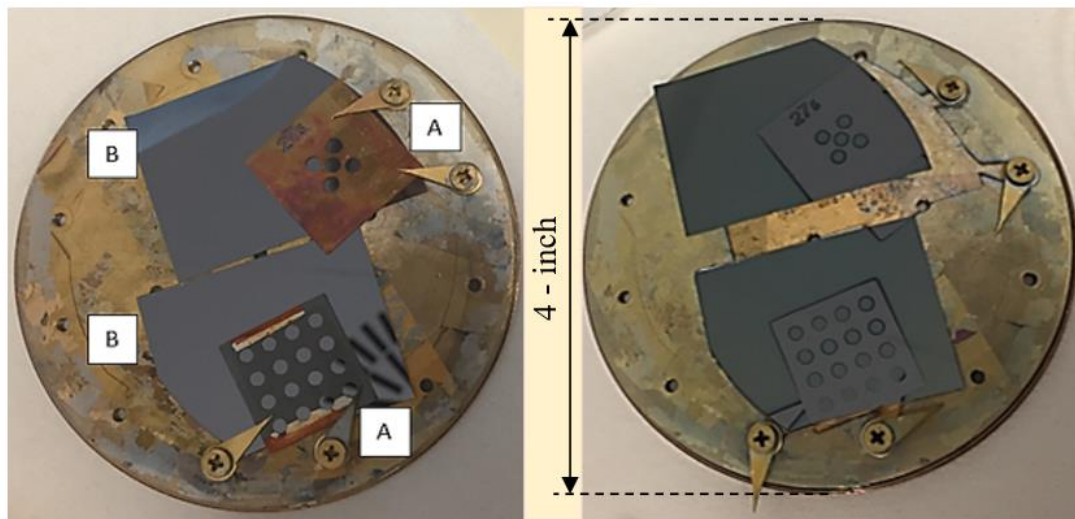


Figure 18. Wafer pieces and shadow masks. Left: (A) shadow masks, (B) wafer pieces before deposition, right: after deposition.

The first sputtering process trial was conducted on the samples shown in left of Figure 18, for 45 minutes at 150 W RF power, 20 rpm substrate rotation, 100 sccm Ar flux, 65% gate valve position, and 4.5 mTorr chamber pressure. The resulting wafer surfaces, which were successfully coated, are shown in right side of Figure 18. Once the wafer pieces were coated, the resulting SiC film thickness was determined by measuring the height difference between coated and uncoated regions, using a profiler device (KLA Tencor P-6).

During thickness measurement, the scan speed was 20 $\mu\text{m}/\text{sec}$, applied force was 20 mg, and sampling rate was 20 Hz, with a varied scan length. In Figure 19, the regions where the thickness data were taken are shown with numbers 1 - 4. Mainly, inside of the circles and right side of the patterned part (with a relatively darker green color) were coated by SiC, while lighter green areas were covered by the shadow masks and thus left uncoated. The profiler output taken all along the region 4 is added to Figure 19, showing a thickness of 107 nm – 107.5 nm, as an example.

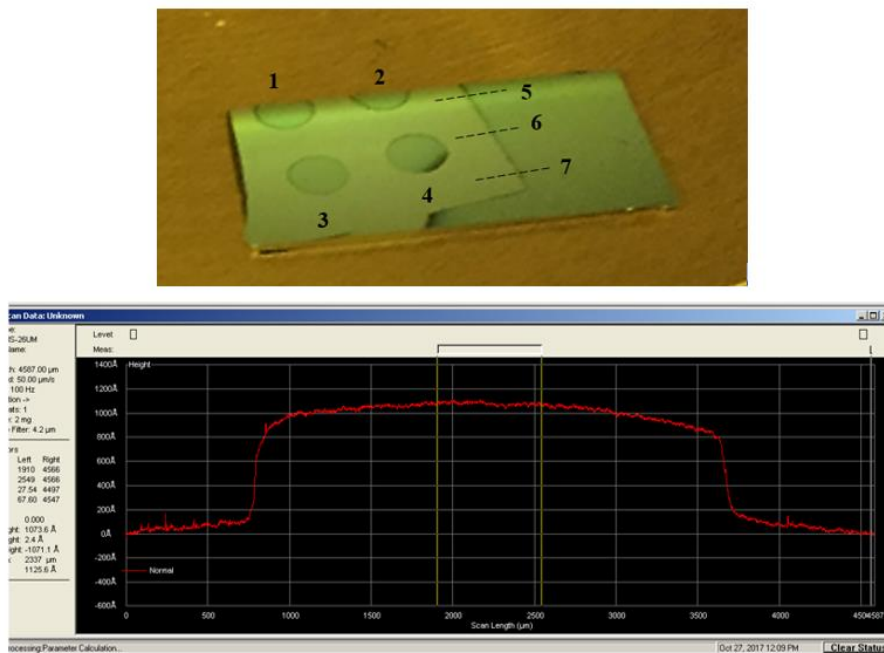


Figure 19. SiC film thickness data collection points (top), example data output (bottom).

The thicknesses measured at the other numbered regions are 121.5 nm (from the right) and 121 nm (from the left) for the region 1, 113 nm – 114 nm (from the right) and 112 nm (from the left) for the region 2, 118 nm - 119 nm (from the right) and 72 nm (from the left) for the region 3, 107 nm (from the right) and 107.5 nm (from the left) for the region 4, 70 nm (from the left) for the region 5, 70 nm (from the left) for the region 6, and 50 nm (from the left) for the region 7. In this explanation, measurement from the left indicates the difference in heights of the left bottom (uncoated) and the top (coated) of the step, while that from the right is the difference in heights of the right

bottom (uncoated) and the top (coated) of the step. The difference in coating thicknesses shows that the thickness was not uniform throughout the coated surface, which results from the location that the wafer piece was placed on the sample holder with 4-inch diameter.

After a number of depositions, it was seen that In (i.e., target-backing plate binder) in the bonded sputtering target melted, and resulted in contamination inside the target location, although the target was water-cooled during processes. Contamination prevented plasma formation, which is essential for initiating the deposition process. The target after this situation and the melted In pieces are as shown in Figure 20.

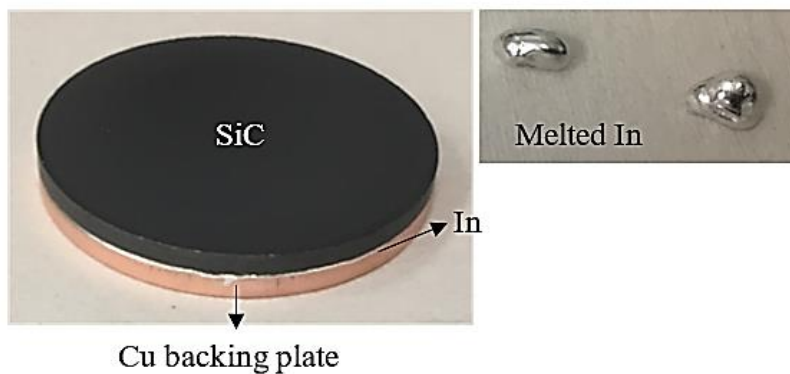


Figure 20. Targets situation and melted In pieces.

Regarding this issue, the manufacturer informed us that the RF power density on this bonded assembly should not exceed 20 W/inch^2 . For this case, considering the diameter of the target (2-inch), the surface area is $\pi \text{ inch}^2$, resulting a maximum of 62.8 W RF power to be applied for the sputtering operation. It was also advised that the power ramp-up and -down rates should not exceed $10 - 20 \text{ W/min}$. It is deduced from the information provided by the manufacturer that melting of In (at $\approx 156^\circ\text{C}$) might be originated from application of high RF power than allowed power limit (i.e., 62.8 W) which might have led to high process temperatures (compared to the melting point of In). After this situation, the contaminated place in the chamber was cleaned.

Use of a bonded target may require limiting of RF power such that the temperature in the chamber would not increase up to the melting temperature of binder during processes. At this point, use of a monolithic (not-bonded) target would be an alternative, but it also has challenges specific to its monolithic nature. Deciding on the use of either a bonded or a monolithic sputtering target should be done depending on the process needs. While monolithic targets consist of the target material only; a bonded target consists of the target material, a conductive backing plate, and an intermediate binder material (mostly In, or an elastomer). Use of a conductive backing plate makes the use of a binder material a necessity, in order to be safely attached to target. Cooling of the target during sputtering is easier when a conductive backing plate is used. Also, in case of a target cracking (for example, due to thermal shocks), the backing plate can keep the pieces together. For the case of monolithic targets (used in the Part II of the fabrication process), process parameters (especially RF power) should be carefully chosen such that the target would not experience any thermal shocks and be cracked, since a cracked monolithic target cannot be used [121].

With this insight, a calibration sputtering process was performed considering the maximum RF power limit of, i.e., 62 W. The wafer piece was cleaned as stated before. After setting the initial parameters, the gate position was 60% and Ar flux was 100 sccm. Next, the RF mode switch was turned on and the power was increased to 10 W. At this power value, plasma was formed. Next, the density, Z-ratio, and tooling factor for SiC were set respectively to 3.22, 1, and 100%. During the increase of RF power by 10 W/min up to 60 W, the Ar flux was adjusted to 150 sccm. Simultaneously, rotation to the substrate was given as 15 rpm to obtain a uniform coating thickness as much as possible. On the other hand, during this stage, the deposited layer thickness shown by the thickness monitor (TM) of the device was fluctuating between -0.2 \AA/s , 0 \AA/s , 0.2 \AA/s , and 0.4 \AA/s . Although the value shown by the TM of the device is not by necessity accurate, a negative deposition rate was considered as a sign of zero or extremely low deposition rate. Having seen this result, the RF power was increased to 100 W (lower than the power resulted in In contamination, 150 W), with chamber pressure of 4.5 mTorr and Ar flux of 115 sccm. With this recipe, a SiC film thickness of 80 nm - 90 nm was obtained.

Although no further contamination of In in the magnetron was observed at 100 W and deposition rates close to zero was seen for deposition trial at 62 W, a trial was conducted at this lower RF power (62 W), as well. From the literature review in Chapter 2, it can be seen that most of the previous works were concerned with deposition of SiC at high RF powers and power densities, up to 8.7 W/cm^2 [59], while in this work, 62 W RF power corresponds to a much lower power density, i.e., 3.06 W/cm^2 . After performing the process 62 W, it is seen that although the TM showed a zero or a negative rate value, a slow deposition was actually taking place. The calibration for 62 W was conducted on a Si wafer cleaned as previously indicated (by immersion into dilute HF solution and then DIW rinse), and dried. A full-wafer was used here; since depending on the target diameter, target-substrate distance, substrate diameter, location on the holder, and so on; non-uniformities in the coating thickness could be observed.

In this case, a polytetrafluoroethylene (PTFE) tape (Taega Seal PTFE Tape) was used to cover a small region throughout the wafer, to have an uncoated part (e.g., a step) to measure both the coating thickness and thickness non-uniformities more easily. The parameters for this process were: 150 sccm Ar flux and 75% gate valve position (resulting in 1.3×10^{-2} Torr pirani vacuum gauge pressure, 1.6×10^{-3} Torr ion gauge pressure) and 15 rpm substrate rotation. A power ramp-up and -down rate of 10 W/min was used. During the power ramp-up, the recorded working voltage and corresponding power values were as in Table 8.

Table 8. RF power and corresponding voltages for low RF power calibration deposition.

RF Power (W)	Working Voltage (V)
10 W	57 V (plasma formation)
20 W	104 V
After the plasma was formed, parameters were set to 100 sccm Ar flux, 60% gate valve position, 4.3 mTorr pirani vacuum gauge value, 1.3 mTorr ion gauge pressure.	
30 W	137 V
At this point, material density and Z values were inserted so that the thickness monitor (TM) could calculate thin film thickness.	
40 W	172 V
50 W	204 V
60 W	229 V
62 W	237 V

Until the last step in Table 8, the shutter was closed and deposition did not take place. This phase is called pre-sputtering, during which target surface is cleaned due to Ar bombardment. After RF power was 62 W, deposition parameters were 100 sccm Ar flux, 61% gate valve position, and 15 rpm substrate rotation. Once the substrate rotation was started, the shutter was opened and the deposition was started. In Table 9 below, the thicknesses (kÅ) recorded periodically from the TM are given.

Table 9. TM outputs recorded during the process.

Duration	Thickness read from TM
30 min	0.226 kÅ
50 min	0.325 kÅ
60 min	0.380 kÅ
70 min	0.438 kÅ
80 min	0.495 kÅ
90 min	0.553 kÅ
100 min	0.608 kÅ
110 min	0.665 kÅ
120 min	0.718 kÅ
130 min	0.771 kÅ
140 min	0.829 kÅ
150 min	0.886 kÅ
160 min	0.942 kÅ
170 min	1000 kÅ
180 min	1058 kÅ
190 min	1114 kÅ

After this process, a SiC film thickness of 140 nm (at the extreme outer region) - 190 nm (near the middle region) was obtained throughout the wafer. As it is presented in Figure 21, the coating thickness was greater in and around the middle of the wafer and it decreased through the outer edges. Difference in coating thickness can be optimized by adjusting the deposition rate together with the substrate rotation. The areas marked by colored circles in Figure 21 are estimated to have SiC thickness in a similar range (if the tape was not used and the middle region was covered).

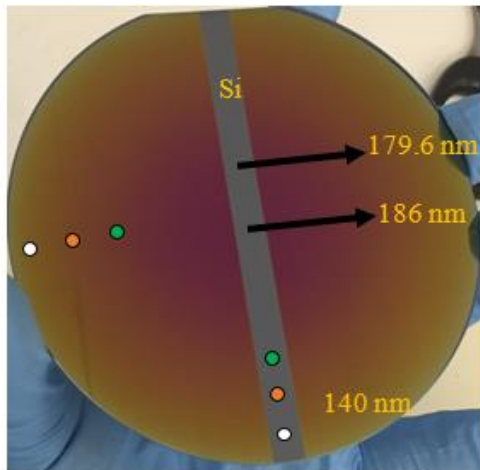


Figure 21. SiC-on-Si surface appearance dependent on SiC film thickness.

After this deposition, a 90 nm SiC film thickness was aimed. A full wafer was cleaned and covered by the tape as indicated previously. Parameters of the calibration work were used, i.e., 150 sccm Ar flux, 75% gate valve, 15 rpm substrate rotation, with power ramp-up and -down rate of 10W/min. This time, a process duration of 90 minutes was planned to obtain a thickness of 90 nm. Actual thickness measurements with the profiler confirmed a thickness of around 90 nm (range: 80.63 nm-89.5 nm). It can be observed from Figure 22 that SiC surface color changes significantly with SiC film thickness. A color chart was reported for 3C-SiC films of different thicknesses, grown on Si substrates by [69]. It was stated in [69] that this surface color chart may as well be applied to poly-crystalline and amorphous SiC thin films. As a reminder, the as-deposited films of this work are assumed to be amorphous, since no substrate heating was applied throughout the depositions.

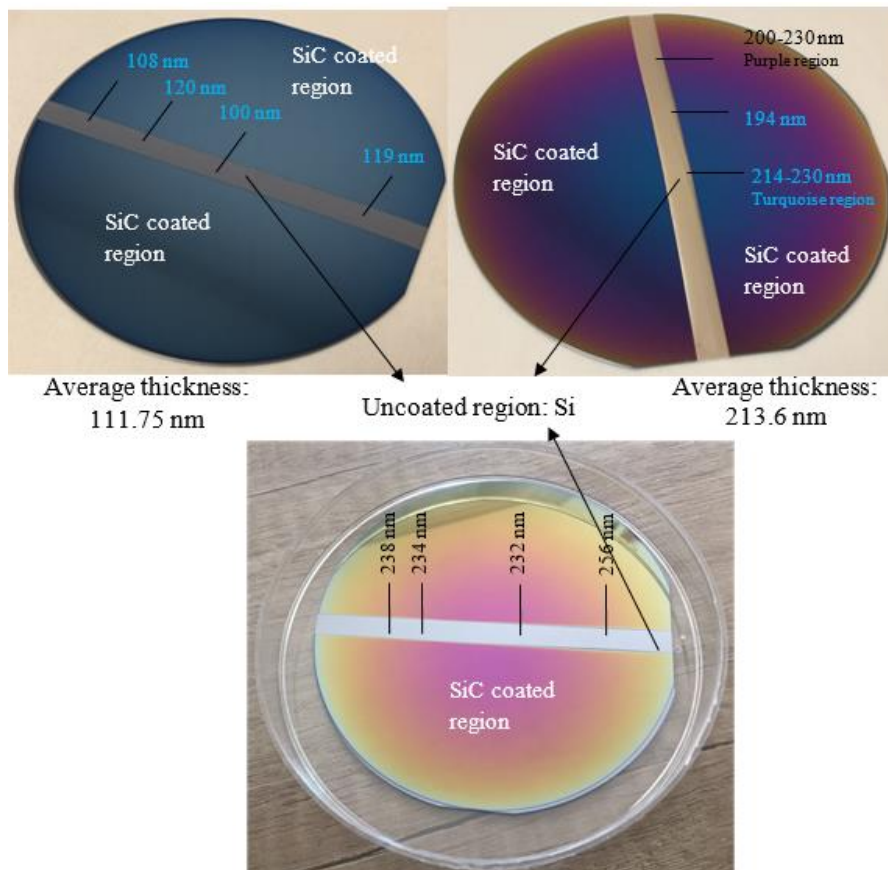







Figure 22. Photographs of deposited SiC thin films on full-size Si wafers.

Colors in Figure 22 are obtained reproducibly for the thinner (≈ 85 nm - 100 nm) and thicker (≈ 200 nm) SiC samples. Authors of [69] fabricated 3C-SiC thin films on Si substrates via LPCVD, and observed the colors under the bright field of an optical microscope. The colors reported by [69] are in partial agreement with the samples fabricated in this work, at (i) the regions of ≈ 140 nm thickness with yellow-like color, on (ii) the thinner film (90 nm thickness) with blue color, and (iii) ≈ 230 nm - 240 nm thickness with purple color. A relevant part of the SiC surface colors reported by [69] are given in Table 10, below.

Table 10. Surface colors for certain SiC thin film thicknesses. Adapted from [69].

Thickness	Image	Color
110 nm		Dark khaki
196 nm		Yellow green
230 nm		Brown
240 nm		Violet
253 nm		Blue violet

Wang et al. [69] stated that similar colors might be observed at different thickness intervals. Also, expression of colors may vary, since one may interpret the surface appearance of 230 nm as purple/violet, while it was denoted as brown in [69].

In Figure 23, the working voltage - RF power characteristics are given for the recipe developed for 62 W RF power. In 6 of the 8 processes, plasma was formed immediately after the power was raised from 0 W to 10 W, while in the two of the processes (on 26.10.2017 and 9.11.2017), plasma was formed at 20 W. This difference did not cause any considerable alterations in the sputtering rate presented in Figure 23.

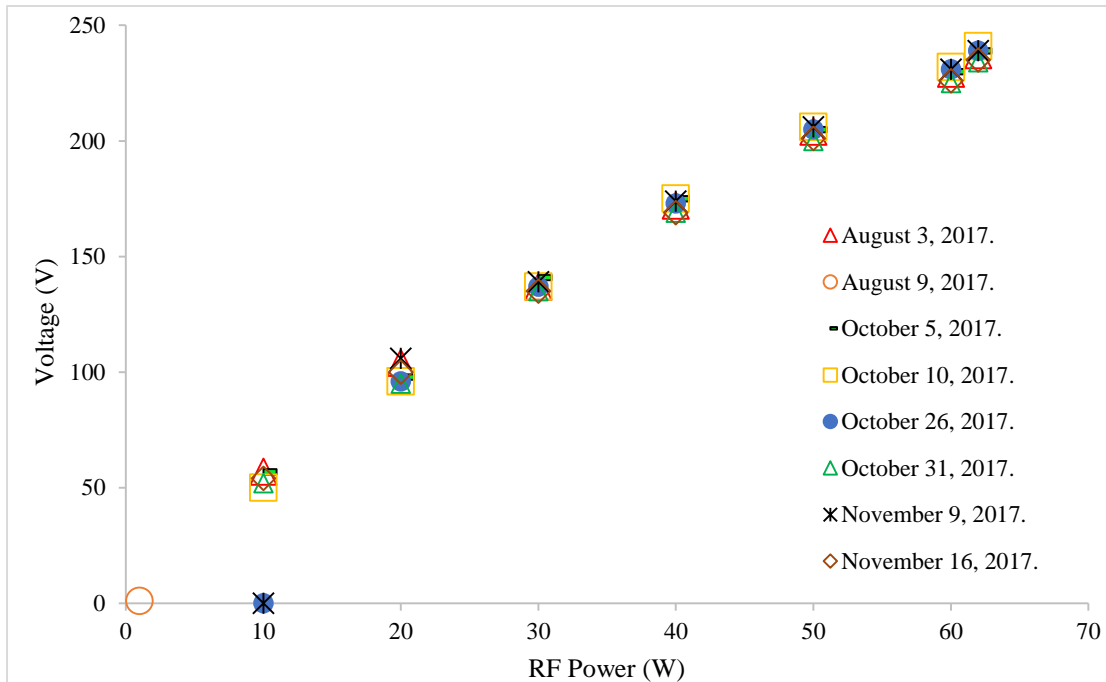


Figure 23. Voltage - RF power characteristics of the developed sputtering recipe (along with the dates of the processes).

The thickness monitor (TM) provides a value indicator of the thickness of the deposited film. This value was periodically recorded during the deposition, and presented in Figure 24. The TM output is not the same as the actual (measured) thickness, but is in proportionality with it. Apart from one deviation, the TM output is almost unchanged with the deposition duration.

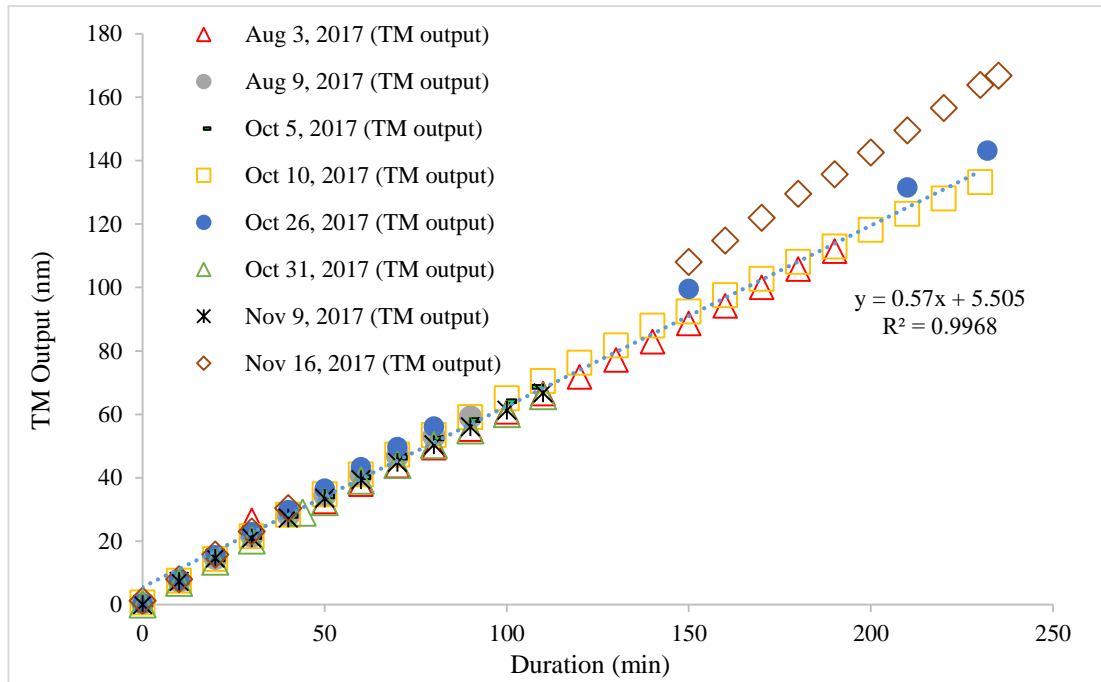


Figure 24. TM output during depositions (along with the dates of the processes).

The sputter rate (as shown by the TM output-duration ratio) shown by the device is linear except the variation of the TM output on 16.11.2017, which is attributed to possible alterations in base pressure level of the chamber.

Due to low RF power, the deposition rate is low (≈ 1 nm/min) compared to for example [60] which reports rates up to 50 nm/min at high RF power densities (e.g., 6.58 W/cm²). On the other hand, low growth rates are considered advantageous since better crystal qualities are likely to be obtained in comparison to high growth rates [122].

4.2.2. Wet Etching of SiC – Trial Study Results

In the initial process design as depicted in Figure 15, the bonding surfaces were considered to be of SiC, which has been changed to SiO₂ due to its lower thermal conductivity than that of SiC. This selection is to assist in suppressing heat conduction between emitter and receiver when compared to the use of SiC as bonding surfaces. In the initial design, to pattern the coated SiC films, wet etching trials were performed.

SiC is known with its hardness and durability even in harsh conditions, and its etching is challenging. Especially monocrystalline SiC is very difficult to etch due to the very strong chemical bond of C-Si. For amorphous SiC, the atomic bonds are weaker and Alok and Baliga [123]; Edmond et al. [124]; and Roper et al. [125] presented the use of HF and HNO₃ for the wet etching of amorphous SiC films. It was reported [123] that the etch rate for SiC at 45°C with 1:1 volumetrically mixed HF and HNO₃ as 3000 Å/min. Janz [86] stated that phosphoric acid at 215°C and alkaline solution of K₃Fe(CN)₆ at higher than 100°C could be also be used, but the former might be disadvantageous due to low etch rate and leaving a SiO₂ etch-stop layer on the surface.

It was predicted that the as-sputtered SiC films are amorphous since high temperatures (via substrate heating or post-deposition thermal annealing) are needed to obtain crystalline SiC thin films (as outlined in Chapter 2). A 1 cm × 1 cm piece was cut from this coated wafer piece shown in Figure 25 for a controlled etch, with a dilute version of HF and HNO₃ to 1:1, at lower temperatures than reported by [123]. For this process 50 ml of HF and 10 ml of HNO₃ was mixed in a plastic cup, placed on an already cooled container filled with coolant. To differentiate etched parts conveniently, part of the SiC surface was coated with a photoresist (PR), AZ9260. After PR baking, the sample was placed in the solution for 2.5 minutes. After etching, the PR was removed by washing with acetone. Although the PR preserved the SiC surface a bit, both the PR coated and uncoated SiC surface were damaged. Although a certain portion of the amorphous SiC layer was etched away, it was seen that the backside (uncoated Si) of the wafer was significantly damaged.

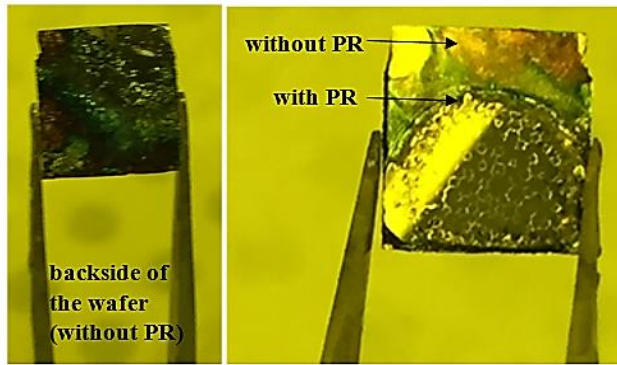


Figure 25. Samples, after etching a 1 cm \times 1 cm coated wafer piece.

In other words, even though HF and HNO₃ is reported as a rare and successful etchant of SiC, it etches Si isotropically as well. It is expected for the device in Figure 15 that the etchant would etch the SiC coated Si wafers from the bottom and the sides. Use of this etchant to make a patterned SiC surface requires protecting Si, and selectively etching SiC.

4.2.3. Photolithography and Lift-off – Trial Study Results

The aim here is to determine the type of PR, enabling the highest level of surface cleanliness, since non-uniformities and contamination is critical for the forthcoming wafer-level bonding process. An uncoated Si wafer was used for this trial to examine which of the PR alternatives would result in a surface as clean as possible, due to the fact that surface condition is critical for the wafer bonding process. The scheme in Figure 26 is performed using different PR materials. Resulting surfaces after step 6 are evaluated using optical microscope.

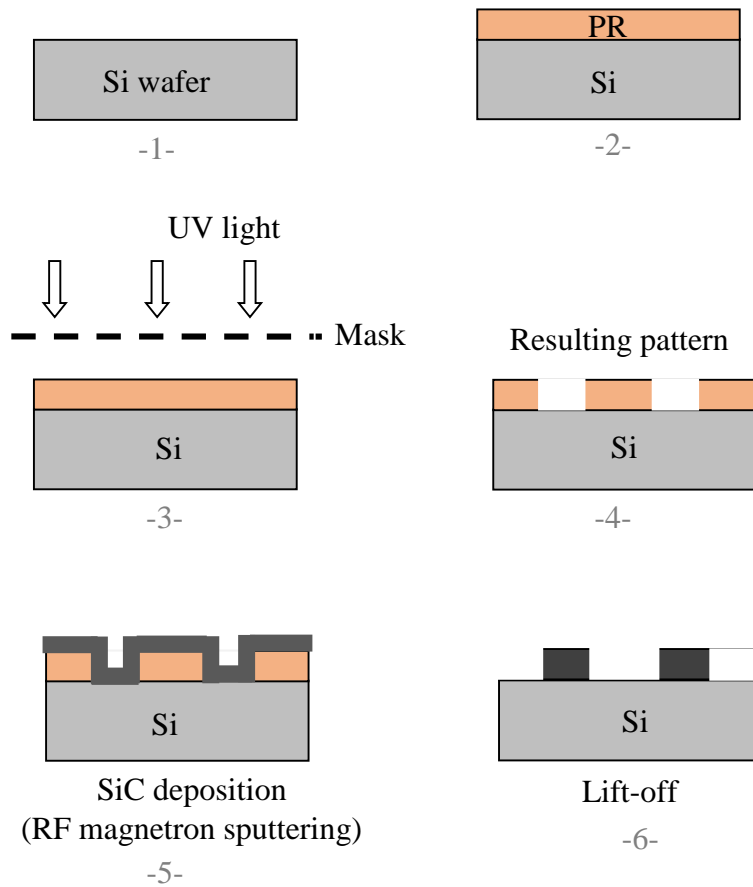


Figure 26. Photolithography and lift-off trial scheme.

For this purpose, a Si wafer piece was cut into pieces of 9 mm × 8 mm using scriber, and cleaned as described previously. The PR materials used were AZ 9260, AZ 5214, and SU-8. AZ 9260 and AZ 5214 are positive PR's, while SU-8 is a negative PR. The process parameters are given in Table 11.

Table 11. Photolithography and lift-off parameters.

PR materials	PR spin coating		Soft-bake		UV exposure
	Speed	Duration	Temperature	Duration	Duration
AZ 9260	3000 rpm	60 sec	105°C	60 sec	60 sec
AZ 5214	3000 rpm	35 sec	105°C	60 sec	30 sec
SU-8	3000 rpm	30 sec	65°C, then 95°C	60 sec, then 60 sec	30 sec

The exposed surfaces were submerged in the developer solution depending on the PR type. Time period of this stage is important since periods longer than required might cause over-develop of the solution. This process was performed controllably such that the samples were taken off once the patterns became visible, as shown in Figure 27.

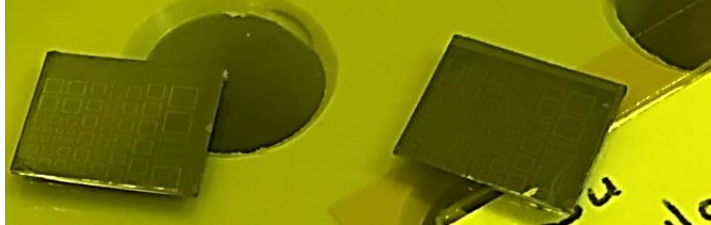


Figure 27. Sample surfaces after step 4.

At step 5 of the scheme in Figure 26, SiC coating was performed at 100W RF power for 1 hour, resulting in a SiC thickness of ≈ 120 nm. Following a lift-off process in acetone, surfaces of the samples were as shown in Figure 28.

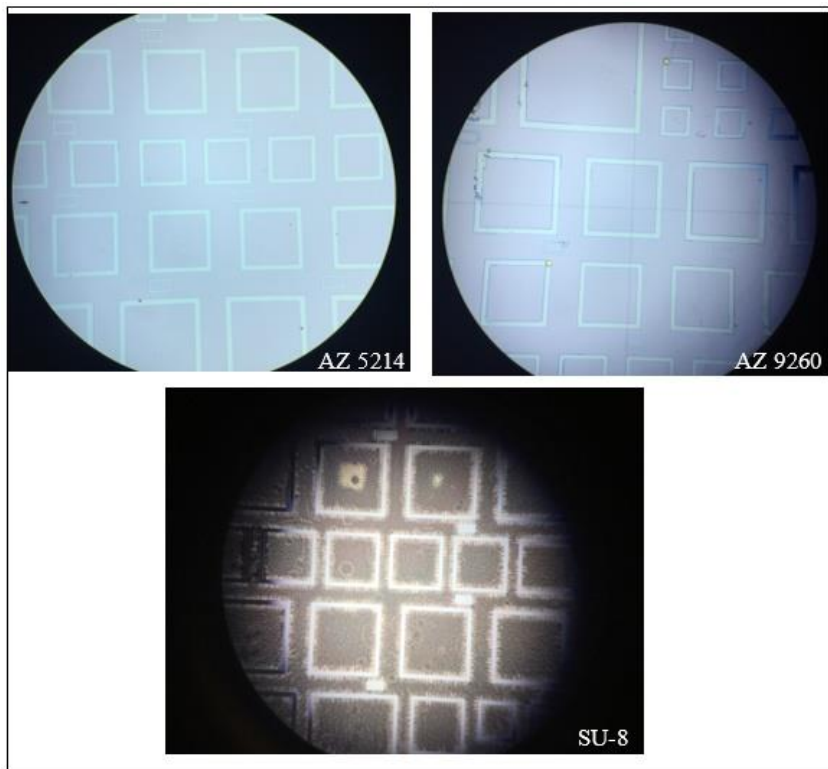


Figure 28. Surfaces of the SiC coated samples after lift-off process.

It can be seen from the microscopy images presented in Figure 28 that the surface with the highest cleanliness was obtained with AZ 5214. During sputtering, SU-8 adhered to the surface due to increase of the temperature during process and its removal from the surface during the lift-off process was more challenging in comparison to those for AZ 5214 and AZ 9260.

4.2.4. Thermal Annealing of SiC: Part I

As indicated previously, one of the aims of this work is to determine whether an amorphous SiC layer's phonon transport ability differ from that of a crystalline SiC layer. As it was presented in Figure 12, index of refraction and extinction coefficient of SiC, and thus the dielectric function, depends on the internal structure, which is directly correlated to the spectral NFRT flux, as defined in Eq. (1). Crystallization of SiC thin films deposited on Si wafers has been a widely studied topic, as outlined in Chapter 2. Generally, as-sputtered SiC films are amorphous, if not accompanied by substrate heating during deposition.

Within the scope of this dissertation, the SiC film deposition was conducted without any intentional substrate heating. These samples were then annealed via a Rapid Thermal Processing (RTP) furnace (the process is referred to as Rapid Thermal Annealing, RTA), and in a conventional furnace.

The RTA device (device: Annealsys-100, model: PLF 120/10) by definition is capable of providing high heating up- and –down rates, while this rate is essentially lower in a conventional furnace. In addition to the RTA process, a conventional annealing furnace (Protherm tube furnace, model: PTF) allowing higher temperatures and longer durations was also used. The samples were then characterized by FTIR spectroscopy and optical microscopy at Nanoboyut Laboratory of Eskişehir Technical University, and by XRD and SEM at Central Research Laboratory Application and Research Center of Eskişehir Osmangazi University. The FTIR data were collected in transmission (T) and reflection (R) modes.

Measurements were done in the wavenumber range of 400-6000 cm^{-1} with a resolution of 4 cm^{-1} . The sample scan time and background scan time were 16 scans. The beam splitter was KBr and the source setting was MIR. The XRD analyses covered a 2θ range of 10° - 90° . The step size was 0.0130° , scan step time (time per step) was 73.7 sec, and scan speed was $0.044^\circ/\text{sec}$. Hardness and elastic modulus measurements were performed at the Central Laboratory of Middle East Technical University, using CSM Instruments Indentation Tester, by applying 80 mN force for 1 minute.

The RTP device of the Nanoboyut Laboratory has the temperature and process duration limits provided in Table 12.

Table 12. Allowed temperature and process duration limits of the RTP device.

Temperature	Maximum duration
1300 °C	1 min
1250 °C	3 min
1200 °C	5 min
1150 °C	6 min
1100 °C	7 min
1050 °C	10 min
1000 °C	12 min
900 °C	60 min
<800 °C	120 min
The sensor temperature range	
Thermocouple: 0 - 1000°C	
Low temperature pyrometer: 150 - 1100°C	
High temperature pyrometer: 400 - 1400°C	

As shown in Table 13, the RTA processes are performed at different temperatures and process durations than those allowed. The first RTA processes started with samples previously coated with SiC, at 150 W RF power, 62% gate valve position, 20 rpm substrate rotation, 4.4 mTorr chamber pressure, 100 sccm Ar flux for 45 minutes. The thickness range on the wafer varied between 90-140 nm. This might be due to possible fluctuations due to the RF power applied on the target, when higher than 62 W.

The peak positions in the IR spectrum of samples are correlated with molecular structures [126], and chemical and structural information can be obtained by FTIR spectroscopy.

Considering the relatively high temperature range reported in the literature that enabled partial or full crystallization of SiC (greater than 900°C), the lower temperature limit in the RTA processes was taken 900°C. Annealing of the samples are conducted in forming gas (95 vol. % N₂ + 5 vol. % H₂, abbreviated as FG herein), vacuum (2.44×10^{-1} mbar – 4.88×10^{-1} mbar), and N₂ to observe annealing environments' effect on SiC internal structure improvement. Parameters of this first RTA process are given in Table 13.

Table 13. RTA process parameters (Part I).

Sample	Temperature	Duration	Environment
FG1	900°C	-*	Forming gas
FG2	900°C	40 min	Forming gas
FG3	1000°C	8 min	Forming gas
FG4	1100°C	4 min	Forming gas
FG5	1200°C	3 min	Forming gas
V1	900°C	40 min	Vacuum
V2	1000°C	8 min	Vacuum
V3	1100°C	4 min	Vacuum
V4	1200°C	3 min	Vacuum

* After the process, it is seen that the sample FG1 was misplaced. It was therefore not considered in the successive stages.

In Table 12 and Table 13, it is shown that the maximum allowed durations were not approached, and a safety factor of 2/3 was applied to process durations.

Optical properties in transmission (*T*) and reflection (*R*) mode could be collected in the FTIR device used, while absorbance (*A*) values were calculated from *T* and *R*. The transmission spectra for the samples annealed under forming gas and those for the samples annealed in vacuum were provided respectively in Figure 29 and Figure 30. In both Figures, transmission spectrum of an untreated sample is given for comparison.

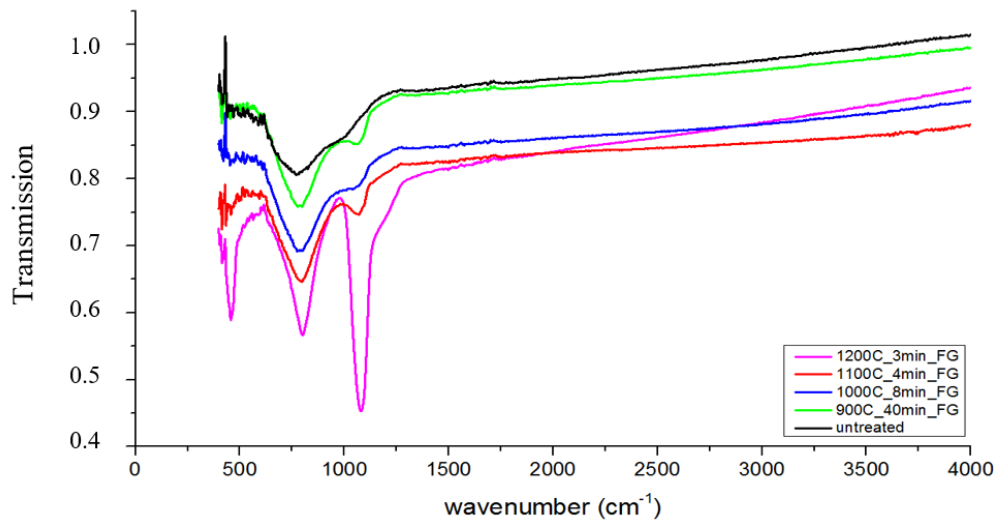


Figure 29. FTIR transmission spectra of the samples annealed in forming gas.

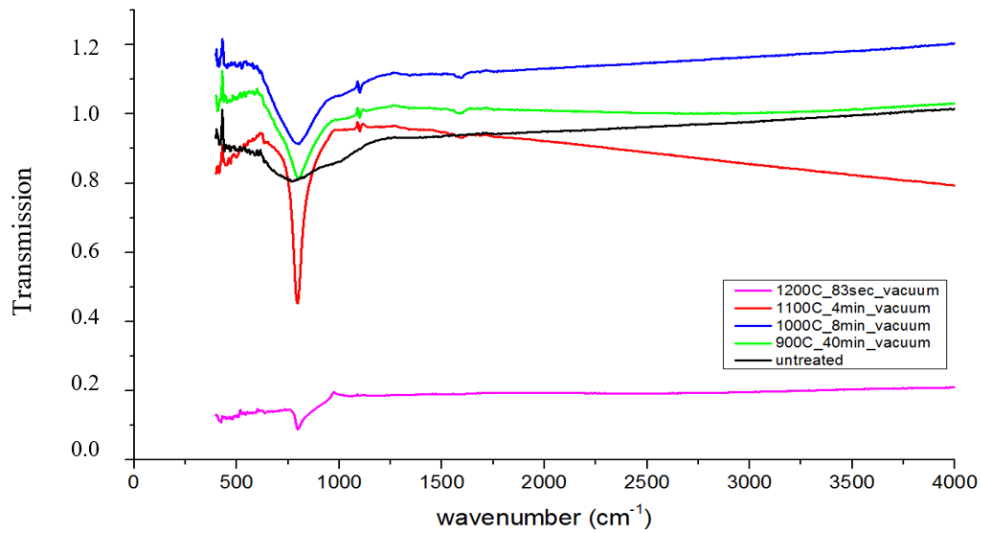


Figure 30. FTIR transmission spectra of the samples annealed under vacuum.

Both in Figure 29 and Figure 30, an overlapping band at around 800 cm^{-1} is seen for annealed and untreated samples. These bands are assigned to the Si-C stretching vibration. Absorbance of the samples are obtained through $A = -\log_{10}(T)$, since measurements in the transmission mode was possible at that time. The absorbance data

for the samples annealed at 900°C in forming gas and vacuum are provided comparatively below in Figure 31.

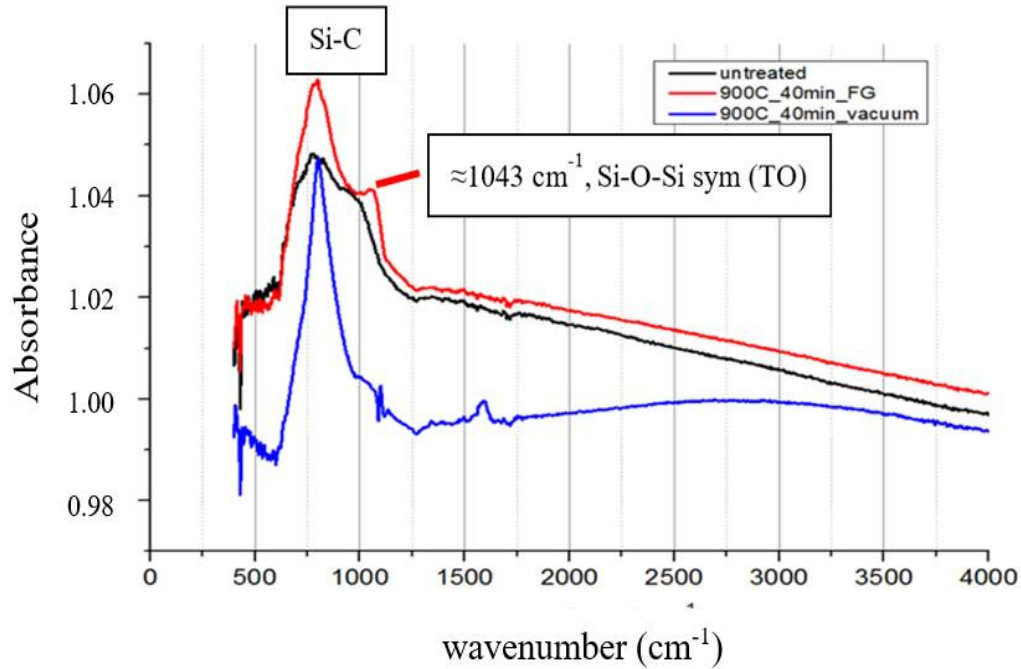


Figure 31. FTIR absorbance values of samples annealed at 900°C (forming gas and vacuum).

When compared to the spectrum of the untreated sample, the Si-C band width decreased with RTA both under forming gas and vacuum. Along with the Si-C vibration, Si-O-Si (TO) mode can also be observed, suggesting the presence of O₂ in the samples. The results corresponding to RTA at 1000°C and 1100°C are presented below respectively in Figure 32 and Figure 33.

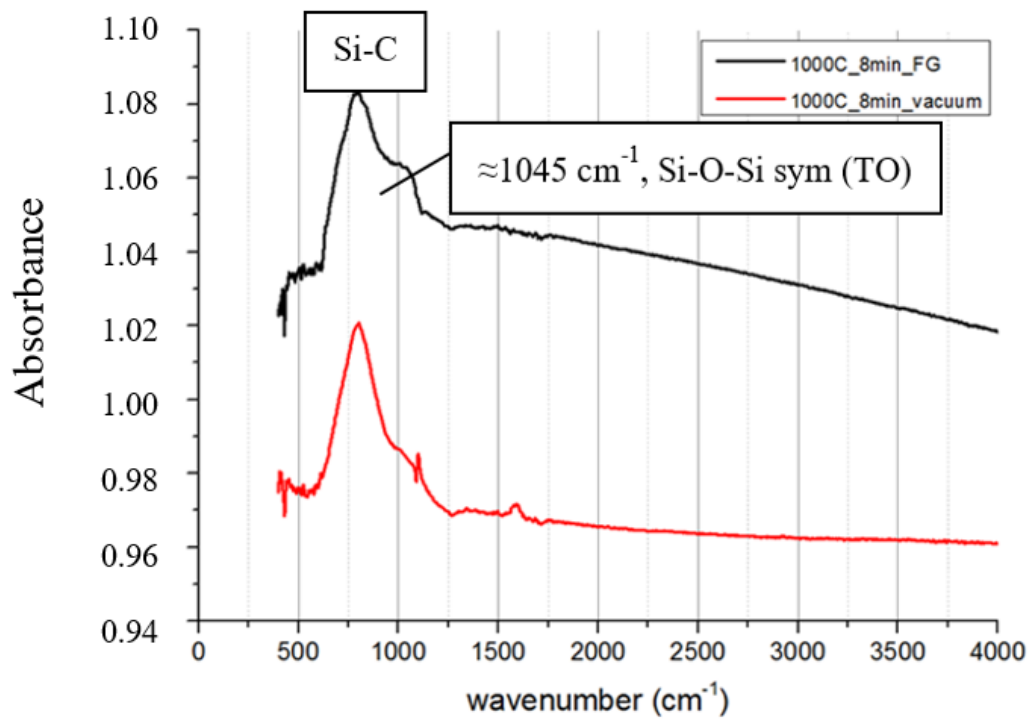


Figure 32. FTIR absorbance values of samples annealed at 1000°C (forming gas and vacuum).

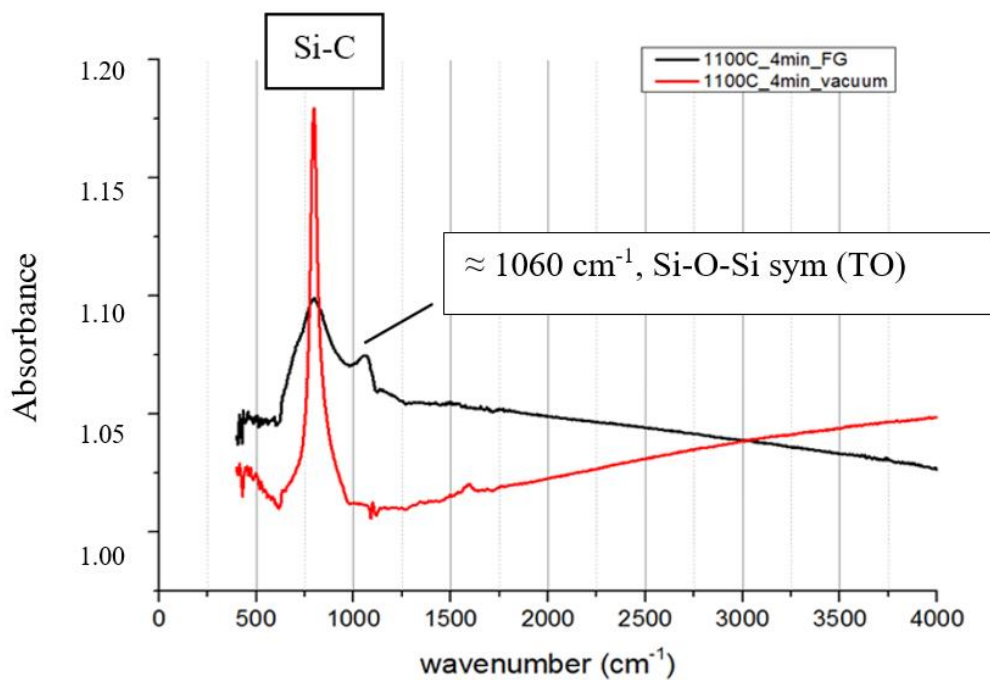


Figure 33. FTIR absorbance values of samples annealed at 1100°C (forming gas and vacuum).

Decrease of the Si-C bandwidth of the sample annealed at 1100°C under vacuum is clearly observed, which could be indicative of a structural transition into a more ordered network. Results for the samples treated at 1200°C are provided in Figure 34.

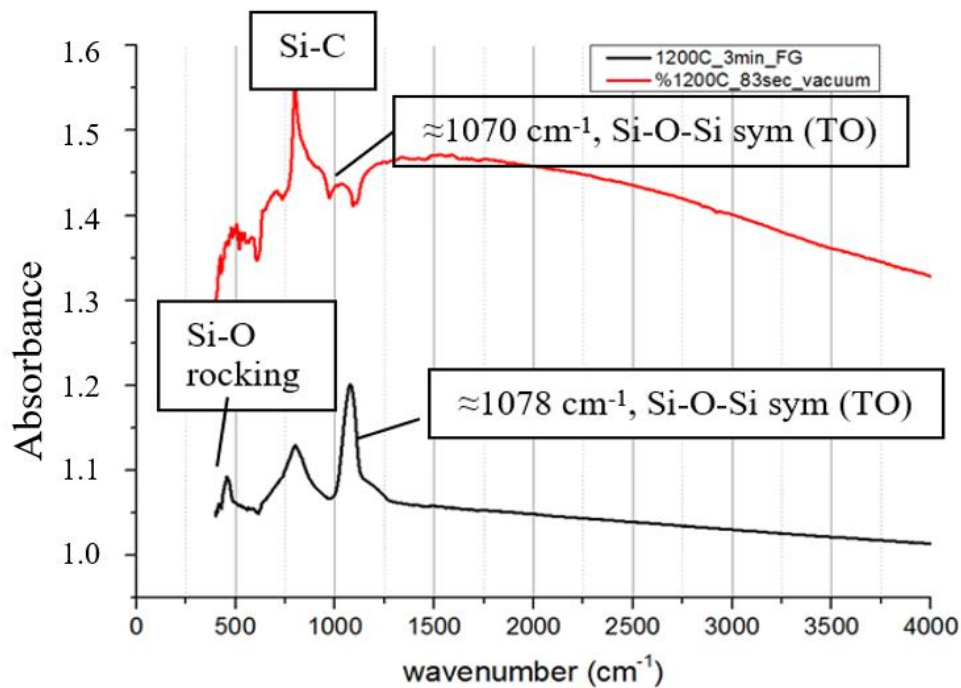


Figure 34. FTIR absorbance values of samples annealed at 1200°C (forming gas and vacuum).

The difference between the absorbance values of the samples annealed under vacuum and forming gas at 1200°C can be clearly seen in Figure 34, although the spectral properties of the absorbencies are similar. During the annealing under vacuum at 1200°C, the RTA devices' controllers stopped the process, since the thermocouple stopped working. During that process, temperature of the sample was kept at 1200°C for 83 seconds, before the annealing was terminated. This outcome was attributed to temperature oscillations that might yield to higher temperatures.

A common approach in the literature in observing whether the heat treatment worked in obtaining a more ordered structure has been evaluating the character of Si-C band shape. A Gaussian line shape is a sign of an amorphous phase by indicating a Gaussian distribution of bond lengths and bond angles, while a Lorentzian line shape indicates

a smaller bond angle distortion and narrow bond length distribution, and thus a more uniform, ordered and crystalline phase [10]. In order to see the line shapes of the Si-C bands, they are fitted to Gaussian and Lorentzian functions, using Origin Pro software. Results are given in Figure 35 and Figure 36 respectively for the samples annealed under forming gas and vacuum environments.

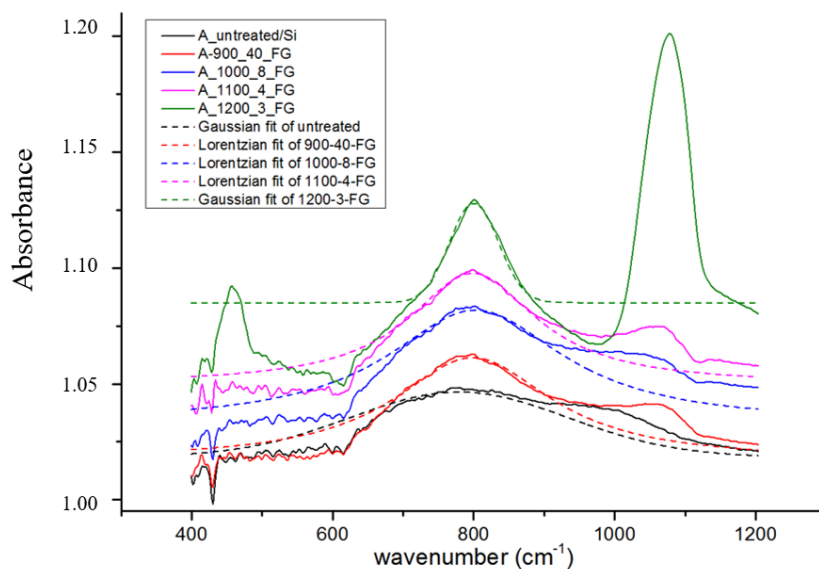


Figure 35. Si-C stretching band shape and curve fits for forming gas annealed samples.

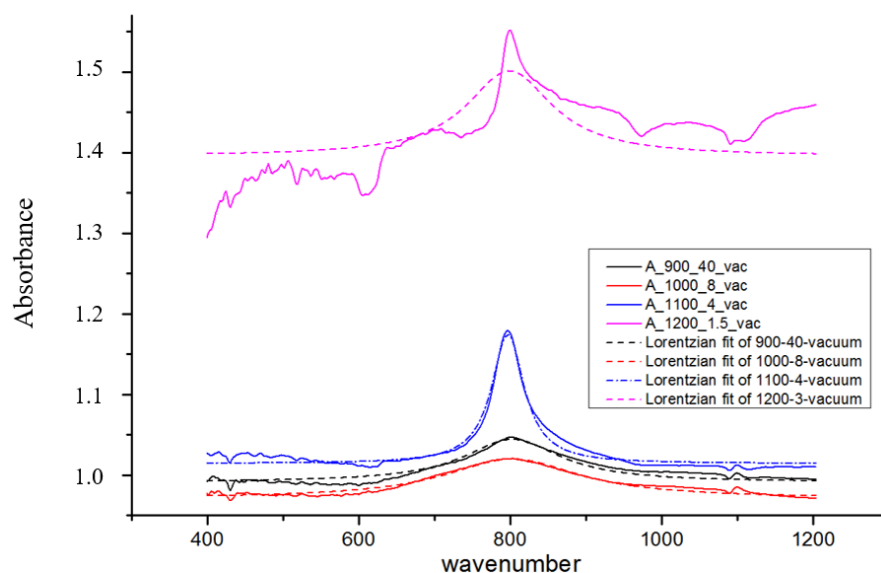


Figure 36. Si-C stretching band shape and curve fits for vacuum annealed samples.

Inspection of Figure 35 and Figure 36 reveals that, the untreated samples Si-C band has a Gaussian line shape, indicating an amorphous structure, as expected. As the annealing temperature increased from 900°C to 1100°C, the line shapes approach to Lorentzian distributions, which was considered as a sign of a more ordered and possibly a crystalline structure. Spectra of the samples annealed at 1200°C do not have a Lorentzian line shape, which was attributed to other structural changes (e.g., possible oxidation from the low density regions, estimated from the increased intensity of the oxygen related bands; or contaminations from the residual material in the RTA chamber) that resulted in disturbances in the internal structure of the films.

When the before and after annealing conditions of the samples are compared, it can be seen that the samples experienced changes that were chemical (some confirmed by FTIR spectroscopy) and/or physical (observed by visual examination). An example photograph comparing the surface appearances of the annealed (under forming gas) and untreated samples are given in Figure 37, below. An untreated SiC surface and an uncoated Si wafer surface were also captured for comparison. As it is presented in Figure 37, surfaces of the samples turned into blueish color, after annealing.

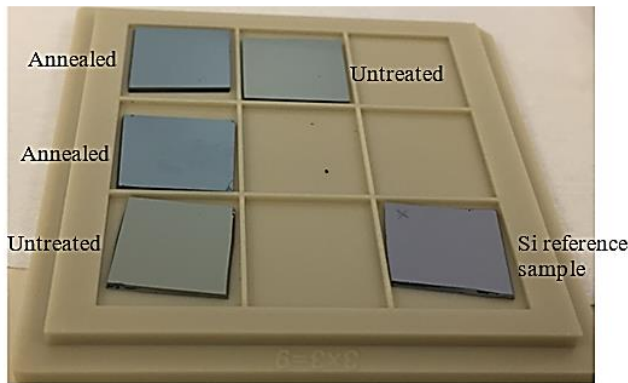


Figure 37. Surface colors of the samples before and after annealing.

Changes in the surface morphologies of the samples due to annealing are presented as light microscope and SEM (JEOL JSM-5600LV) images, in Figure 38 and Figure 39.

Crystallization attempts and/or high temperature deposition methods (especially $>1000^{\circ}\text{C}$) might negatively affect SiC-Si interface quality and could lead to defect formation [127]. In addition, a 20% mismatch between lattice constants (5.431 \AA for Si, and 4.3596 \AA for 3C-SiC) and 8% mismatch in thermal expansion coefficients of 3C-SiC (cubic SiC) and Si also result in high amount of defects at the SiC-Si interface and propagate in the SiC layer [128].

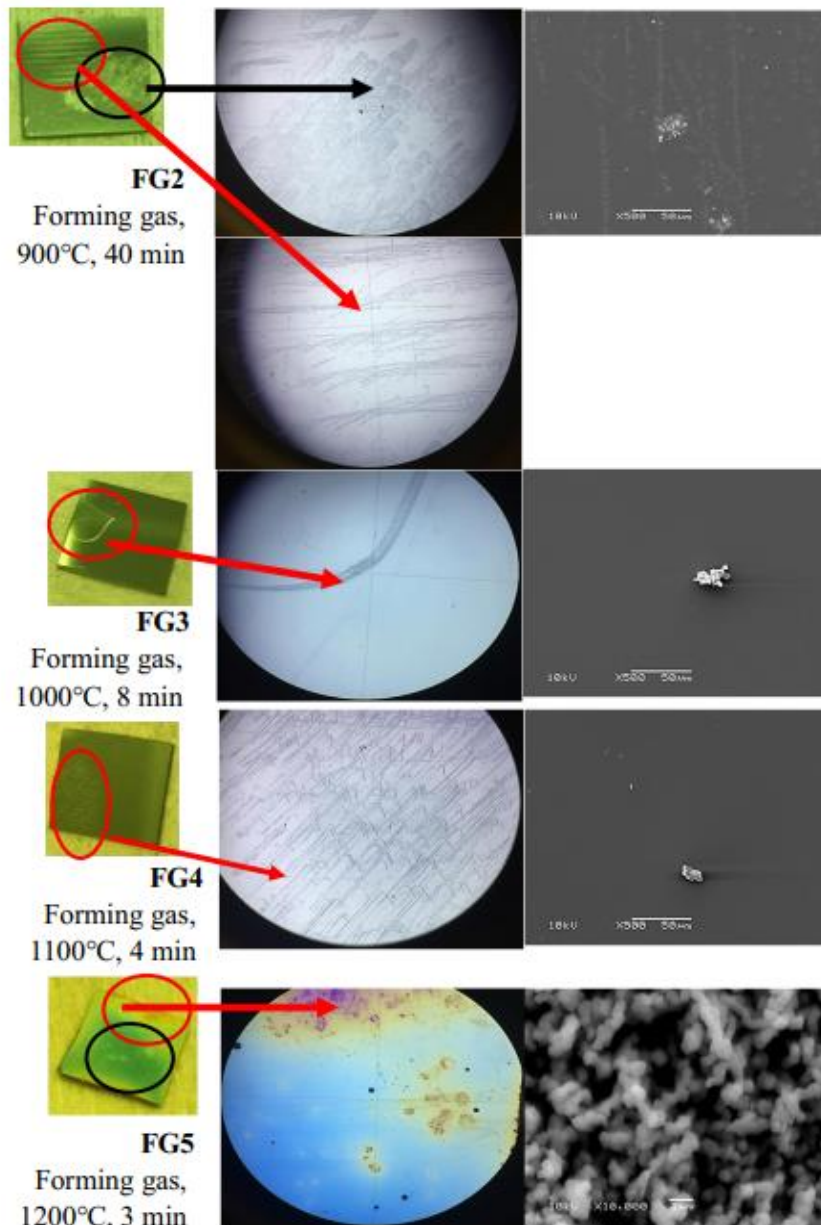


Figure 38. Surface changes after forming gas annealing.

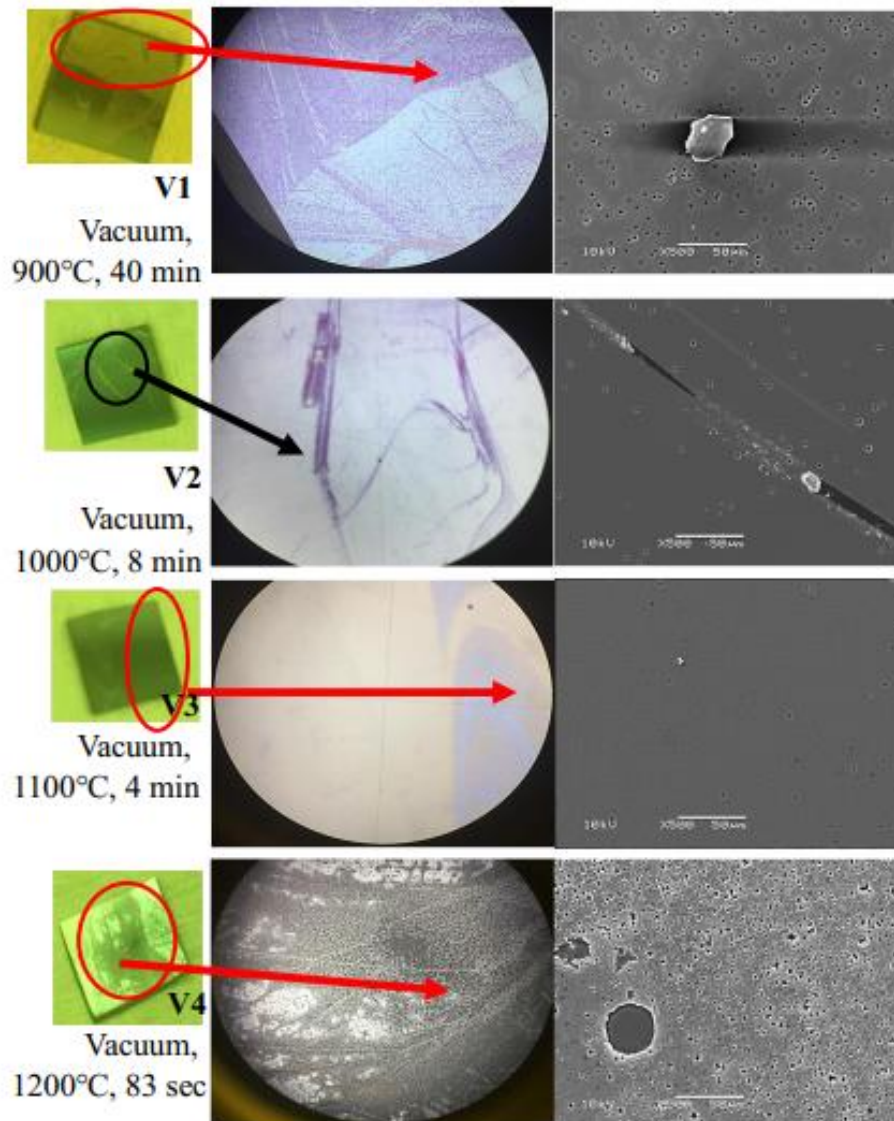


Figure 39. Surface changes after vacuum annealing.

It has been stated in the literature that additional formation of Si-C bonds in the film may lead to film contracting due to the electro-negativities of Si and C, and increased tensile stress [129]. In this dissertation, upon annealing, surface defects in the samples annealed at higher temperatures were observed to be more significant than those in the ones annealed at lower temperatures, in Figure 38 and Figure 39. A similar behavior was explained by [62] with the increase in number of Si atoms diffusing from the substrate to the thin film as the temperature approached to the melting point of Si (\approx

1400°C), leading to formation of defects along the thin film-substrate interface, and in the thin film. In the present case, especially the samples annealed at 1200°C undergone significant chemical and physical changes. This behavior is discussed in more depth in Part II and Part III of the thermal annealing, i.e., Section 4.2.5 and Section 4.2.6, respectively; where more pronounced annealing-induced changes is observed.

In Figure 40, XRD spectra of the samples annealed under forming gas are plotted. Peaks corresponding to various phases of Si and SiC (when present) are labeled onto the plots. Throughout the XRD results' plots, diffraction peaks corresponding to various phases of Si are marked by (*) in order not to complicate the figures.

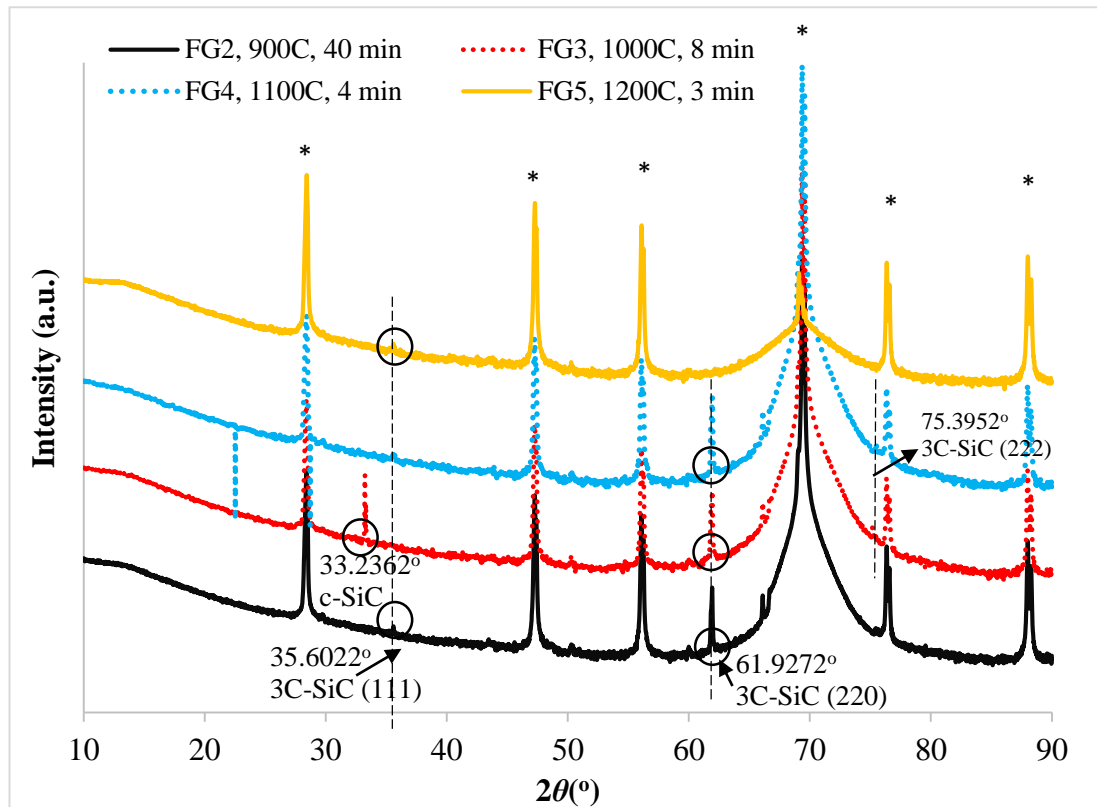


Figure 40. XRD spectra of the samples annealed under forming gas.

XRD spectra of the forming gas annealed samples in Figure 40 are examined along with the reference XRD data presented in Table 2 with certain crystal orientations for SiC and Si. Around $2\theta = 35.6^\circ$, 3C-SiC (111) phase appears.

As summarized in Table 2, $2\theta = 61^\circ$ belongs to 3C-SiC (220) plane, and the peaks centered at around 61.9° may be due to the newly forming 3C-SiC (220) planes. This 0.9° difference might be due to structure related deviations. Similarly, a SiC peak was reported to be centered around 62° by [130]. The peak for 3C-SiC (111) is disappeared in the spectra of FG3 and FG4, and reappeared in the spectra of FG5 with a low intensity. This low intensity may be explained by possible contamination from the residual materials in the RTA chamber, especially at such high temperatures. This conclusion may also be supported and confirmed by the Gaussian line shape of Si-C peak in the FTIR spectra of FG5. The peak at $\approx 75.4^\circ$ 3C-SiC (222) phase [86] is present in FG3 and FG4. The grain sizes (L) corresponding to 3C-SiC (220) diffraction peak with relatively higher magnitude than other 3C-SiC peaks in Fig. 7 are calculated using Scherrer's formula, as in Eq. (7) [61]:

$$L = \frac{K \cdot \lambda \cdot (57.3)}{H_B \cdot \cos\theta} \quad (7)$$

In Eq. (7), λ , H_B , and θ stand respectively for the x-ray wavelength, full width half maximum of the corresponding peak (in $^\circ$), and Bragg reflection angle. The factor 57.3 is for rad to ($^\circ$) conversion. Using this formula, the approximate grain sizes for FG2, FG3, and FG4 were determined as 87.46 nm, 59.06 nm, and 90.27 nm, respectively. XRD spectra of the samples fast-annealed under vacuum are presented in Figure 41.

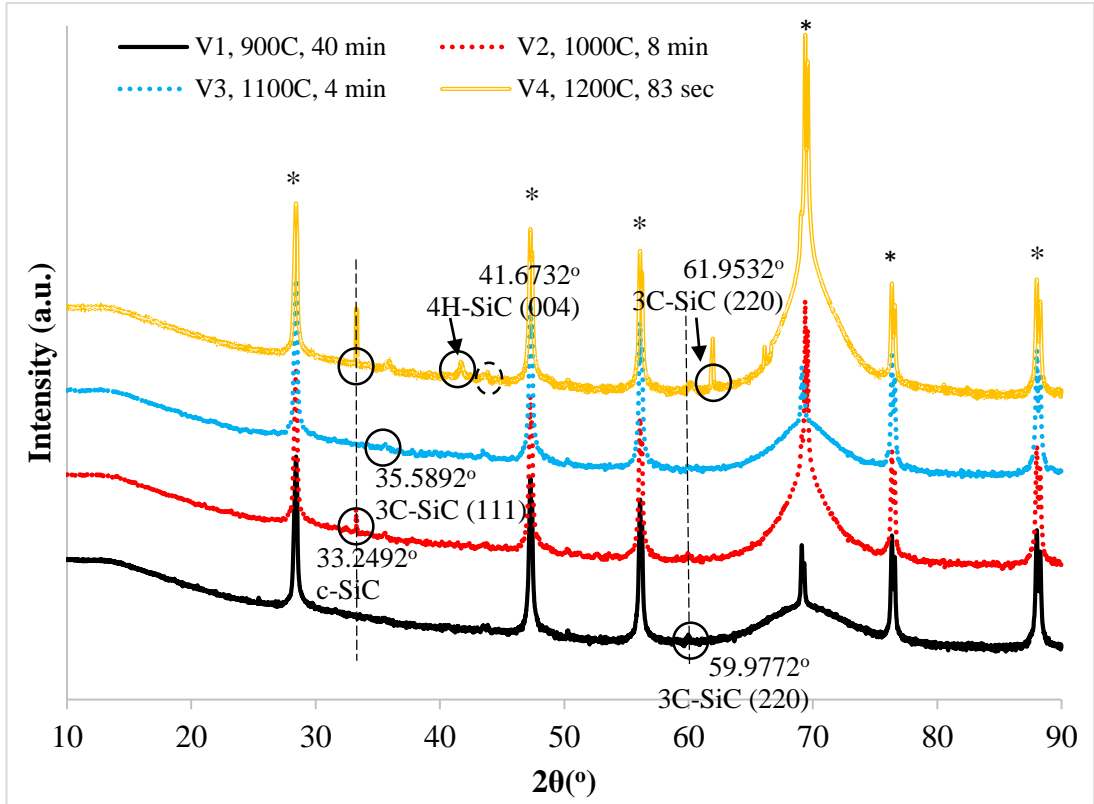


Figure 41. XRD spectra of samples annealed under vacuum.

Through inspection of Figure 41, it can be observed for vacuum annealed samples that crystallization started at 900°C by the diffraction peak at 59.9°, very near to $2\theta = 60^\circ$. Starting from annealing at 1000°C; in addition to the 3C-SiC (111), other SiC polytypes occurred at around $2\theta = 33.4^\circ$ and 41.7° and the latter is attributed to the presence of 4H-SiC. The dashed circle emphasizes the occurrence of a diffraction peak at around 43.8442° which can be due to the presence of graphite (100) due to possible carbon clustering in the thin film or carbon contamination. For sample V4, the grain size for 3C-SiC (220) is 89.45 nm, 4H-SiC (004) is 40.93 nm, and 3C-SiC (111) is 73.05 nm.

4.2.5. Thermal Annealing of SiC: Part II

In this Section, thermal annealing on the samples coated by the recipe developed for SiC sputtering at 62 W RF power is presented. This time, annealing under N₂ and vacuum were performed, since these environments have been by far the most commonly employed for SiC crystallization (details can be found in the literature review in Chapter 2). Details of the process variables are given in Table 14.

Table 14. RTA process variables (Part II).

Sample	Environment	Temperature	Duration
A	N ₂	900°C	40 min
B	N ₂	1000°C	8 min
C	N ₂	1050°C	6 min
D	Vacuum	900°C	40 min
E	Vacuum	1000°C	8 min
F	Vacuum	1050°C	6 min

In [131], cubic (β -) SiC samples were fabricated and their T and R were measured within 10.5 μm - 14 μm (i.e., 713.501 cm^{-1} – 944.876 cm^{-1}) range. Evaluation of samples structures via electron diffraction revealed that they were of polycrystalline and β -SiC phase. For comparison, the data of [131] for 120 nm thick β -SiC were extracted from Figure 48 using Engauge Digitizer. Data for β -SiC films of 40 nm and 60 nm thickness in Figure 42 were not used in this study for comparisons, since these thickness values are much smaller than our samples thicknesses, and as shown in Figure 42, transmission behavior is thickness dependent.

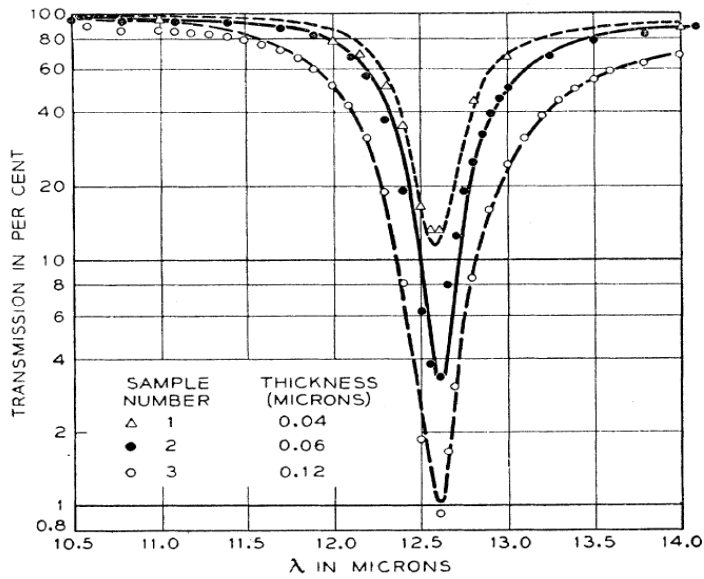


Figure 42. Transmission spectra of SiC samples, by Spitzer et al. [131] "Reprinted (figure) with permission from [W. G. Spitzer, D. A. Kleinman, C. J. Frosch, *Physical Review*, 113, 1, 133-136, 1959.] Copyright (2018) by the American Physical Society. <https://doi.org/10.1103/PhysRev.113.133>"

Below the FTIR characterization results are presented for vacuum annealed samples, first. Calculated FTIR absorbance values of the samples annealed under vacuum are presented in Figure 43 and Figure 44 for 100 nm SiC and 200 nm SiC respectively. During the RTP of these samples, devices default ramp-up and –down rates were used.

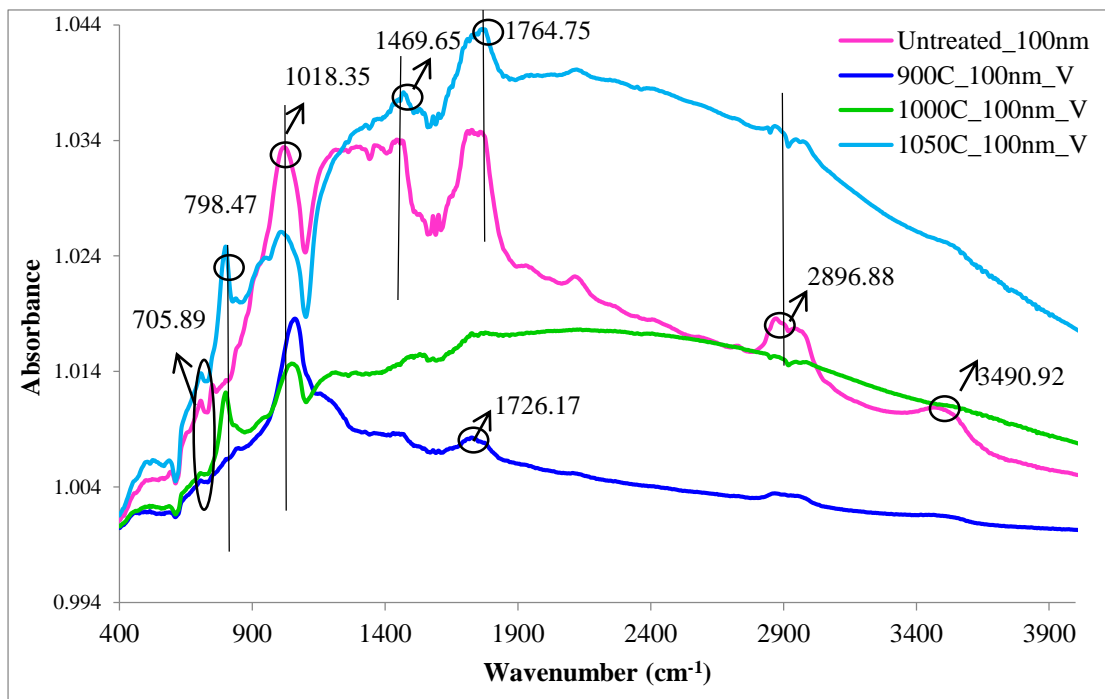


Figure 43. FTIR absorbance of untreated and vacuum annealed 100 nm SiC samples.

The Si-C stretching vibration at $700\text{--}840\text{ cm}^{-1}$ is observed in all samples of 100 nm SiC-on-Si, annealed under vacuum. The bands at around 1000 cm^{-1} are due to oxygen related bonds, which might be due to oxidation of thin films at high temperatures from possible O_2 residuals in the annealing chamber. For samples annealed at 1000°C and 1050°C , the Si-C band has two significant peaks located at around 700 cm^{-1} and 800 cm^{-1} , which may be indicative of a change in internal structure, related to formation of Si-C bonds. The peaks at around $1720\text{--}1760\text{ cm}^{-1}$ evident in all samples is attributed to C=O stretch. Small magnitude peaks at around $1400\text{--}1600\text{ cm}^{-1}$ may be due to $\text{C}=\text{C}$ aromatic stretching mode [82].

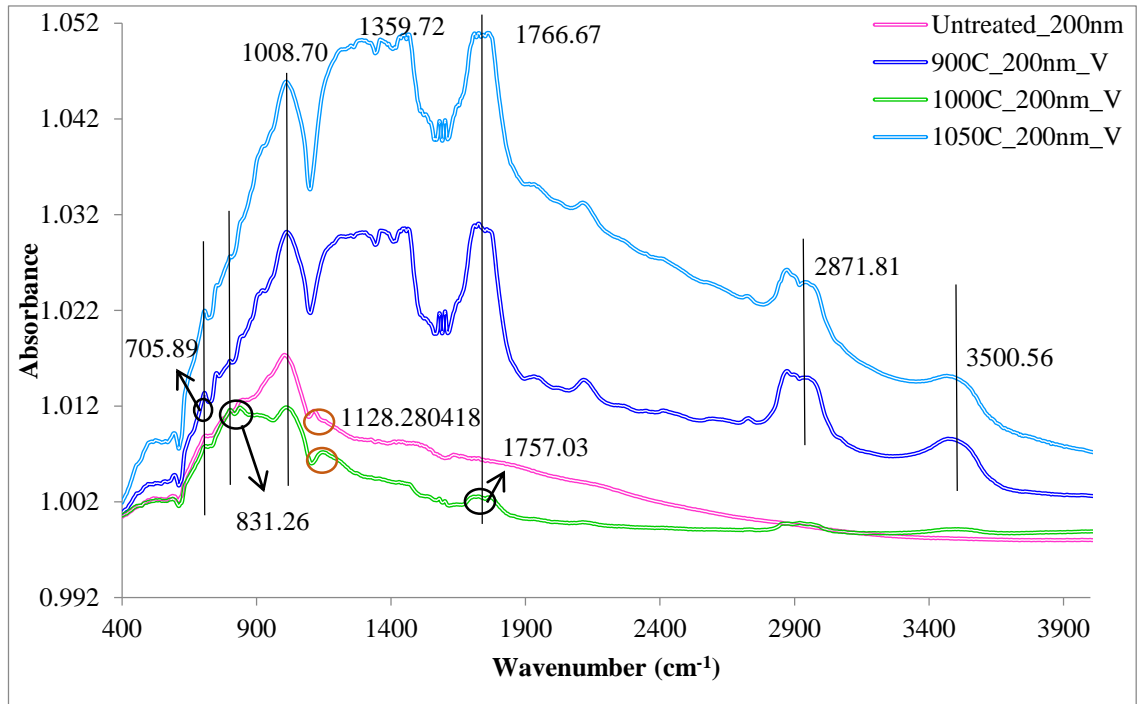


Figure 44. FTIR absorbance of untreated and vacuum-annealed 200 nm SiC samples.

Similar to the observations made from Figure 43, the fundamental Si-C vibration mode around $700\text{-}800\text{ cm}^{-1}$ are observed for all 200 nm SiC-on-Si samples annealed under vacuum. For samples annealed at 900°C , oxygen content is increased when compared to thinner SiC thin film system. For the untreated 200 nm SiC-on-Si sample, oxygen content is reduced significantly in comparison to 100 nm SiC-on-Si sample, since the oxygen-related peak at around 1128 cm^{-1} has a very small magnitude. Apart from the untreated sample, all annealed samples have the C=O stretching vibration; which may be due to the residual oxygen in the annealing chamber before it was evacuated, leading to formation of carbon-oxygen bonds. Peaks at around $1400\text{-}1600\text{ cm}^{-1}$ may be due to -C=C- aromatic stretching mode [82].

In addition to the aforementioned, absorbance variations around high wavenumbers are not common and have not been attributed to specific bands of chemical bonds, as in Table 1. In order to reflect the reasons for these variations clearly, raw T data (as collected) are plotted in Figure 45 for all vacuum annealed samples and Si. In this way,

it is aimed at reflecting whether such variations are caused by the sample structure or the FTIR device.

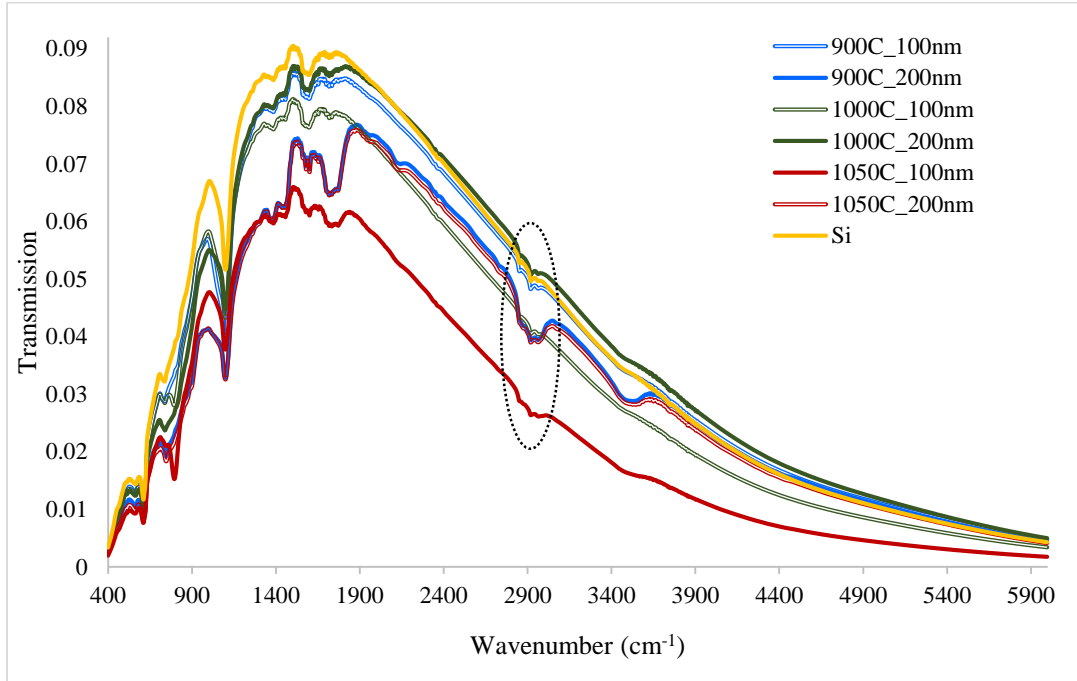


Figure 45. Raw transmission data for vacuum-annealed samples and Si.

As it is seen in Figure 45, the variations in T in the wavenumber region of 2700-3000 cm^{-1} (marked with dashed black circle) is present in all samples, including Si. This range can also be attributed to a number of CH_n related modes, as summarized in Table 1. On the other hand, the deposition method is not expected to cause intense hydrogenation, since the only H_2 source would be from DIW used for sample rinse and from cleaning with dilute HF. Since the behavior is also observed for the uncoated Si wafer, its presence was attributed to the background of the measurement system. Also, variation of T around 3500 cm^{-1} may be attributed to the presence of H_2O , since transmission of H_2O in the atmospheric window is located at $\approx 3 \mu\text{m}$ (3333 cm^{-1}) [132].

In order to evaluate whether annealing under vacuum caused internal structure improvements, the collected T data is plotted and compared by those in [131] in Figure 46.

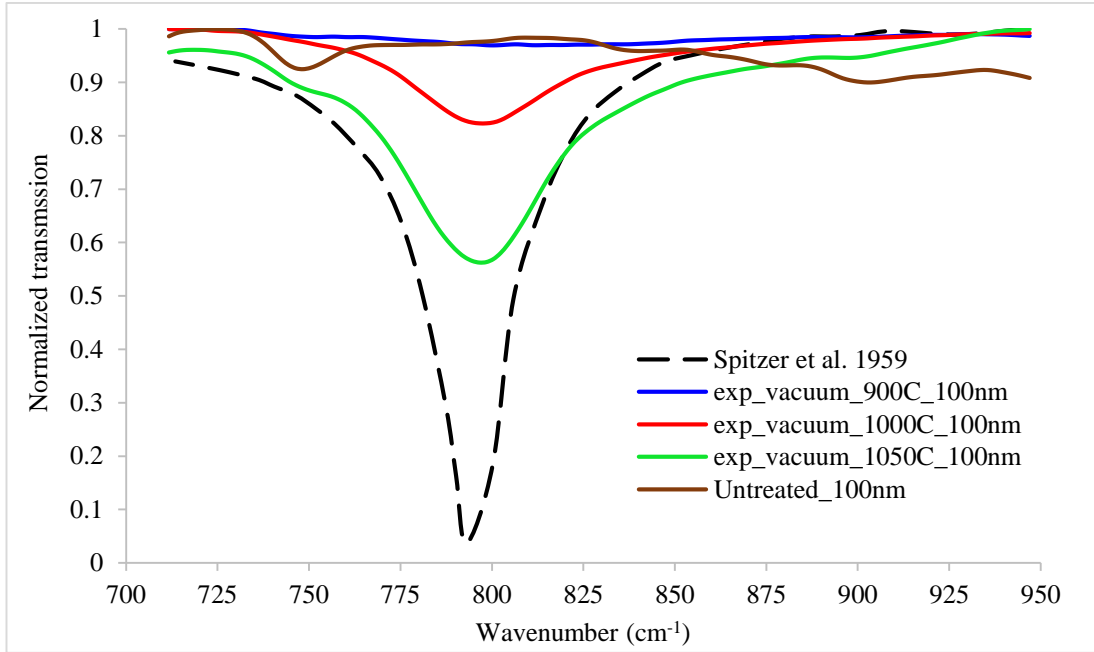


Figure 46. Transmission of vacuum-annealed 100 nm SiC samples, and data of Spitzer et al. [131].

As it can be observed from Figure 46, fast-annealing under vacuum at 1050°C and 1000°C changed the internal structure in such a way that, in terms of the magnitude and location, transmission behavior is closer to 3C-SiC presented by [131].

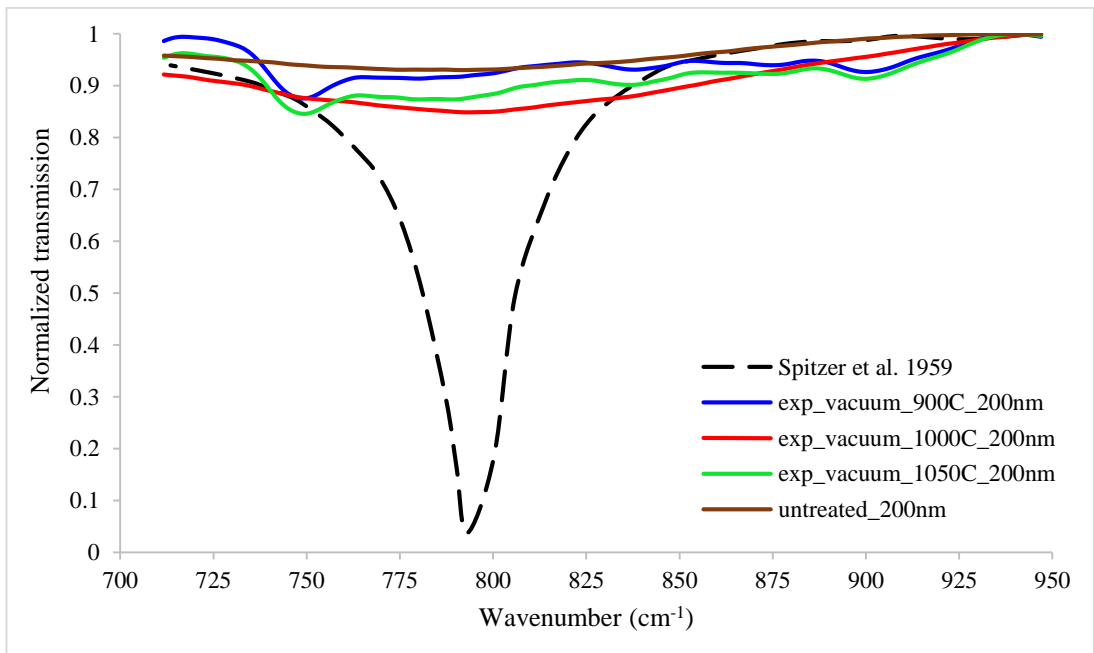


Figure 47. Transmission of vacuum-annealed 200 nm SiC samples, and data of Spitzer et al [131].

Changes in internal structure as for 100 nm SiC-on-Si samples is not present for the 200 nm samples, as depicted in Figure 47. The transmission behavior of the samples are close to each other spectrally but magnitude of transmissions do not approach to 3C-SiC, as presented by [131]. Here it should be noted that the data of [131] is for 120 nm 3C-SiC films. As presented in Figure 42 [131], T behaviors are thickness dependent and a direct comparison with the data of [131] and our 200 nm SiC samples might not be possible.

Comparison of the Si-C peak locations of thermally untreated and annealed samples, and observation of the shifts in their peak locations has been commonly reported. Below the peak location for Si-C vibration for the sample processed by RTA under vacuum are provided, both for the thinner (100 nm) and thicker (200 nm) SiC film, in Table 15.

Table 15. Si-C vibration peak locations of the fast-annealed samples, under vacuum.

Vacuum annealing	Peak location	
	$t_{SiC} = 100 \text{ nm}$	$t_{SiC} = 200 \text{ nm}$
Untreated	748.3 cm^{-1}	790.8 cm^{-1}
$T_a = 900^\circ\text{C}$, $\Delta t = 40 \text{ min}$	800.4 cm^{-1}	748.3 cm^{-1}
$T_a = 1000^\circ\text{C}$, $\Delta t = 8 \text{ min}$	798.5 cm^{-1}	794.6 cm^{-1}
$T_a = 1050^\circ\text{C}$, $\Delta t = 6 \text{ min}$	798.5 cm^{-1}	748.3 cm^{-1}

As it is presented in Table 15, the 100 nm SiC samples' Si-C peak location shifted from 748.3 cm^{-1} to around 800 cm^{-1} after thermal annealing, while the peak location is nearly unchanged between the annealing conditions. For 200 nm SiC samples, the peak location shifted from 748.3 cm^{-1} to around 794 cm^{-1} from $T_a = 900^\circ\text{C}$ to $T_a = 1000^\circ\text{C}$, but at higher temperature, the peak is centered at 748.3 cm^{-1} again, as in the untreated case. Shift of peak position to higher wavenumbers as for the case of 100 nm samples due to annealing and 200 nm samples after annealing at 1000 $^\circ\text{C}$ (in comparison to 900 $^\circ\text{C}$) may be attributed to the reduction of Si-C bond length, thereby increasing the effective force constant and resulting in a shift to higher wavenumbers [72].

On the other hand, shift of the peak position to lower wavenumbers as in the case of annealing of 200 nm samples at 1050°C (in comparison to 1000°C) may be due to the solid-state effect, i.e., decrease of the effective force constant due to the Si-C dipoles surrounding medium's polarization [72].

Crystallographic information obtained through XRD for 100 nm and 200 nm SiC-on-Si samples are given in Figure 48 and Figure 49, respectively. Crystalline SiC phases are labeled by the phase and orientation while peaks indicated by (*) correspond to crystalline Si in different orientations.

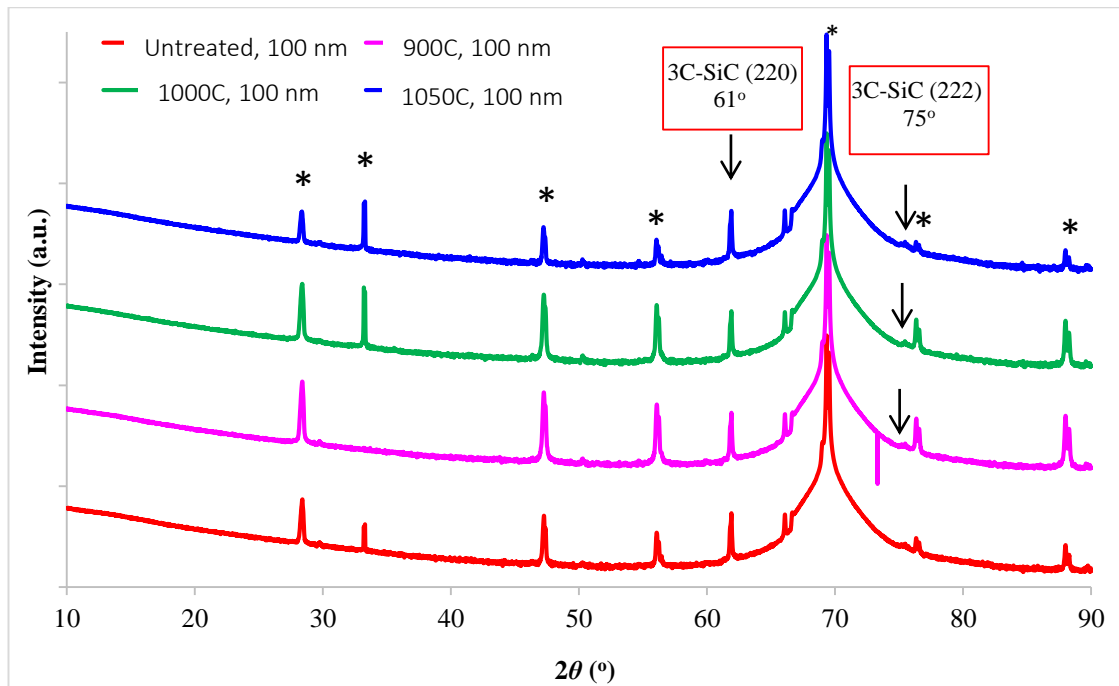


Figure 48. XRD spectra of the 100 nm SiC samples annealed under vacuum.

As shown in Figure 48, all samples have crystalline Si in different orientations (e.g., (111), (220), (331), (004), etc.). After annealing, a peak at around 50.3° is also emerged. This peak is present in all annealed samples (900°C, 1000°C, and 1050°C) and is absent for the case of untreated sample. Thus, appearance of this peak is attributed to annealing. After annealing at 900°C, 1000°C and 1050°C, crystallization into 3C-SiC is observed by the peak located at around 75.5° in the (222) orientation. Also, one peak observed in all samples at around 61.80° - 61.90° is close to that of 3C-

SiC in (220) orientation commonly observed at 61°. The peaks around 33.5° can be originated from either of the α -SiC (100) or Si (002). On the other hand, since its magnitude is very high compared to those for 3C-SiC phases, it is considered that the peak is originated from Si (002).

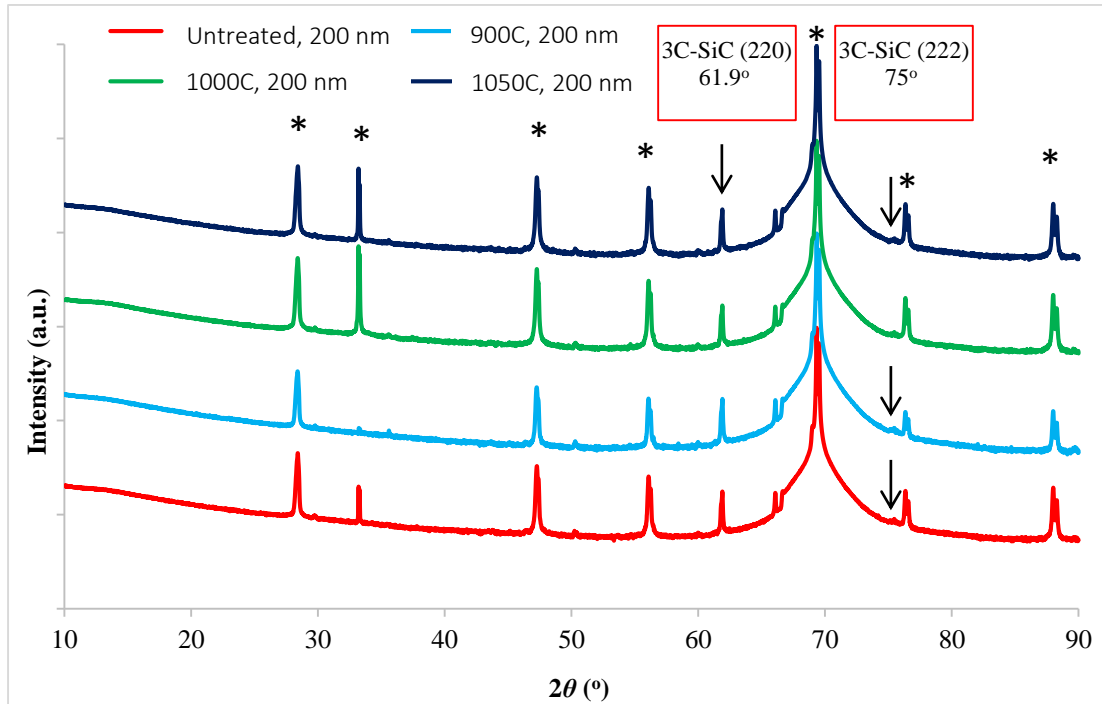


Figure 49. XRD spectra of the 200 nm SiC samples annealed under vacuum.

When the diffraction spectra of both the annealed and untreated samples are compared, unexpectedly, it is seen that (222) orientation of 3C-SiC is present in the untreated film at around 75.33°. This crystal type with given orientation is observed in all cases but the 1000°C annealing case. Similar to the diffraction pattern of 100 nm thick SiC thin film samples, crystalline Si in different orientations are observed for 200 nm SiC thin films, as well. Contrary to the post-annealing appearance of the peak at around 50.3° for 100 nm thin films, all the 200 nm thin film samples showed that peak irrespective of thermal treatment. The peaks around 33.5° position are also present for the 200 nm samples, which is considered to be originated from Si (002). After annealing at 1050°C, 3C-SiC crystalline phase in (222) orientation at around 60.05° and 75.5° are observed. Also, one peak observed in all samples at around 61.80°-61.90°

is close to that of 3C-SiC in (220) orientation commonly observed at 61°. Scherrer's formula yielded an approximate grain size of 57.22 nm for the sample annealed at 1050°C, for 3C-SiC (220).

Photographs of the annealed samples under vacuum are presented in Figure 50 to reflect heat-treatment related changes. As it was shown by T comparisons and XRD analyses, most of the samples experienced onset of crystallization after annealing. Changes in thin film surface morphology could be considered along with structural improvement. In [133], a-SiC:H films deposited on Si substrates were studied. Thermal annealing at 400°C - 900°C, for 3 h, under Ar environment were performed. Surface morphology of samples was strongly affected by annealing temperatures. They expressed that formation of protrusions by increase of annealing temperature could be attributed to phase transition from amorphous to crystalline state. In relation to the reported morphological changes after annealing, the sample pieces cut from the samples deposited at 62 W RF power from the regions of nearly the same surface color (to proceed with similar SiC thicknesses) exhibit annealing induced surface changes, as shown in Figure 50 for vacuum annealing.

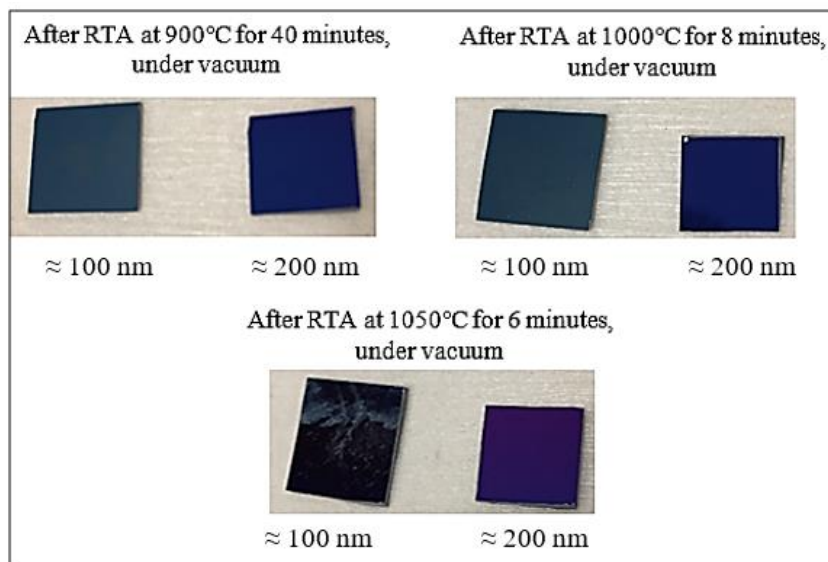


Figure 50. Surface conditions of the samples after RTA under vacuum.

When the annealed samples are visually examined through Figure 50, it is seen that the surface of the sample with the thinner SiC layer is affected by RTA process differently from the other such that some additional features (and some changes) appeared on their surface. These changes were most pronounced for the sample annealed at 1050°C. The sample with the thicker SiC layer does not have any modifications that are visible to eye. In [134] the same phenomenon was mentioned. Increase of sample surface roughness with annealing was related to hydrogen molecule formation and outer-diffusion, while the phenomenon was called the kinetic roughening.

As internal structures manifest in mechanical properties, elastic moduli and hardness of our samples are also measured. In Figure 51, hardness values of our samples are presented in comparison with the literature. In Figure 51 and Figure 52, the data with “min” and “max” labels correspond to the minimum and maximum measurement values. Other than just one measurement (for 100 nm SiC), increasing process temperature increased hardness of the SiC films. This phenomenon can be interpreted by the fact that with increasing process temperature (either the deposition (substrate) temperature or annealing temperature), increase of Si-C bond density is expected. In this case, hardness of SiC samples increase and approach to that of crystalline SiC.

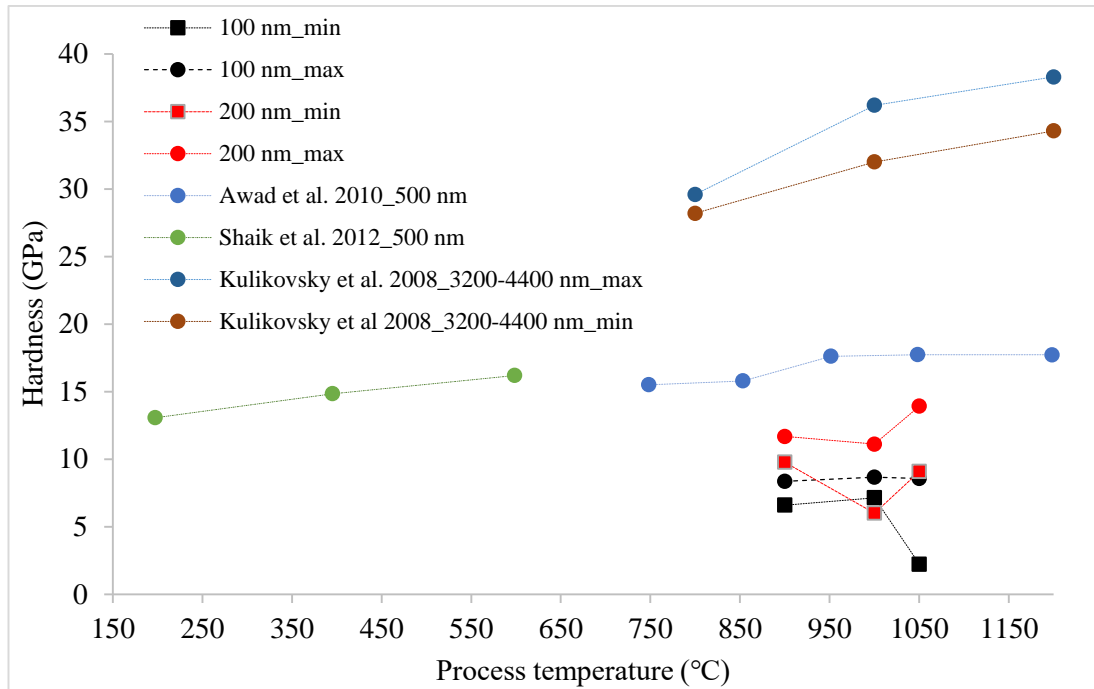


Figure 51. Hardness of the SiC-on-Si samples, in comparison with literature.

The temperature intervals are denoted by the process temperature in Figure 51 and Figure 52. It corresponds to annealing temperatures for the data of the present study, [68] and [135], while it corresponds to substrate temperature for [82].

The hardness and elastic moduli show strong film thickness dependence. As it is denoted in the figure legends, the data of [68] and [82] belong to 500 nm thick SiC thin films while the data presented by [135] are for 3.2 μm - 4.4 μm thick SiC films. As the film thickness increases up to a certain level, high hardness behavior of SiC are easily observed, as for the case of 3.2 μm - 4.4 μm thick films in Figure 52. The sharp decrease of hardness and elastic moduli in Figure 51 and Figure 52 for the 100 nm thick SiC films case (i.e., the lowest film thickness considered in this work) are attributed to high temperature induced changes in the film structure.

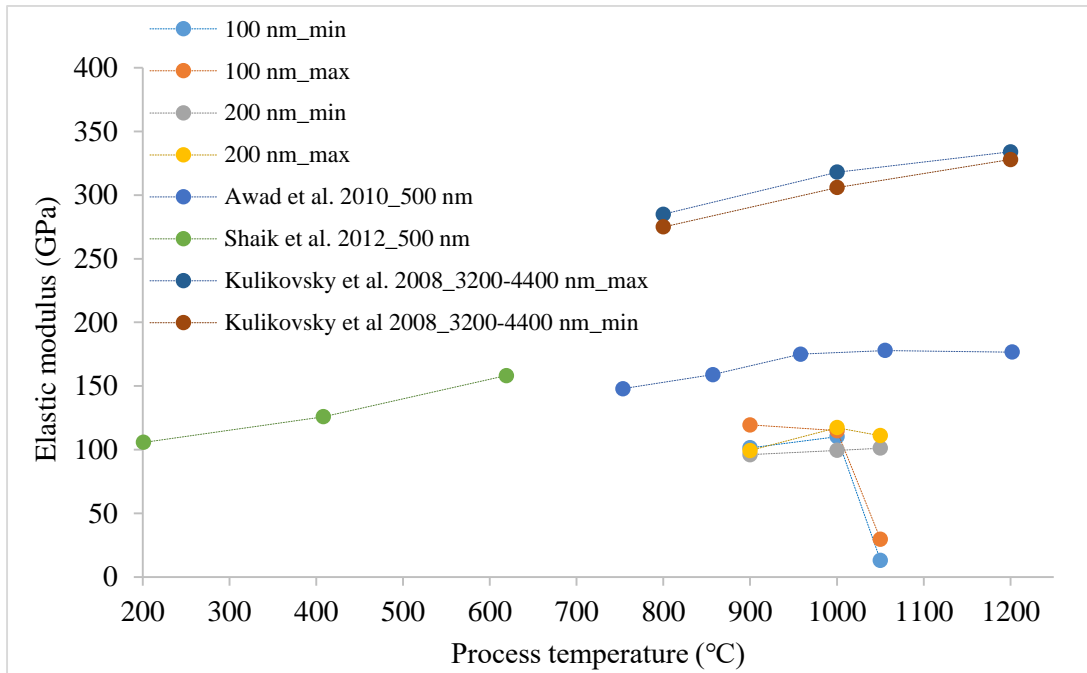


Figure 52. Elastic moduli of the SiC-on-Si samples, in comparison with literature.

The characterization results for the samples treated by RTA under N₂ are provided herein. Calculated absorbance of these samples is presented in Figure 53 and Figure 54, respectively for 100 nm SiC and 200 nm SiC cases. In order to reduce the possible ramp-up and -down effects on the film structure, these rates are limited to 10°C/sec for annealing under N₂.

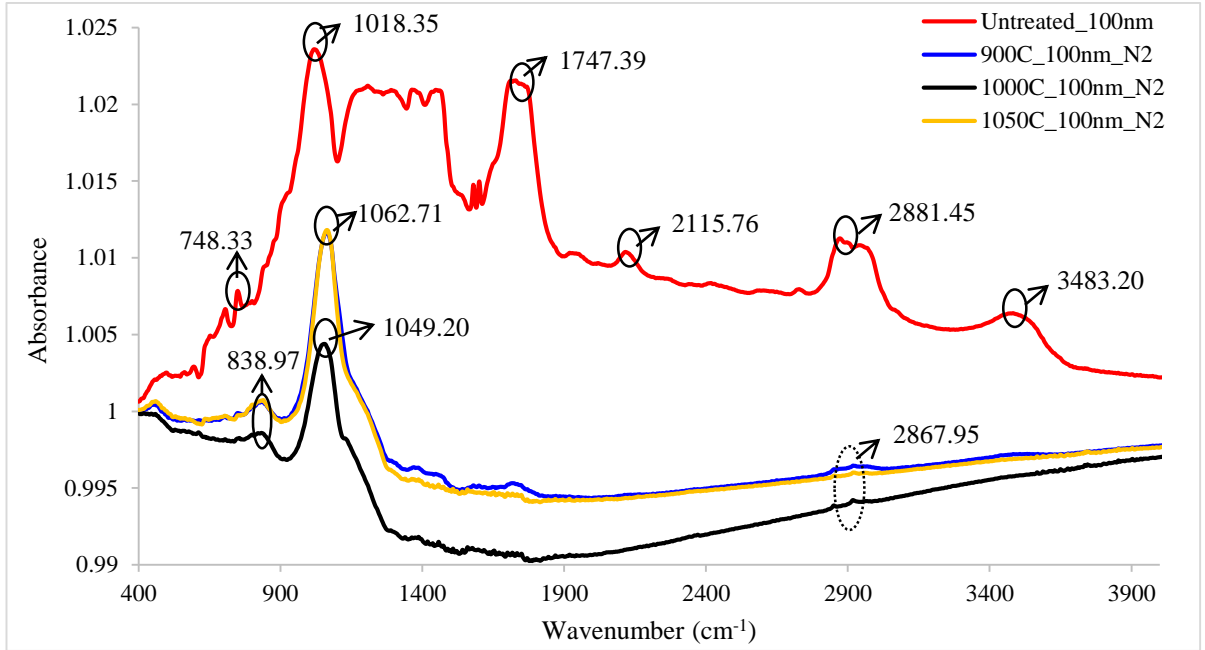


Figure 53. FTIR absorbance of untreated and N₂-annealed 100 nm SiC samples.

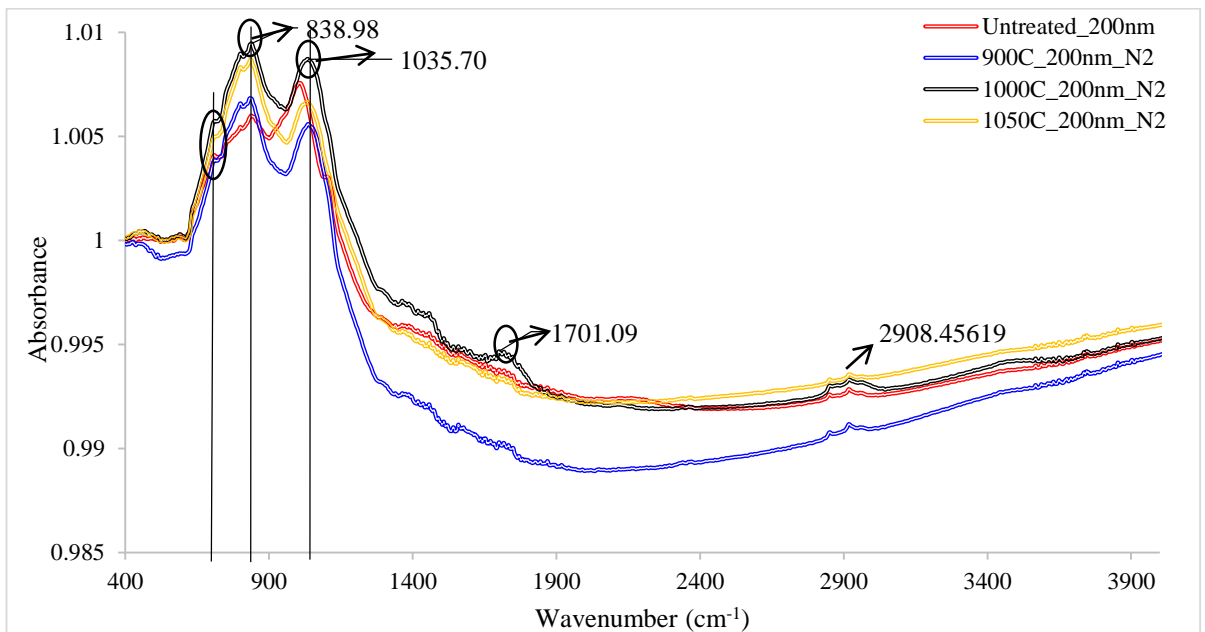


Figure 54. FTIR absorbance of untreated and N₂-annealed 200 nm SiC.

One overlapping peak observed for all samples at around 700-840 cm⁻¹ is due to the Si-C stretching mode. 1000-1070 cm⁻¹ due to Si-O-Si sym (TO) vibration is also present in all cases indicating that samples contain oxides. Peaks at around 1740 cm⁻¹ corresponds to C=O stretch [64]. Similar to the observations made from Figure 45, *T*

variations within 2700-3000 cm^{-1} were present in all samples' spectra (including uncoated Si), and attributed to the background of the measurement system. Another observation is presence of transmission variation at around 3500 cm^{-1} , which may be due to the presence of H_2O in the system [132].

As it was performed for the case of samples fast-annealed under vacuum, T of the samples are compared by the data presented by [131] in Figure 55 and Figure 56.

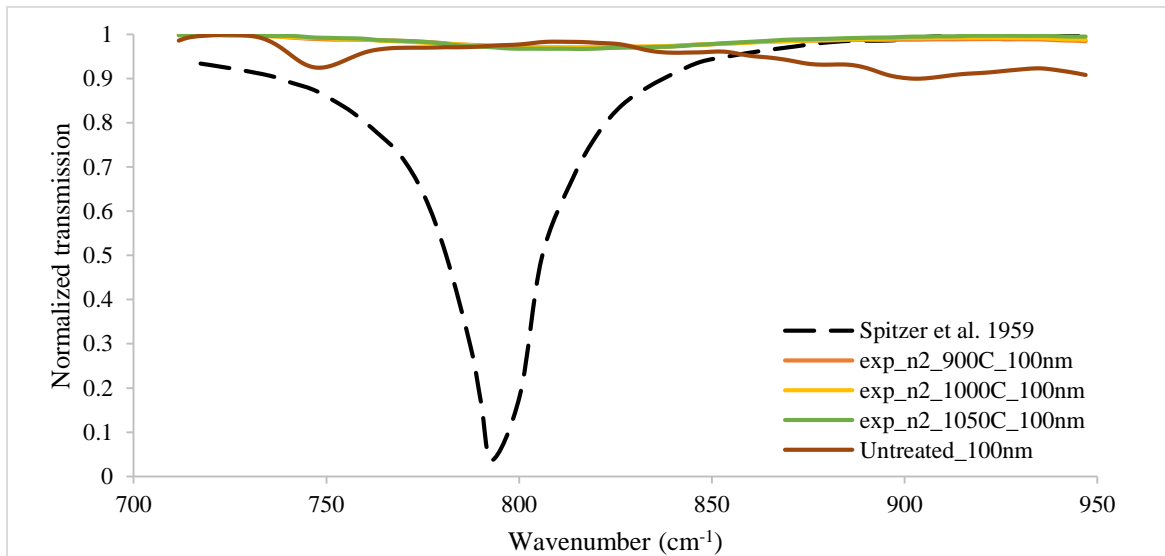


Figure 55. Transmission of N_2 -annealed 100 nm SiC samples, and data of Spitzer et al [131].

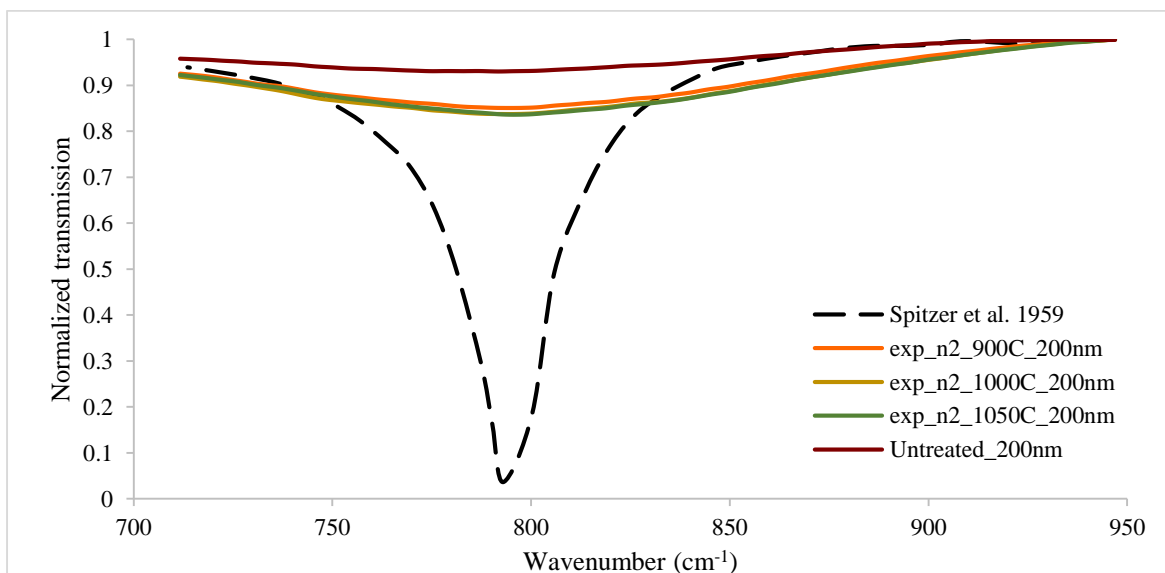


Figure 56. Transmission of N_2 -annealed 200 nm SiC samples, and data of Spitzer et al [131].

The peak locations of the fundamental Si-C vibration are given for RTA process under N₂ environment, in Table 16. Similar to the comparisons made for RTA process under vacuum, it is aimed to observe peak location shifts related to internal structure re-ordering.

Table 16. Si-C vibration peak locations of the fast-annealed samples, under N₂.

N₂ annealing	Peak locations	
	<i>t</i>_{SiC} = 100 nm	<i>t</i>_{SiC} = 200 nm
Untreated	748.3 cm ⁻¹	790.8 cm ⁻¹
<i>T_a</i> = 900 C, Δ <i>t</i> = 40 min	819.7 cm ⁻¹	792.7 cm ⁻¹
<i>T_a</i> = 1000 C, Δ <i>t</i> = 8 min	812 cm ⁻¹	790.8 cm ⁻¹
<i>T_a</i> = 1050C, Δ <i>t</i> = 6 min	815.8 cm ⁻¹	798.5 cm ⁻¹

Table 16 shows that the peak location for the Si-C stretching band is shifted to higher wavenumbers for 100 nm thick SiC case, when untreated and annealed samples were compared. The peak location did not change significantly for different annealing conditions. Shift of the Si-C peak location to higher wavenumbers is commonly considered as a sign of a more ordered internal structure. For the 200 nm SiC samples, the peak location for the Si-C stretching band is also shifted to higher wavenumbers, when untreated sample and sample annealed at the highest temperature are compared. On the other hand, the amount of the shift is not as pronounced as in 100 nm film thickness case.

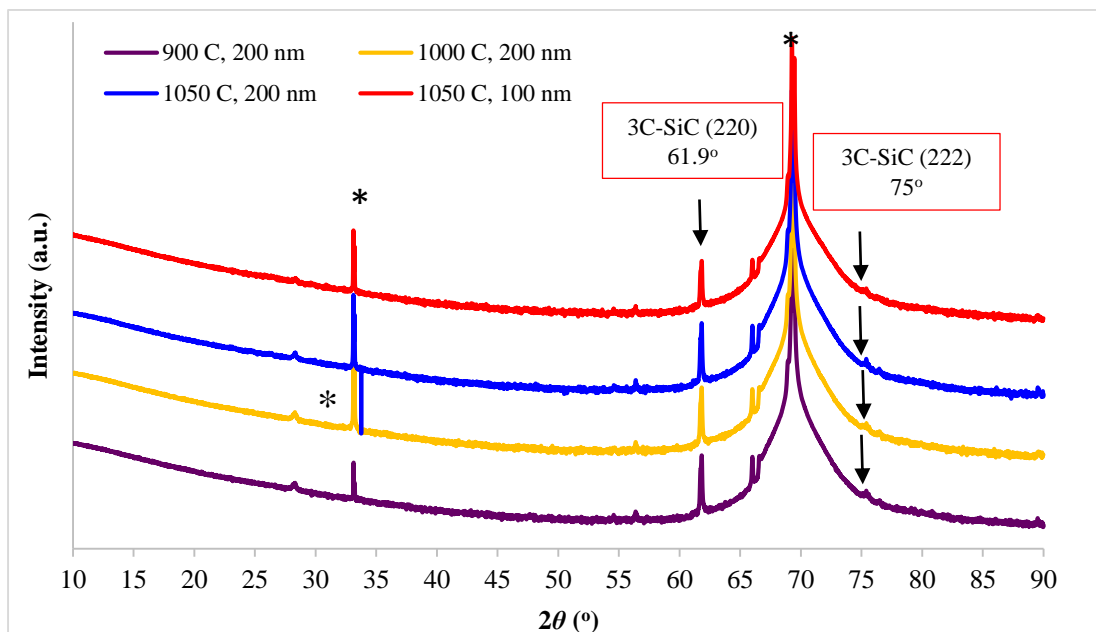


Figure 57. XRD spectra of the samples annealed under N₂ (Part II).

From Figure 57 showing the XRD spectra of the samples fast-annealed under N₂, it is seen that crystalline Si in different orientations such as (111), (311) and (004) are present in all samples considered. The peaks around 33.5° position are also present for the 200 nm samples, which are considered to be originated from Si (002). All samples annealed under N₂ has 3C-SiC phase in (222) orientation, which is revealed by the diffraction peak at around 75.4°, and 3C-SiC (220) around 61.9°. The peaks near 55° can be due to the presence of graphite or carbon contamination during the processes.

4.2.6. Thermal Annealing of SiC: Part III

In addition to the processes and characterizations presented in Section 4.2.4 and Section 4.2.5, a conventional furnace allowing processes under Ar environment, at higher temperatures for longer durations, along with lower temperature ramp-up and -down rates was also utilized. This furnace is located at the Department of Materials Science and Engineering of Eskişehir Technical University.

A RTP device allowing high temperature ramp-up and ramp-down rates could be considered an advantage, due to a relatively short periods of sample heating to or cooling down from the annealing temperature. On the other hand, such high rates may cause increased stress both in the film and film-substrate interface. In a conventional annealing furnace, temperature ramp-up and -down rates are significantly slower than those in an RTP device, allowing for much longer processes with a decreased tendency of defect formation due to the stress. The temperature ramp-up and -down rates are important in terms of defect formation, since the thermal expansion coefficients of the thin film and substrate are different for SiC and Si. As it was expressed by [86], difference in thermal expansion coefficients of the thin film and substrate material might cause cracking of layers or even more critical situations. In the RTP device, rates up to 40°C/sec can be achieved, while in the conventional furnace rates up to 5°C/min are used. The process parameters for conventional furnace annealing are presented in Table 17.

Table 17. Conventional furnace annealing process parameters (Part III).

Temperature	Environment	Duration	Sample holder
1300°C	Ar	3 hours	Alumina on Alumina
1200°C	Ar	3 hours	Alumina on Alumina
Temperature ramp-up and ramp-down rate: 5°C/s			

The processes outlined in Table 17 were designed to perform processes at higher annealing temperatures than those achieved via the RTA process. The calculated FTIR absorbance spectra of these samples are presented in Figure 58.

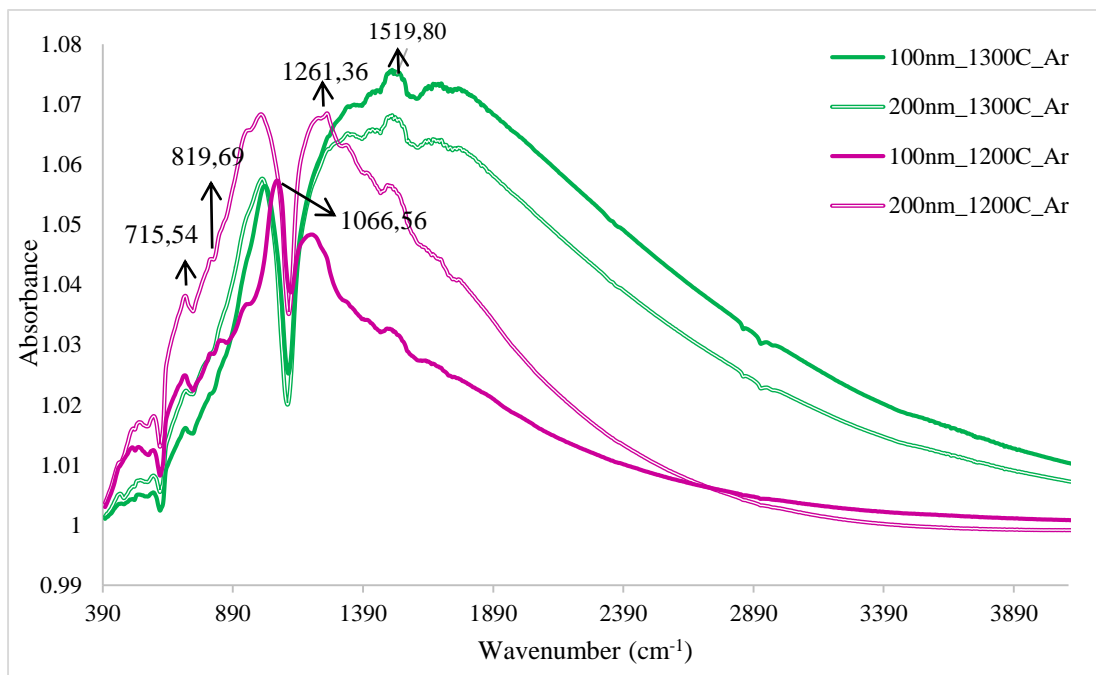


Figure 58. FTIR absorbance of the samples (100 nm, 200 nm) annealed in Ar.

When Figure 58 is examined, the band around 700 -800 cm^{-1} due to the Si-C stretching vibration is seen. Also the peak at around 1000 cm^{-1} reveals oxygenation of the samples. As it was stated by [82], small bump-like peaks at around 1400-1600 cm^{-1} might be due to aromatic stretching modes of $-\text{C}=\text{C}-$. Similar to the FTIR results presented in Part II, presence of variations at higher wavenumbers around 3000 cm^{-1} are attributed to the background of the measurement device. XRD spectra of the samples annealed at 1300°C are provided in Figure 59.

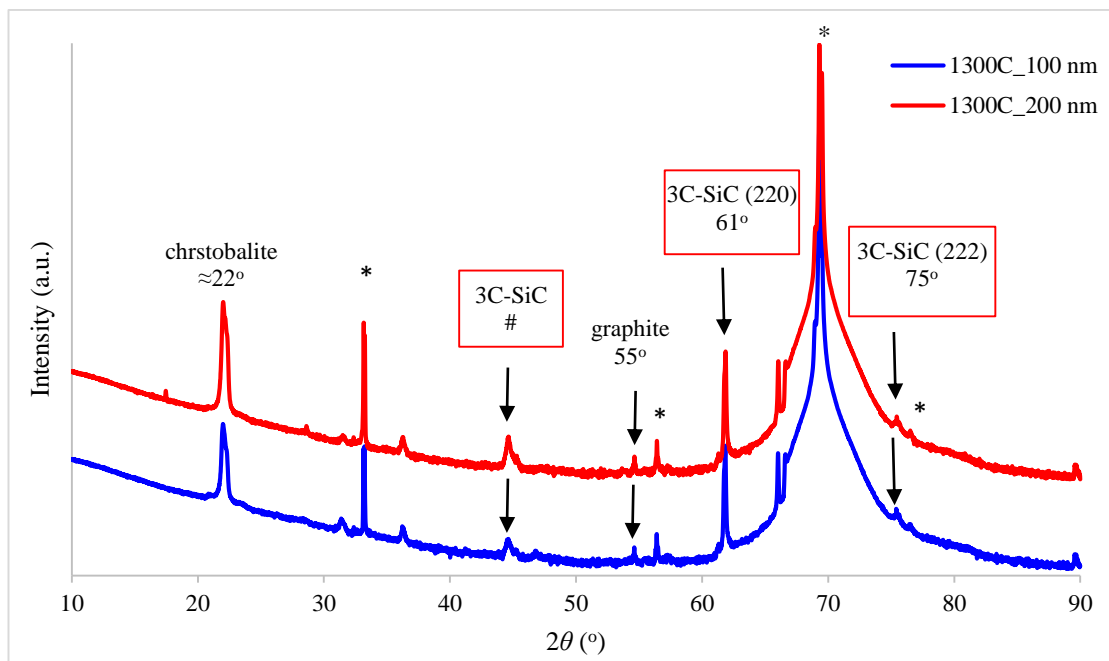


Figure 59. XRD spectra of the SiC samples annealed under Ar, at 1300°C.

Similar to the other samples studied, crystalline Si in different orientations, such as (311), (400), and (331) are evident in the XRD spectra of samples in Figure 59. Peaks at around 33.2°, which can be originated either from α -SiC (100) or Si (002) is attributed to Si (002) due to its high magnitude. Peaks at around 54.6° are attributed to the presence of graphite in the thin films, or possible carbon contamination. In both 100 nm and 200 nm thick SiC-on-Si samples, 3C-SiC phase in (220) and (222) orientations are present. Also, around 44°, another 3C-SiC phase is observed (Reference code: 98-018-2362 in XRD library literature). It should be noted that this peak (at around 44°) for cubic SiC phase is not present in other samples studied. The peaks located at around low diffraction angles (around 22°) are not observed in the other samples. This peak corresponds to the main peak of chrstobalite (SiO₂). In this case, presence of these two peaks is attributed to the conventional annealing process.

The annealing induced surface changes are explored by investigating surface conditions of the samples after thermal annealing. As it is seen in the post-annealing photographs for 1300°C process in Figure 60, morphology of the films changed

significantly and even in some cases the film partially peeled off from the substrate from the sides.

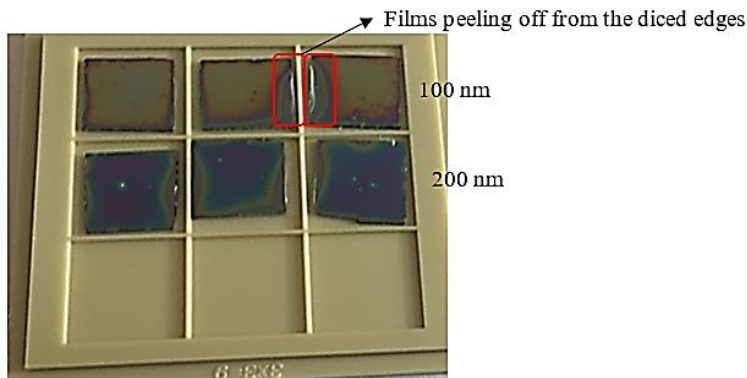


Figure 60. Photographs of the samples after annealing at 1300°C, in Ar.

High temperature processing caused differences in SiC structure as well as its morphology is reported in a number of studies. Although high temperature processes (at around 1300°C) is considered required for the growth of 3C-SiC via CVD, it causes unintentional doping of impurities in the fabricated epi-layers, and Si atoms might diffuse from the Si substrate into the growing film, causing defect formations within the film and at the film-substrate interface [62].

When the transmittance spectra of the samples annealed at 1300°C is compared to the spectrum given by [131], it is seen that the characteristic peak for Si-C could not be identified (Figure 61). This result is attributed to annealing induced chemical changes that took place in the sample, as the characteristic Si-C peak in the untreated (not annealed) sample was present. The changes might be caused by diffusion of Si from the substrate to the thin film at these temperatures close to the substrate melting point [62], or possible contamination from previous processes in the annealing chamber, as well as from (or to) the alumina sample holder at 1300°C. Also, if the diffusion of Si is the case, increase of Si-Si bonds decreased the density of Si-C bonds, thereby making more room for oxidation.

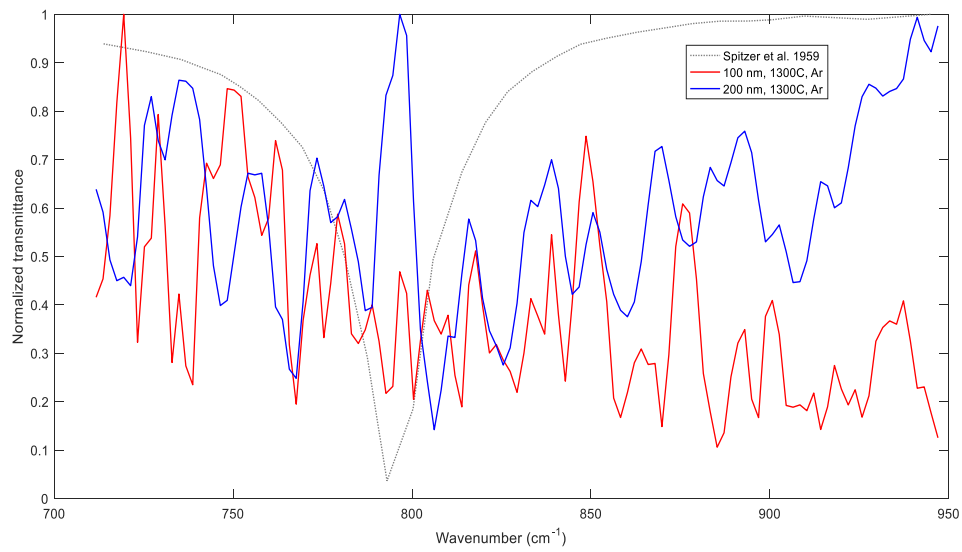


Figure 61. Transmission of Ar-annealed samples at 1300°C, and data of Spitzer et al [131].

For the case of 1200°C annealing, better surface quality compared to 1300°C is obtained, as shown in Figure 62. FTIR transmission and absorbance spectra of these samples are presented in Figure 63 and Figure 64, respectively.

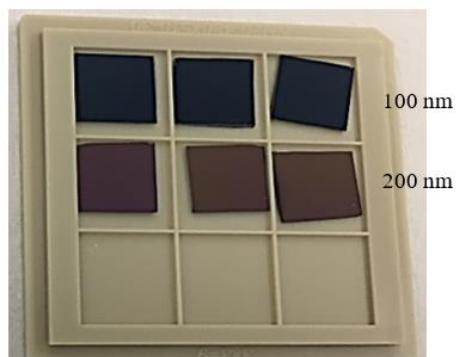


Figure 62. Photographs of the samples after annealing at 1200°C, in Ar.

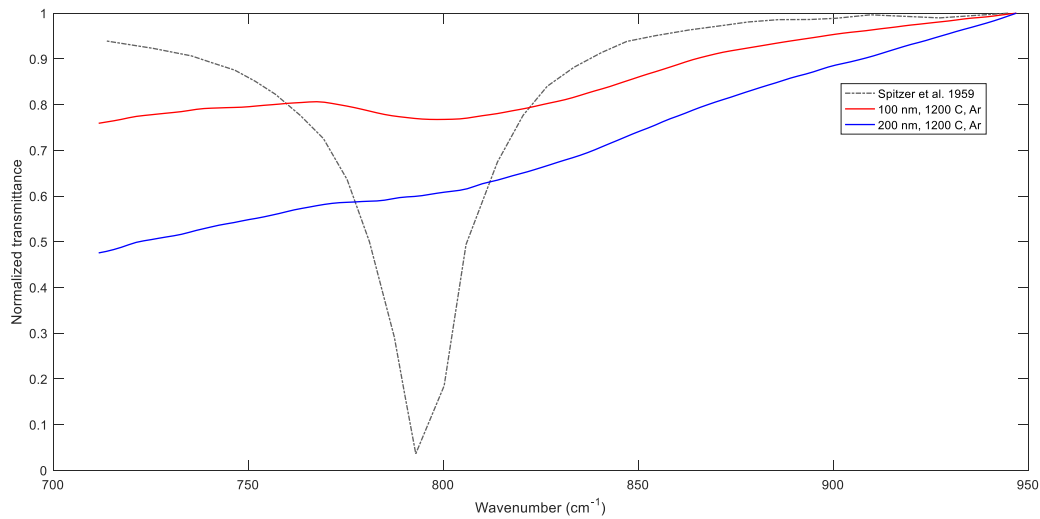


Figure 63. Transmission of Ar-annealed samples at 1200°C, and data by of Spitzer et al [131].

When the normalized transmissions of the samples annealed at 1200°C are compared to those presented in Figure 61, it is seen that the samples approach to having the characteristic fundamental Si-C vibration peak. Surface condition of the samples processed at this temperature is also better compared to those annealed at 1300°C.

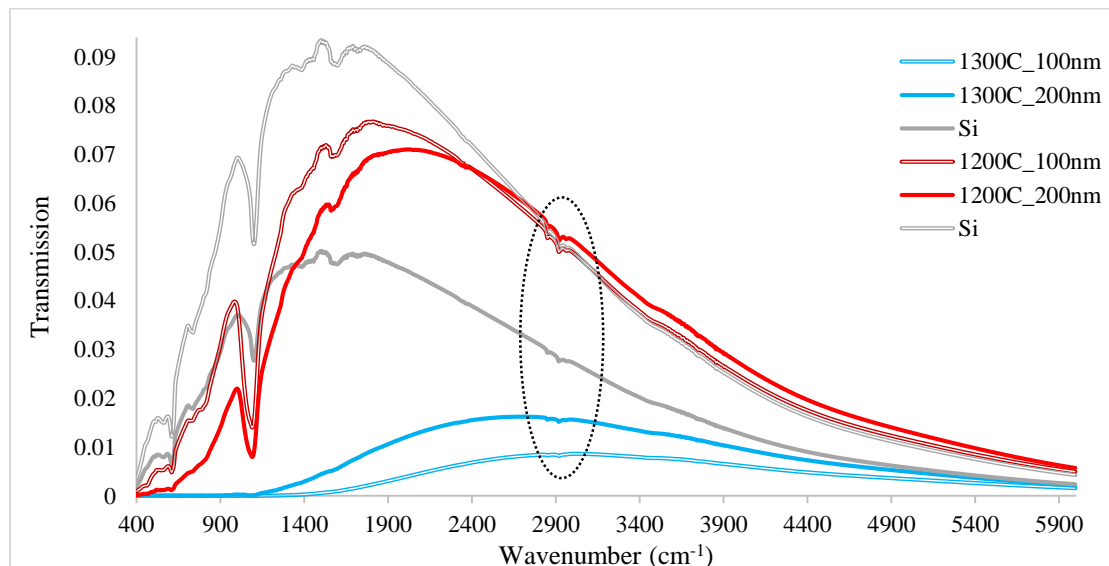


Figure 64. Raw transmission data for Ar-annealed samples and Si.

T variations within $2700\text{-}3000\text{ cm}^{-1}$ are emphasized in Figure 64 by a circle. Two different spectra for Si is included in Figure 64 to accompany the measurements made in the same set. The variations within $2700\text{-}3000\text{ cm}^{-1}$ are attributed to the background of the measurement system. On the other hand, for samples annealed under Ar, no variations are observed around 3500 cm^{-1} , indicating the absence of H_2O in the system [132].

4.3. Fabrication Processes- Part II

In this Section, processes performed at the Micro Electro Mechanical Systems Research and Applications Center of Middle East Technical University are presented.

4.3.1. Fabrication Scenarios and Process Steps

Two conclusive fabrication scenarios (denoted as Scenario A and Scenario B, herein) were conducted at the facilities of METU-MEMS Center. Processes of Scenario A and Scenario B are given below with their processes in order.

Scenario A:

- 1- Wafer cleaning: standard piranha and HF clean.
- 2- SiC thin film deposition: by RF magnetron sputtering.
- 3- SiO_2 thin film deposition: on the surface obtained from step-2, by PECVD.
- 4- Photolithography.
- 5- Wet-etching of SiO_2 surface: using BHF.
- 6- PR removed from the surface (i.e., PR strip).
- 7- Bonding of two wafers structured by steps 1 - 6, under vacuum, so that a vacuum cavity is formed between the structured wafers.
- 8- Wafer dicing to obtain individual devices.

Scenario B:

- 1- Wafer cleaning: standard piranha and HF clean.
- 2- SiO₂ thin film deposition: by PECVD.
- 3- Photolithography.
- 4- Wet-etching of SiO₂ surface: using BHF.
- 5- SiC thin film deposition: on the surface obtained from step 4, by RF magnetron sputtering.
- 6- Lift-off process: to remove the PR and the SiC on it.
- 7- Bonding of two wafers structured by steps 1 - 6, under vacuum, so that a vacuum cavity is formed between the structured wafers.
- 8- Wafer dicing to obtain individual devices.

Flowcharts depicting the process steps of the Scenario A and Scenario B are schematically presented respectively in Figure 65 and Figure 66.

Scenario A

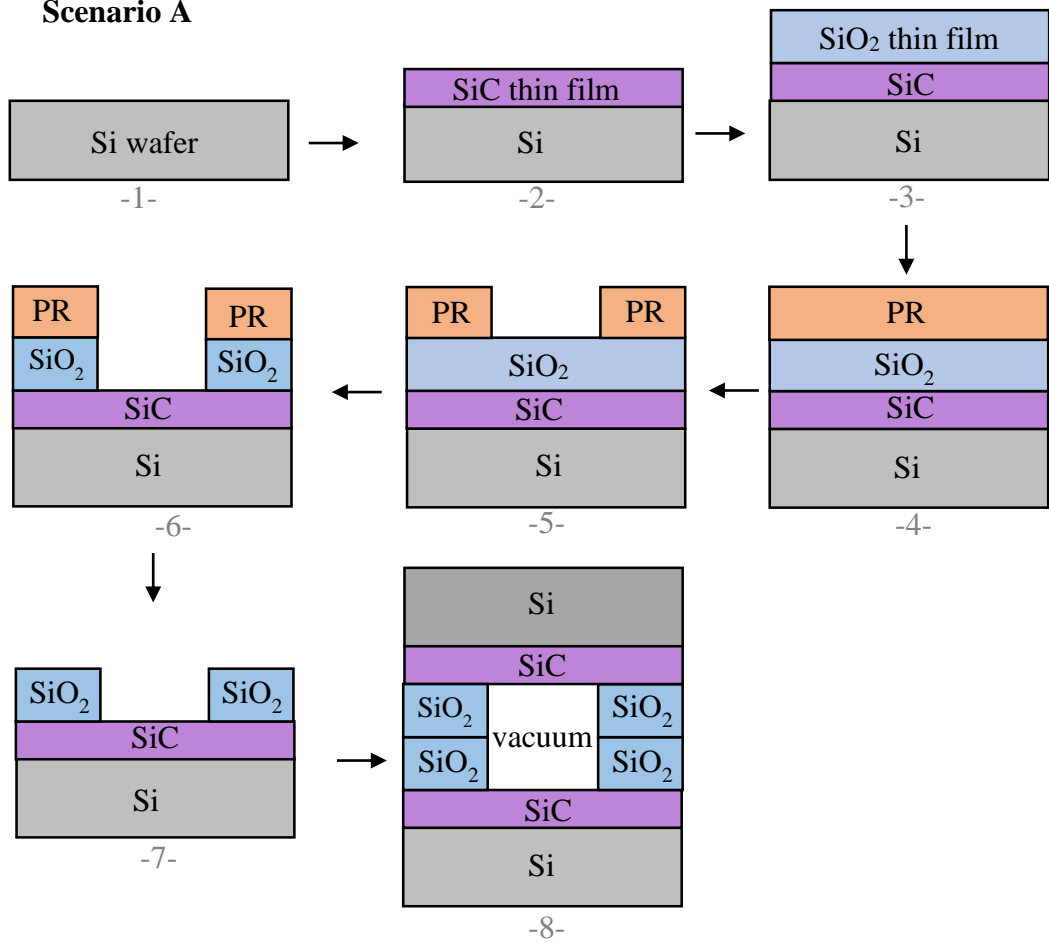


Figure 65. Process stages of Scenario A. The dimensions are not drawn to scale.

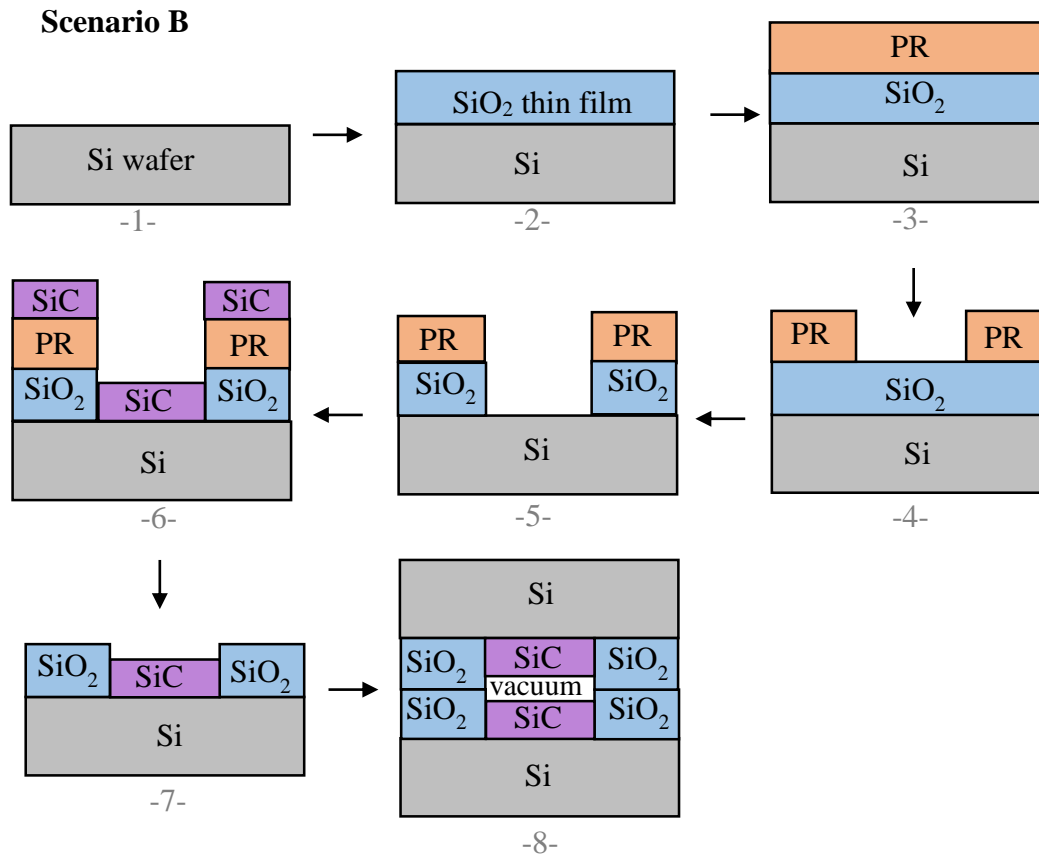


Figure 66. Process stages of Scenario B. The dimensions are not drawn to scale.

When Scenario A and Scenario B are compared, it is seen that the one main difference between them is the process sequence of SiC and SiO₂ thin film depositions. Using both scenarios, the NFRT device depicted by item 8 can be fabricated. On the other hand, to obtain the same structure in the end, both by using the samples obtained from Griffith University and starting with Si wafers, Scenario A was considered more convenient.

In a more general frame, determination of the more promising scenario depends not only on the SiO₂ pattern of the bonded structure in the end. It also depends on device's ability of holding the vacuum inside for a reasonable time. This can be achieved by ensuring a strong bond between structured wafers. As it is elaborated later in this text, a strong and durable bond between the structured wafers depends on micro-roughness, flatness, and total thickness variation of the bonding surfaces. Majee et al. [136] reported that, characteristics of SiO₂ films deposited by PECVD and thermal oxidation

was different. For SiO₂ films of 1 μm thickness, they reported average surface roughness (R_a) of 0.8 nm and 1.5 nm respectively for PECVD and thermal oxidation. In this case, one may also proceed with thermal oxidation to obtain SiO₂. Following Scenario B, it is interpreted that performing a wet etching instead of dry etching for the removal of SiO₂ would be more beneficial, since forming an undercut would be possible in case of wet-etching [137], which would serve as an ease for more convenient lift-off process.

4.3.2. SiO₂ Wall Geometry and Photolithography Mask Design

Before performing the SiC and SiO₂ thin film deposition processes, the patterns desired to be integrated on SiO₂ films forming the walls between SiC surfaces were determined. As it was illustrated in Figure 65 and Figure 66 respectively for Scenario A and Scenario B, vacuum is encapsulated by SiO₂ walls and SiC surfaces.

It is aimed at obtaining 4 individual devices with 3 cm × 3 cm surface area at step 8 of Scenario A, by dicing a bonded full-wafer size pair. After dicing, the vacuum cavity is still enclosed, and SiC-on-Si surfaces are separated by SiO₂ walls of different configurations.

In design of these configurations, the critical parameters are radiation area to conduction area ratio (i.e., A_r/A_c), and deflection of the surfaces. Conduction takes place due to the contact of SiO₂ walls. Convective effects between SiC surfaces are neglected due to the presence of vacuum. In order to clearly differentiate the NFRT between SiC surfaces, conduction heat transfer is desired to be minimized. Therefore, A_r/A_c should be maximized. Besides, as a result of the large pressure difference between the vacuum cavity and outside environment, deflection of the surfaces can take place. Large deflections could lead to contact of SiC surfaces and device failure. Therefore, the amount of deflection should be minimized.

The vacuum gap, $d = 200$ nm was formed by SiO₂ walls height. Therefore, the configurations with maximum deflections smaller than 100 nm are considered promising in terms of low deflection.

With these parameters in mind, Ahmet Güngör from our research group, performed structural analyses via ANSYS by considering 11 different configurations. Among these configurations, three configurations (3, 6, and 11) exhibiting maximum A_r/A_c value and minimum deflection are selected. These are optimum patterns among those investigated. One other configuration (2) is also added for comparison purposes. These configurations are given schematically in Figure 67.

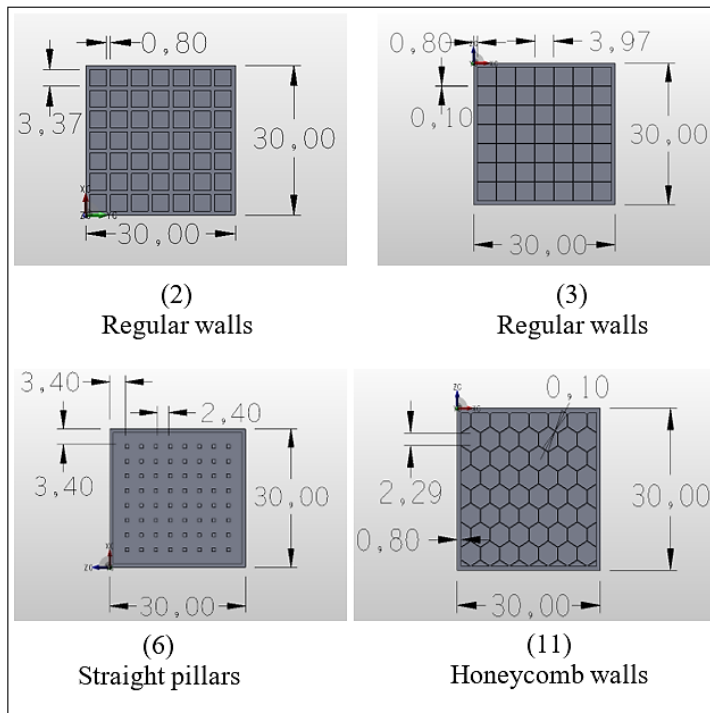


Figure 67. SiO₂ wall structures integrated in NFRT device. Units are in millimeters.

As shown in Figure 67, configurations 2 and 3 consist of square shaped walls with different thicknesses; while configurations 6 and 11 respectively consist of pillars and hexagonal honeycomb walls. Hexagonal honeycomb walls were chosen by inspiration from nature, at Nanoboyut Laboratory, from the fact that honeybees store maximum amount of honey with minimum amount of wax in six-sided honeycombs. In this way, it is aimed to obtain a durable structure with less conduction area. The amount of maximum deflection for configurations 2, 3, 6, and 11 are 58.41 nm, 71.553 nm, 90.684 nm, and 65.384 nm, respectively. The A_r/A_c values of these configurations are

1.620, 6.078, 5.696, and 5.965, respectively. Considering these values with the physical features of configurations enables comparison of different geometries effects on NFRT with each other, and also observation of the effect of the conduction area for the same geometry (configurations 2 and 3) on the NFRT.

These configurations were integrated on the photolithography mask by AutoCAD 2018 (student version, licensed, product version: O.49.0.0) first. Review of these configurations and the shadings were performed by Layout Editor, at METU-MEMS Center. Locating these configurations was performed by the criteria reported by EVG, for a strong and durable bond. The specialists informed us that the minimum remaining bond line thickness after dicing should be 800 μm . This limit and the mark to be left by the dicer are considered in the mask design. Considering the fact that the thickness uniformity of the sputter-deposited layers is better through the center of the wafer rather than the outer edges, configurations (2, 3, 6, 11) are located as close as possible to the center. The final photolithography mask design is shown below in left of Figure 68.

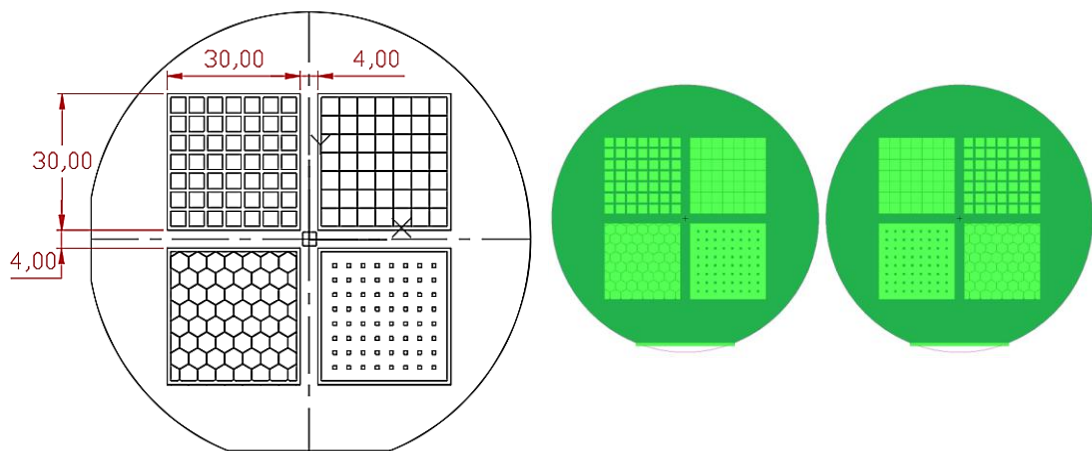


Figure 68. Photolithography mask design with optimized configurations. The dimensions are in millimeters.

For the other component of the wafer pair to be bonded, exact symmetrical version of the pattern in Figure 68 was also designed and fabricated. The symmetry of the surface patterns is also shown at the right of Figure 68.

The configurations in Figure 68 are in the inside of the bonded device; and another mask was also designed to guide the bonding process by hosting alignment markers, and also the dicing process. This mask, shown in Figure 69 includes the configuration numbers 2, 3, 6, and 11; coinciding to each of the configurations for their identification from each other.

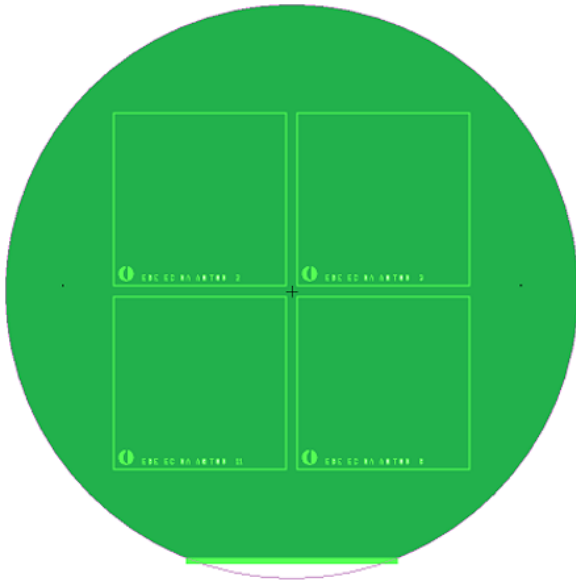


Figure 69. Photolithography mask design for the outer surface of the device.

4.3.3. SiC Thin Film Deposition by RF Magnetron Sputtering

Previously, efforts on developing and optimizing a SiC sputtering recipe at Nanoboyut Laboratory (i.e., within Part I) was presented. Although a reliable and repeatable SiC sputtering recipe was already developed, within Scenario A (Part II) a new recipe should be developed for the sputtering device at METU-MEMS Center, which enables the use of a sputtering target of different size (4-inch diameter). Here, the aim is to perform as many processes as possible in a single clean room to avoid contamination, which could be detrimental to bonding process.

For the development of this SiC sputtering recipe in Part II and Scenario A, a number of parameters were considered. Briefly, the sputtering target was monolithic, i.e., not-bonded to a conductive backing plate. It was therefore crucial to avoid any damages to the target, since reusing a cracked monolithic target was impossible. The target

purchased from Sindlehauser Materials was fabricated using vacuum hot pressing (VHP) method, starting from SiC powders and performing high temperature and high pressure processes. The sputtering process parameters were carefully selected such that the sputtering process would not cause any damage to the target. During this period, we were in contact with the specialists at Sindlehauser Materials for a controlled optimization of the sputtering process.

The device (AJA ATC Orion Sputter system) is capable of providing RF powers up to 300 W and able to operate near 5 mTorr deposition pressure. In one process, coating of up to three wafers can be performed, and substrate heating can be applied. In order not to overexpose the target to process loads, the sputtering recipe consists of middle-high values of process parameters. Briefly, the RF power was 150 W, process pressure was 3 mTorr with 50 sccm Ar flux. The process was performed discontinuously, by 30-minute deposition, followed by a break, and another 30-minute deposition.

The device outputs during this process were 148 W and 75 V respectively for the RF power and working voltage. The process was performed discontinuously to avoid thermal shocks to the target, as much as possible. Limiting the RF power value to 150 W (and thereby obtaining a reduced deposition rate) was due to the same reason. With these parameters, deposition of a SiC film of 48.6 – 49 nm thickness was achieved. This deposition rate (≈ 0.833 nm/min) is comparable to that obtained at the Nanoboyut Laboratory in Part I (i.e., ≈ 1 nm/min).

After this calibration work, three Si wafers (of n-type, 4-inch diameter, and single-side polished- SSP) was cleaned with piranha solution (1:1 (3.5 lt: 3.5 lt) 96% H_2SO_4 + 30% H_2O_2 mixture (at 110°C - 130°C)) for 30 minutes, rinsed in DIW, and dried. After that, the native oxide (a few nanometers thick) on the wafer was removed using BHF (1:7), the wafer was rinsed in DIW again, and spin-dried. After this cleaning process, three of the wafers were coated by ≈ 50 nm thick SiC film at once, without any intentional substrate heating. After the process, the target was not damaged.

As a result of our correspondence with specialists at Sindlehauser Materials, we were informed on the following measures to be taken in order to avoid target damage:

- A thin foil of a conductive material (e.g., graphite) could be placed under the target to let it utilize more of the cooling, and be better protected from excess temperatures.
- Tight clamping of the target should be avoided in order to let the target expand freely with increasing temperatures.
- Thermal shock resistance of the target should be taken into consideration.

With the mentioned measures taken and the process parameters determined to be safe, the specialists at Sindlehauser Materials suggested proceeding with these parameters.

4.3.4. SiO₂ Thin Film Deposition by PECVD

SiO₂ films on sputtered SiC films were deposited by PECVD. The process parameters are presented below in Table 189.

Table 18. PECVD parameters for SiO₂ thin film deposition.

Recipe name	SiH₄ flux	N₂O flux	N₂ flux	Pressure	RF Power	Temperature
LFSiO	12 sccm	1420 sccm	392 sccm	550 mTorr	60 W	300 °C

4.3.5. Photolithography

For the application of the inner pattern (depicted in Figure 68), a positive PR, S1813 was used with the below processes and parameters, in order.

- 1- Dehydration bake: Conducted at 110°C for 10 minutes, in the oven (Ultra Clean 100). Samples temperature to drop down to the room temperature was needed to proceed with the next step.
- 2- Spin coating of the PR: Before the application of the PR, a primer (HDMS) was applied on the surface to provide better adhesion of PR. Spin coating of HDMS was performed at 3000 rpm for 30 seconds. After that, S1813 was dropped on the surface and spin coated using the same parameters. The resulting PR thickness was around 1.3 μm.

- 3- Soft bake: Performed at 115°C for 1 minute by using the hot plate.
- 4- Exposure to UV light: Performed at EVG 620 for 5 seconds.
- 5- Hard bake: For this step, the sample was heated up to 110°C (for around 15 minutes) and kept at 110°C for 5 minutes. The sample was kept in the oven (Ultra Clean 100) until the temperature was dropped down to 70°C or less, to avoid damages to the structure due to abrupt temperature changes.
- 6- Developing: using MF319 for 60 seconds.

The surface structure after completion of the above 6 stages was photographed and presented in Figure 70.

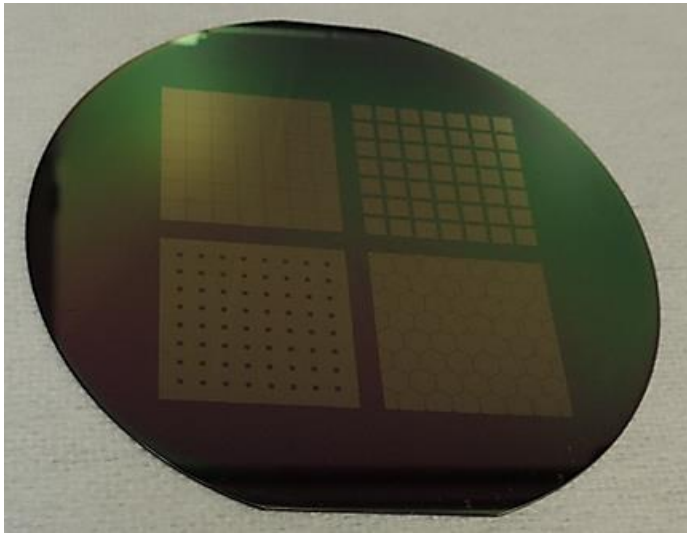


Figure 70. Sample surface after step 6 of photolithography.

4.3.6. Wet Etching of SiO₂ and Removal of the PR

Wet etching of SiO₂ was performed using BHF (1:7) solution. For this process, the etch rate was determined by a controlled process approximately as 100 nm/min. After etching of SiO₂, removal of the PR (i.e., PR strip) was performed via immersion of the sample in PRS-2000 and DIW.

4.3.7. Surface Characterization Using Atomic Force Microscopy

As it was stated previously, bonding surfaces (SiO_2) is required to be as smooth as possible. For this purpose, while processes for Scenario A are ongoing, another sample that would provide an insight on the surface characteristic representing Scenario B was also fabricated. The sample characterized for suitability of Scenario A was obtained using the processes presented through Sections 4.3.2 - 4.3.7, while the sample providing insight for Scenario B was obtained by only depositing a SiO_2 thin film onto a Si wafer. In other words, the sample obtained through Scenario A consisted of 200 nm thick SiO_2 thin film on 50 nm thick SiC film, while the sample representing Scenario B had 200 nm thick SiO_2 thin film only.

The surface characteristics were determined by AFM measurements performed by NanoMagnetics Instruments, at Ankara, Turkey. Measurements were performed according to the variables given in Table 19. AFM surface characterization results for the samples fabricated through Scenario A and B are given respectively in Figure 71 and Figure 72.

Table 19. AFM imaging and measurement parameters.

Mode	Tapping mode
Resolution (pixel)	512×512
Software	hpSPM 4.6.2.2
Cantilever	PPP-NCLR
Vibration amplitude	$1 V_{\text{RMS}}$
Free vibration amplitude	$2 V_{\text{RMS}}$
Microscope	hpSPM

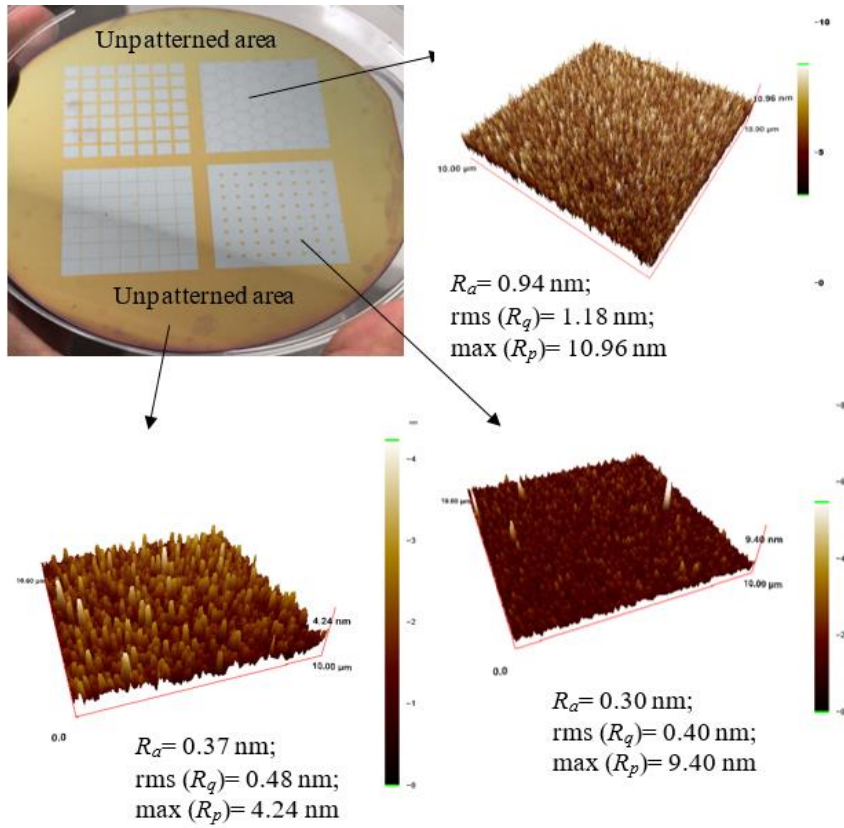


Figure 71. AFM characterizations: Scenario A.

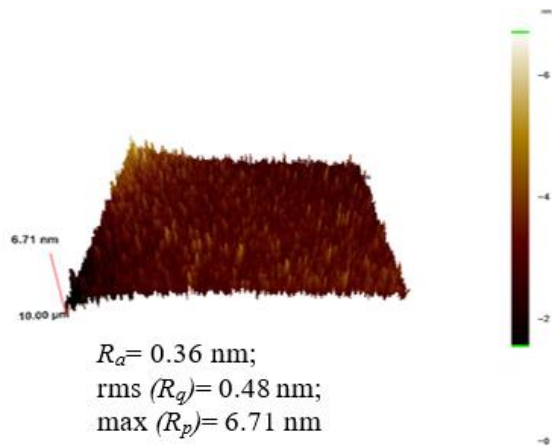


Figure 72. AFM characterizations: Scenario B.

Examination of the results summarized in Figure 71 and Figure 72 yielded the following findings:

- Surface states of the samples obtained through Scenario A and Scenario B were very good. Although some structures were observed locally on the surfaces, the average roughness values of the surfaces were within 0.5 nm – 1 nm. In terms of bonding, specialists at EVG (Austria) reported that the rms roughness < 0.5 nm would be ideal, while an rms roughness < 1 nm would be normal. In this respect, it could be concluded that the criteria reported by EVG for a durable and strong bonding was fulfilled.
- Surface state is dependent on the pattern, in Scenario A. The maximum roughness measured from the unpatterned outer area was determined as lower than those measured at the patterned areas. The average roughness values also varied between patterned regions.

4.3.8. Wafer Bonding at METU-MEMS Center: Part I

Wafer bonding is a critical stage in both Scenario A and Scenario B. Bonding process is defined as joining two accurately aligned wafers together, permanently [120]. A generic classification of bonding technologies can be done based on the presence of an intermediate material between wafers, as direct bonding (without an intermediate adhesive layer) and indirect bonding (with an intermediate adhesive layer) [120].

For the bonding of patterned Si wafers from their SiO₂ bonding surfaces, a fusion bonding scheme was preferred, and previously performed by EVG, for example for [25]. One challenge that fusion bonding exhibits is the requirement of excellent surface quality. The process is very sensitive to roughness and contamination on the bonding surfaces [120]. To ensure a satisfactory bonding quality for materials with roughness greater than allowed, chemical mechanical polishing (CMP) has been a widely applied and trusted procedure to make the rough and contaminated surfaces flat and smooth [138].

Review of previous works revealed that wafer-level bonding is a multi-variate process. Suni et al. [139] bonded hydrophilic (with native oxide layer on) and thermally

oxidized (to 500 nm thickness) Si wafers (<100>, of 100 mm diameter), in air or in vacuum. The bonding took place right after drying of the samples after RCA-1 clean. They examined the suitability of using either of N₂, Ar, or O₂ plasma, for 10 seconds to 10 minutes exposure, by a reactive ion etcher (at 50 mTorr -150 mTorr, 30 sccm gas flow, 50 W-150 W RF power, and 125 V - 280 V bias voltage) for surface activation, and also the effect of RCA-1 cleaning duration right after activation on the surface roughness of the bonding surfaces. Bonding temperature varied between room temperature and 150°C. After bonding, first annealing was carried out at 100°C for 2 hours, and then at 100°C - 500°C for 2-100 hours. For SiO₂-SiO₂ bonding, the surface energies were around 1500 mJ/m². Medvecká et al. [140] bonded Si wafers (of both p-, and n-type) in hydrophilic state and studied the effects of plasma activation, surface treatment and annealing on bond quality. It was expressed that the presence of a native oxide layer with a certain amount of –OH groups is advantageous in obtaining greater surface energy. After chemical cleaning, some of the samples were cleaned with DIW as well. After bonding, post-annealing was performed at 150, 200 and 250°C for 6-12 hours. The authors suggested that the post-annealing could be performed at 200°C for 12 hours or 250°C a 10 hours.

Before performing the actual process, a trial was performed for optimization, starting from the bonding recipe developed by EVG, for [25], as initial parameters. The first fusion bonding trial was performed using one patterned 200 nm thick SiO₂ coated (by PECVD) wafer and one unpatterned 200 nm thick SiO₂ coated (by PECVD) wafer. These samples did not involve a SiC layer for simplicity, since bonding took place between SiO₂ – SiO₂. Below, the wafer bonding scheme suggested by EVG for [25] are elaborated, and explanations are added where necessary about the details and alternative/additional processes performed at METU-MEMS Center.

1- PECVD oxide deposition: Done.

Additional step: The wafer pair used had been stored in a wafer container for some time. To avoid any contamination, the wafers are cleaned with piranha solution.

2- Oxide densification at 300°C - 400°C, for 1-2 hours, under vacuum: Done at 300°C for 1.5 hours under vacuum, in EVG 520 bonder.

3- Chemical Mechanical Polishing (CMP): This process was advised for wafers with high surface roughness. CMP was not performed, since the average surface roughness range determined through AFM measurements was expected to be within the advised range, and the CMP device was also out of use at METU-MEMS.

4- Megasonic clean: Not performed.

5- Plasma activation: Activation is an essential step for the increase of surface energies. Medvecká et al. [140] classified the surface treatment methods as wet chemical and dry physical methods. This process was advised to activate the surfaces for bonding. For [25], use of O₂ and N₂ plasma were suggested by EVG. In [139], Suni et al. pointed out that activating the bonding surfaces of Si-SiO₂ with plasma resulted in sharp increases in the surface energies. The plasma exposure time was also critical, since a treatment lasting 30 seconds was enough, when compared to longer activations lasting several minutes. For hydrophilic Si-SiO₂ bonds realized under vacuum, Ar and N₂ plasma outperformed O₂ plasma. In [140], it was reported that N₂ plasma outperformed O₂ plasma in terms of the obtained surface energy. On the other hand, the rms roughness values increased sharply in N₂ plasma, while O₂ plasma treatment did not cause much alterations in rms roughness when compared to reference sample. Authors suggested the use of O₂ and N₂ gas mixture for plasma activation.

At the time this bonding trial was performed, the plasma activation device was out of use at METU-MEMS Center. An alternative approach was needed for surface activation. Literature review (especially [141] and [142]) revealed that chemical activation was a prominent approach to activate the bonding surfaces. Mai et al. [141] aimed at bonding of two DSP silica glass pieces outside of a clean room. Surface roughness of the samples approached 6 nm. After the components were rinsed in acetone and methanol, they were further cleaned in H₂SO₄:H₂O₂ mixture (4:1) and boiled in standard RCA-1 solution. In between stages, the components were rinsed in DIW. The samples were then rinsed in NH₄OH: H₂O₂: H₂O (6:1:3) at 80°C for 30 minutes, followed by rinsing in running DIW. After keeping the samples in DIW for 5 minutes, the samples were bonded together under DIW, and dried. Post-annealing of the components was done at 100-250°C for 2-10 hours.

It was reported that the optimum process variables were annealing at 250°C for 10 hours under around 30 MPa, which provided the highest bond strength (4.5 MPa) among those of the studied samples. In [142], Mai et al. bonded DSP Si wafer pieces with SiO₂ layers on (either native oxide or thermal SiO₂) with a peak-to-peak roughness (for wafers) of around 4 nm. With the optimized bonding process parameters, they obtained a maximum bond strength of around 4.15 MPa for pairs with native oxide.

For the purpose of activation, as reported by [141] and [142], NH₄OH: H₂O₂: H₂O (6:1:3) is used as the activation solution. Addition sequence of the chemicals is H₂O, H₂O₂, and NH₄OH, respectively. A hot plate was used for increasing the solution temperature monitored both by a thermocouple and a standard thermometer. A significant amount of vaporization was observed during the heating of the process. The samples to be bonded were immersed in this solution at 80°C, for 30 minutes. To increase the temperature of the solution to 80°C, the plate was held at 450°C. Prior to bonding, the samples are washed with running DIW for 5 minutes and dried via a vacuum drying oven.

6- Bonding in vacuum (EVG 520IS), 300°C, 1.5 h: At this stage, in addition to the process temperature and process duration, applied mechanical pressure is an important variable. For the structure of [25], magnitude of the applied contact force was 10 kN. The bonding specialists at METU-MEMS Center suggested that the magnitude of the contact force should be determined based on the contact area. Considering the SiO₂ bonding area of [25] with 10 kN contact force applied, it is determined that a force around 6973 kN would provide the same amount of pressure i.e. 1425677 Pa, for the samples of the current work. While the magnitude of the force was determined, 10 kN magnitude was applied to be on the safe side for this trial.

7- IR inspection: Not performed. At this stage, since the wafers were not plasma activated and the strength to be originated from the chemical activation was not exactly known, characterization with Confocal Scanning Acoustic Microscopy (c-SAM) was directly applied.

8- Annealing in oven at 300°C for 1 hour, at ambient atmosphere: Not performed, since the bonding process was already conducted at the same temperature for 1.5 hours.

This process is suggested in the literature since it was shown that post-annealing could increase the bond quality. In [139], increasing surface energies with increasing annealing temperatures was reported. The authors of [140] suggested that the post-annealing could be performed at 200°C for 12 hours or at 250°C for 10 hours.

9- IR inspection (c-SAM and mechanical test): At this stage, c-SAM imaging was performed. Mechanical test was not performed since it is destructive. The primary objective here was to see whether a sufficiently large bond strength was established. In the literature, the crack-opening method was another method used (e.g., by [139]) to measure surface energies of the bonded surfaces. Authors of [139] also used SAM for imaging of voids.

In the current work, characterization of the bonded pair was achieved by c-SAM imaging, at 200 MHz. Characterizations started from a lower resolution, as depicted in Figure 73. This process took about 2-3 minutes. In Figure 73, the images of the SiO₂ wall patterns were identified, with some unbonded areas.

Once this image is taken, the resolution was increased to 10 μm. Image obtained from such very high resolution is presented in Figure 74. A closer look at Figure 73 confirms that the mechanical force exerted for bonding (10 kN) was appropriate and did not cause crashing of the upper wafer onto the lower wafer. It is seen from the contrast that the SiO₂ wall patterns (with darker color) are joined to the SiO₂ surface successfully, and the inner areas (with lighter color) are not touching each other, holding vacuum inside.

One local region was marked with a circle in Figure 81, the SiO₂ walls are seen in lighter, and the region expected to form the cavity is seen in darker color. This situation is attributed to low resolution (500 μm) of the imaging in capturing 100 μm thick inner walls, since a full lighter or a full darker color would respectively be demonstrating a non-touching or a crushed part. One other alternative reason with a less possibility might be touching of the surfaces separated by SiO₂ walls by deflection, leading to their contact and thereby possibly breaking the contact between SiO₂ walls and SiO₂ surface. Nevertheless, this exactly reversed condition could not be explained by the expected mechanisms.

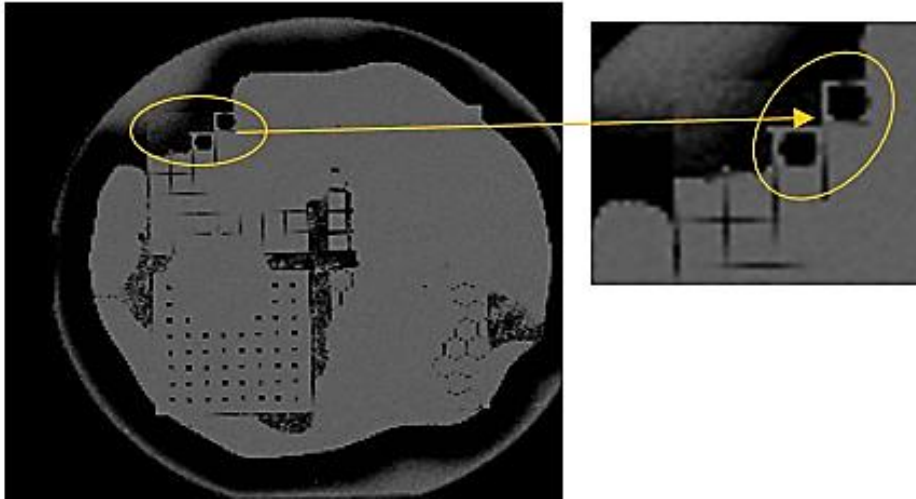


Figure 73. c-SAM image of the bonded pair at 500 μm resolution.

After the image shown by Figure 73 was taken, a high resolution image (presented in Figure 74) was taken. Obtaining this high resolution image took ≈ 6 hours. In this image, the bonded regions are not visible, implying that the initially achieved bonding was not sustained within the measurement period, i.e., with the followed scheme including chemical activation, the bonding lifetime was shorter than a couple of hours, in water, for c-SAM imaging. It could be argued that if it were placed under ambient air, the bonding lifetime would be longer.



Figure 74. c-SAM image of the bonded pair at 10 μm resolution.

Besides the parameters outlined, bonding quality depends also on the surface cleaning scheme, such that longer than required cleanings were reported to be harmful. As reported by [139], RCA-1 clean for 45 seconds was appropriate while extended periods up to 5 minutes deteriorated the bond strength sharply. For example, although a 5 nm thick layer from the surface was activated through plasma treatment, this layer was consumed by extended durations of RCA-1 cleaning process. Medvecká et al. [140] performed two-liquid and three-liquid cleaning schemes before plasma treatment. Bonding was not achieved between the samples cleaned with 3-liquid cleaning. Also, additional cleaning in DIW was advantageous in obtaining better bonding quality by increasing the amount of -OH groups.

4.3.9. Sample Preparation for Wafer Bonding at EVG

A durable bond requires low micro-roughness at the bonding surfaces. Contamination on the surfaces should also be avoided since it could prevent contact of bonding surfaces.

Having observed some mechanisms that might be responsible for prevention of bonding during the trial presented in Section 4.3.8, the samples were prepared with contamination possibility as lower as possible, and better surface state for bonding. For this purpose, the wafers EF 3677 and EF 3679 with 200 nm SiC deposited on both sides of the wafer were used. As a reminder, these samples were fabricated by hetero-epitaxy (at Griffith University), and have nearly excellent thickness uniformity. As it was indicated in Table 7, they represent low rms roughness, which was considered to be beneficial as a start point to build patterned SiO₂ films on. At this point, contamination from any foreign surfaces should be avoided.

Photolithography was applied on both sides of EF 3677 to obtain double-sided pattern, while only one surface of EF 3679 was patterned. On the front side of EF 3677, the pattern with the optimized SiO₂ wall configurations was applied, while on the backside of the same wafer, the backside pattern with configuration numbers was applied.

As the backside pattern was applied only on EF 3677, the more critical surface (front side, for bonding) required careful handling and protection. For this purpose, the

scheme illustrated in Figure 75 was developed for the two-side patterning of EF 3677. This scheme was further used in the subsequent double-side patterning to be used in bonding processes. The process started with coating the front side by a thick PR (SPR 220-7), such that in the following step, this front surface (in contact, for example with the holder of spin coater) was not contaminated from previously processed materials.

Before the start of the processes depicted in Figure 75, the following were done:

- 1- Inspection of the sample surfaces via optical microscopy.
- 2- Cleaning via standard piranha procedure.
- 3- Deposition of 100 nm thick SiO₂ film on the front side and 300 nm thick SiO₂ film on the back side of the wafer by PECVD. The SiO₂ film thickness on the backside was not a variable to NFRT, since it only served for hosting the outer pattern. (In the subsequent processes, the outer-side pattern was alternatively applied by Si etching, rather than SiO₂ deposition on the backside.)
- 4- Dicing of the samples EF 3677 and EF 3679 (of 6-inch diameter) to 4-inch diameter, to perform the processes (e.g., photolithography). The blade used was of 2050-K and the tape type is 0805MCE. The cut speed was CC (circle cut): 0.4 mm/sec and FC (flat cut): 1 mm/sec with a standard water flow setting. With these parameters, the dicing process lasted for 1.5 hours.
- 5- Cleaning via piranha procedure to remove any particulates left on the surface.

Schematics in Figure 75 started with the structure obtained at step 5. All samples obtained from Griffith University were double-side coated with SiC. For simplicity, SiC-Si-SiC layers of EF 3677 are not shown in Figure 75.

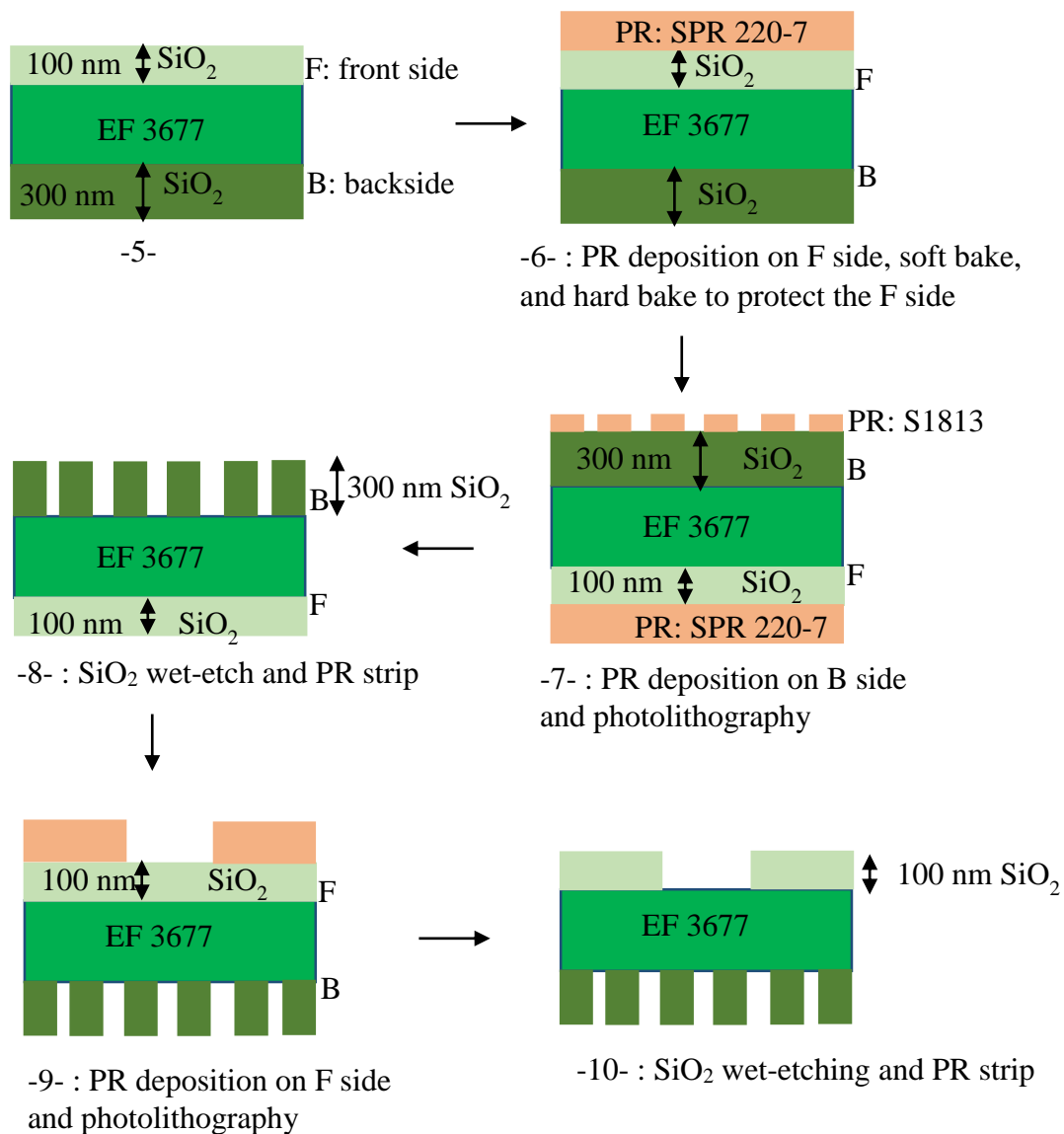


Figure 75. Fabrication scheme designed for the double-sided patterning of EF 3677.

The SiO₂ film thickness on the backside was chosen to be larger than 100 nm, i.e., 300 nm. This selection was to prevent excessive removal the SiO₂ from the backside during the wet etching of SiO₂ on the front side by full immersion of the sample into BHF solution. The processes depicted in Figure 75 are concerned with a DSP Si wafer with double-sides deposited by SiC films. When a SSP Si wafer was used, the PR type used at step 7 was again SPR 200-3, because the back surface is more rough and a thicker PR is needed to properly apply the backside pattern.

The resulting inner surfaces of EF 3677 and EF 3679, as well as the outer surface of EF 3677 were photographed as in Figure 76.

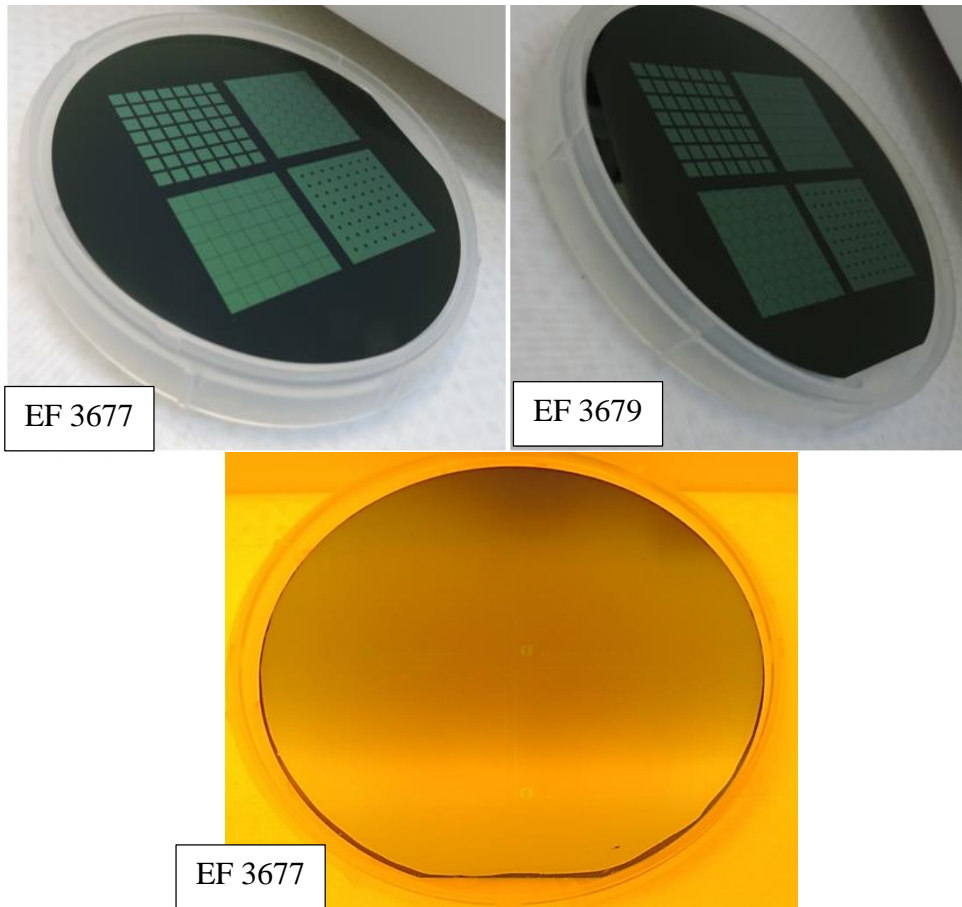


Figure 76. Inner patterns of the samples EF 3677 and EF 3679.

Alignment accuracy is critical for patterned interfaces. For this purpose, alignment markers at the inner (front) sides of EF 3677 and EF 3679 were placed as in Figure 77.

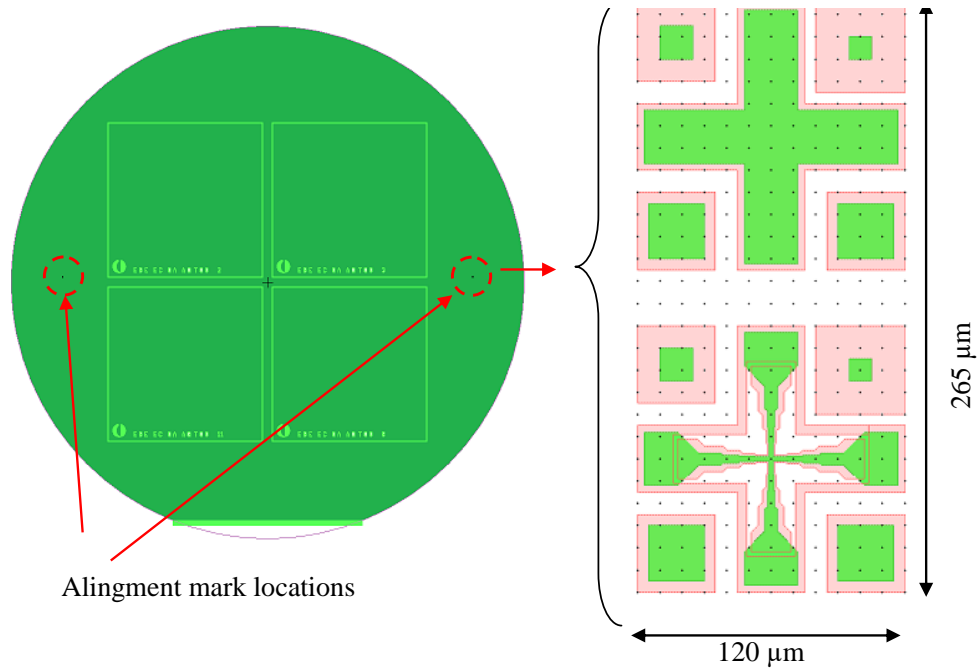


Figure 77. Alignment markers on EF 3677 and EF 3679.

4.3.10. Wafer Bonding Efforts at EVG

Bonding process was performed under vacuum (10^{-5} mbar). The patterned EF 3677 and EF 3679 were aligned via backside alignment, with an estimated accuracy of around $1 \mu\text{m}$. IR imaging was performed after bonding.

Before the bonding process, some characterizations were performed to estimate the bonding quality. EVG performs surface characterizations on the samples by AFM imaging and measurements by scanning $2 \mu\text{m} \times 2 \mu\text{m}$ areas.

The characterizations started by EF 3677, from two points, one of which is close to the center and the other is close to the end of the patterned (i.e., start of the unpatterned) region, as shown in Figure 78.

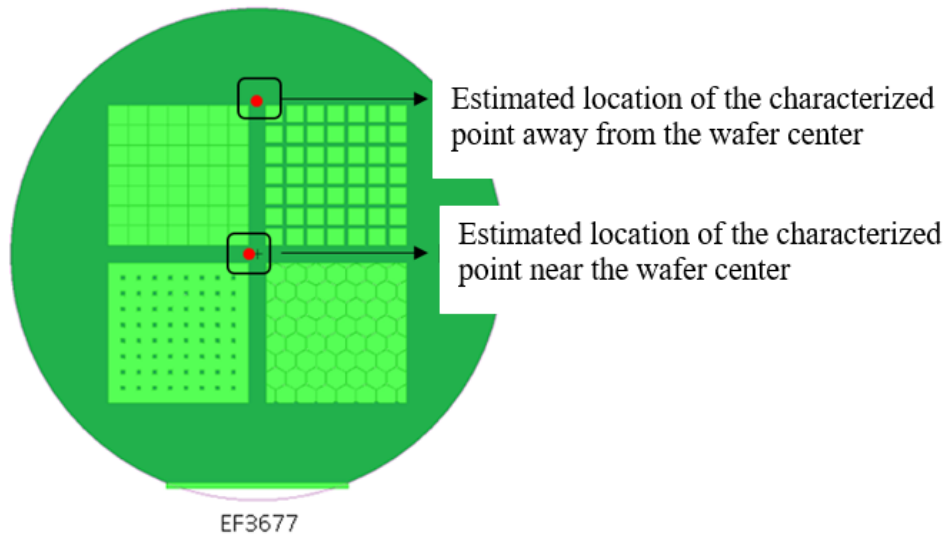


Figure 78. AFM characterization locations on EF 3677.

It is seen through inspection of Figure 79 that contamination was present on the wafer surface, although utmost care was given in sample handling and cleaning. Data taken inside of the area encapsulated by the dashed rectangle (containing less number of structures with relatively smaller size) exhibited an rms (R_q) value of 0.829 nm, while the entire area ($2\ \mu\text{m} \times 2\ \mu\text{m}$) has $R_q = 1.66\ \text{nm}$. This increase in the rms roughness of the $2\ \mu\text{m} \times 2\ \mu\text{m}$ area compared to the dashed rectangle area resulted from the contaminations seen in light pink color.

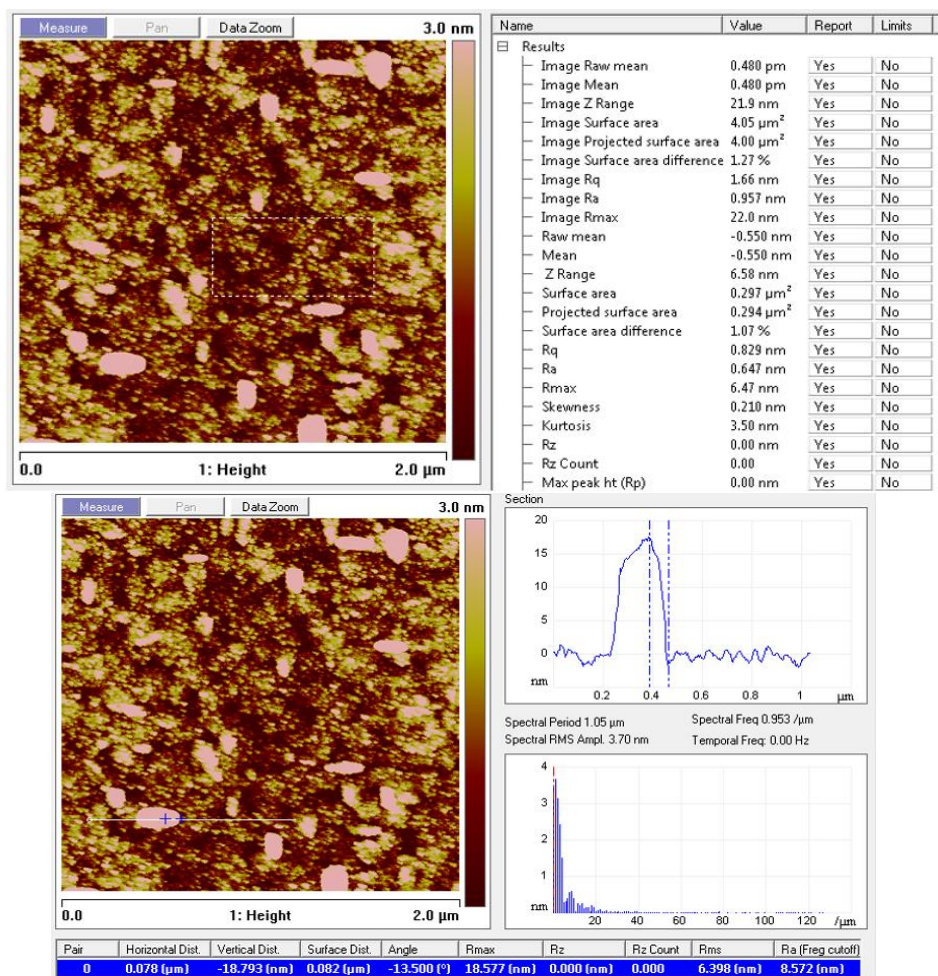


Figure 79. AFM image and roughness characterization from near the center of EF 3677.

Although an rms roughness value of 1.66 nm is very close to the upper limit of the allowed rms roughness (i.e., 1 nm), examination of the contaminations showed that their heights can reach up to 18 nm.

Data and images taken from the point away from the center are provided below in Figure 80. The area encapsulated by the dashed rectangle (with less contamination) exhibited $R_q = 0.749$ nm, while the entire area ($2 \mu\text{m} \times 2 \mu\text{m}$) had $R_q = 1.28$ nm. This even closer result to 1 nm maximum rms roughness limit also comes with structures of nearly 10 nm height.

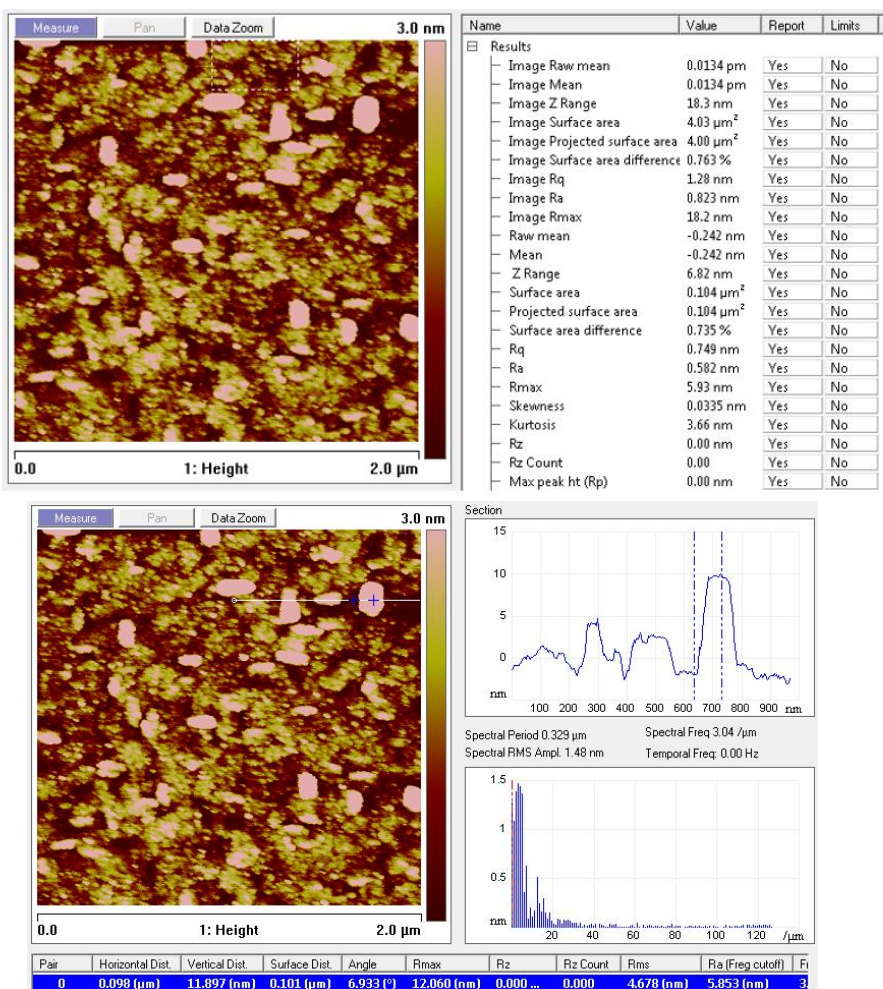


Figure 80. AFM image and roughness characterization away from the center of EF 3677.

These characterizations were interpreted jointly with the specialists at EVG. After discussions, it was concluded that a partially successful bond was possible between the samples. Presence of particles of nearly 10 nm - 18 nm height would locally prevent the contact of SiO₂ bonding surfaces. In this case, vacuum lifetime would be negatively affected. A closer look at the contaminations is possible by the optical microscopy images in Figure 81. Specific areas marked with red arrows indicate presence of contaminants on EF 3677 and EF 3679.

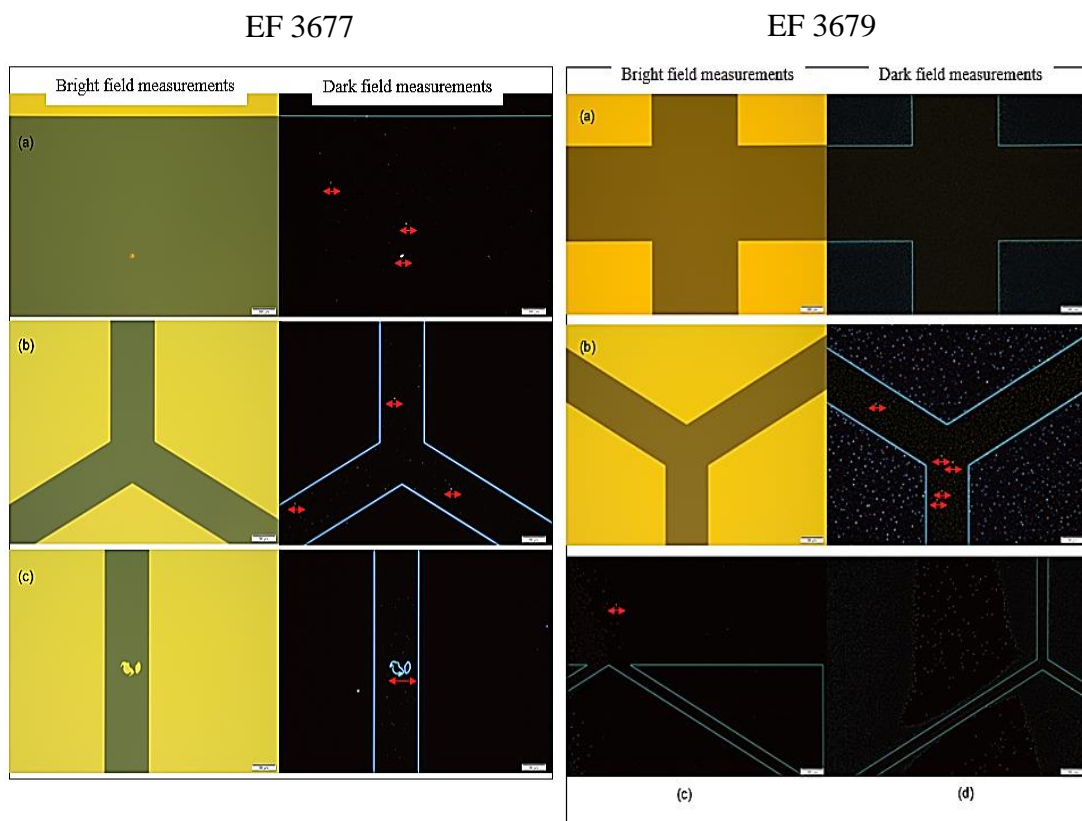


Figure 81. Optical microscope images from the surfaces of EF 3677 and EF 3679.

Examining Figure 81 reveals that the size of particles on the sample surfaces is smaller for the case of EF 3679 than that of EF 3677. This result is reasonable considering the fact that EF 3677 experienced a double-sided process with a higher contamination possibility when compared to EF 3679 with a single side pattern.

Having seen these results, it was decided to perform a chemical cleaning procedure to see if the particles would be removed. For this purpose, EF 3677 was cleaned in 2% NH_4OH at room temperature and rinsed in DIW. AFM results from near the center of EF 3677 are given in Figure 82.

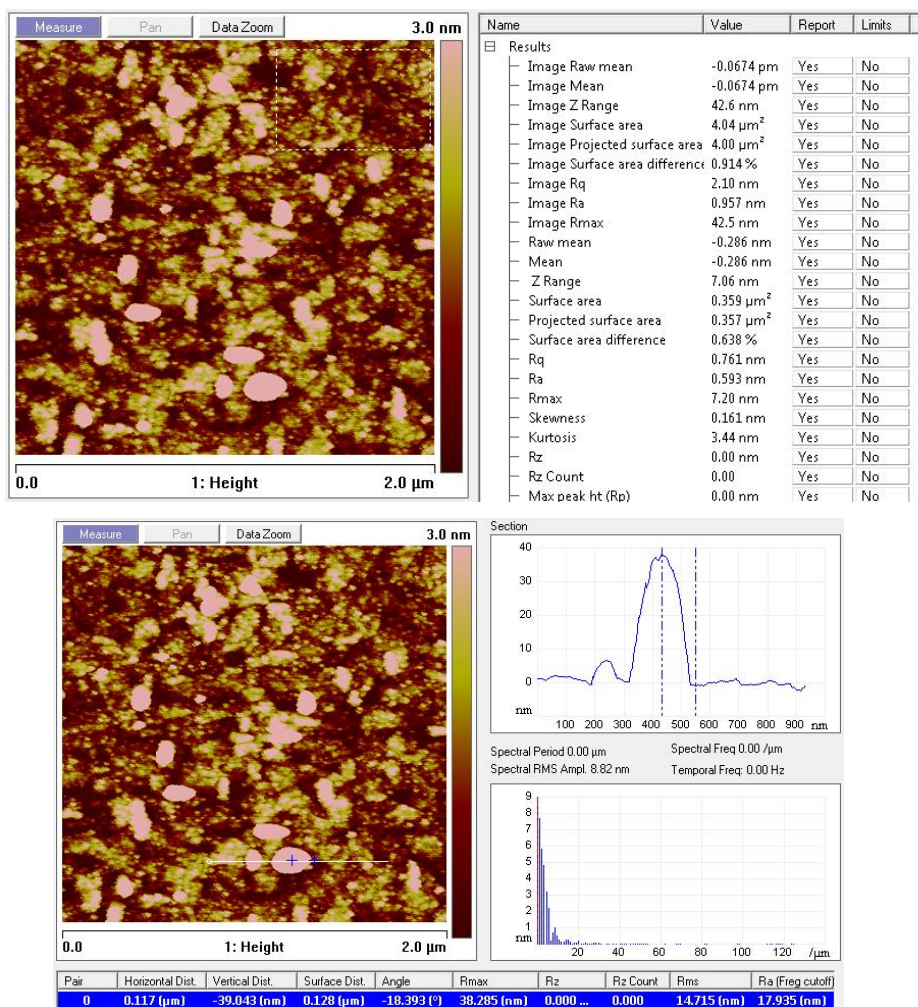


Figure 82. AFM characterization from near the center of EF 3677, after chemical cleaning.

Figure 82 showed that after cleaning $R_q = 2.1$ nm was observed in the entire scanned area ($2 \mu\text{m} \times 2 \mu\text{m}$) on EF 3677. This value is slightly greater than the pre-cleaning value. Also, contaminants with heights up to 40 nm were spotted.

Figure 83 showed that after cleaning $R_q = 1.48$ nm was observed in the entire scanned area ($2 \mu\text{m} \times 2 \mu\text{m}$) on EF 3677. This value is nearly the same as the pre-cleaning value. In addition, contaminants with heights up to nearly 15 nm were observed.

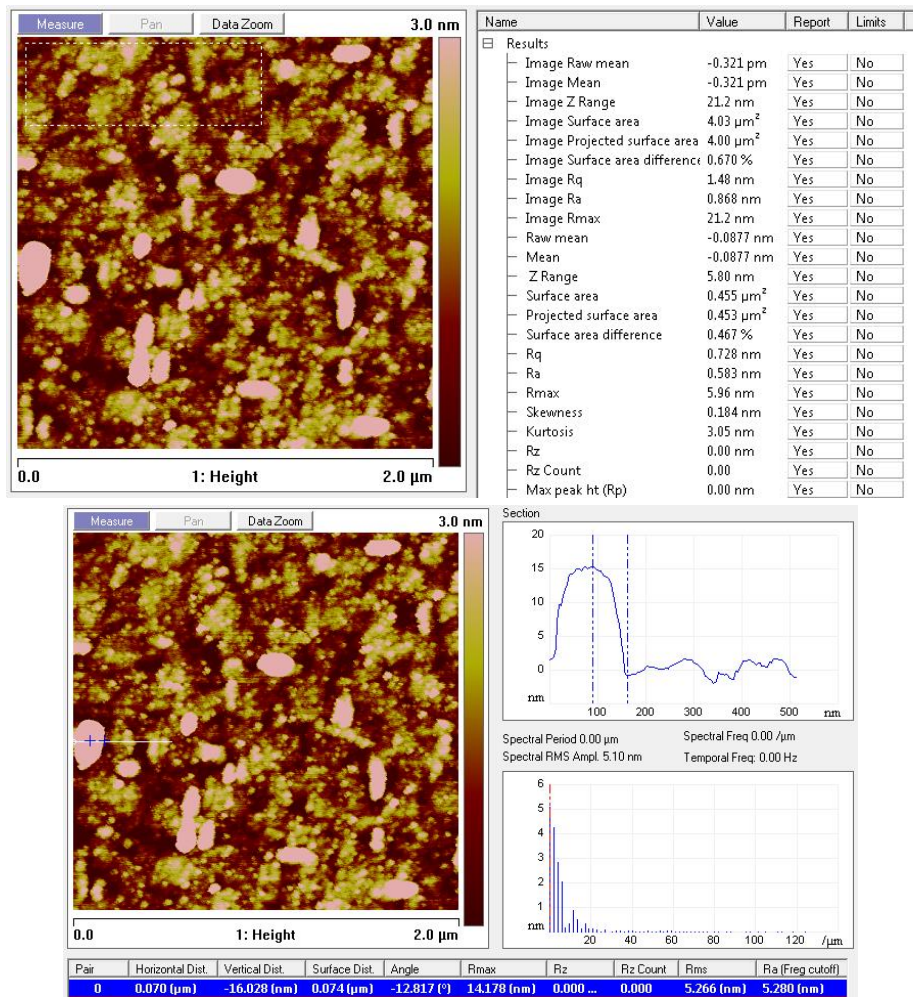


Figure 83. AFM characterization away from the center of EF 3677, after chemical cleaning.

The after chemical cleaning characterizations showed that the contamination could not be removed by the chemical cleaning. These contaminants could be removed by CMP, if the device was present at EVG. CMP is a commonly used process in smoothing and flattening surfaces. Gui et al. [138] reported the importance of CMP in Si fusion bonding. They demonstrated that KOH etched Si wafers, Si wafers with heavy B diffusion, Si wafers coated by LPCVD $\text{Si}_{3+x}\text{N}_4$ and poly-Si could be bonded at room temperature and standard atmosphere, after CMP. The Si (100) wafers used were SSP, and 380 μm thick. Before diffusion and coating, the samples were cleaned in fuming HNO_3 and 70% hot HNO_3 , and then rinsed in DIW. The authors stressed that after CMP, particles were accumulated on the surfaces.

Cleaning after CMP was therefore crucial, which was realized by brushing under DIW. The surfaces were then cleaned by RCA process to remove sodium contamination from the slurry. Before bonding, the wafers were RCA cleaned at 80°C for 20 minutes and then by a standard procedure. The wafers were bonded after spin drying. Post-annealing was performed at 1000°C for 2 hours, under N₂. After CMP, the rms roughness of surfaces reduced by an order of magnitude to 3 Å - 4 Å. They reported that the bonding failures before CMP could be attributed to larger than allowed surface roughness. After CMP, all mentioned pairs were either bonded spontaneously after bonding or by applying pressure. In another work, Gui et al. [143] reported bonding of surfaces with 0.8 nm rms roughness and bonding failure for surfaces with rms roughness of 6.3 nm. The specific surface energies (in mJ/m²) was also reported to be increased by post-annealing.

Since performing a CMP process was not possible, fusion bonding of EF 3677 and EF 3679 was performed. The IR characterization result is presented in Figure 84. The interference patterns are indicative of the absence of a bond between the wafers. The wafers were also said to be separated during their unloading from the IR inspection system.

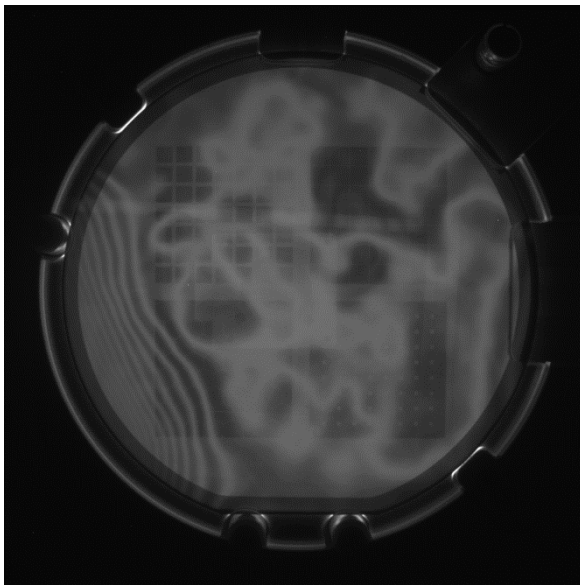


Figure 84. IR inspection on the bonded EF 3677-EF 3679 pair.

4.3.11. Wafer Bonding at METU-MEMS Center: Part II

The wafer bonding trial at METU-MEMS Center with chemical activation was presented in Section 4.3.8. After the plasma activation device was put into use, wafer bonding process accompanied with a plasma activation was performed.

The first trial for this scheme was performed following the same stages as in Section 4.3.8, along with the use of megasonic clean and the plasma activation process, on two identical and unpatterned, 100 nm thick PECVD SiO₂ coated Si wafer. In this way, it was aimed to see if the plasma activation parameters were sufficient. Both wafers were subjected to O₂ plasma for 30 seconds. The resulting c-SAM image of this bonded pair is presented in Figure 85.

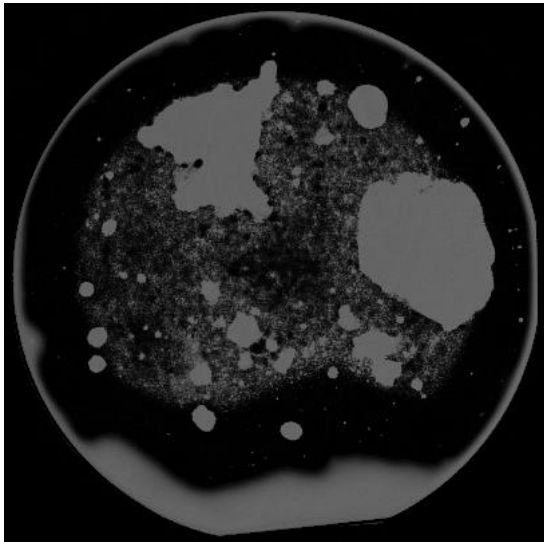


Figure 85. c-SAM image of the test pair, after plasma activation, at METU-MEMS.

Inspection of Figure 85 reveals that the bonding quality was better than that in Figure 84. Although some areas in lighter color indicate locally unbonded areas, these wafers have good bonding quality, in average. Having seen this result, wafers for the actual NFRT device were prepared. These wafers have 50 nm thick SiC films deposited by RF magnetron sputtering and 100 nm PECVD coated and patterned SiO₂ films. Plasma activation of these samples took 60 seconds, with O₂ plasma. Figure 86 shows the c-SAM images of this bonding.

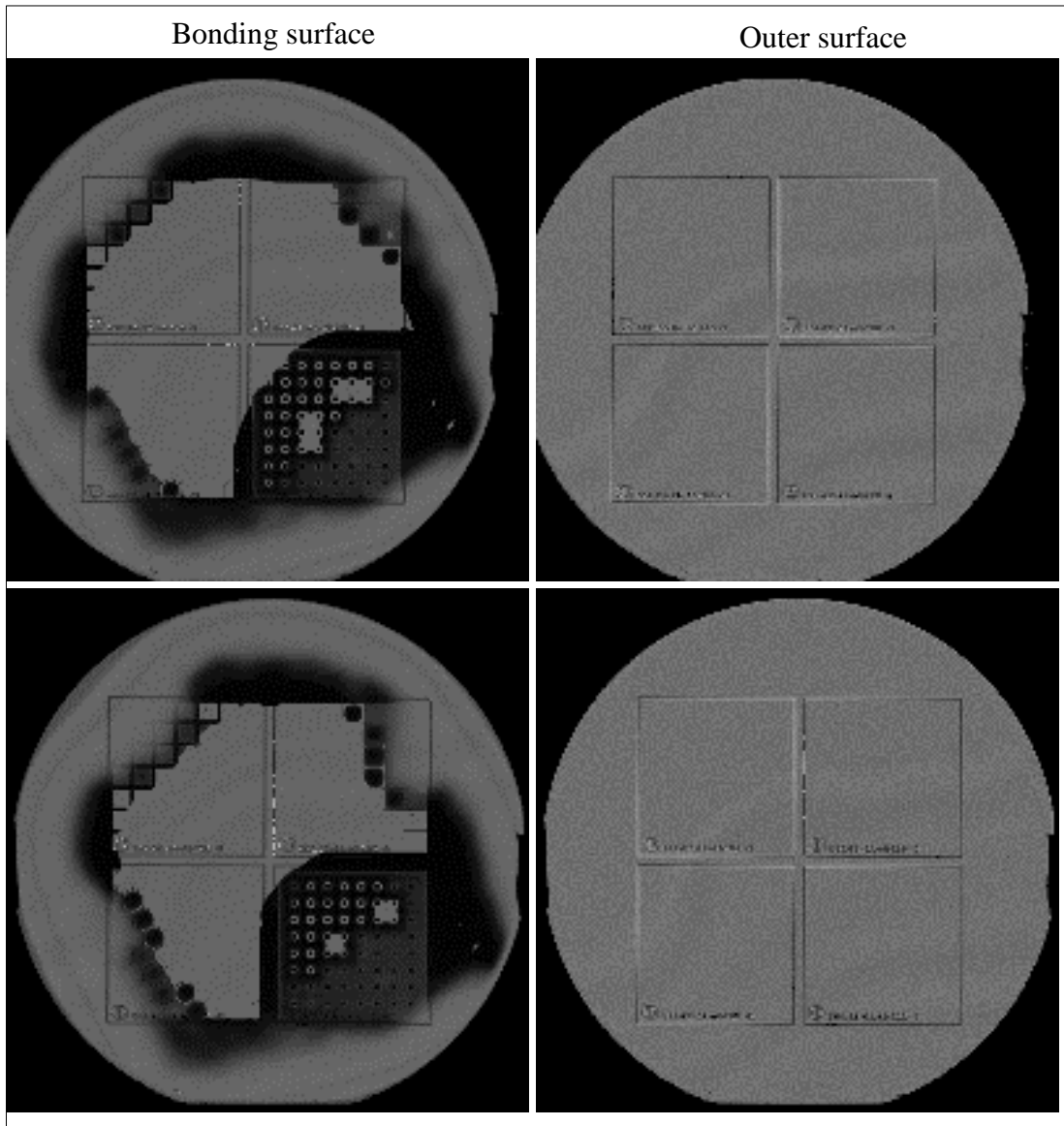


Figure 86. c-SAM image of the actual pair, after plasma activation, at METU-MEMS.

By examining Figure 86, it is determined that the wafers were partially bonded. The areas through the middle of the wafer pair were in darker color, indicating contact. Some regions in lighter color were not in contact, but the bonding quality was good especially the region with pillars.

The bonding lifetime was less than a couple of hours, since the contact was observed to be not sustained after the high resolution imaging (took ≈ 6 hours).

4.3.12. Wafer Bonding at METU-MEMS Center: Part III

This part of the bonding process was performed on two thick (1.2 μm) thermal oxide coated Si wafers. In this way, it was aimed at determining the relative differences in the bond quality, by the nature of the SiO_2 film itself, either being deposited (via PECVD) or grown (by thermal oxidation). As a reminder, the previous bonding efforts resulted in a bonding lifetime less than ≈ 6.5 hours.

During the processes summarized in Sections 4.3.8 and 4.3.11, the bonding stage (bringing the wafers into contact and applying pressure) was performed in a way that the samples were first heated to 300°C and then brought into contact under vacuum ($\approx 10^{-6}$ mbar). This was to maximize the vacuum quality by minimizing the amount of gasses in the cavity (by outgassing with heating). After bringing into contact, 10 kN force was applied in each case. On the other hand, in this process, samples were brought into contact first, and then heated to 300°C .

With the same process stages, with this difference in heating and bringing into contact sequence for thermal-oxide bonding, below are the c-SAM images with high resolution (15 μm , horizontal) characterizing the bond quality.

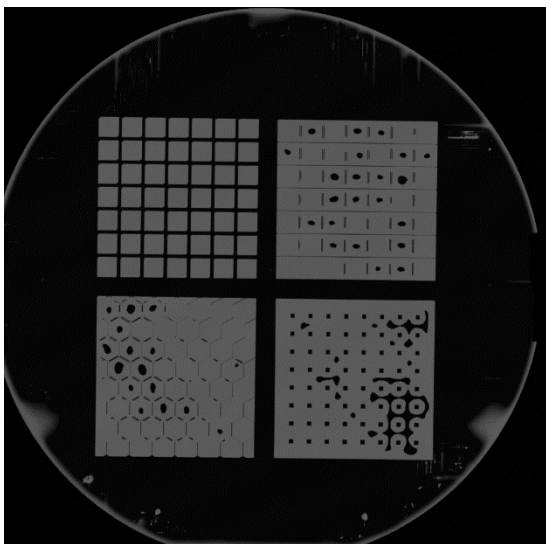


Figure 87. High resolution c-SAM image of the bonded (thermal-oxide) pair.

Figure 87 reveal that two wafers were successfully bonded together. The interfaces were in good contact, as indicated with black color towards the outer edge. The patterns were visible especially in the top left and bottom right (configurations with square shaped walls, and pillars) devices, with good contrast between the SiO₂ walls (in black color) and SiC walls (not in contact) enclosing the cavity (in gray color). Bonded condition of this pair was permanent.

4.4. Results and Discussions

Results of the fabrication work, some obtained through inspection of samples before and after processes, are presented below with discussion:

- Use of a bonded target requires sputtering to be performed at low RF powers. Low powers resulted in low deposition rates and thereby a controlled process with a more ordered amorphous network in SiC thin films. The sputtering recipe developed for 62 W RF power and use of a bonded SiC sputtering target are differences of the sputtering part of this work from the literature. In this process (Part I), a deposition rate of around 1 nm/min is obtained.
- Wet etching of SiC is a challenging process. If the application is sensitive to SiC shape after etching and the substrate is also attacked by the wet etchant, dry etching schemes could be used.
- Thermal annealing is a crucial process if crystallization of an already deposited amorphous SiC film is required.
- SiC films coated at 150 W and annealed under both forming gas and vacuum experienced onset of crystallization at 900°C-1100°C, as indicated by the good fit of a Lorentzian line-shape to their Si-C band of absorbance spectra. Presence of 3C-SiC (111) and (220) were seen in the XRD spectra of the sample annealed at 1000°C under forming gas. Crystallization under vacuum started at 900°C, and annealing at 1200°C for 83 seconds resulted in the formation of graphite (or alternatively carbon contamination) and 4H-SiC (004) (while this diffraction peak is close to the one for 3C-SiC (200) as well) along with 3C-SiC (111) phase.

- SiC films deposited at 62 W also experienced onset of crystallization. When compared with the transmission spectra reported for cubic SiC [131], it was seen that the sample annealed under vacuum at 900°C started showing changes when compared to the thermally untreated sample, and this change to approaching to the spectra of cubic SiC was very pronounced for the sample annealed at 1050°C. XRD spectra of the vacuum-annealed samples revealed the presence of 3C-SiC (220) and (222).
- Surface changes after annealing (e.g., formation of protrusions) should be considered along with structural changes (via FTIR, XRD analyses) since they could be indicative of improved internal structures.
- Samples annealed under Ar at 1300°C exhibited an exceptional case. At this temperature one may expect a good extent of crystallization. Although the XRD analyses suggested the presence of 3C-SiC (220) and (222), the transmission spectra in comparison to that reported by [131] exhibited a highly oscillatory behavior, such that the Si-C band was nearly not identifiable. For the case of annealing at the same environment at 1200°C, oscillations in the transmission behavior were reduced.
- Within Part II of sample fabrication, SiC sputtering was performed at a higher RF power (150 W) using a monolithic sputtering target. In this case, one should be careful with avoiding more than enough powers to the target to prevent cracking due to thermal shocks.
- SiO₂ deposition onto SiC thin films was achieved via PECVD at 60 W RF power, 300°C, 550 mTorr pressure under the presence of SiH₄, N₂O and N₂ as process gases.
- Different SiO₂ wall patterns (square-shaped, six-sided honeycomb, pillar) providing different amount of conduction areas between SiC-on-Si media were applied by photolithography.
- Bonding of two wafers by a chemical activation scheme characterizations showed that the bonding between wafers was successful for a certain time, but not permanent.

- Although great care was given to avoid contamination, particles were detected on the structured wafers (EF 3677 and EF 3679) sent to EVG for bonding. A chemical cleaning was tried but seen to be inefficient in removing these particles.
- Fusion bonding process is very sensitive to surface roughness and presence of contamination. In the current case, although the rms roughness of the surfaces was slightly larger than the limit reported by EVG, presence of particles might have prevented the bonding of the two wafers. Therefore, CMP process is a must to obtain a safe and durable bond, which is crucial in maintaining the vacuum lifetime.
- Fusion bonding efforts at METU-MEMS Center with plasma activation yielded better results than those processed at EVG. The bonded pair with SiO₂-on-SiC-on-Si revealed a limited bonding and vacuum lifetime.
- Fusion bonding of two Si wafers with thick SiO₂ films grown by thermal oxidation revealed a significantly improved bonding quality, as observed through the inspection of c-SAM images. The bonding lifetime was determined to be significantly greater, such that even after days, the bonding was sustained, and the pair was diced to obtain individual devices enclosing vacuum.

CHAPTER 5

NEAR-FIELD RADIATIVE TRANSFER MEASUREMENTS

The samples fabricated within the scope of this dissertation were tested for their NFRT behavior by two different experiment set-ups.

The first set of measurements were performed under vacuum, within the scope of a collaboration with Assoc. Prof. Dr. Keunhan (Kay) Park and Mohammad Ghashami at the University of Utah, Dept. of Mechanical Engineering. This collaboration also include sub-continuum air conduction measurements between the samples fabricated in this work, by the use of the same vacuum chamber without evacuation [144].

The second set of measurements were performed by an experiment set-up developed at Middle East Technical University, Dept. of Mechanical Engineering (within the scope of the TÜBİTAK research project, grant no: 214M308), to work under ambient conditions. This Chapter provides a summary of the principles of the tests and the results.

2.5. Near-Field Radiative Transfer Tests: Part I (Vacuum)

The set-up located at the Utah Nano-Energy Laboratory allows NFRT measurements between emitter and receiver objects of $5 \text{ mm} \times 15 \text{ mm}$ size, separated by distances down to 200 nm [23], inside a vacuum chamber. Details of the experiment set-up can be found in [23]. Before measurements, the samples were attached to glass carriers for placement in the vacuum chamber, having a $5 \text{ mm} \times 5 \text{ mm}$ overlapping area after alignment, resulting in 0.25 mm^2 contact area.

NFRT behaviors of the full wafer size SiC-on-Si samples with SiC thicknesses of $\approx 231 \text{ nm}$ were investigated. Thermometer and contact pad were deposited and patterned

on the samples by photolithography (as in Figure 88), to accurately monitor the temperatures of the opposing surfaces.

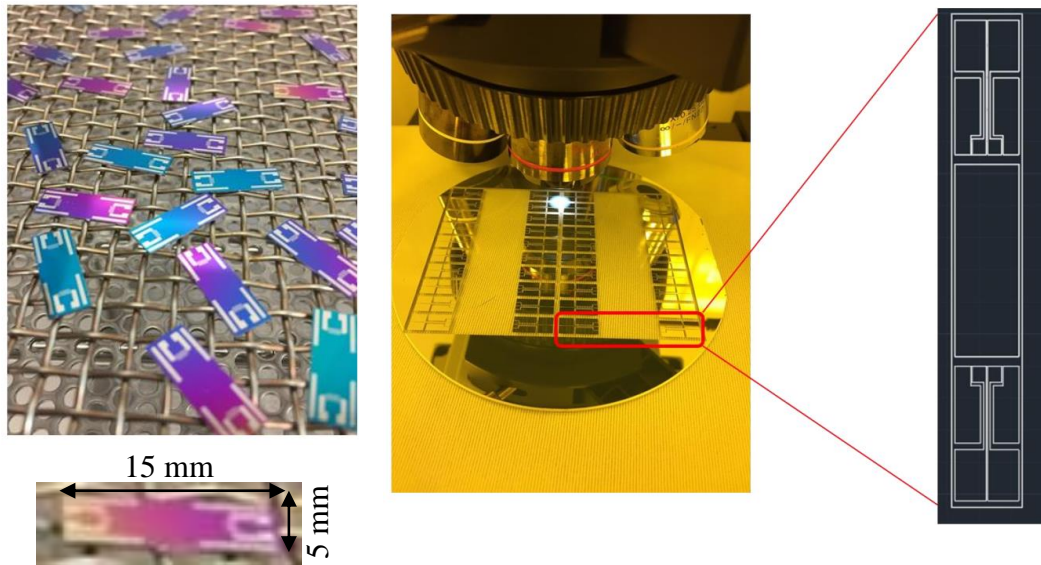


Figure 88. Samples preparation for measurements (left), electrical connection pads (right).

After samples preparation, they were mounted on the nano-positioner to establish a certain gap between emitter and receiver objects, and mounted in the vacuum chamber, as shown in Figure 89.

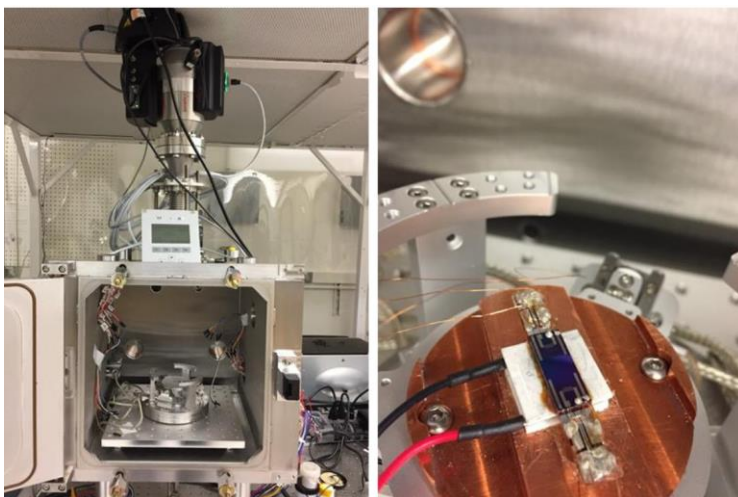


Figure 89. The vacuum chamber hosting NFRT measurements (left), sample mounting on the nano-positioner (right).

The separation between the samples was adjusted by first establishing contact. At this stage, the samples were approached slowly by 5 nm/s. The point of contact is realized by the sudden jump in the temperature of receiver by conductive transfer from the emitter. After this reference point, the objects are retracted by 4 nm/s to establish a certain gap value.

The amount of heat transfer can be realized by monitoring the change in the power supplied to the heater to keep the emitter's temperature constant during measurements. This heater power includes far-field radiation losses to the environment, near-field radiative transfer between emitter and receiver, and conductive heat transfer at the point of contact [23]. Results for the ≈ 231 nm SiC-on-Si samples are presented in Figure 90. In this set of experiments, the emitter and receiver temperatures were set respectively to 320 K and 300 K.

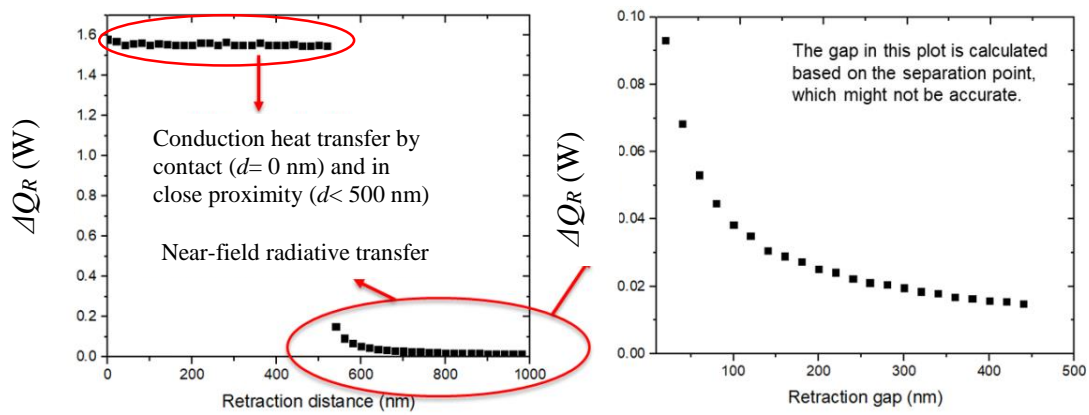


Figure 90. NFRT experiment results with 231 nm SiC-on-Si samples.

Results in Figure 90 suggest that starting from gap sizes of around 500 nm, the near-field effects were seen by considerable diminishing of the heat rate. The nearly constant portion in the left of Figure 90 was attributed to conduction heat transfer, which was measured to be around 8 times greater than the near-field radiative transfer, starting from 500 nm retraction gap, for this particular sample. This trend is visible up to $d < 500$ nm, since the samples were pushed more into each other with mechanical force to ensure good mechanical contact in the approach phase. After this point, since

the experiments were performed in vacuum, the only heat transfer mechanism left is thermal radiation once the conduction is disregarded by preventing contact. The diminishing radiative heat rate with increasing separation distance is typical to NFRT. The data for 50 nm SiC-on-Si systems, as well as 200 nm SiC-on-Si systems prepared through processing of EF 3680 (details provided in Table 7) are presented in Appendix C.

2.6. Near-Field Radiative Transfer Tests: Part II (Ambient Environment)

The set-up located at the Heat Transfer Laboratory of the Dept. of Mechanical Engineering, Middle East Technical University has been developed by the research team under the scope of the TÜBİTAK Research Project (grant no: 214M308). The set-up aims at measuring the amount of heat flux between objects thermally insulated from the environment, under ambient conditions. Figure 91 illustrates the total amount of heat flux measured from the samples processed as elaborated in Section 4.3.11 with c-SAM characterizations in Figure 86.

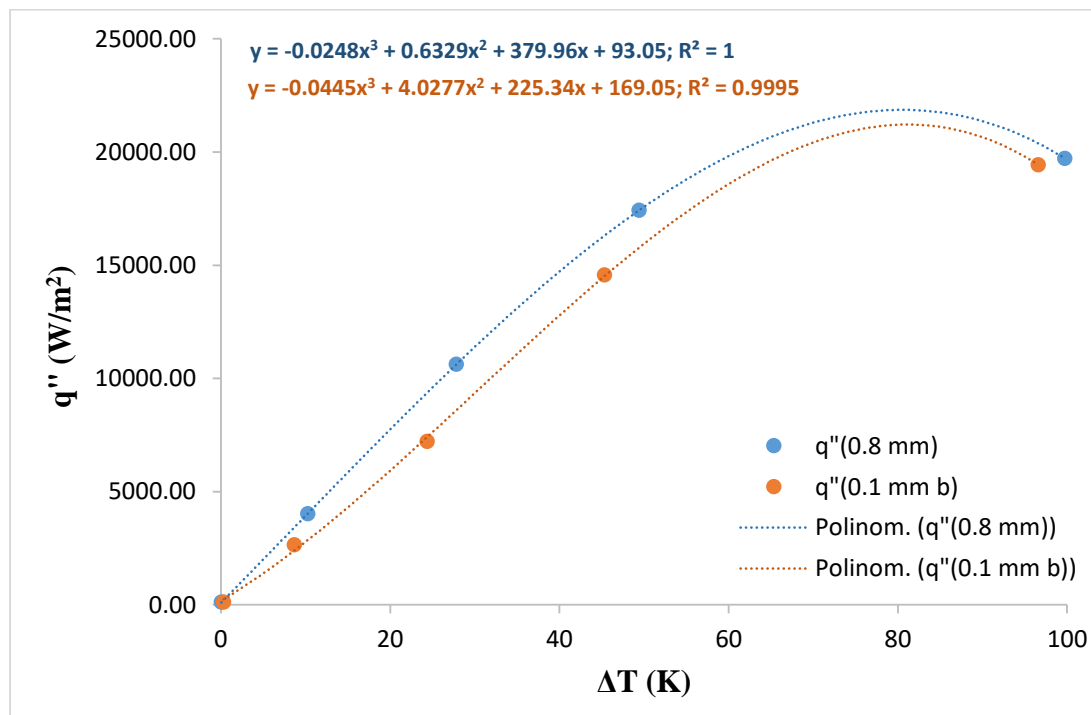


Figure 91. Experiment results with 100 nm SiO₂ on 50 nm SiC-on-Si samples (with air-gap).

The trends depicted in Figure 91 correspond to square shaped SiO₂ wall designs. The design with thicker walls (0.8 mm) provided greater amount of heat flux (shown with blue) when compared against that (shown with orange) obtained with the thinner wall (0.1 mm) design. These data were acquired by manually aligning the 50 nm SiC-on-Si samples with 100 nm SiO₂ patterns on, since these wafers sustained the bond for around a couple of hours. Dicing process was performed after separating the wafer pair. Therefore, the cavity (gap) between these samples were not evacuated, and contained air.

As it was elaborated in Section 4.3.12, the wafer pair with SiO₂ walls thermally grown on Si wafers. These wafers were fusion bonded and the bond between them was permanent. Therefore, the bonded pair was diced and individual devices with vacuum-enclosing cavities were obtained after dicing. Figure 92 presents the total amount of heat flux for each of the devices.

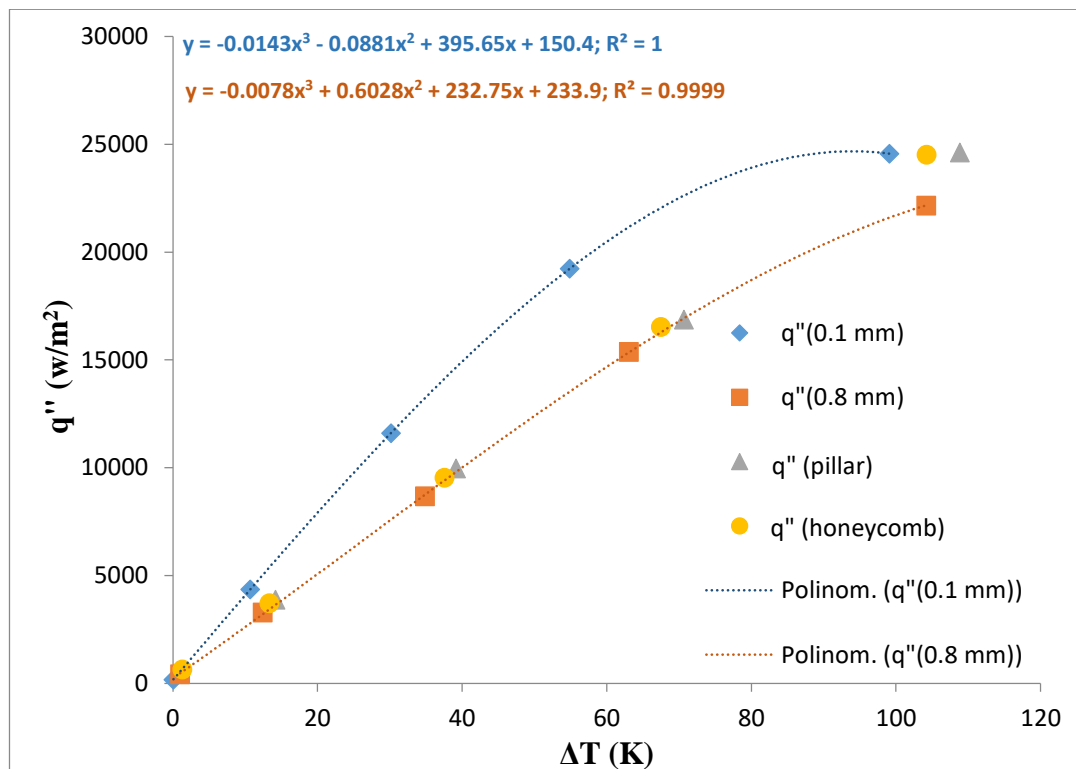


Figure 92. Experiment results with 100 nm SiO₂ on 50 nm SiC-on-Si samples (with vacuum gap).

The results in Figure 92 present the total amount of heat fluxes for each of the 4 SiO₂ wall designs (2 square shaped walls, 1 pillar walls, and 1 hexagonal honeycomb walls). It is seen that the variation of heat fluxes differs between the SiO₂ configurations, suggesting the use of different wall patterns with different radiation area to conduction area ratios and amount of deflections, to optimize NFRT device operation. Square shaped walls with 0.8 mm thickness, pillars, and six-sided hexagonal configurations yielded similar behaviors when their heat fluxes are compared against the temperature difference for up to 100 K.

2.7. Summary of the Near-Field Radiative Transfer Tests

In this Chapter, details of the results of the tests conducted on the samples fabricated in this work were presented. Results showed within Part I of the tests that the near-field effects in the radiative transfer were present. Within the scope of the collaborative work with Utah Nano-Energy Laboratory, more analyses are to be performed to relate the retraction gap to the actual separation between objects, in more depth. The Part II of the test results compare the total amount of heat flux between the hot and cold sides of the devices. These results contain conductive heat transfer along with the radiative transfer between objects. It can be deduced that near-field effects could be differentiated after accounting for conductive heat transfer, for each of the SiO₂ wall designs.

CHAPTER 6

CONCLUSIONS AND FUTURE WORK

This dissertation focuses on fabrication of a device for realization of near-field radiative transfer between parallel media formed via deposition of SiC thin films onto Si wafers. These media were bonded together via fusion bonding through SiO₂ walls with varying deflection and radiative transfer over conductive transfer areas. This work provides in depth discussions on crystallization behavior of SiC, and integrating wafer-level bonding in device fabrication scheme. Analytical comparisons also suggested that effects of material-related parameters should be considered in building NFRT systems.

Below, the main conclusions drawn from this work are discussed. After that the list of ideas for future studies is given.

6.1. Conclusions

Within the scope of this dissertation, the aim has been fabricating a vacuum-enclosing device that could operate under ambient conditions, to explore a large number of applications where NFRT holds potential.

In order to gain insight about the physics of the NFRT phenomenon, an analytical work was performed by comparing different doped and undoped wafer materials' performances; along with the main material of this work, SiC. The results of the analytical work are interesting from device fabrication point of view, since the n-type and p-type versions of the same type of wafer were shown to exhibit different NFRT characteristics.

NFRT behavior of SiC was shown to be strongly dependent on the internal structure, such that the dielectric properties of fully amorphous or sputtered SiC differ significantly from crystalline SiC, exceeding the blackbody limit. GaAs, InSb, and InP as III-V group compound semiconductors were also studied and shown to provide higher radiative fluxes than the blackbody limit at certain spectral ranges.

In this dissertation, SiC thin films were deposited on Si (100) wafers by means of RF magnetron sputtering. Deposition of SiC via RF magnetron sputtering is a viable and practical choice. The SiC sputtering recipe obtained at 62 W RF power is novel to the literature, since performing deposition at higher powers and power densities (thereby resulting in high deposition rates) has been a common approach. Sputtering target structure should be selected based on the application's needs. In this work, both bonded and monolithic SiC targets were used, both of which require specific measures during deposition.

SiC, as a very stable and durable material is difficult to etch, when liquid etchants are used. One of the few solutions reported in the literature, i.e., HNO₃ and HF mixture, was evaluated for its performance. It was observed that if etching of SiC is to be done using this solution; the substrate should be selected such that it can withstand the etching process, or alternatively it should be protected from the solution. In this case, Si was affected by the solution and it was considered impractical to etch SiC-on-Si samples using this wet etchant mixture.

Crystallization of amorphous SiC thin films is a challenging task, since it requires high processing temperatures, when crystallization is attempted to be induced by thermal annealing. Practical challenges are: (i) difference in thermal expansion coefficients of SiC (thin film) and Si (substrate), which highly reflects at high temperatures due to substrate and thin film expanding differently and causing defects at the SiC-Si interface; (ii) temperature ramp-up and ramp-down rates used in the annealing process, i.e., if high, both the substrate and thin film do not have enough time to expand comfortably and the interaction effect of (i) and (ii) would be more pronounced, (iii) difference in lattice constants of Si and SiC, which makes an epitaxial growth of SiC on Si (if aimed) very challenging. In the literature, both the conventional furnaces and

rapid thermal processing devices are used for SiC thin films' crystallization, at temperatures up to 1300°C. Devices operating at around these temperatures are difficult to find and use. Most of such devices are designed to be used for heat treatment of bulk ceramics; therefore, use of a proper sample holder specific to small scale samples is a mostly a requirement. It was seen that use of a lower temperature ramp-up and -down rates in the thermal annealing process would be a safer choice in obtaining annealed samples with less stress and defects. Thermal annealing under forming gas, vacuum, N₂ and Ar environments at certain temperatures and durations revealed the onset of crystallization of amorphous as-deposited SiC thin films.

In developing an integrated device to work under ambient conditions, bonding of the two identically fabricated SiC-on-Si samples is required. The bonding took place between SiO₂ patterns made onto the SiC thin films. It has been shown in the literature that surfaces with very low roughness and very low level of contamination would be bonded together after proper sample cleaning between steps, surface activation, and thermal annealing. First, a chemical activation scheme was used in activating the SiO₂ surfaces before bonding, as an alternative to the more commonly used plasma activation processes under N₂, O₂, etc. It was observed through c-SAM imaging that this activation resulted in successful bonding of surfaces, initially. On the other hand, after a couple of hour's period of c-SAM imaging, the bonding was seen to be not sustained. Bonding being formed but not permanently can be attributed to insufficient surface activation, absence of thermal annealing after bonding, or the nature of the SiO₂ walls (either deposited by PECVD or grown by thermal oxidation). Plasma activation processes were also performed, using O₂ plasma, both on patterned and unpatterned samples. It was observed that, for longer bonding and vacuum lifetime, plasma activation process may be further optimized. Although utmost care was given to obtain samples as free as possible from contaminants, it was observed in pre-bonding characterizations that CMP process is an essential process to obtain flat and smooth PECVD SiO₂ surfaces for bonding. Bond between plasma activated thermally grown SiO₂ films were observed to be significantly better when compared against that of PECVD SiO₂ films.

Both PECVD SiO₂ and thermally grown SiO₂ including samples were tested. Part I of the tests revealed that near-field radiative transfer was observable for the case of amorphous ≈ 231 nm SiC-on-Si media. In Part II of the test results emphasize the importance of the interface wall design, such that square-shaped, pillar, and six-sided honeycomb walls produce different amount of total heat fluxes.

6.2. Future Work

The present work can be extended by:

- Preparing SiC-on-Si samples with micro- and nanostructures respectively by utilizing photolithography or e-beam lithography, and integrating them in a bonded pair. Constructing such a system would allow the theoretically shown enhancements in LDOS and NFRT flux for the case of the presence of nanostructures in NFRT systems.
- Integrating getter films into the bonded NFRT device to maintain a satisfactory vacuum lifetime. Getters could be placed in where it could absorb the gases in the cavity without disturbing surface polariton coupling.
- Study of 2D materials (e.g., borophene, indiene, germanene, etc.) in addition to the widely studied graphene may lead to interesting results and designs.
- Experimental works can be designed to cover a wider range of thermal gradients and gap values.

REFERENCES

- [1] “Key World Energy Statistics 2016,” France, 2018.
- [2] M. Iqbal, M. Azam, M. Naeem, A. S. Khwaja, and A. Anpalagan, “Optimization classification, algorithms and tools for renewable energy: A review,” *Renew. Sustain. Energy Rev.*, vol. 39, pp. 640–654, 2014.
- [3] M. Carbajales-Dale, C. J. Barnhart, A. R. Brandt, and S. M. Benson, “A better currency for investing in a sustainable future,” *Nat. Clim. Chang.*, vol. 4, no. 7, pp. 524–527, 2014.
- [4] T. Bauer, *Thermophotovoltaics Basic Principles and Critical Aspects of System Design*. Berlin, Heidelberg: Springer-Verlag, 2011.
- [5] E. B. Elçioğlu, A. Güngör, G. Akseli, E. Camadan, T. Okutucu Özyurt, and M. P. Mengüç, “SiC-on-Si Based Near-Field Radiative Transfer Device Design, Fabrication and Experimental Setup Development,” in *NanoTR-14, 14th Nanoscience and Nanotechnology Conference Book of Abstracts*, 2018, p. 266.
- [6] R. Feynmann, “There’s Plenty of Room at the Bottom,” *Eng. Sci.*, vol. 23, no. 5, pp. 22–36, 1960.
- [7] M. Planck, *The Theory of Heat Radiation*. Philadelphia: P. Blakiston’s Son & Co., 1914.
- [8] M. Francoeur and M. Pinar Mengüç, “Role of fluctuational electrodynamics in near-field radiative heat transfer,” *J. Quant. Spectrosc. Radiat. Transf.*, vol. 109, no. 2, pp. 280–293, 2008.
- [9] G. E. Moore, “Craming more components onto integrated circuits,” *Electronics*, vol. 38, no. 8, pp. 114–117, 1965.
- [10] P. Ben-Abdallah, “Energy harvesting from lukewarm photons,” *Nat. Nanotechnol.*, vol. 13, pp. 772–773, 2018.
- [11] M. Laroche, R. Carminati, and J. J. Greffet, “Near-field thermophotovoltaic energy conversion,” *J. Appl. Phys.*, vol. 100, no. 063704, pp. 1–10, 2006.
- [12] C. M. Hargreaves, “Anomalous Radiative Transfer Between Closely-Spaced Bodies,” *Phys. Lett.*, vol. 30A, no. 9, pp. 491–492, 1969.

- [13] G. A. Domoto, R. F. Boehm, and C. L. Tien, “Experimental investigation of radiative transfer between metallic surfaces at cryogenic temperatures,” *J. Heat Transfer*, vol. 92, no. 3, pp. 412–416, 1970.
- [14] K. Ito, A. Miura, H. Iizuka, and H. Toshiyoshi, “Parallel-plate submicron gap formed by micromachined low-density pillars for near-field radiative heat transfer,” *Appl. Phys. Lett.*, vol. 106, no. 083504, pp. 1–4, 2015.
- [15] L. Hu, A. Narayanaswamy, X. Chen, and G. Chen, “Near-field thermal radiation between two closely spaced glass plates exceeding Planck’s blackbody radiation law,” *Appl. Phys. Lett.*, vol. 92, no. 133106, pp. 1–3, 2008.
- [16] R. S. Ottens *et al.*, “Near-Field Radiative Heat Transfer between Macroscopic Planar Surfaces,” *Phys. Rev. Lett.*, vol. 107, no. 014301, pp. 1–4, 2011.
- [17] T. Kralik, P. Hanzelka, M. Zobac, V. Musilova, T. Fort, and M. Horak, “Strong near-field enhancement of radiative heat transfer between metallic surfaces,” *Phys. Rev. Lett.*, vol. 109, no. 224302, pp. 1–5, 2012.
- [18] R. St-Gelais, B. Guha, L. Zhu, S. Fan, and M. Lipson, “Demonstration of strong near-field radiative heat transfer between integrated nanostructures,” *Nano Lett.*, vol. 14, no. 12, pp. 6971–6975, 2014.
- [19] T. Ijiro and N. Yamada, “Near-field radiative heat transfer between two parallel SiO₂ plates with and without microcavities,” *Appl. Phys. Lett.*, vol. 106, no. 023103, pp. 1–5, 2015.
- [20] M. Lim, S. S. Lee, and B. J. Lee, “Near-field thermal radiation between doped silicon plates at nanoscale gaps,” *Phys. Rev. B*, vol. 91, no. 195136, pp. 1–7, 2015.
- [21] J. I. Watjen, B. Zhao, and Z. M. Zhang, “Near-field radiative heat transfer between doped-Si parallel plates separated by a spacing down to 200 nm,” *Appl. Phys. Lett.*, vol. 109, no. 203112, pp. 1–5, 2016.
- [22] M. P. Bernardi, D. Milovich, and M. Francoeur, “Radiative heat transfer exceeding the blackbody limit between macroscale planar surfaces separated by a nanosize vacuum gap,” *Nat. Commun.*, vol. 7, no. 12900, pp. 1–7, 2016.

- [23] M. Ghashami, H. Geng, T. Kim, N. Iacopino, S. K. Cho, and K. Park, “Precision measurement of phonon-polaritonic near-field energy transfer between macroscale planar structures under large thermal gradients,” *Phys. Rev. Lett.*, vol. 120, no. 175901, pp. 1–6, 2018.
- [24] E. Rousseau, A. Siria, G. Jourdan, S. Volz, and F. Comin, “Radiative heat transfer at the nanoscale,” *Nat. Photonics*, vol. 3, pp. 514–517, 2009.
- [25] Z. Artvin, “Fabrication of nanostructured samples for the investigation of near field radiation transfer,” Middle East Technical University, 2012.
- [26] K. Webb, M. P. Mengüç, H. Ertürk, and B. Başım, “Technique for measurement of near-field radiation heat transfer between parallel planes with nano-scale spacing,” in *Proceedings of 6th International Symposium of Radiative Transfer RAD-10*, 2010, pp. 1–4.
- [27] K. Webb, “Near-field radiative heat transfer measurements between parallel plates,” in *Proceedings of 7th International Symposium of Radiative Transfer RAD-13*, 2013, pp. 4–6.
- [28] A. Kittel, W. Müller-Hirsch, J. Parisi, S.-A. Biehs, D. Reddig, and M. Holthaus, “Near-field heat transfer in a scanning thermal microscope,” *Phys. Rev. Lett.*, vol. 95, no. 224301, pp. 1–4, 2005.
- [29] A. Narayanaswamy, S. Shen, and G. Chen, “Near-field radiative heat transfer between a sphere and a substrate,” *Phys. Rev. B*, vol. 78, no. 115303, pp. 1–4, 2008.
- [30] S. Shen, A. Mavrokefalos, P. Sambegoro, and G. Chen, “Nanoscale thermal radiation between two gold surfaces,” *Appl. Phys. Lett.*, vol. 100, no. 233114, pp. 1–4, 2012.
- [31] J. Shi, B. Liu, P. Li, L. Y. Ng, and S. Shen, “Near-field energy extraction with hyperbolic metamaterials,” *Nano Lett.*, vol. 15, no. 2, pp. 1217–1221, 2015.
- [32] L. Cui *et al.*, “Study of radiative heat transfer in Ångström- and nanometre-sized gaps,” *Nat. Commun.*, vol. 9, no. 14479, pp. 1–9, 2018.
- [33] M. Francoeur, “Nanostructures feel the heat,” *Nat. Nanotechnol.*, vol. 10, no. 3, pp. 206–208, 2015.

- [34] S. Basu and Z. M. Zhang, “Ultrasmall penetration depth in nanoscale thermal radiation,” *Appl. Phys. Lett.*, vol. 95, no. 133104, pp. 1–3, 2009.
- [35] M. Francoeur, M. P. Mengüç, and R. Vaillon, “Coexistence of multiple regimes for near-field thermal radiation between two layers supporting surface phonon polaritons in the infrared,” *Phys. Rev. B*, vol. 84, no. 075436, pp. 1–9, 2011.
- [36] P. Ben-Abdallah, K. Joulain, J. Drevillon, and G. Domingues, “Near-field heat transfer mediated by surface wave hybridization between two films,” *J. Appl. Phys.*, vol. 106, no. 044306, pp. 1–11, 2009.
- [37] M. Francoeur, M. P. Mengüç, and R. Vaillon, “Spectral tuning of near-field radiative heat flux between two thin silicon carbide films,” *J. Phys. D: Appl. Phys.*, vol. 43, no. 075501, pp. 1–12, 2010.
- [38] S. Basu and M. Francoeur, “Penetration depth in near-field radiative heat transfer between metamaterials,” *Appl. Phys. Lett.*, vol. 99, no. 143107, pp. 1–3, 2011.
- [39] S. Basu and M. Francoeur, “Maximum near-field radiative heat transfer between thin films,” *Appl. Phys. Lett.*, vol. 98, no. 243120, pp. 1–3, 2011.
- [40] C. J. Fu and W. C. Tan, “Near-field radiative heat transfer between two plane surfaces with one having a dielectric coating,” *J. Quant. Spectrosc. Radiat. Transf.*, vol. 110, no. 12, pp. 1027–1036, 2009.
- [41] S. Basu, Y. Yang, and L. Wang, “Near-field radiative heat transfer between metamaterials coated with silicon carbide thin films,” *Appl. Phys. Lett.*, vol. 106, no. 033106, pp. 1–4, 2015.
- [42] A. Didari, E. B. Elçioğlu, T. Okutucu Özyurt, and M. P. Mengüç, “Near-field radiative transfer in spectrally tunable double-layer phonon-polaritonic metamaterials,” *J. Quant. Spectrosc. Radiat. Transf.*, vol. 212, pp. 120–127, 2018.
- [43] B. Czapla and A. Narayanaswamy, “Nanoscale thermal radiation between coated spheres,” in *Proceedings of the ASME 2017 Heat Transfer Summer Conference HT2017*, 2017, pp. 1–7.

- [44] K. Hanamura and K. Mori, “Nano- gap TPV generation of electricity through evanescent wave in near- field above emitter surface,” in *AIP Conference Proceedings*, 2007, vol. 890, no. 2007, pp. 291–296.
- [45] S. Molesky and Z. Jacob, “Ideal near-field thermophotovoltaic cells,” *Phys. Rev. B*, vol. 91, no. 205435, pp. 1–7, 2015.
- [46] K. Park, S. Basu, W. P. King, and Z. M. Zhang, “Performance analysis of near-field thermophotovoltaic devices considering absorption distribution,” *J. Quant. Spectrosc. Radiat. Transf.*, vol. 109, no. 2, pp. 305–316, 2008.
- [47] M. Elzouka and S. Ndao, “Towards a near-field concentrated solar thermophotovoltaic microsystem : Part I – Modeling,” *Sol. Energy*, vol. 141, pp. 323–333, 2015.
- [48] M. Francoeur, R. Vaillon, and M. P. Mengüç, “Thermal impacts on the performance of nanoscale-gap thermophotovoltaic power generators,” *IEEE Trans. Energy Convers.*, vol. 26, no. 2, pp. 686–698, 2011.
- [49] A. Lenert *et al.*, “A nanophotonic solar thermophotovoltaic device,” *Nat. Nanotechnol.*, vol. 9, no. 2, pp. 126–130, Feb. 2014.
- [50] K. Chen, P. Santhanam, and S. Fan, “Suppressing sub-bandgap phonon-polariton heat transfer in near-field thermophotovoltaic devices for waste heat recovery,” *Appl. Phys. Lett.*, vol. 107, no. 091106, pp. 1–4, 2015.
- [51] M. Lim, S. S. Lee, and B. J. Lee, “Effects of multilayered graphene on the performance of near-field thermophotovoltaic system at longer vacuum gap distances,” *J. Quant. Spectrosc. Radiat. Transf.*, vol. 197, pp. 84–94, 2017.
- [52] T. Liao, Z. Yang, Q. Dong, X. Chen, and J. Chen, “Performance evaluation and parametric optimum choice criteria of a near-field thermophotovoltaic cell,” *IEEE Trans. Electron Devices*, vol. 64, no. 10, pp. 4144–4148, 2017.
- [53] Y. Yang, J. Chang, P. Sabbaghi, and L. Wang, “Performance analysis of a near-field thermophotovoltaic device with a metallodielectric selective emitter and electrical contacts for the photovoltaic cell,” *J. Heat Transfer*, vol. 139, no. 052701, pp. 1–9, 2017.

- [54] A. Fiorino, L. Zhu, D. Thompson, R. Mittapally, P. Reddy, and E. Meyhofer, “Nanogap near-field thermophotovoltaics,” *Nat. Nanotechnol.*, vol. 13, no. 9, pp. 806–811, 2018.
- [55] B. N. Pushpakaran, A. S. Saubburaj, S. B. Bayne, and J. Mookken, “Impact of silicon carbide semiconductor technology in photovoltaic energy system,” *Renew. Sustain. Energy Rev.*, vol. 55, pp. 971–989, 2016.
- [56] P. M. Sarro, “Silicon carbide as a new MEMS technology,” *Sensors Actuators, A Phys.*, vol. 82, no. 1–3, pp. 210–218, 2000.
- [57] A. K. Costa, S. S. Camargo Jr, C. A. Achetea, and R. Cariusb, “Characterization of ultra-hard silicon carbide coatings deposited by RF magnetron sputtering,” *Thin Solid Films*, vol. 377–378, pp. 243–248, 2000.
- [58] T. Kimoto, “Bulk and epitaxial growth of silicon carbide,” *Prog. Cryst. Growth Charact. Mater.*, vol. 62, no. 2, pp. 329–351, 2016.
- [59] D. T. Shelberg, “Physical and chemical properties of ambient temperature sputtered silicon carbide films,” Case Western Reserve University, 2010.
- [60] A. V. Singh, S. Chandra, S. Kumar, and G. Bose, “Mechanical and structural properties of RF magnetron sputter-deposited silicon carbide films for MEMS applications,” *J. Micromechanics Microengineering*, vol. 22, no. 025010, pp. 1–7, 2012.
- [61] M. Kuenle, S. Janz, O. Eibl, C. Berthold, V. Presser, and K. G. Nickel, “Thermal annealing of SiC thin films with varying stoichiometry,” *Mater. Sci. Eng. B.*, vol. 159–160, pp. 355–360, 2009.
- [62] L. Calcagno, P. Musumeci, F. Roccaforte, C. Bongiorno, and G. Foti, “Crystallisation mechanism of amorphous silicon carbide,” *Appl. Surf. Sci.*, vol. 184, no. 1–4, pp. 123–127, 2001.
- [63] U. Coscia *et al.*, “Laser annealing study of PECVD deposited hydrogenated amorphous silicon carbon alloy films,” *Appl. Surf. Sci.*, vol. 254, no. 4, pp. 984–988, 2007.

- [64] A. M. Hartel, M. Künle, P. Löper, S. Janz, and A. W. Bett, "Amorphous $\text{Si}_x\text{C}_{1-x}:\text{H}$ single layers before and after thermal annealing: Correlating optical and structural properties," *Sol. Energy Mater. Sol. Cells*, vol. 94, no. 11, pp. 1942–1946, 2010.
- [65] Y. Wang, J. Lin, C. H. A. Huan, Z. C. Feng, and S. J. Chua, "High temperature annealing of hydrogenated amorphous silicon carbide thin films," *Thin Solid Films*, vol. 384, no. 2, pp. 173–176, 2001.
- [66] D.-S. Wu, R.-H. Horng, C.-C. Chan, and Y.-S. Lee, "Plasma-deposited amorphous silicon carbide films for micromachined fluidic channels," *Appl. Surf. Sci.*, vol. 144–145, pp. 708–712, 1999.
- [67] M. Hossain, M. Yun, V. Korampally, and S. Gangopadhyay, "Low temperature crystallization of amorphous silicon carbide thin films for p-n junction devices fabrication," *J. Mater. Sci. Mater. Electron.*, vol. 19, no. 8–9, pp. 801–804, 2008.
- [68] Y. Awad *et al.*, "Effect of thermal annealing on the structural and mechanical properties of amorphous silicon carbide films prepared by polymer-source chemical vapor deposition," *Thin Solid Films*, vol. 518, no. 10, pp. 2738–2744, 2010.
- [69] L. Wang *et al.*, "Color chart for thin SiC films grown on Si Substrates," *Mater. Sci. Forum*, vol. 740–742, pp. 279–282, 2013.
- [70] R. J. Iwanowski, K. Fronc, W. Paszkowicz, and M. Heinonen, "XPS and XRD study of crystalline 3C-SiC grown by sublimation method," *J. Alloys Compd.*, vol. 286, no. 1–2, pp. 143–147, 1999.
- [71] S. Merazga, A. Keffous, A. Brighet, and M. Kechouane, "Effect of thermal annealing on the optical and structural Properties of the a-SiC thin films deposited by DC magnetron sputtering," *Nano World J.*, vol. 3, no. 3, pp. 54–58, 2017.
- [72] D. K. Basa and F. W. Smith, "Annealing and crystallization processes in a hydrogenated amorphous Si-C alloy film," *Thin Solid Films*, vol. 192, no. 1, pp. 121–133, 1990.

- [73] A. Carbone, F. Demichelis, and G. Kaniadakis, "Annealing temperature dependence of the optical properties of sputtered hydrogenated amorphous silicon carbide," *J. Non. Cryst. Solids*, vol. 128, no. 2, pp. 139–145, 1991.
- [74] S. Inoue, K. Yoshii, M. Umeno, and H. Kawabe, "Crystallization Behaviour of Amorphous SiC Films Prepared by R.F. Sputtering," *Thin Solid Films*, vol. 151, no. 3, pp. 403–412, 1987.
- [75] D. Song *et al.*, "Evolution of Si (and SiC) nanocrystal precipitation in SiC matrix," *Thin Solid Films*, vol. 516, no. 12, pp. 3824–3830, 2008.
- [76] K. Xue, L.-S. Niu, H.-J. Shi, and J. Liu, "Structural relaxation of amorphous silicon carbide thin films in thermal annealing," *Thin Solid Films*, vol. 516, no. 12, pp. 3855–3861, 2008.
- [77] A.-İ. El khalfi *et al.*, "FTIR and Raman study of rapid thermal annealing and oxidation effects on structural properties of Silicon-rich $\text{Si}_x\text{C}_{1-x}$ thin films deposited by R.F co-sputtering," *Vib. Spectrosc.*, vol. 89, pp. 44–48, 2017.
- [78] S. Ulrich, T. Theel, J. Schwan, V. Batori, M. Scheib, and H. Ehrhardt, "Low temperature formation of β -silicon carbide," *Diam. Relat. Mater.*, vol. 6, no. 5–7, pp. 645–648, 1997.
- [79] B. Akaoglu, K. Sel, I. Atilgan, and B. Katircioğlu, "Carbon content influence on the optical constants of hydrogenated amorphous silicon carbon alloys," *Opt. Mater. (Amst.)*, vol. 30, no. 8, pp. 1257–1267, 2008.
- [80] G. Ambrosone, U. Coscia, S. Ferrero, F. Giorgis, P. Mandracci, and C. F. Pirri, "Structural and optical properties of hydrogenated amorphous silicon-carbon alloys grown by plasma-enhanced chemical vapour deposition at various rf powers," *Philos. Mag. B*, vol. 82, no. 1, pp. 35–46, 2002.
- [81] P. Musumeci, R. Reitano, L. Calcagno, F. Roccaforte, A. Makhtari, and M. G. Grimaldi, "Relaxation and crystallization of amorphous silicon carbide probed by optical measurements," *Philos. Mag. B*, vol. 76, no. 3, pp. 323–333, 1997.
- [82] H. Shaik, K. H. T. Raman, and G. M. Rao, "Influence of Si–C bond density on the properties of $\text{a-Si}_{1-x}\text{C}_x$ thin films," *Appl. Surf. Sci.*, vol. 258, no. 7, pp. 2989–2996, 2012.

- [83] T. Chen, F. Köhler, A. Heidt, Y. Huang, F. Finger, and R. Carius, "Microstructure and electronic properties of microcrystalline silicon carbide thin films prepared by hot-wire CVD," *Thin Solid Films*, vol. 519, no. 14, pp. 4511–4515, 2011.
- [84] T. Rajagopalan, X. Wang, B. Lahlouh, C. Ramkumar, P. Dutta, and S. Gangopadhyay, "Low temperature deposition of nanocrystalline silicon carbide films by plasma enhanced chemical vapor deposition and their structural and optical characterization," *J. Appl. Phys.*, vol. 94, no. 8, pp. 5252–5260, 2003.
- [85] G. De Cesare *et al.*, "Crystallization of amorphous silicon carbide thin films by laser treatment," *Surf. Coatings Technol.*, vol. 80, no. 1–2, pp. 237–241, 1996.
- [86] S. Janz, "Amorphous Silicon Carbide for Photovoltaic Applications," Fraunhofer Institut für Solare Energiesysteme, 2006.
- [87] C.-K. Jung *et al.*, "Hydrogenated amorphous and crystalline SiC thin films grown by RF-PECVD and thermal MOCVD; comparative study of structural and optical properties," *Surf. Coatings Technol.*, vol. 171, no. 1–3, pp. 46–50, 2003.
- [88] D. K. Basa, G. Ambrosone, U. Coscia, and A. Setaro, "Crystallization of hydrogenated amorphous silicon carbon films with laser and thermal annealing," *Appl. Surf. Sci.*, vol. 255, no. 10, pp. 5528–5531, 2009.
- [89] M. Künle *et al.*, "Si-rich a-SiC:H thin films: Structural and optical transformations during thermal annealing," *Thin Solid Films*, vol. 519, no. 1, pp. 151–157, 2010.
- [90] G. Attolini, F. Rossi, F. Fabbri, M. Bosi, G. Salviati, and B. E. Watts, "Cubic SiC nanowires : growth, characterization and applications," in *Nanowires*, P. Prete, Ed. InTechOpen, 2010, pp. 1–23.

- [91] R. K. Tripathi, O. S. Panwar, A. K. Kesarwani, and S. Chockalingam, “Phosphorous doped hydrogenated amorphous silicon carbide films deposited by filtered cathodic vacuum arc technique,” in *Physics of Semiconductor Devices*, V. K. Jain and A. Verma, Eds. Switzerland: Springer International Publishing, 2014, pp. 383–386.
- [92] S. M. Kahar *et al.*, “Synthesis of SiC nanowhiskers from graphite and silica by microwave heating,” *Mater. Sci.*, vol. 34, no. 4, pp. 770–779, 2016.
- [93] Q. Nian *et al.*, “Direct laser writing of nanodiamond films from graphite under ambient conditions,” *Sci. Rep.*, vol. 4, no. 6612, pp. 1–8, 2014.
- [94] J. Fan and P. K.-H. Chu, “General properties of bulk SiC,” in *Silicon Carbide Nanostructures Fabrication, Structure, and Properties*, Springer, 2014, pp. 7–114.
- [95] A. Didari and M. Pinar Mengüç, “A design tool for direct and non-stochastic calculations of near-field radiative transfer in complex structures: The NF-RT-FDTD algorithm,” *J. Quant. Spectrosc. Radiat. Transf.*, vol. 197, pp. 95–105, 2017.
- [96] T. Okutucu-Özyurt, E. B. Elçioğlu, R. Denker, A. Didari, and M. P. Mengüç, “towards nano-scale thermophotovoltaic applications: discussions for material selection and measuring system,” in *Proceedings of the 8th International Symposium on Radiative Transfer, RAD-16*, 2016.
- [97] E. B. Elçioğlu, T. Okutucu Özyurt, and M. P. Mengüç, “impacts of material types and fabrication methods to enhance near field radiative transfer for energy harvesting devices,” in *THERMAM 2016 3rd International Conference on Thermophysical and Mechanical Properties of Advanced Materials, Full Text Proceedings*, 2016, pp. 1–11.
- [98] E. B. Elçioğlu, R. Denker, A. Didari, T. Okutucu-Özyurt, and M. P. Mengüç, “termofotovoltaik sistemlerde yakın alan ışınımı ile enerji harmanlama çalışmalarının derlemesi (review of near field thermal radiation harvesting studies in thermophotovoltaic systems),” in *20. Ulusal Isı Bilimi ve Tekniği Kongresi ULIBTK’15 Bildiriler Kitabı*, 2015, pp. 1491–1498.

- [99] A. Didari and M. P. Mengüç, “Near-field thermal emission between corrugated surfaces separated by nano-gaps,” *J. Quant. Spectrosc. Radiat. Transf.*, vol. 158, pp. 43–51, 2015.
- [100] A. Didari, E. B. Elçioğlu, T. Okutucu-Özyurt, and M. P. Mengüç, “Tailoring near-field thermal radiation with mesoporous GaN and h-BN designer metamaterials,” in *Proceedings of Eurotherm Seminar 110 – Computational Thermal Radiation in Participating Media - VI*, 2018.
- [101] A. Didari, E. B. Elçioğlu, T. Okutucu-Özyurt, and M. P. Mengüç, “Near-Field Thermal Emission from GaN-SiC Double-layer Structures,” in *Proceedings of 3rd International Workshop on Nano-Micro Thermal Radiation*, 2017.
- [102] E. B. Elçioğlu, A. Didari, T. Okutucu-Özyurt, and M. P. Mengüç, “GaN-SiC Katmanlı Nano-Yapılar ve Yakın-Alan Işınımına Sıcaklık Farkı ve Mesafenin Etkileri,” in *21. Ulusal Isı Bilimi ve Tekniği Kongresi ULIBTK’17 Bildiriler Kitabı*, 2000, no. 1, pp. 924–930.
- [103] E. B. Elçioğlu, M. Korkmaz, M. Kulakcı, and T. Okutucu-Özyurt, “Deposition of Silicon Carbide Thin Films at Low RF Power and their Thermal Annealing for Improved Structure,” *Submitt. to Thin Solid Films*, 2018.
- [104] E. B. Elçioğlu, T. Okutucu Özyurt, and M. P. Mengüç, “Near-Field Radiative Transfer Between Doped Silicon Wafers and Silicide Films,” in *NanoTR-14, 14th Nanoscience and Nanotechnology Conference Book of Abstracts*, 2018, p. 290.
- [105] E. B. Elçioğlu, A. Didari, T. Okutucu Özyurt, and M. P. Mengüç, “Tunable near-field radiative transfer by III-V group compound semiconductors,” *Submitt. to J. Phys. D Appl. Phys.*, 2018.
- [106] S. Basu, “Near-field radiative energy transfer at nanometer distances,” Georgia Institute of Technology, 2009.
- [107] M. Francoeur, “Near-field radiative transfer: thermal radiation, thermophotovoltaic power generation and optical characterization,” University of Kentucky, 2010.

- [108] A. J. Huber, B. Deutsch, L. Novotny, and R. Hillenbrand, “Focusing of Surface Phonon Polaritons,” *Appl. Phys. Lett.*, vol. 92, no. 203104, pp. 1–3, 2008.
- [109] S. Shen, A. Narayanaswamy, and G. Chen, “Surface phonon polaritons mediated energy transfer between nanoscale gaps,” *Nano Lett.*, vol. 9, no. 8, pp. 2909–2913, 2009.
- [110] S. Basu and Z. M. Zhang, “Maximum energy transfer in near-field thermal radiation at nanometer distances,” *J. Appl. Phys.*, vol. 105, no. 093535, pp. 1–6, 2009.
- [111] M. van Exter and G. Grischkowsky, “Carrier dynamics of electrons and holes in moderately doped silicon,” *Phys. Rev. B*, vol. 41, no. 17, pp. 12140–12149, 1990.
- [112] J. W. Cleary *et al.*, “IR permittivities for silicides and doped silicon,” *J. Opt. Soc. Am. B*, vol. 27, no. 4, pp. 730–734, 2010.
- [113] L. J. Chen, “Metal silicides: An integral part of microelectronics,” *J. Miner. Met. Mater. Soc.*, vol. 57, no. 9, pp. 24–30, 2005.
- [114] D. Manchon *et al.*, “Plasmonic coupling with most of the transition metals: a new family of broad band and near infrared antennas,” *Nanoscale*, vol. 7, no. 3, pp. 1181–1192, 2015.
- [115] J. Chochol *et al.*, “Plasmonic behavior of III-V semiconductors in far-infrared and terahertz range,” *J. Eur. Opt. Soc. Publ.*, vol. 13, pp. 1–8, 2017.
- [116] S. Adachi, *Properties of Group-IV, III-V and II-VI Semiconductors*. West Sussex, England: John Wiley & Sons, 2005.
- [117] F. Bechstedt *et al.*, “Polytypism and Properties of Silicon Carbide,” *Phys. Status Solidi*, vol. 202, no. 1, pp. 35–62, 1997.
- [118] Y. M. Lei *et al.*, “Investigation and modeling of the infrared optical properties of direct current sputtered SiC films on silicon,” *J. Appl. Phys.*, vol. 88, no. 5, pp. 3053–3058, 2000.
- [119] T. E. Tiwald *et al.*, “Carrier concentration and lattice absorption in bulk and epitaxial silicon carbide determined using infrared ellipsometry,” *Phys. Rev. B*, vol. 60, no. 16, pp. 11464–11474, 1999.

- [120] C. Liu, *Foundations of MEMS: International Edition*, 2nd ed. Pearson Education Limited, 2014.
- [121] “Kurt J. Lesker Company, Benefits of Bonding Sputtering Targets in Indium Target Bonding Service.” [Online]. Available: https://www.lesker.com/newweb/deposition_materials/depositionmaterials_targetbonding_indium.cfm.
- [122] R. Anzalone *et al.*, “Growth Rate Effect on 3C-SiC Film Residual Stress on (100) Si Substrates,” *Mater. Sci. Forum*, vol. 645–648, pp. 143–146, 2010.
- [123] D. Alok and B. J. Baliga, “A Novel Method for Etching Trenches in Silicon Carbide,” *J. Electron. Mater.*, vol. 24, no. 4, pp. 311–314, 1995.
- [124] J. A. Edmond, J. W. Palmour, and R. F. Davis, “Chemical Etching of Ion Implanted Amorphous Silicon Carbide,” *J. Electrochem. Soc. Solid-State Sci. Technol.*, vol. 133, no. 3, pp. 650–652, 1986.
- [125] C. S. Roper, R. T. Howe, and R. Maboudian, “Room-Temperature Wet Etching of Polycrystalline and Nanocrystalline Silicon Carbide Thin Films with HF and HNO₃,” *J. Electrochem. Soc.*, vol. 156, no. 3, pp. D104–D107, 2009.
- [126] B. C. Smith, *Fundamentals of Fourier Transform Infrared Spectroscopy*, 2nd Ed. FL: Taylor and Francis Group, LLC, 2011.
- [127] M. A. Fraga, R. S. Pessoa, H. S. Maciel, and M. Massi, “Recent Developments on Silicon Carbide Thin Films for Piezoresistive Sensors Applications,” in *Silicon Carbide Materials, Processing and Applications in Electronic Devices*, M. Mukherjee, Ed. InTechOpen, 2009, pp. 369–388.
- [128] R. Vasiliauskas, “Sublimation Growth and Performance of Cubic Silicon Carbide,” Linköping University, 2012.
- [129] H. L. Juan, “Structural and Electrical Characterisations of Amorphous Silicon Carbide Films,” National University of Singapore, 2000.
- [130] A. L. Leal-Cruz and M. I. Pech-Canul, “In situ synthesis of Si₃N₄ from Na₂SiF₆ as a silicon solid precursor,” *Mater. Chem. Phys.*, vol. 98, no. 1, pp. 27–33, 2006.


- [131] W. G. Spitzer, D. A. Kleinman, and C. J. Frosch, “Infrared Properties of Cubic Silicon Carbide Films,” *Phys. Rev.*, vol. 113, no. 1, pp. 133–136, 1959.
- [132] “Atmospheric window.” [Online]. Available: http://www.ccpo.odu.edu/SEES/veget/class/Chap_2/2_Js/2-03.jpg. [Accessed: 20-Nov-2017].
- [133] Y. T. Kim, S. G. Yoon, H. Kim, S. J. Suh, G. E. Jang, and D. H. Yoon, “Crystallization of a-Si : H and a-SiC : H thin films deposited by PECVD,” *J. Ceram. Process. Res.*, vol. 6, no. 4, pp. 294–297, 2005.
- [134] Y.-T. Kim, S.-M. Cho, B. Hong, S.-J. Suh, G.-E. Jang, and D.-H. Yoon, “Annealing Effect on the Optical Properties of a-SiC:H Films Deposited by PECVD,” *Mater. Trans.*, vol. 43, no. 8, pp. 2058–2062, 2002.
- [135] V. Kulikovskiy, V. Vorlí, P. Bohá, and M. Stranyánek, “Hardness and elastic modulus of amorphous and nanocrystalline SiC and Si films,” *Surf. Coat. Technol.*, vol. 202, no. 9, pp. 1738–1745, 2008.
- [136] S. Majee, D. Barshilia, S. Kumar, and P. Mishra, “Signature of growth-deposition technique on the properties of PECVD and thermal SiO₂,” *AIP Conf. Proc.*, vol. 1989, no. 1, pp. 1–8, 2018.
- [137] T. Cui, “Dry Etching.” [Online]. Available: http://me.umn.edu/courses/me8254/attfiles/Lecture 07 Dry Etching_Full.pdf.
- [138] C. Gui, H. Albers, J. G. E. Gardeniers, M. Elwenspoek, and P. V. Lambeck, “Fusion bonding of rough surfaces with polishing technique for silicon micromachining,” *Microsyst. Technol.*, vol. 3, no. 3, pp. 122–128, 1997.
- [139] T. Suni, K. Henttinen, I. Suni, and J. Mäkinen, “Effects of Plasma Activation on Hydrophilic Bonding of Si and SiO₂,” *J. Electrochem. Soc.*, vol. 149, no. 6, pp. G348–G351, 2002.
- [140] V. Medvecká, A. Zahoranová, T. Plecenik, D. Kováčik, and M. Černák, “Possibility of Wafer Direct Bonding Using Low-temperature Atmospheric Pressure Plasma,” in *WDS’13 Proceedings of Contributed Papers, Part III*, 2013, pp. 122–127.
- [141] C. Mai, M. Li, and S. Yang, “Low temperature direct bonding of silica glass via wet chemical surface activation,” *RSC Adv.*, vol. 5, no. 53, pp. 42721–42727, 2015.

- [142] C. Mai, J. Sun, H. Chen, C.-K. Mai, and M. Li, “Silicon direct bonding via low-temperature wet chemical surface activation,” *RSC Adv.*, vol. 43, no. 1–3, pp. 1–7, 2016.
- [143] C. Gui *et al.*, “Selective wafer bonding by surface roughness control,” *J. Electrochem. Soc.*, vol. 148, no. 4, pp. G225–G228, 2001.
- [144] M. Ghashami, J. Bailey, E. Mitchell, E. B. Elcioglu, A. Didari, and M. P. Menguc, “Sub-Continuum Air Conduction Measurement between Planar Structures,” in *Nanoscale and Microscale Heat Transfer 2018, NMHT-VI, Eurotherm 111*, 2018, pp. 1–2.

APPENDICES

A. Permission for the Reuse of Figure 5

08.11.2018 Rightslink® by Copyright Clearance Center

 **Copyright Clearance Center**  [Home](#) [Account Info](#) [Help](#) 

 **ACS Publications** Most Trusted. Most Cited. Most Read. **Title:** Surface Phonon Polaritons Mediated Energy Transfer between Nanoscale Gaps **Author:** Sheng Shen, Arvind Narayanaswamy, Gang Chen **Publication:** Nano Letters **Publisher:** American Chemical Society **Date:** Aug 1, 2009 **Copyright © 2009, American Chemical Society**

Logged in as:
Elif Begum Ecioglu
Account #: 3000952905
[LOGOUT](#)

PERMISSION/LICENSE IS GRANTED FOR YOUR ORDER AT NO CHARGE

This type of permission/license, instead of the standard Terms & Conditions, is sent to you because no fee is being charged for your order. Please note the following:

- Permission is granted for your request in both print and electronic formats, and translations.
- If figures and/or tables were requested, they may be adapted or used in part.
- Please print this page for your records and send a copy of it to your publisher/graduate school.
- Appropriate credit for the requested material should be given as follows: "Reprinted (adapted) with permission from (COMPLETE REFERENCE CITATION). Copyright (YEAR) American Chemical Society." Insert appropriate information in place of the capitalized words.
- One-time permission is granted only for the use specified in your request. No additional uses are granted (such as derivative works or other editions). For any other uses, please submit a new request.

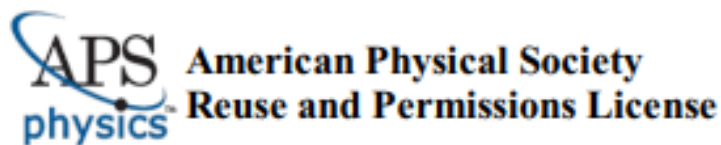
If credit is given to another source for the material you requested, permission must be obtained from that source.

[BACK](#)

[CLOSE WINDOW](#)

Copyright © 2018 [Copyright Clearance Center, Inc.](#) All Rights Reserved. [Privacy statement](#). [Terms and Conditions](#).
Comments? We would like to hear from you. E-mail us at customerscare@copyright.com

B. Permission for the Reuse of Figure 42



08-Nov-2018

This license agreement between the American Physical Society ("APS") and Elif Begum Ekioglu ("You") consists of your license details and the terms and conditions provided by the American Physical Society and SciPris.

Licensed Content Information

License Number: RNP/18/NO V009191
License date: 08-Nov-2018
DOI: 10.1103/PhysRev.113.133
Title: Infrared Properties of Cubic Silicon Carbide Films
Author: W. G. Spitzer, D. A. Kleinman, and C. J. Frosch
Publication: Physical Review
Publisher: American Physical Society
Cost: USD \$ 0,00

Request Details

Does your reuse require significant modifications: No
Specify intended distribution locations: Worldwide
Reuse Category: Reuse in a thesis/dissertation
Requestor Type: Student
Items for Reuse: Figures/Tables
Number of Figure/Tables: 1
Figure/Tables Details: Transmission of three SiC windows in the spectral region of the resonance absorption band
Format for Reuse: Print and Electronic
Total number of print copies: Up to 1000

Information about New Publication:

University/Publisher: Middle East Technical University
Title of dissertation/thesis: FABRICATION OF SILICON CARBIDE-ON-SILICON BASED DEVICES FOR EFFECTIVE NEAR-FIELD THERMAL RADIATION TRANSFER
Author(s): Elif Begum Ekioglu
Expected completion date: Nov. 2018

License Requestor Information

Name: Elif Begum Ekioglu
Affiliation: Individual
Email Id: ebegumekioglu@gmail.com
Country: Turkey

TERMS AND CONDITIONS

The American Physical Society (APS) is pleased to grant the Requestor of this license a non-exclusive, non-transferable permission, limited to Print and Electronic format, provided all criteria outlined below are followed.

1. You must also obtain permission from at least one of the lead authors for each separate work, if you haven't done so already. The author's name and affiliation can be found on the first page of the published Article.
2. For electronic format permissions, Requestor agrees to provide a hyperlink from the reprinted APS material using the source material's DOI on the web page where the work appears. The hyperlink should use the standard DOI resolution URL, <http://dx.doi.org/{DOI}>. The hyperlink may be embedded in the copyright credit line.
3. For print format permissions, Requestor agrees to print the required copyright credit line on the first page where the material appears: "Reprinted (abstract/excerpt/figure) with permission from [(FULL REFERENCE CITATION) as follows: Author's Names, APS Journal Title, Volume Number, Page Number and Year of Publication.] Copyright (YEAR) by the American Physical Society."
4. Permission granted in this license is for a one-time use and does not include permission for any future editions, updates, databases, formats or other matters. Permission must be sought for any additional use.
5. Use of the material does not and must not imply any endorsement by APS.
6. APS does not imply, purport or intend to grant permission to reuse materials to which it does not hold copyright. It is the requestor's sole responsibility to ensure the licensed material is original to APS and does not contain the copyright of another entity, and that the copyright notice of the figure, photograph, cover or table does not indicate it was reprinted by APS with permission from another source.
7. The permission granted herein is personal to the Requestor for the use specified and is not transferable or assignable without express written permission of APS. This license may not be amended except in writing by APS.
8. You may not alter, edit or modify the material in any manner.
9. You may translate the materials only when translation rights have been granted.
10. APS is not responsible for any errors or omissions due to translation.
11. You may not use the material for promotional, sales, advertising or marketing purposes.
12. The foregoing license shall not take effect unless and until APS or its agent, Aptara, receives payment in full in accordance with Aptara Billing and Payment Terms and Conditions, which are incorporated herein by reference.
13. Should the terms of this license be violated at any time, APS or Aptara may revoke the license with no refund to you and seek relief to the fullest extent of the laws of the USA. Official written notice will be made using the contact information provided with the permission request. Failure to receive such notice will not nullify revocation of the permission.
14. APS reserves all rights not specifically granted herein.
15. This document, including the Aptara Billing and Payment Terms and Conditions, shall be the entire agreement between the parties relating to the subject matter hereof.

Additional Note on the Reuse and Permission License from American Physical Society (APS), for the reuse of Figure 4 of W. G. Spitzer, D. A. Kleinman, C. J. Frosch, Physical Review, 113, 1, 133-136, 1959. Copyright (2018) by the American Physical Society. <https://doi.org/10.1103/PhysRev.113.133>" (i.e., Figure 42 in this dissertation)

Item 1 in page 3 of the Reuse and Permission License document (on the previous page) states that, in addition to the permission obtained from APS, one should also obtain permission from at least one of the lead authors of each separate work. On the other hand, permission from authors could not be obtained as the authors contact addresses could not be found. The author of the present work contacted the relevant persons at Aptara's SciPris helpdesk for this issue. Below is the letter they sent, stating that the permission with the license number RNP/18/NO V/009191 is sufficient.



AMERICAN PHYSICAL SOCIETY

One Physics Ellipse, College Park, MD 20740 · <http://www.aps.org>

November 20, 2018

Elif Begum Elcioglu
ebegumelcioglu@gmail.com

Re: Reuse of one figure from Spitzer et al. (1959) Physical Review, 113, 1, 133-136

APS appreciates every effort made to contact the original authors. However, due to the age of the article, you may proceed without fulfilling this requirement.

Sincerely,

A handwritten signature in black ink that reads "Jamie L. Casey". The signature is written in a cursive style.

Jamie L. Casey
Publication Account Coordinator

C. Preliminary Near-Field Radiative Transfer Test Results from Utah Nano-Energy Laboratory

The results presented below belong to the samples with 50 nm SiC-on-Si fabricated at METU-MEMS Center, and EF 3680 (purchased from Griffith University). The heater power stands for the amount of power to be supplied to the heater in order to keep the temperature of the emitter constant. In these experiments, the emitter temperatures were fixed to $\approx 55^{\circ}\text{C}$ and 60°C respectively for 50 nm and 200 nm thick SiC thin film cases, while the receiver temperatures were not controlled.

After the contact of the samples at the smaller edge of the retraction distance (starting from 0 nm), it is possible to observe the near-field effects on radiative transfer. On the other hand, these data are preliminary and need more analyses.

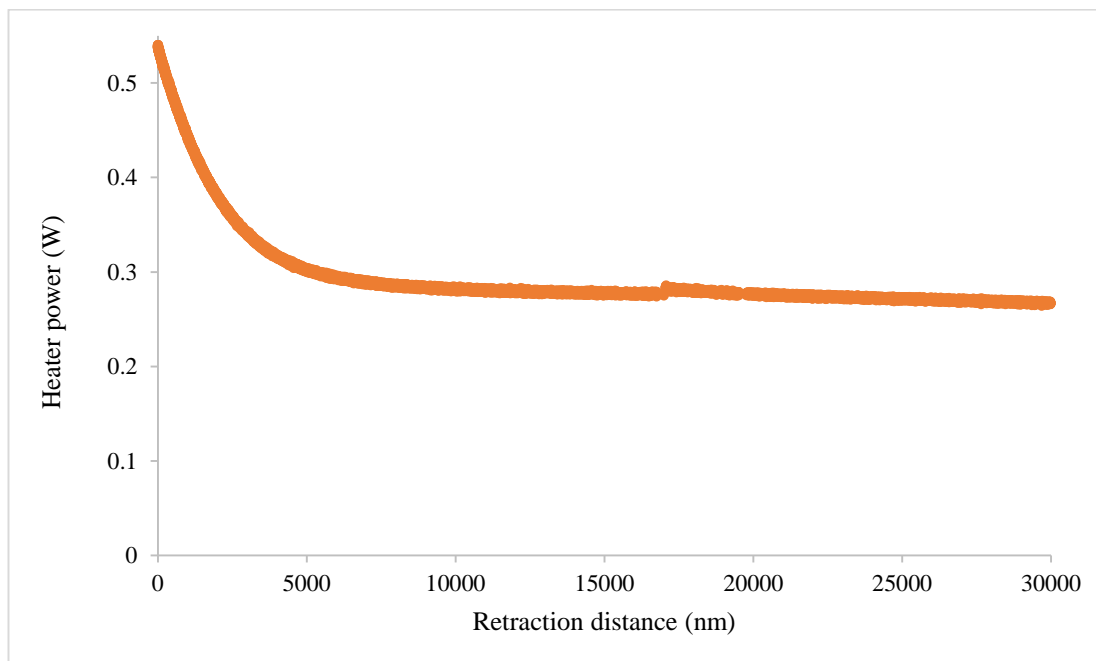


Figure 93. NFRT experiment results with 50 nm SiC-on-Si samples.

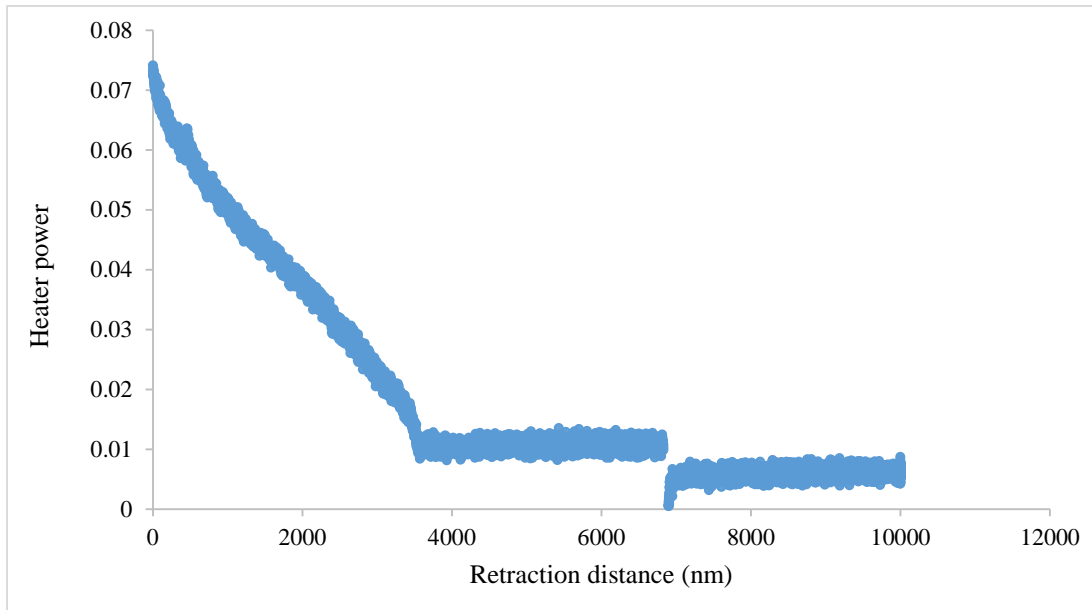


Figure 94.NFRT experiment results with 200 nm SiC-on-Si samples.

CURRICULUM VITAE

PERSONAL INFORMATION

Surname, Name: Elçioğlu, Elif Begüm
Nationality: Turkish (TC)
Date and Place of Birth: 9 October 1989, Eskişehir
Marital Status: Single
Phone: +90 222 712 53 05/4936
Fax: +90 222 712 54 04
email: elcioglu.begum@metu.edu.tr

EDUCATION

Degree	Institution	Year of Graduation
MS	Middle East Technical University Mechanical Engineering	2013
BS (major)	Eskişehir Osmangazi University Mechanical Engineering	2011
BS (minor)	Eskişehir Osmangazi University Industrial Engineering, Quality Control Program	2011
High School	Mat-FKB Özel Gelişim Lisesi, Eskişehir	2006

WORK EXPERIENCE

Year	Place	Enrollment
2014-Present	Eskişehir Osmangazi University, Sivrihisar Vocational School, Mechanics Program	Instructor
2015-Present	Eskişehir Osmangazi University, Sivrihisar Vocational School, Mechanics Program	Erasmus Coordinator
2016-Present	Eskişehir Osmangazi University, Women Research Application and Research Center (ESKAM)	Board Member
2014-Present	Eskişehir Osmangazi University, Atatürk's Principles and History of Turkish Revolution Research and Application Center (ATAM)	Board Member
2018-Present	METU-MEMS Research and Application Center	Researcher
2015-2018	TÜBİTAK Research Project (grant no: 214M308)	Project Scholar
2012-2013	TÜBİTAK Research Project	Project Scholar

	(grant no: 110M057)	
Jan-Feb, 2011	Tusaş Engine Industries (TEI), Eskişehir	CO-OP Intern Engineering Student
June-Aug, 2010	Tusaş Engine Industries (TEI), Eskişehir	CO-OP Intern Engineering Student
Jan-Feb, 2010	NSK Armatür ve Aksesuar San. Tic. A.Ş., Eskişehir	Intern Engineering Student
Aug-Sep, 2009	NSK Armatür ve Aksesuar San. Tic. A.Ş., Eskişehir	Intern Engineering Student
June-July, 2009	1. Hava İkmal Bakım Merkezi Komutanlığı, Eskişehir	Intern Engineering Student

FOREIGN LANGUAGES

English (proficient), German (intermediate), French (developing).

PUBLICATIONS

Book Chapters (International)

1. Elçiöğlü E. B., Şimşek, E. and Okutucu-Özyurt, T. “Stability of Nanofluids: Fundamentals, State of the Art, and Potential Applications” (Chapter 6), in *Microscale and Nanoscale Heat Transfer Analysis, Design, and Applications* (Ed: Rebay, M., Kakaç, S., Cotta, R.M.), pp. 155-183, Taylor and Francis Group, LLC (2016).

Articles in Peer-Reviewed Journals (SCI and SCI-Expanded)

1. Mahbulul, I. M., Elcioglu, E. B., Amalina, M. A., Saidur, R., Stability, Thermophysical Properties and Performance Assessment of Alumina-Water Nanofluid with Emphasis on Ultrasonication and Storage Period, *under review by Powder Technology*.
2. Elçiöğlü, E. B., Didari, A., Okutucu Özyurt T., Mengüç, M. P., “Tunable Near-Field Radiative Transfer by III-V Group Compound Semiconductors”, *submitted to Journal of Physics D: Applied Physics*.
3. Elçiöğlü, E. B., Korkmaz, M., Kulakcı, M., Okutucu Özyurt, T., “Deposition of Silicon Carbide Thin Films at low RF Power and Their Thermal Annealing for Improved Structure”, *submitted to Thin Solid Films*.
4. Didari, A., Elçiöğlü, E. B., Okutucu Ozyurt, T. and Menguc, M. P., “Near-Field Radiative Transfer in Spectrally Tunable Double-Layer Phonon-Polaritonic Metamaterials”, *Journal of Quantitative Spectroscopy and Radiative Transfer* 212, 120-127 (2018).

5. Elçioğlu, E. B., Güvenç Yazıcıoğlu, A., Turgut, A. and Anagün, A. S., “Experimental Study and Taguchi Analysis on Alumina-Water Nanofluid Viscosity”, *Applied Thermal Engineering* 128, 973-981 (2018).
6. Mahbubul, I. M., Elçioğlu, E. B., Saidur, R. and Amalina, M. A., “Optimization of Ultrasonication Period for Better Dispersion and Stability of TiO₂-water Nanofluid”, *Ultrasonics Sonochemistry* 37, 360-367 (2017).
7. Elçioğlu, E. B. and Okutucu-Özyurt, T., “An Experimental Study on the Dispersion Stability of Alumina-Water Nanofluids via Particle Size Distribution and Zeta Potential Measurements”, *High Temperatures-High Pressures*, 45(3), 239-250 (2016).
8. Mahbubul, I. M., Saidur, R. Amalina, M. A., Elcioglu, E. B. and Okutucu-Ozyurt, T., “Effective Ultrasonication Process for Better Dispersion of Nanofluid”, *Ultrasonics Sonochemistry* 26, 361-369 (2015).
9. Elçioğlu, E. B., Güvenç Yazıcıoğlu, A. and Kakaç, S. “Nanoakışkan Viskozitesinin Karşılaştırmalı Değerlendirmesi (A Comparative Evaluation of Nanofluid Viscosity)”, *Journal of Thermal Science and Technology (ISI Bilimi ve Tekniği Dergisi)*, 34(1), 137-151 (2014).

Full Papers in the Proceedings of International Scientific Meetings

1. Ghashami, M., Bailey, J., Mitchell, E., Elcioglu, E. B., Didari, A., Okutucu-Ozyurt, T., Menguc, M. P. and Park, K. “Sub-Continuum Air Conduction Measurement between Planar Structures”, no. 142, *Nanoscale and Microscale Heat Transfer 2018, NMHT-VI, Eurotherm 111*, 2-7 Dec, 2018, Levi, Lapland, Finland.
2. Didari, A., Elçioğlu, E. B., Okutucu-Özyurt, T. and Mengüç, M. P., “Tailoring Near-Field Thermal Radiation with Mesoporous GaN and h-BN Designer Metamaterials”, *Eurotherm Seminar 110 – Computational Thermal Radiation in Participating Media – VI*, April 11-13, 2018, Cascais, Portugal.
3. Didari, A., Elçioğlu, E.B., Okutucu Ozyurt, T. and Menguc, M.P., “Near-Field Thermal Emission from GaN-SiC Double-Layer Structures”, *3rd International Workshop on Nano-Micro Thermal Radiation*, June 26-28, 2017, Daejeon, Korea.
4. Elçioğlu, E.B., Okutucu-Özyurt, T. and Mengüç, M. P., “Impacts of Material Types and Fabrication Methods to Enhance Near Field Radiative Transfer for Energy Harvesting Devices”, Article number: 64, *3rd International Conference on Thermophysical and Mechanical Properties of Advanced Materials - THERMAM 2016*, 1-3 September 2016, İzmir, Turkey.
5. Okutucu-Özyurt, T., Elçioğlu, E. B., Denker, R., Didari, A. and Mengüç, M. P., “Towards Nano-Scale Thermophotovoltaic Applications: Discussions for

Material Selection and Measuring System”, The 8th International Symposium on Radiative Transfer RAD-16, 6-10 June 2016, Cappadocia, Turkey.

6. Elçioğlu, E. B. and Okutucu-Özyurt, T., “An Experimental Study on the Dispersion Stability of Alumina-Water Nanofluids via Particle Size Distribution and Zeta Potential Measurements”, in Full Text Proceedings, p. 186-194, THERMAM 2014, June 12-15, 2014, Çeşme, İzmir, Turkey.
7. Şimşek, E., Elçioğlu, E. B. and Okutucu-Ozyurt, T., “Stability of Nanofluids – A Critical Review”, in CONV-14 Proceedings USB as CONV-14 - 314, Convective Heat and Mass Transfer, CONV-14, June, 8-13, 2014, Kuşadası, Turkey.
8. Guvenc Yazicioglu, A. and Elçioğlu, E. B., “Nanofluid Viscosity: An Emerging Research Field”, in Proc. of the ANBRE 13, p.120, The 2013 World Congress on Advances in Nano, Biomechanics, Robotics and Energy Research (ANBRE13), August 25-28, 2013, Seoul, South Korea.

Abstracts in the Proceedings of International Scientific Meetings

1. Elçioğlu, E. B., Didari, A., Okutucu-Özyurt, T. and Mengüç, M. P., “Near-Field Radiative Transfer Between Doped Silicon Wafers and Silicide Films”, ID: 228 (Oral presentation), p. 256, in Proceedings of NanoTR-14, 22-25 September 2018, Çeşme, İzmir, Turkey.
2. Elçioğlu, E. B., Güngör, A., Akseli, G., Camadan, E., Okutucu-Özyurt, T. and Mengüç, M. P., “SiC-on-Si Based Near-Field Radiative Transfer Device Design, Fabrication, and Experimental Setup Development”, ID: 253 (Poster presentation), p. 266, in Proceedings of NanoTR-14, 22-25 September 2018, Çeşme, İzmir, Turkey.
3. Elçioğlu, E.B. and Şaylıgil, Ö., “The First Women Workers Battalion in Ottoman Empire (1917-1919) (Osmanlı Ordusu’nda Birinci Kadın İşçi Taburu (1917-1919))”, 1st International Women Research Symposium (Eskişehir Osmangazi Üniversitesi I. Uluslararası Kadın Araştırmaları Sempozyumu), October 13-14, 2017, Eskişehir, Turkey.
4. Elçioğlu, E.B., Guvenc Yazicioglu, A. and Kakac, S., “Nanofluid Viscosity: A Comparative Summary of Experimental Work in Literature”, 8th Nanoscience and Nanotechnology Congress, June 25-29, 2012, Book of the Abstracts, Accepted Poster Presentations, pp. 508-509, Ankara, Turkey.

Full Papers in the Proceedings of National Scientific Meetings

1. Elçioğlu, E. B., Didari, A., Okutucu-Özyurt, T. and Mengüç, M. P., “GaN-SiC Katmanlı Yapılar Arasındaki Yakın-Alan Işınımına Sıcaklık ve Mesafenin Etkileri”, ULİBTK'17 21. Ulusal Isı Bilimi ve Tekniği Kongresi, 13-16 Eylül 2017, Çorum, Turkey.

2. Elçiöđlu, E. B., Denker, R., Didari, A., Okutucu-Özyurt, T. and Mengüç, M. P., “Termofotovoltaik Sistemlerde Yakın Alan Işınımı İle Enerji Harmanlama Çalışmalarının Derlemesi”, ULIBTK’15 Proceedings (ULİBTK’15 Bildiriler Kitabı), pp. 1491-1500, September, 2-5, 2015, Balıkesir, Turkey.
3. Elçiöđlu, E. B., Güvenç Yazıcıođlu, A. and Kakaç, S., “Nanoakışkan Viskozitesi ve Bağıl Viskozite Denklemlerinin Parametrik Analizi ve Deđerlendirmesi”, ULIBTK’13 Bildiri Özetleri Kitabı, s. 60, 19. Ulusal Isı Bilimi ve Tekniđi Kongresi, 9-12 Eylül 2013, Samsun, Turkey.

Reviewer Appointments

1. 4th Thermal and Fluids Engineering Conference – American Society of Thermal and Fluid Engineers (ASTFE), to be held at April 14-17, 2019, Las Vegas, NV, USA.

HOBBIES

Amateur astrophotography, reading (Ancient Greek philosophy, history of science, science fiction), hiking.